

A remote sensing and geospatial statistical approach to  
understanding distribution and evolution of ignimbrites in  
the Central Andes with a focus on Southern Peru



Dissertation

zur Erlangung des mathematisch-naturwissenschaftlichen Doktorgrades

„Doctor rerum naturalium“

der Georg-August-Universität zu Göttingen

im Promotionsprogramm Geowissenschaften

der Georg-August-University School of Science (GAUSS)

vorgelegt von

Melanie Brandmeier

aus Augsburg

Göttingen 2014

Betreuungsausschuss:

Prof. Dr. Gerhard Wörner, Abteilung Geochemie, GZG

Dr. Stefan Erasmi, Geographisches Institut, GZG

Mitglieder der Prüfungskommission

Referent: Prof. Dr. Gerhard Wörner

Korreferent: Dr. Stefan Erasmi

2. Korreferent: Prof. Dr. Martin Kappas

Weitere Mitglieder der Prüfungskommission:

Prof. Dr. Sharon Webb

Prof. Dr. Hilmar von Eynatten

Prof. Dr. Jonas Kley

Tag der mündlichen Prüfung: 24.02.2014

*„Das Leben ist wert, gelebt zu werden, sagt die Kunst, die schönste Verführerin; das Leben ist wert, erkannt zu werden, sagt die Wissenschaft.“*

Friedrich Nietzsche (1844-1900)

Dedicated to love, an infinite fountain of joy, creativity, strength,  
inspiration and, with the same measure, pain.

## TABLE OF CONTENTS

---

ACKNOWLEDGEMENTS .....	I
PREFACE .....	II
ABSTRACT .....	III
KURZFASSUNG.....	VI

### CHAPTER I:

---

INTRODUCTION.....	1
1 Geological background.....	1
2 Introduction and outline of the thesis.....	3
References .....	5

### CHAPTER II:

---

MANUSCRIPT I: Remote sensing of Carhuarazo volcanic complex using ASTER imagery in Southern Peru to detect alteration zones and volcanic structures – a combined approach of image processing in ENVI and ArcGIS/ArcScene

Abstract .....	7
1 Introduction.....	8
2 Geological setting.....	9
3 Hydrothermal alteration associated to ore deposits .....	11
4 Methods.....	11
4.1 Spectral analysis and ratio images .....	12
4.1.1 Ratio images and mineral indices.....	14
4.1.2 VNIR and SWIR Spectral analysis .....	20
4.1.2.1 <i>Extracting mineralogical information from endmember spectra</i> .....	21
4.1.2.2 <i>Matched filter processing in target areas</i> .....	25
5 Conclusions.....	27
References .....	29

### CHAPTER III:

---

MANUSCRIPT II: Mapping patterns of mineral alteration in volcanic terrains using ASTER data and field spectrometry in Southern Peru

Abstract .....	31
1 Introduction.....	33
2 Location and Geological setting .....	35
3 Methods.....	36

## Table of contents

3.1	Alteration Mapping .....	36
3.2	Ground-truthing .....	39
3.3	Geochemical analysis .....	41
3.3.1	X-ray Fluorescence Spectrometry (XRF) .....	41
3.3.2	Electron Microprobe Analysis (EMPA) .....	41
3.3.3	X-ray Diffraction (XRD) .....	42
3.4	Classification Mapping of Alteration Patterns .....	42
4	Results and Discussion .....	45
4.1	ASTER mineral indices and abundance maps .....	45
4.2	Geochemical analysis- major elements and mineral content (RFA, EMP and XRD) .....	49
4.2.1	X-ray Fluorescence Spectrometry (XRF) .....	49
4.2.2	Electron Micro Probe (EMP) .....	52
4.2.3	X-ray Diffraction .....	52
4.3	ASD hyperspectral data .....	52
4.4	Alteration intensity, mineral abundances and whole rock compositions .....	57
4.5	Classification and alteration mapping using ASTER reflectance and emissivity data .....	59
5	Discussion .....	62
5.1	Chemical effects and styles of alteration .....	62
5.2	Can calderas be identified by use of ASTER spectral mapping? .....	67
6	Summary and conclusions .....	69
	References .....	71

## CHAPTER IV:

---

MANUSCRIPT III: Age and distribution of Neogene ignimbrites in Southern Peru as tracers for uplift, erosion and changes in the Andean drainage divide between the Pacific and Atlantic Oceans

Abstract .....	75	
1	Introduction .....	77
2	Methods .....	78
2.1	Sample collection .....	78
2.2	$^{40}\text{Ar}/^{39}\text{Ar}$ Geochronology .....	78
2.3	Stratigraphy and DEM analysis .....	80
3	Results and Discussion .....	81
3.1	$^{40}\text{Ar}/^{39}\text{Ar}$ Geochronology and Stratigraphy .....	81
3.1.1	Urayama valley .....	83
3.1.2	Río Soras valley .....	86
3.1.3	Río Visca/Mayobamba valley .....	88
3.1.4	Río Caracha valley .....	90
3.1.5	Santa Ana Caldera .....	93

## Table of contents

3.2	Ignimbrite distribution, timing and implications for uplift, erosion and geomorphologic evolution .....	95
3.2.1	General considerations.....	95
3.2.2	Timing and extent of ignimbrites.....	96
3.2.3	Constraints of uplift, erosion and morphological evolution on the eastern Andean margin .....	100
4	Summary and Conclusions .....	105
	References .....	108

### CHAPTER V:

---

#### MANUSCRIPT IV: Temporal and compositional patterns and variations in ignimbrite volcanism in the Andes over the past 30 Ma

Abstract .....	111
1 Introduction .....	114
2 Methods .....	115
2.1 X-ray Fluorescence Spectrometry (RFA).....	115
2.2 Inductively Coupled Plasma Mass Spectrometry (ICP-MS) analysis.....	116
2.3 Database compilation and mapping.....	116
2.4 Statistical analysis.....	118
2.4.1 Geospatial statistics.....	118
2.4.1.1 <i>Kriging models for variations in isotopes reflecting crustal domains</i> .....	118
2.4.1.2 <i>Areal extent and volumes of ignimbrites through time as a measure of ignimbrite “flare-ups” during Andean orogeny</i> .....	119
2.4.2 Multivariate statistics on compositional data .....	120
3 Results and Discussion .....	121
3.1 Database compilation and mapping.....	121
3.2 Statistical analysis.....	124
3.2.1 Geospatial statistics.....	124
3.2.1.1 <i>Kriging models and Principal Component analysis (PCA) for variations in lead, strontium and neodymium isotopes reflecting crustal domains</i> .....	124
3.2.1.1.1 <i>Exploratory data analysis</i> .....	124
3.2.1.1.2 <i>Kriging</i> .....	125
3.2.1.2 <i>Areal extent and volume estimates for ignimbrites through time as a measure of ignimbrite “flare-ups” during Andean orogeny</i> .....	130
3.2.2 Multivariate statistics on compositional data .....	141
3.2.2.1 <i>Cluster analysis applied to Ignimbrite whole-rock geochemistry</i> .....	142
3.2.2.1.1 <i>How does clustering without a-priori assumptions relate to traditional geochemical parameters?</i> .....	147

## Table of contents

3.2.2.1.2 <i>Are there systematic correlations with age, location or volume?</i> .....	152
3.2.2.2 <i>Whole-rock compositional signatures as a “fingerprint” for discriminating ignimbrites</i> .....	154
4 Summary and Conclusions .....	161
References .....	164

### CHAPTER VI:

---

SUMMARY, CONCLUSIONS AND OUTLOOK.....	170
References .....	175

### APPENDIX (PROVIDED ON DVD)

---

#### MANUSCRIPT I:

- ✓ Video clips

#### MANUSCRIPT II:

- ✓ kml file with sample locations and geochemical data

#### MANUSCRIPT III:

- ✓ Summary of  $^{40}\text{Ar}/^{39}\text{Ar}$  dating

#### MANUSCRIPT IV:

- ✓ Appendix: A: Kriging Model summaries  
B: Volume calculations
- ✓ GIS database
  - Andean ignimbrite database (AID) (samples, mapping database and structures)
  - DEM analysis (ASTER DEM and drainage analysis)
  - Statistical analysis (Kriging models, cluster analysis results)
  - Additional master table of analyzed samples in excel format
- ✓ Andes evolution film

## ACKNOWLEDGEMENTS

Most notably, I would like to thank Prof. Gerhard Wörner, who fulfilled my wish to work in the Andes by agreeing to write the DFG proposal that eventually funded the project. He was always open to new ideas, especially to new methods I wanted to use, and supported me with his extensive knowledge of the Andes and in geoscience in general. Furthermore, I thank my co-supervisor, Dr. Stefan Erasmi for his constant support in all questions concerning remote sensing and GIS.

Special thanks to my Australian colleagues T. Cudahy, M. Caccetta and Carsten Laukamp for allowing me to stay at CSIRO for three weeks to learn how to better process ASTER data. Many thanks to Dr. M. Mamani for her help when I first arrived in Göttingen, her support during fieldwork in Peru and, especially, for her sympathetic ear for all my concerns and doubts.

I sincerely thank John Hora for manifold discussions and linguistic corrections of my manuscripts. Furthermore I want to thank Rosanne Heistek who was always full of encouragement and the best officemate ever. For encouraging words during the whole PhD I want to thank Prof. Dr. W. Siebel.

I am grateful to all staff members of the Department of Geochemistry, who supported me in all questions regarding laboratory work. Many thanks to Dr. K. Simon and Dr. G. Hartmann, who spent hours making ICP MS and XRF measurements and Dr. B. Jicha of Wisconsin-Madison University for Ar/Ar dating. Special thanks to Erwin Schiffczyk and Angela Reitz for their support during sample preparation and Stefan Möller-McNett for assisting in all questions concerning IT.

Many thanks to S. Pospiech and M. Kohno for final corrections. For help with sample preparation, I want to thank B. Heller, G. Breedveld and M. Brinckmann who worked hard to get all work done in time. Furthermore, I want to thank A. Höweling, K. Nitzsche, T. Ohlendorf and C. Hansen for assistance during fieldwork and with sample preparations and measurements.

Finally, I wish to thank my parents, who in the first place enabled my scientific education and were always full of encouragement and love.

The studies included in this thesis were funded by the German National Science Foundation, DFG grant Wo 362-43-1.



## PREFACE

This doctoral thesis comprises the following articles that are either published or in preparation, as indicated below:

Brandmeier, M., 2010. Remote sensing of Carhuarazo volcanic complex using ASTER imagery in Southern Peru to detect alteration zones and volcanic structures – a combined approach of image processing in ENVI and ArcGIS/ArcScene. *Geocarto International* 25, 629-648.

Brandmeier, M., Erasmi, S., Hansen, C., Höweling, A., Nitzsche, K., Ohlendorf, T., Mamani, M., Wörner, G., 2013. Mapping patterns of mineral alteration in volcanic terrains using ASTER data and field spectrometry in Southern Peru. *Journal of South American Earth Sciences* 48, 296-314.

Brandmeier, M., Mamani, M., Jicha, B., Wörner, G. (in preparation). Age and distribution of Neogene ignimbrites in Southern Peru as tracers for uplift, erosion and changes in the Andean drainage divide between the Pacific and Atlantic Oceans

Brandmeier, M., Wörner, G. (in preparation). Temporal and compositional patterns and variations of ignimbrite volcanism in the Andes over the past 30 Ma.

## ABSTRACT

This PhD thesis investigates timing, cause and location of “ignimbrite flare ups” during the evolution of the Central Andean uplift and relates volcano-tectonic structures and calderas with shallow intrusive stocks to mineralization by applying methods of remote sensing, GIS and geospatial statistics together with traditional geological fieldwork,  $^{40}\text{Ar}/^{39}\text{Ar}$  geochronology and geochemical analysis.

**Chapters II to IV** focus on Southern Peru, while **Chapter V** puts local results on an Andean scale, investigating compositional differences in ignimbrites and modelling ignimbrite eruptions in space and time.

### CHAPTER II:

In this chapter we present first results from a reconnaissance study using ASTER data in Southern Peru. A combined approach to detect hydrothermal alteration zones and their mineral distribution is proposed for a relatively remote area around the Carhuarazo volcanic complex in Southern Peru encompassing 2,222 km<sup>2</sup>. In this region, tertiary volcanic structures associated with hydrothermal alteration are well known to host epithermal ore deposits. We make an attempt to detect and to quantify alteration minerals based on spectral analysis using ASTER reflectance data product provided by LP-DAAC. Besides commonly used ratio images, mineral indices (MI) and relative band depth images (RBD), we also extracted end-member spectra using Pixel-Purity-Processing, preceded by minimum noise fraction transformation. These spectra are thought to represent the spectrally purest pixel of the image and show the typical absorption features of the main constituents. Based on this assumption, we used different spectral analysis methods in order to extract the most important alteration minerals for such an environment. These minerals were then used for matched filter processing in areas showing high values in MIs and RBDs. Using this method, we detected and mapped argillic alteration and variations in the distribution of important minerals like alunite, kaolinite or nacrite. There were no indications for the presence of propylitization at ASTER spatial resolutions. Our method can be applied easily to any ASTER scene and provides information about the intensity of alteration and the character of alteration zones. The intensity is highest in the center of the Carhuarazo volcanic complex and is mostly argillic with a high content of alunite, dickite and other clay minerals.

### CHAPTER III:

This chapter further develops results presented in **Chapter II**, focusing on mineral and lithological mapping in an extended area in Southern Peru to better characterize and understand the Tertiary volcanic evolution in this region. Our goal was to characterize volcanic regions near Puquio (Ayacucho) by correlating areas of intense alteration and related ignimbrite outflow sheets. In particular, we spectrally and mineralogically mapped different types and intensities of alteration based on remote sensing and ground-truth data. ASTER ratio images, alteration indices and false color composites were used to select ground-training areas for sample collection and field spectrometry. Alteration samples were characterized geochemically, mineralogical and spectrally. Absorption features correlate with chemical properties and an Index of Absorption was proposed as a measure for alteration intensity. Hyperspectral data from field spectrometry allows identification of important alteration minerals such as kaolinite and smectite. Alteration mineral assemblages range from silicic to argillic to “zeolite-type”. Using a support vector machine classification (SVM)

algorithm on ASTER data, we mapped the different types and intensities of alteration, along with unaltered ignimbrite and lava flows with an accuracy of 80%. We propose a preliminary model for the interpretation of alteration settings, discuss the potential eruption sites of the ignimbrites in the region and, propose pH and temperature estimates for the respective classes based on the mineral assemblages identified.

#### CHAPTER IV:

In this chapter, we present geological and chronological data for the ignimbrites of the area spectrally characterized in **Chapters II and III** in order to constrain the Neogene evolution of Southern Peru.

We present 31  $^{40}\text{Ar}/^{39}\text{Ar}$  ages of ignimbrites and related lava samples from three major valleys draining to the Amazon River and one valley west of the present drainage divide in the area. We combine these with drainage and DEM analysis and present a new stratigraphy for the western side of the drainage divide. We discuss timing, extent and possible eruptive centers for the ignimbrites and propose a “Santa Ana Caldera” with an age of ~5 Ma and a diameter of ~20 km. Ignimbrite ages correspond to the ~20 Ma (Nazca age) and four age ranges within the “Formación Andamarca”: 14 Ma (Andamarca 1), 7.5-9.5 Ma (Andamarca 2), 5-6.5 Ma (Andamarca 3) and 3.5-4 Ma (Andamarca 4).

Based on the position of the samples in the valleys, we found a minimum incision of ~300 m prior to 14 Ma, of ~500-800 m after ~6 Ma and renewed incision after ~3.8 Ma of 200 to 300 m. For the Visca valley, we know of at least one additional event (~9.4 Ma) that filled the valley and cannot be quantified in terms of re-incision. Causes for incision and changes in incision rates are uplift (mainly between 14 Ma to 3.8 Ma) and a change in climate and drainage system with related base-level changes.

Our findings agree with an increase of erosion rates and headwater erosion found by other authors in the Eastern Cordillera at 15-10 Ma that would have shifted the drainage divide in a westerly direction. Uplift on the order of 2000-3500 m found in the Altiplano and Eastern Cordillera since ~ 10 Ma are reflected by river incision of at least 1 km during that time, with at least one more phase of incision (9-6 Ma) that cannot be quantified. Re-incision after 3.8 Ma is probably related to the wetter climate and glaciation history of the area

Comparing the stratigraphic record of the three valleys east of the drainage divide to the one valley west of it and stratigraphies found by other authors for the western escarpment, we found that the 20 Ma Nazca age (and mostly the 14 Ma age) are completely absent on the eastern part of the drainage divide. This striking difference argues for high rates of incision and denudation in that direction whereas the plateau-forming Nazca and Huaylillas ignimbrites are so well preserved on the western escarpment. Assuming that eruptions of these ignimbrites were not completely asymmetric, we argue that this is due to uplift caused by the arrival of the Nazca ridge at that latitude after ~12 Ma, accompanied by a change in precipitation toward more humid conditions on the eastern side of the orogen.

#### CHAPTER V:

This chapter puts our regional findings on an Andean scale. We analyzed temporal and compositional patterns of large volume ignimbrite magmatism in the Central Andes during the Neogene using geostatistical modeling and tested the hypothesis whether we can use compositional signatures to “fingerprint” ignimbrites. In order to examine the spatiotemporal pattern of so-called “ignimbrite flare-ups”, we mapped 201 ignimbrites, together with 1,602 ignimbrite samples (with geochronological and chemical data) using satellite imagery,

available literature, maps and new data presented in **Chapter IV**, creating a Web Mapping Application (WMA) that is now globally available.

Applying cluster analysis to clr-transformed major and trace element data, we grouped ignimbrites according to geochemical characteristics and compared our results to traditional geochemical parameters. Based on major elements, we found a rhyolitic and a dacitic “end-member”. Those “end-members” overlap in REE compositions with more or less pronounced negative Eu anomaly, depletion of MREEs and enrichment/depletion in LREEs. Based on these results, we argue, that a mere distinction between “rhyolitic, crystal-poor, small-volume” and “large-volume, crystal-rich monotonous intermediate” seems to be insufficient to capture differences in ignimbrite evolution and genesis. The large-volume, rhyolitic, ~19 Ma Oxaya ignimbrite, for example, is compositionally distinct from the young, dacitic ~4 Ma APVC Atana ignimbrite, implying a different genesis model than suggested for the large-volume APVC ignimbrites, with accumulation of large bodies of dacitic magma in the upper crust with time, fed by mantle power input. This finding agrees with differences in Sr isotopes, arguing for less crustal assimilation, possibly due to the thinner and colder crust at that time.

To test our hypothesis that compositional signatures can be used to “fingerprint” ignimbrites, we applied discriminant analysis to selected ignimbrites. Classification gave an 87.5% overall classification accuracy and we therefore propose to apply this technique more widely on compositional signatures.

Spatiotemporal pattern of so-called “ignimbrite flare-ups” were simulated by calculating the cumulative areal extent and volume of ignimbrites over time. We propose minimum estimates for the whole CVZ and for five N-S segments. In total, we estimate eruptive volumes of 31,000 km<sup>3</sup>, with 2,400 km<sup>3</sup> for Southern Peru, 2,700 km<sup>3</sup> for Southernmost Peru, 8,400 km<sup>3</sup> for the Altiplano, 14,200 km<sup>3</sup> for the Northern Puna and 3,100 km<sup>3</sup> for the Southern Puna segments. As ignimbrite eruptions represent the surface manifestation of plutonic activity, eruptive volumes can help us to understand processes taking place in the upper crust. Using the same assumptions as De Silva and Gosnold (2007), we calculate a minimum plutonic input of 7,200 km<sup>3</sup>, 8,100 km<sup>3</sup>, 25,200 km<sup>3</sup>, 42,600 km<sup>3</sup> and 9,300 km<sup>3</sup> for the respective segments during the past 30 Ma and observe a N-S “younging” of eruption ages and “ignimbrite pulses”. Major pulses occurred at 19-24 Ma, 13-14 Ma, 6-10, 3-6 Ma with only minor ignimbrites after 3 Ma. We propose that large-volume ignimbrite eruptions occurred in the wake of the subducting Juan-Fernandez ridge, with compression, uplift, shallow subduction and fluid release in a first stage, upon arrival of the ridge, and melting of the so “conditioned” crust due to renewed asthenospheric mantle flow above a steepening slab after the passing of the ridge.

The total estimates for the northern segments 1-3 and the Northern Puna are sub-equal, however, calderas and thus intra-caldera volumes for ignimbrites in these segments are not known and due to higher age, preservation level for the ignimbrites is much lower. Thus, it may be possible, that the latter ignimbrites represent volumes greater than in the Northern Puna. If further studies show that this is the case, the concept of an APVC flare-up should be revised and not viewed as a regionally and temporally restricted event of high-magma flux and batholith construction. Instead, we suggest a paradigm shift towards a dynamic model, with the “flare up” as a moving entity that has progressed across the Andes during the past 25 Ma, probably related to ridge subduction, with the Northern Puna flare up only being the most recent and best preserved remnant, and the Southern Puna Cerro Galán eruption possibly heralding another flare-up.

## KURZFASSUNG

Die vorliegende Doktorarbeit befasst sich mit der zeit-räumlichen Beziehung so genannter „Ignimbrite flare-ups“ während der Hebung der Zentralanden und der damit im Zusammenhang stehenden vulkanisch-tektonischen Strukturen und Calderen, die von lagerstättenkundlichem Interesse sind. Dabei bedienen wir uns, neben traditionellen Methoden der Geologie und Argon Datierungen, der Methoden der Fernerkundung, GIS und Geostatistik. Während **Kapitel II bis IV** Regionalstudien in Süd-Peru darstellen, werden in **Kapitel V** darin erzielte Ergebnisse auf einen Andenmaßstab übertragen um sowohl geochemische Charakteristika, als auch Unterschiede der Ignimbriteruptionen in Raum und Zeit zu modellieren.

### KAPITEL II:

In diesem Kapitel werden die ersten Ergebnisse einer ASTER-Daten basierten Fernerkundungsstudie in Süd-Peru vorgestellt. Ein Ansatz zur Satellitendaten basierten Kartierung hydrothermalen Alterationszonen wird für ein relativ abgelegenes, ca. 2.222 km<sup>2</sup> umfassendes Gebiet um den Carhuarazo Vulkankomplex, vorgestellt. Die hydrothermal alterierten tertiären vulkanischen Strukturen sind hier bekannt für ihre epithermalen Lagerstätten. Mittels VNIR und SWIR Reflektanzdaten wird versucht, Alterationsminerale qualitativ und quantitativ zu kartieren. Dabei wird, neben herkömmlichen Bandkombinationen und spektralen Indizes, versucht, über „Pixel-Purity-Processing“ spektrale Endglieder zu extrahieren. Diese Endglieder sollten die spektral „reinsten“ Pixel der Szene darstellen und entsprechend die Absorptionseigenschaften der Hauptbestandteile tragen. Entsprechend wurden mit spektralanalytischen Methoden die wichtigsten Alterationsminerale ermittelt und im Folgenden mit einem Entmischungsalgorithmus auf jene Gebiete der ASTER Szene angewendet, welche hohe Werte bei den Spektralindizes aufwiesen.

Mittels dieser Methode konnten wir argillitische Alteration detektieren und Unterschiede in der Verbreitung wichtiger Alterationsminerale, wie z.B. Alunit oder Kaolinit, kartieren. Wir fanden, basierend auf der spektralen Auflösung der ASTER Daten, keine Hinweise auf propylitische Alteration. Unsere Methode kann leicht auf andere ASTER Szenen übertragen werden und liefert Informationen über Intensität und Art von Alteration. Im Studiengebiet wurde die höchste Intensität im Zentrum des Carhuarazo kartiert und ist hauptsächlich argillitisch mit hohen Gehalten von Alunit, Kaolinit und anderen Tonmineralen.

### KAPITEL III:

In diesem Kapitel werden die Ergebnisse von **Kapitel II** weiterentwickelt und auf ein größeres Gebiet ausgedehnt. Ziel war es, mittels der lithologischen und Alterationskartierung die tertiäre vulkanische Entwicklung des Gebiets besser zu charakterisieren. Der Zusammenhang zwischen intensiver Alteration und möglichen Ignimbriteruptionen sollte aufgezeigt werden.

Verschiedene Alterationstypen und -intensitäten wurden mittels Fernerkundungs- und Geländedaten kartiert. Absorptionsmerkmale hyperspektraler „ground-truth“ Daten wurden mit geochemischen und mineralogischen Befunden korreliert und ein Absorptionsindex als Maß für die Intensität der Alteration vorgeschlagen. Hyperspektraldaten erlauben die Identifikation wichtiger Alterationsminerale und entsprechend konnten Mineralvergesellschaftungen charakterisiert werden. Diese reichten von starker Silifizierung über argillitische bis

hin zu „zeolithischer“ Alteration von Ignimbriten. Mittels eines Stützvektorenklassifikationsalgorithmus konnten wir diese verschiedenen Alterationstypen, Lava und Ignimbrite mit einer Genauigkeit von 80% klassifizieren.

Basierend auf unseren Ergebnissen, schlagen wir ein Modell zur Interpretation der Alterations-zonen und potenzieller Eruptionszentren der Ignimbrite vor, und präsentieren pH und Temperaturabschätzungen für die jeweiligen Mineralvergesellschaftungen.

#### KAPITEL IV:

In diesem Kapitel präsentieren wir geologische und chronologische Daten der Ignimbrite aus dem in den **Kapiteln II und III** spektral charakterisierten Gebiet mit dem Ziel, die neogene Entwicklung Süd-Perus besser zu belegen.

Anhand 31 neuer  $^{40}\text{Ar}/^{39}\text{Ar}$  Alter für Ignimbrite und Laven von drei Haupttälern östlich der Hauptwasserscheide und einem Tal im Westen wurde eine neue Stratigraphie für das östliche Drainagesystem erarbeitet. Ignimbritalter, Verbreitung und mögliche Eruptionszentren werden diskutiert und eine Calderastruktur („Santa Ana Caldera“) mit einem Durchmesser von ~20 km und einem Alter von ~5 Ma vorgeschlagen. Die Ignimbritalter korrelieren mit dem ~20 Ma Nazca Alter sowie vier Altersklassen innerhalb der „Formación Andamarca“: 14 Ma (Andamarca 1), 7,5-9,5 Ma (Andamarca 2), 5-6,5 Ma (Andamarca 3) und 3,5-4 Ma (Andamarca 4).

Auf Grundlage der stratigraphischen Lage der Ignimbrite wurde ein Minimum von ~300 m Taleintiefung vor ~14 Ma, von ~500-800 m nach ~6 Ma und eine erneute Eintiefungsphase mit ~200-300 m nach ~3,8 Ma ermittelt. In dem Visca-Tal gab es mindestens ein weiteres Eintiefungsereignis nach 9,4 Ma, das jedoch nicht quantifiziert werden kann. Die Gründe für Änderungen in Eintiefungsraten sind Hebung (hauptsächlich zwischen 14 Ma und 3,8 Ma), klimatische Veränderungen und damit einhergehende Änderungen im Abflusssystem und -niveau.

Diese Ergebnisse stimmen mit Befunden anderer Studien überein, die erhöhte Erosionsraten und rückschreitende Taleintiefung für die Ostkordillere zwischen 15 und 10 Ma, deren Folge eine westliche Verschiebung der Wasserscheide wäre, vorschlagen. Die Hebung von 2000 bis 3500 m in den vergangenen 10 Ma ist für das Altiplano und die Ostkordillere dokumentiert. Sie spiegelt sich in der Flusseinschneidung von mindestens einem Kilometer und mindestens einer weiteren, nicht quantifizierbaren Eintiefungsphase zwischen 9 und 6 Ma in unserem Studiengebiet, wider. Erneute Einschneidung nach 3,8 Ma ist wahrscheinlich auf ein humideres Klima und Vergletscherung in dem Gebiet zurückzuführen.

Ein Vergleich der Stratigraphie von drei Tälern östlich der Wasserscheide mit dem Tal im Westen und anderen Stratigraphien für die Westabdachung der Anden Süd-Perus zeigt, dass die 20 Ma Nazca (und großteils die 14 Ma) Ignimbrite im Osten fehlen. Dieser signifikante Unterschied ist auf höhere Erosions- und Denudationsraten in östliche Richtung zurückzuführen, während diese mächtigen Plateau-Ignimbrite auf der Westabdachung der Anden so gut erhalten sind. Unter der Voraussetzung, dass die Eruptionen nicht vollkommen asymmetrisch waren, führen wir die höheren Erosionsraten auf Hebung durch die Subduktion des Nazca-Rückens in diesen Breiten nach ~12 Ma mit einer gleichzeitigen Änderung der Niederschlagsverhältnisse zu humideren Bedingungen auf der Ostseite der Anden, zurück.

## KAPITEL V:

In diesem Kapitel werden die Ergebnisse der regionalen Studien von **Kapitel II-IV** auf einen Andenmaßstab übertragen. Zeitliche und räumliche Muster der neogenen, großvolumigen Ignimbriterruptionen der Zentralanden wurden mittels geostatistischer Modellierung analysiert. Die Hypothese, ob die Gesamtgesteinszusammensetzung von Ignimbriten als „geochemische Signatur“ verwendet werden kann, die eine eindeutige Unterscheidung zwischen einzelnen Ignimbriten erlaubt, wurde getestet. Um zeitliche und räumliche Muster der „Ignimbrite flare-ups“ zu untersuchen, wurden mittels Satellitendaten, geologischen Karten, verfügbarer Literatur und den in Kapitel 4 vorgestellten neuen Daten, 201 Ignimbrite kartiert und zusammen mit 1.602 Ignimbritproben in einer Datenbank zusammengeführt. Die Daten sind nun als „Web Mapping Application“ (WMA) global zugänglich.

Die Clusteranalyse an clr-transformierten Haupt- und Spurenelement Daten erlaubte eine Gruppierung von Ignimbriten nach geochemischen Charakteristika und wurde mit traditionellen geochemischen Parametern verglichen. Basierend auf Hauptelementen wurde ein rhyolitische und ein dazitische „Endglied“ definiert. Diese Endglieder überlappen in ihrer REE Zusammensetzung mit mehr oder weniger ausgeprägten negativen Eu Anomalien, Verarmung an MREEs und Anreicherung/Verarmung der LREEs. Basierend auf diesen Ergebnissen, ist eine vereinfachte Unterscheidung zwischen „rhyolitischen, kristallarmen, kleinvolumigen Ignimbriten“ und „dazitischen, kristallreichen, monotonen, großvolumigen Ignimbriten“ nicht ausreichend, um die Genese der Anden-Ignimbrite darzustellen. Der großvolumige, rhyolitische, 19 Ma Oxaya Ignimbrit, z.B., ist in seiner Zusammensetzung signifikant verschieden von dem ca. 4 Ma alten APVC Äquivalent, dem Atana Ignimbrit. Dies impliziert ein unterschiedliches Genesemodell als es für die APVC Ignimbrite angenommen wird. Dieses beruft sich auf eine Akkumulation von großen, dazitischen Magmenkörpern in der oberen Kruste, durch Mantelinput genährt mit einem hohen Anteil krustaler Assimilation. Dieser Befund wird durch Unterschiede in der Sr Isotopie gestärkt, die für die Oxaya Ignimbrite weniger radiogen ist und für weniger Assimilation in der oberen Kruste spricht. Dies ist möglicherweise auf die vor ~19 Ma dünnere und kältere Kruste zurückzuführen.

Um unsere Hypothese, dass die Gesamtzusammensetzung von Ignimbriten für die Unterscheidung einzelner Ignimbrite genutzt werden kann zu testen, wurde eine Diskriminanzanalyse durchgeführt. Ein Ergebnis mit 87,5% allgemeiner Klassifikationsgenauigkeit spricht für eine zukünftige Anwendung dieser Methode.

Die räumliche und zeitliche Verteilung der „Ignimbrite flare-ups“ wurde mit Hilfe neuer Verbreitungs- und Volumenberechnungen modelliert. Minimumabschätzungen für die gesamte CVZ sowie für fünf einzelne N-S Segmente werden vorgestellt. Wir schätzen das Gesamtvolumen auf 31.000 km<sup>3</sup>, wobei 2.400 km<sup>3</sup> auf Süd-Peru, 2.700 km<sup>3</sup> auf das südlichste Peru, 8.400 km<sup>3</sup> auf das Altiplano, 14.200 km<sup>3</sup> auf die Nord-Puna und 3.100 km<sup>3</sup> auf die Süd-Puna entfallen. Da Ignimbrite als Oberflächenmanifestationen von plutonischer Aktivität gesehen werden können, kann man mittels der Eruptivvolumen auch Prozesse der oberen Kruste besser eingrenzen. Auf den gleichen Annahmen wie von De Silva und Gosnold (2007) basierend, haben wir minimale plutonische Volumen von 7.200 km<sup>3</sup>, 8.100 km<sup>3</sup>, 25.200 km<sup>3</sup>, 42.600 km<sup>3</sup> und 9.300 km<sup>3</sup> für die jeweiligen Segmente über die vergangenen 30 Ma hinweg berechnet und stellen eine Verjüngung der Eruptionsalter von Nord nach Süd fest. Haupterupsionsphasen finden sich um 19-24 Ma, 13-14 Ma, 6-10 Ma, 3-6 Ma, gefolgt von lediglich untergeordneten Eruptionen nach 3 Ma. Gemäß unserer Vorstellung fanden große Ignimbriterruptionen im Gefolge des subduzierenden Juan-

Fernández Rückens statt. Nach einem kompressiven tektonischen Setting, verbunden mit Hebung, flacher Subduktion und der Freisetzung der in der subduzierenden Platte enthaltenen Fluide, konnten in der so „konditionierten“ Kruste nach dem Durchzug des Rückens durch erneuten asthenosphärischen Mantelfluss über einer sich versteilenden Platte leicht Schmelzen gebildet werden.

Die Volumenabschätzungen für die drei nördlichen Segmente und das Nord-Puna Segment sind nicht ausgeglichen, allerdings konnten für die nördlichen Segmente intra-Caldera Volumen nicht berücksichtigt werden, da die meisten Calderen aufgrund des höheren Alters und schlechteren Erhaltungsgrades nicht bekannt sind. Deshalb ist es sehr wahrscheinlich, dass diese Ignimbrite Volumen repräsentieren, die größer sind als für die Nord-Puna angenommen wird. Wenn zukünftige Studien diese Annahme belegen sollten, muss das Konzept eines APVC flare-ups modifiziert werden. Anstelle eines statischen Modells mit hoher Magmenproduktion und Batholithbildung, schlagen wir einen Paradigmenwechsel zu einem dynamischen Modell vor. Der „flare-up“ wird in dieser Vorstellung als dynamische Einheit gesehen, der sich, wahrscheinlich gekoppelt an die Subduktion des Juan-Fernández Rückens, über die vergangenen 25 Ma von Nord nach Süd über die Anden bewegt hat. Der Nord-Puna „flare-up“ wäre dann lediglich die jüngste und am besten erhaltene Manifestation und die Süd-Puna Cerro Galán Eruption möglicherweise eine Ankündigung eines neuen „flare-ups“.



## INTRODUCTION AND OUTLINE OF THIS THESIS

### 1 Geological background

---

The Andean Cordillera extends for 5,000 km along the western coast of South America and is a typical example of a convergent plate margin and all of the associated processes that affect the internal architecture, thermal and geochemical character of continental lithosphere (Oncken et al., 2006). Subduction of the Nazca-Farallon plate and arc magmatism has occurred since Jurassic times, with a change in convergence angle from continent-parallel to almost orthogonal at approximately 26 Ma (Pardo-Casas and Molnar, 1987). The tectonic style of the orogen changes along and across strike and defines distinct domains (along strike) and morphotectonic provinces (across strike) (Gregory-Wodzicki, 2000) (Fig.1). Along-strike variations represent present-day differences in plate geometry, with flat-slab (subduction angle  $5^{\circ}$  to  $10^{\circ}$ ) segments between  $2^{\circ}\text{S}$  and  $15^{\circ}\text{S}$  and  $28^{\circ}\text{S}$  and  $33,5^{\circ}\text{S}$  that lack Miocene to Holocene volcanic activity, and steeply dipping segments (subduction angle of  $30^{\circ}$ ) manifesting areas of young volcanism. Andean domains correspond to the volcanic zones (Northern, Central and Southern Volcanic zones) with the Central Volcanic zone consisting of two subdomains, the Altiplano ( $15^{\circ}\text{S}$  to  $24^{\circ}\text{S}$ ) and the Puna ( $28^{\circ}\text{S}$  to  $33,5^{\circ}\text{S}$ ). The morphotectonic provinces, generally speaking, reflect the eastward shift of Andean arc magmatism and deformation through time (Gregory-Wodzicki, 2000). These units are slightly different for the Andean domains, but basically consist of the Coastal Cordillera, the Western Cordillera, the Altiplano-Puna plateau and the Eastern Cordillera.

With an average elevation of 4 km and an extent of  $\sim 400$  by 2,000 km, the Altiplano and Puna Plateau of the Central Andes are a still hotly debated orogen, with many open questions concerning geodynamical and magmatic evolution. Neogene crustal shortening during the continuous subduction of the Nazca Plate, accompanied by intense volcanism and vertical thickening lead to the development of the second highest continental plateau in the world (Trumbull et al., 2006) and crustal thicknesses reaches values of  $> 70$  km, particularly along the main arc (Beck et al., 1996; James, 1971; Yuan et al., 2006). The close relationship between deformation, uplift, magmatism, crustal growth and ore formation makes this convergent plate margin an excellent setting to study external and internal mechanisms responsible for the evolution of the Andes and the Altiplano Puna Plateau (as defined by the 3 km elevation contour (Allmendinger et al., 1997)).

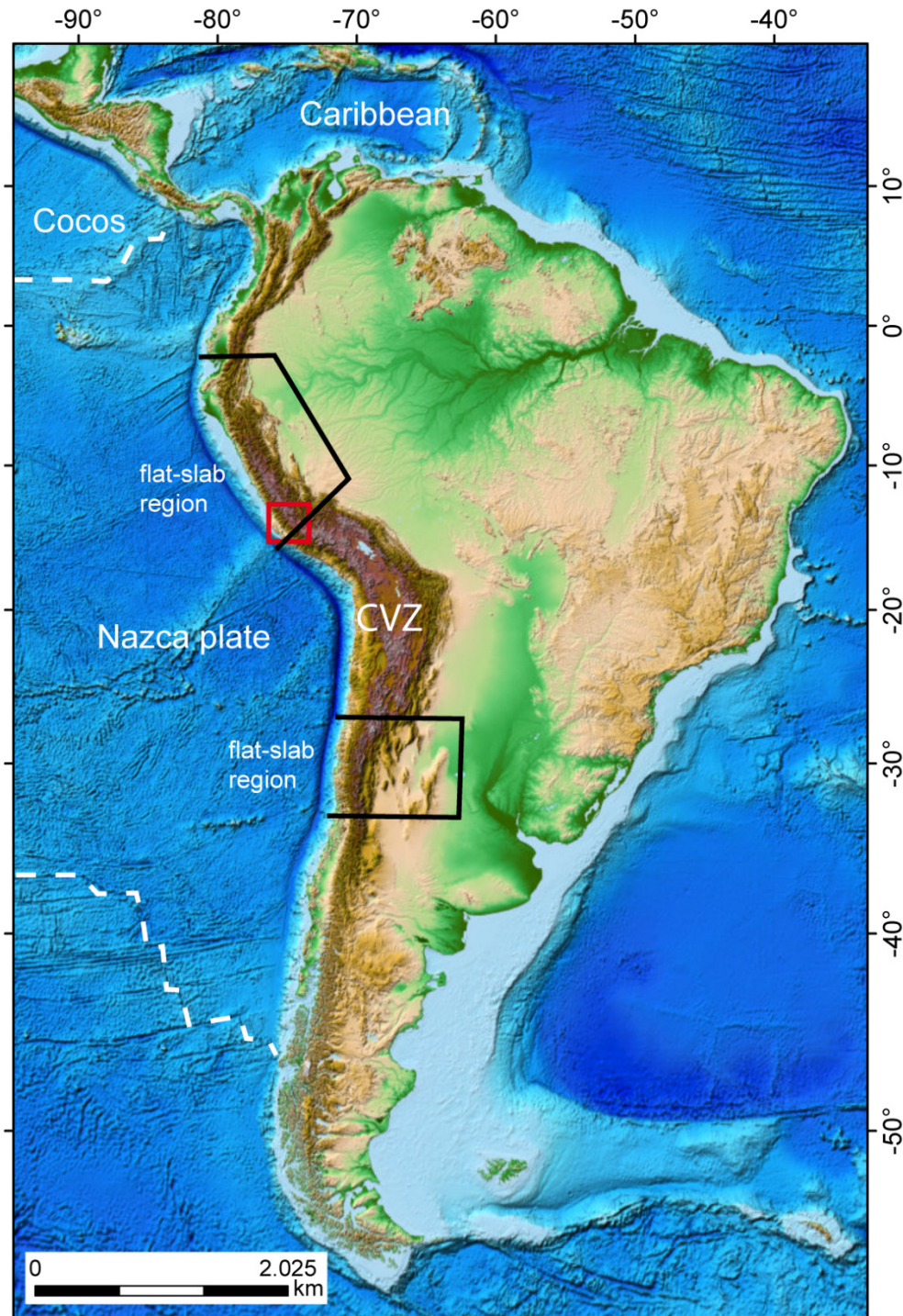


Fig. 1: Shaded relief map (Amante, 2009) of South America with present plate configurations and seafloor topography. The red square highlights the local focus of the present study in Southern Peru. The Central Andean Orocline between the northern and southern flat-slab segments represents the largest orogenic volume that decreases towards the north and south (Central Volcanic Zone, CVZ).

It is now generally accepted that magmatic addition to the lower crust has only a minor effect on crustal growth (Allmendinger et al., 1997; Francis, 1994) as most of the crustal

thickening can be explained by shortening and estimates for magmatic addition are too low to explain the observed thickness (Trumbull et al., 2006; Wörner et al., 2000; Wörner et al., 2002). However, Isacks (1988) argued, that the thermal effect of magmatism may well be significant and precondition the upper plate for plateau formation by thermal weakening, an idea further developed by James and Sacks (1999) who argued that hydration from dewatering of a shallow-slab and not heating -is the principal cause for weakening the upper plate. Testing this hypothesis is difficult because timing of crustal thickening, magmatic and deformation events is not very well constrained and variable both from north to south and east to west. Consensus exists, that the Altiplano was at sea level until about 60 Ma and attained 25% to 30% of its present elevation in the early Miocene and only 50% of the modern elevation by 10 Ma (Gregory-Wodzicki, 2000). Seismicity levels are very low in the Central Andes due to the unusually thick and weak crust (Beck et al., 1996; Wigger, 1988; Zandt et al., 1996). Crustal thickening in the Central Andes is thought to have been initiated in the Palaeocene in the Western Cordillera (DeCelles and Horton, 2003) and migrated in the Late Oligocene to Early Miocene in an easterly direction, possibly triggered by compressional failure of the supra-subduction zone lithosphere and accommodated in a mid-crustal décollement zone (De Silva et al., 2006; DeCelles and Horton, 2003; Isacks, 1988; McQuarrie, 2002). Gubbels et al. (1993) argued, that shortening shifted to the eastern foreland at ~10 Ma with a transtensional tectonic regime on the plateau thereafter. Shortening and thickening therefore preceded the big ignimbrite eruptions that occurred after 10 Ma (De Silva et al., 2006).

## 2 Introduction and outline of this thesis

---

The Central Andes represent one of the world's largest Miocene ignimbrite provinces with more than 15,000 km<sup>3</sup> of erupted magma within 10 Ma on the Altiplano Puna Volcanic Complex (APVC) (De Silva et al., 2006). Timing of ignimbrites, their composition and volume are closely linked to the thermal and structural evolution of the crust and partial crustal melting and magmatism in the mantle wedge related to the subduction of the Nazca plate and can therefore be used as tracers of these processes. This study was undertaken in the framework of a project funded by the **German Science Foundation (DFG)** with the aim of investigating timing, cause and location of "ignimbrite flare ups" during the evolution of the Central Andean uplift. A second focus of research was to relate volcano-tectonic structures and calderas with shallow intrusive stocks to mineralization by applying methods of remote sensing, GIS and geospatial statistics together with traditional geological fieldwork, <sup>40</sup>Ar/<sup>39</sup>Ar geochronology and geochemical analysis.

The concept of “ignimbrite flare ups” in the Central Andes was first proposed by De Silva (1989) and De Silva and Francis (1989), referring to the large volumes of silicic magma that were erupted in relatively short period of time in the APVC. In the present study, this concept will be expanded to Southern Peru and to the large plateau ignimbrites located on the Western escarpment of the Andes (e.g. Oxaya, Nazca and Huaylillas ignimbrites). The northern termination of the Central Volcanic zone and the present “steep-slab” region is also characterized by abundant ignimbrite deposits that are not very well studied. This area is characterized by higher precipitation, compared to the the drier northern Chilean, Bolivian and Argentinean Altiplano-Puna. It is dissected by deep valleys and was the regional focus of this study. On this local scale, we determined age and extent of ignimbrites to better understand the stratigraphy and geomorphologic evolution of the area, especially the differences between the arid western escarpment and the more humid eastern part of the drainage system. This topic is covered in **CHAPTER IV**. Furthermore, by applying methods of remote sensing, we studied hydrothermal alteration and its relationship to volcano-tectonic structures. This served to better constrain the location of eruptive centers of ignimbrites that are largely unknown in Southern Peru, and also concerns the location and origin of epithermal ore deposits. The multispectral remote sensing approach was chosen because of the deeply eroded and covered nature of caldera centers in Southern Peru that hinders the recognition of calderas by morphology alone, in contrast to the well preserved structures of the Altiplano (e.g. La Pacana caldera, Vilama caldera). Due to the close spatial and temporal association between pulses of silicic volcanism and epithermal alteration (and mineralization) of Miocene volcanoes (Echavarría, 2006; Palacios, 2008), studying possible eruptive centers of ignimbrites also addresses the possible location of epithermal ore deposits as is shown in **CHAPTERS II and III**.

Results from this local-scale approach were then integrated in an Andean-scale ignimbrite database (**CHAPTER IV**) with the aim of calculating eruptive volumes over time. We then use a multivariate statistical approach on (1) isotope data to propose kriging models to better delineate the crustal domains that were established by Mamani et al. (2010) and (2) on log-ratio transformed geochemical (major and trace elements) data as a tool for discriminating between different ignimbrites and to find possible relationships between, for example, ignimbrite age, location and composition. Temporal and spatial variations of ignimbrite eruptions were thus analyzed and put into the context of the Miocene evolution and uplift history of the Andes with the aim of establishing a model to explain timing and location of “flare-ups” based on those findings. The ignimbrite database is provided as Web Mapping Application (WMA) and can be edited, expanded and used for future projects.

## REFERENCES:

- Allmendinger, R.W., Jordan, T.E., Kay, S.M., Isacks, B.L., 1997. The Evolution of the Altiplano-Puna Plateau of the Central Andes. *Annu. Rev. Earth Planet. Sci.* 27, 139-174.
- Amante, C.E., B.W., 2009. ETOPO1 1 Arc Minute Global Relief Model: Procedures, Data Sources and Analysis. NOAA Technical Memorandum NESDIS NGDC-24, 19 pp.
- Beck, S.L., Zandt, G., Myers, S.C., Wallace, T.C., Silver, P.G., Drake, L., 1996. Crustal-thickness variations in the Central Andes. *Geology* 24, 407-410.
- De Silva, S., Zandt, G., Trumbull, R., Viramonte, J.G., Salas, G., Jiménez, N., 2006. Large ignimbrite eruptions and volcano-tectonic depressions in the Central Andes: a thermomechanical perspective. Geological Society, London, Special Publications 269, 47-63.
- De Silva, S.L., 1989. Altiplano-Puna volcanic complex of the central Andes. *Geology* 17, 1102-1106.
- De Silva, S.L., Francis, P.W., 1989. Correlation of large ignimbrites - two case studies from the central Andes of Northern Chile. *J. of Volc. and Geotherm. Res.* 37, 133-149.
- DeCelles, P.G., Horton, B.K., 2003. Early to middle Tertiary foreland basin development and the history of Andean crustal shortening in Bolivia. *Geological Society of America Bulletin* 115, 58-77.
- Echavarría, L.N., E.; Humphrey, J.; Chavez, J.; Escobedo, L.; Iriondo, A., 2006. Geologic Evolution of the Caylloma Epithermal Vein District, Southern Peru. *Econ. Geol.* 101, 843-863.
- Francis, P.W.H., C. J., 1994. Late Cenozoic rates of magmatic activity in the Central Andes and their relationships to continental crust formation and thickening. *Journal of the Geological Society, London* 151, 845-854.
- Gregory-Wodzicki, K.M., 2000. Uplift history of the Central and Northern Andes; a review. *GSA Bulletin* 112, 1091-1105.
- Gubbels, T., Isacks, B., Farrar, E., 1993. High-level surfaces, plateau uplift, and foreland development, Bolivian Central Andes. *Geology* 21, 695-698.
- Isacks, B.L., 1988. Uplift of the Central Andean Plateau and Bending of the Bolivian Orocline. *Journal of Geophysical Research* 93, 3211-3231.
- James, D.E., 1971. Plate tectonic model for the evolution of the Central Andes. *Geological Society of America Bulletin* 82, 3325-3346.
- James, D.E., Sacks, I.S., 1999. Cenozoic formation of the Central Andes: a geophysical perspective. *Geology and Ore Deposits of the Central Andes* 7, 1-25.
- Mamani, M., Wörner, G., Sempere, T., 2010. Geochemical variations in igneous rocks of the Central Andean orocline (13 S to 18 S): Tracing crustal thickening and magma generation through time and space. *Geological Society of America Bulletin* 122, 162-182.
- McQuarrie, N., 2002. The kinematic history of the central Andean fold-thrust belt, Bolivia: Implications for building a high plateau. *Geological Society of America Bulletin* 114, 950-963.
- Oncken, O., Hindle, D., Kley, J., Elger, K., Victor, P., Schemmann, K., 2006. Deformation of the Central Andean Upper Plate System — Facts, Fiction, and Constraints for Plateau Models, In: Oncken, O., Chong, G., Franz, G., Giese, P., Götze, H.-J., Ramos, V., Strecker, M., Wigger, P. (Eds.), *The Andes*. Springer Berlin Heidelberg, pp. 3-27.
- Palacios, C.D., A.; Nelson, E.; Layer, P., 2008. Estilos y Control de Mineralización en el Distrito Minero de Selene, Apurímac, Perú, XIV Congreso Peruano de Geología.

- Pardo-Casas, F., Molnar, P., 1987. Relative motion of the Nazca (Farallon) and south American plates since Late Cretaceous time. *Tectonics* 6, 233-248.
- Trumbull, R., Riller, U., Oncken, O., Scheuber, E., Munier, K., Hongn, F., 2006. The Time-Space Distribution of Cenozoic Volcanism in the South-Central Andes: a New Data Compilation and Some Tectonic Implications, In: Oncken, O., Chong, G., Franz, G., Giese, P., Götze, H.-J., Ramos, V., Strecker, M., Wigger, P. (Eds.), *The Andes*. Springer Berlin Heidelberg, pp. 29-43.
- Wigger, P., 1988. Seismicity and crustal structure of the Central Andes. *The Southern Central Andes* 17, 209 -229.
- Wörner, G., Hammerschmidt, K., Henjes-Kunst, F., Lezaun, J., Wilke, H., 2000. Geochronology ( $^{40}\text{Ar}/^{39}\text{Ar}$ , K-Ar and He-exposure ages) of Cenozoic magmatic rocks from Northern Chile (18-22 degrees S): implications for magmatism and tectonic evolution of the central Andes. *Revista Geologica De Chile* 27, 205-240.
- Wörner, G.U., D.; Kohler, I.; Seyfried, H., 2002. Evolution of the West Andean Escarpment at 18°S (N. Chile) during the last 25 Ma: uplift, erosion and collapse through time. *Tectonophysics*, 183-198.
- Yuan, X., Asch, G., Bataille, K., Bock, G., Bohm, M., Echtler, H., Kind, R., Oncken, O., Wolbern, I., 2006. Deep seismic images of the Southern Andes. *Special papers-Geological Society of America* 407, 61.
- Zandt, G., Beck, S., Ruppert, S., Ammon, C., Rock, D., Minaya, E., Wallace, T., Silver, P., 1996. Anomalous crust of the Bolivian Altiplano, central Andes: Constraints from broadband regional seismic waveforms. *Geophysical research letters* 23, 1159-1162.

## MANUSCRIPT I

---

### Remote sensing of Carhuarazo volcanic complex

Using ASTER imagery in Southern Peru to detect alteration zones and volcanic structures – a combined approach of image processing in ENVI and ArcGIS/ArcScene

Melanie Brandmeier\*

\* Georg-August- Universität Göttingen, GZG, Geochemisches Institut, Goldschmidstr.1, Göttingen D-37077, Germany

Published in: Geocarto International **25** (2010): 629-648

---

#### Abstract

*A combined approach to detect hydrothermal alteration zones and their mineral distribution is proposed for a relatively remote area around the Carhuarazo volcanic complex in Southern Peru encompassing 2,222 km<sup>2</sup>. In this region, tertiary volcanic structures associated with hydrothermal alteration are well known to host epithermal ore deposits. We make an attempt to detect and to quantify alteration minerals based on spectral analysis using ASTER reflectance data product provided by LP-DAAC. Besides commonly used ratio images, mineral indices (MI) and relative band depth images (RBD), we also extracted endmember spectra using Pixel-Purity-Processing, preceded by minimum noise fraction transformation. These spectra are thought to represent the spectrally purest pixel of the image and show the typical absorption features of the main constituents. Based on this assumption, we used different spectral analysis methods in order to extract the most important alteration minerals for such an environment. These minerals were then used for matched filter processing in areas showing high values in MIs and RBDs. Using this method, we detected and mapped argillic alteration and variations in the distribution of important minerals like alunite, kaolinite or nacrite. There were no indications for the presence of propylitization at ASTER spatial resolutions. Our method can be applied easily to any ASTER scene and provides information about the intensity of alteration and the character of alteration zones. The intensity is highest in the centre of the Carhuarazo volcanic complex and is mostly argillic with a high content of alunite, dickite and other clay minerals.*

**KEYWORDS:** *ASTER, Peru, volcanic structures, mineral detection, spectral analysis, ore deposits, alteration zones*

## 1 Introduction

The study area in Southern Peru encompasses approximately 2,222 km<sup>2</sup> at an altitude of 4,000 to 5,000 m (Fig. 1). The region is characterized by its arid climate and therefore sparse vegetation except along river valleys as can be seen in green color in the image. In this paper we evaluate the capacity of ASTER (Advanced Spaceborn Thermal Emission and Reflection Radiometer) data acquired in October 18, 2002 for detecting alteration zones and identifying different minerals in this region using laboratory spectra from the USGS spectral library and different methods of mineral and rock detection. Recognizing alteration zones and geologic structures is very important in large and difficultly accessible areas because ore deposits are often related to zones of weakness and fluid flow. We are interested in finding volcanic structures, especially old calderas which are no longer easily recognized due to erosion and partial cover by younger rocks but may be the source of large ignimbrite sheets along the western Andean slope.

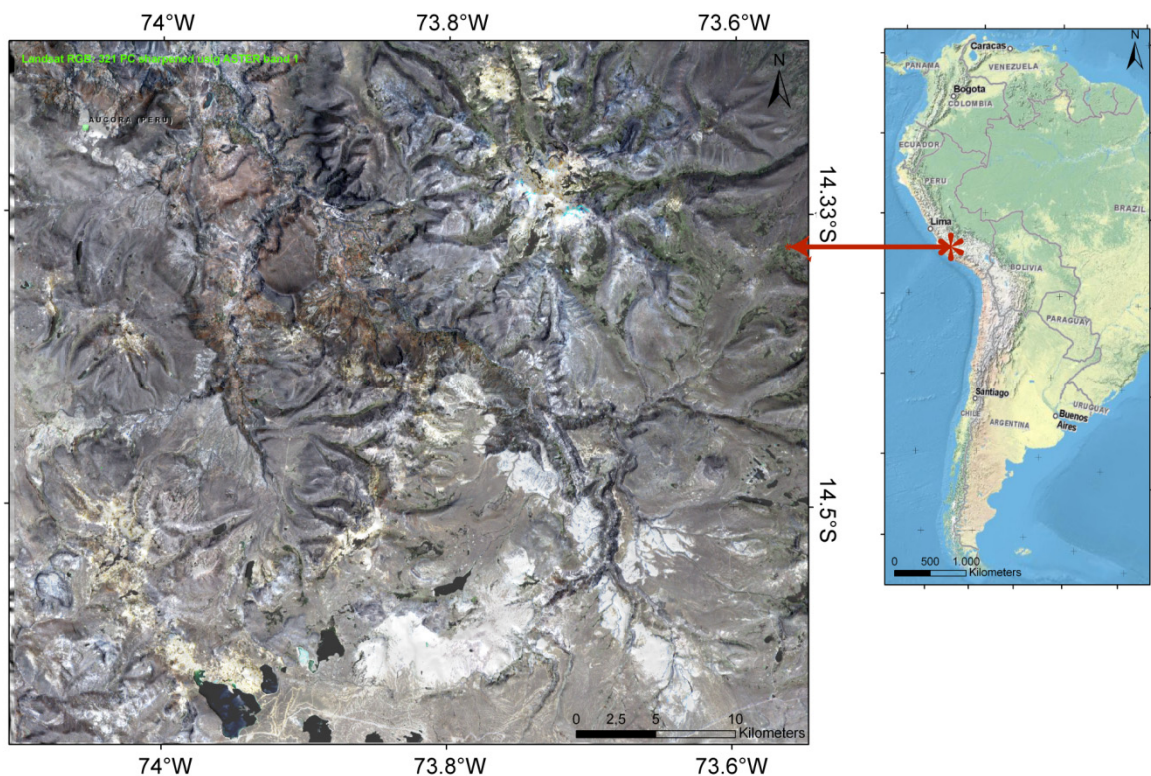


Fig. 1: Landsat subsense of the study area (RGB:321) PC sharpened with panchromatic band 8 and underlain by ASTER DEM

ASTER is a multispectral imaging system on board NASA's TERRA spacecraft, launched in December 1999 that records radiation in 14 spectral bands (Earth Remote Sensing Data Analysis Center (E.E.R.S.D.A.) 2005): reflected radiation in three bands



between 0.52 and 0.86  $\mu\text{m}$  (visible and near infrared radiometer; VNIR) and six bands from 1.6 to 2.43  $\mu\text{m}$  (short wavelength infrared radiometer; SWIR) as well as emitted radiation in five bands from 8.125 to 11.65  $\mu\text{m}$  in the thermal infrared region (thermal infrared radiometer; TIR).

Lithologic mapping and mineral detection using ASTER data products have proven successful in well-defined and well-known study areas (De Souza Filho et al. 2003, Rowan and Mars 2003, Hewson et al. 2005, Ninomiya et al. 2005, Rowan et al. 2005, 2006, Di Tommaso and Rubinstein 2007). We propose a combination of spectral processing in Environment for Visualizing Images; <http://www.itvis.com/ProductServices/ENVI.aspx> (ENVI) and geographic information systems (GIS) in order to define target areas in a large and difficult-to-access area. For this first study, we selected an area of 2222  $\text{km}^2$  in the Southern Peruvian Andes and developed a method to apply to even larger areas in Southern Peru in the future.

In order to visualize data and to build a model that can be further analyzed we exported all results from ENVI to ArcGIS and to ArcScene. Several fly-through clips produced in ArcScene showing not only the research area but also the results of our work can be viewed on our homepage (<http://www.uni-geochem.gwdg.de/>).

## 2 Geological setting

---

The study area is located in the tertiary volcanic arc of the Central Andes which is famous for a large number of ore deposits, particularly located in the Miocene (15–5 Ma) metallogenic provinces (Echavarría et al. 2006 and references therein) hosting precious metal-rich epithermal vein deposits such as Orcopampa, Arcata or Caylloma. The genesis of these deposits is believed to be related to tectonic events such as the subduction of topographic anomalies like the Nazca Ridge (Southern Peru) and the now-consumed Inca Plateau (northern Peru) (Rosenbaum et al. 2005). The relationships between magmatism, tectonism and uplift of the Andes were recognized and investigated by many authors (Tosdal et al. 1984, Sandeman et al. 1995, Mahlburg et al. 1999, 2005, Wörner et al. 2002, Mamani et al. 2009) and it is widely accepted that Mesozoic to Cenozoic evolution of the Central Andean margin was controlled by a variety of subduction parameters such as the rate and obliquity of plate convergence, morphologic heterogeneities, the thermal and geometric evolution of the mantle wedge (Mamani et al. 2009). Major crustal thickening in the Central Andes occurred since the mid-Oligocene (30 Ma) and was accompanied by transpressional to compressional deformation in the northeastern Altiplano, Eastern Cordillera and Sub-Andean Belt while extensional, transtensional and transpressional deformation prevailed in

the forearc, arc and southwestern Altiplano of Southern Peru (Semperé and Jacay 2007). Major eruptions of large volumes of plateau-forming ignimbrites were erupted in Southern Peru in three phases at ~14 to 24 Ma, and many of the caldera centers host precious metal deposits. However, relating ignimbrite sheets to their caldera source and identifying caldera-related alteration zones have been deficient in this remote area. Therefore, we propose to use ASTER reflectance data in order to localize and define distinct types of (caldera-related) alteration zones by spectral analysis and to build a geodatabase in ArcGIS containing remote sensing data as well as a digital elevation model which will be the basis for more data (especially geochemical data) we plan to collect in the future. In this contribution, the focus is on spectral analysis of SWIR (Short Wave Infra-Red) reflectance data in order to gain information about the location, nature and intensity of alteration zones, on creating a basic database in ArcGIS, and on modeling our results in three-dimensional space using ArcScene.

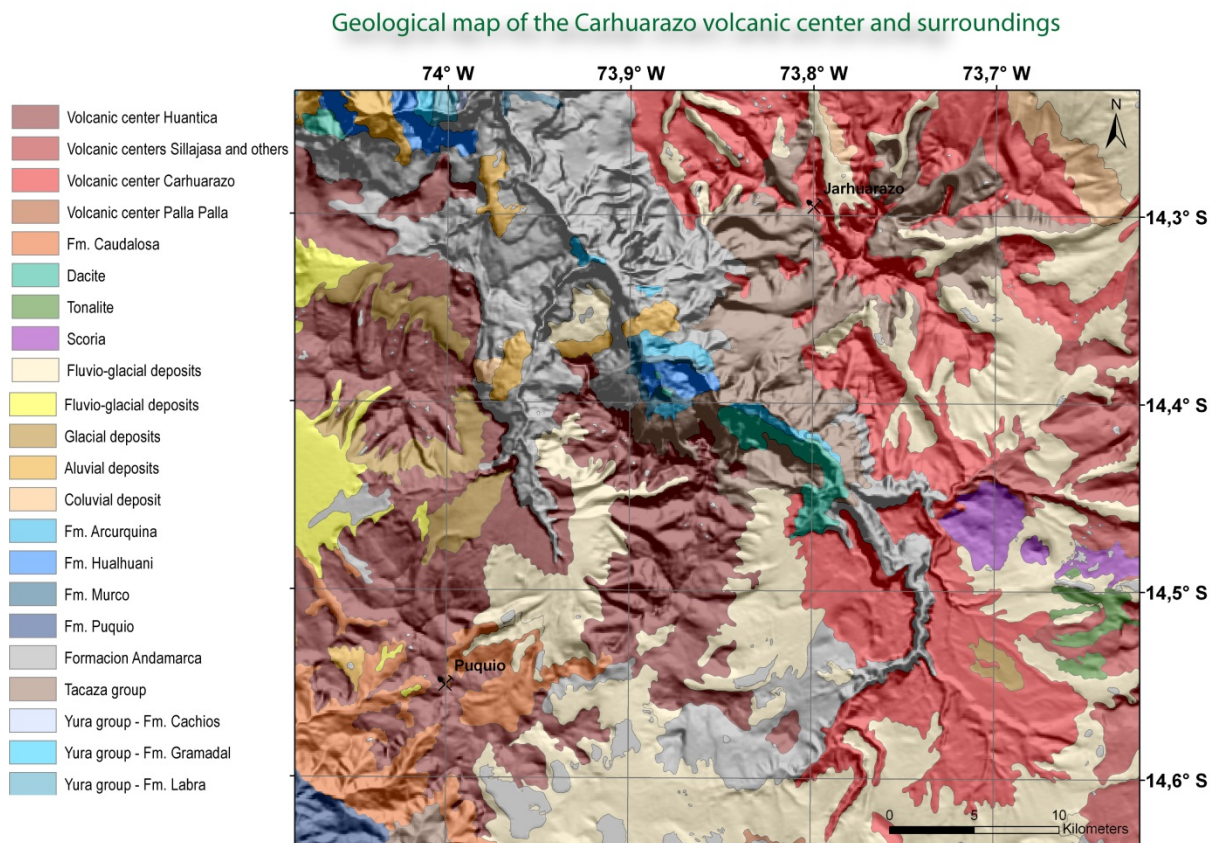


Fig. 2: Geological map overlain on ASTER derived DEM (based on the digital map of Peru provided by INGEMMET). The geological map was produced by generating a shaded relief image from ASTER data which was exported to ArcGIS and overlain by a vector file provided by INGEMMET containing geological information

The area of interest is located south of the village of Aucora in the west of the volcanic complex Carhuarazo (Jarhuarazo) (Fig. 2). Neogene volcanics are underlain by a up to ~65

km thick continental crust composed of deformed Paleozoic and Mesozoic rocks which cover a Proterozoic basement (Clark et al., 1990). The Tacaza Group volcanic sequence (Fig. 2) overlies Yura Group rocks comprising sandstone, grey limestone and calcareous sandstone in this area. Older Tertiary volcanic rocks have andesitic or dacitic composition and occur in the east of the scene. Compositions of sedimentary rocks and sediments are variable. It is obvious that spectral properties of these rocks will always be a mixture of the properties of their respective components.

### 3 Hydrothermal alteration associated to ore deposits

---

Large upper tertiary volcanic centers are the focus of our study as Neogene volcanic structures are well known to be associated with alteration due to hydrothermal activity. Typical minerals occurring in alteration zones like alunite, kaolinite, chlorite or illite have characteristic absorption features and can thus be detected using ASTER data as will be described below.

Zones of hydrothermal alteration are important indicators for the location of ore deposits and may occur as small bands or as large haloes which can be detected by remote sensing methods in regions of arid climate and where atmospheric disturbance are limited. As hydrothermal alteration is related to epithermal ore deposits which typically occur in Tertiary volcanics related to resurgent caldera structures or subvolcanic domes, our aim is to identify through spectral analysis such structures which today may not form an accentuated relief due to weathering and erosion by mineral detection.

Typical forms of alteration are propylitization of andesites/dacites, silicification and argillitisation with typical mineral assemblages of chlorite, epidote, albite and carbonates (propylitization), alunite, sericite, nacrite, dickite, kaolinite, turmaline (argillization) and quartz, opal and chalcedony (silicification) (Pohl, 2005). A zonation according to the direction of fluid-flow is typical and in some cases can be mapped by matched filter processing as will be described below.

### 4 Methods

---

In this study, we use different data products provided by the Land Processes Distributed Active Archive Center (LP-DAAC) in a green-field study in southern Perú. AST14OTH with DEM (Radiance at sensor orthorectified images with digital elevation model) and AST\_07XT (surface reflectance crosstalk corrected) products were analyzed in order to avoid inaccuracy

due to the cross-talk effect. The term ‘crosstalk’ in remote sensing refers to the phenomenon that the electrical or optical signals from one band (ASTER band 4) leak to another band.

We follow a two-step approach, first calculating band ratios, mineral indices (MI) and relative band depth (RBD) images proposed by various authors (Rowan and Mars 2003, Yamaguchi and Naito 2003, Rowan et al. 2005, 2006, Zhang et al. 2007) using the VNIR and SWIR channels 1–9. An overview about the image processing and spectral analysis is given in Fig. 3.

In the second step, we selected reference spectra using the calculated MI and RBD images to support the results of pixel-purity index (PPI) calculation. PPI calculation was preceded by a minimum noise fraction (MNF) transformation and end-member extraction by interactively classifying pixels in the n-D visualizer provided in the ENVI software package. The PC-sharpened Landsat true color composite is also used in the selection process for better visualization as ASTER does not have a band in the spectral range of blue light and therefore Landsat was used to produce a true-color image. PC Spectral Sharpening is a tool to sharpen low-spatial resolution multi-band images using an associated high-spatial resolution panchromatic band. The algorithm assumes that the images correspond to each other and if they are geo-referenced, ENVI automatically co-registers them on the fly. The image was produced using the panchromatic band 8 of Landsat 7 ETM sensor with a spatial resolution of 15 m. The obtained spectra should represent the spectrally purest pixels in the scene and show absorption features of the dominant material. Therefore, we analyzed these spectra with three different methods and the USGS spectral library (resampled to ASTER spectral resolution) in order to identify principal minerals. Spectral angle mapping (SAM), spectral feature fitting (FFM) and binary encoding (BE) were used and the number of spectral bands considered was varied in order to recognize the best fit. The results were then used for matched filtering in areas selected according to the results of MIs and RBDs in order to find a possible zonation or variations in the mineral content and different intensities of hydrothermal alteration which might be explained by the history of the respective structure or by the proximity to the heat source.

#### 4.1 Spectral analysis and ratio images

---

Spectral analysis was conducted with a AST07 XT cross talk corrected reflectance data product. As vegetation and water bodies do not allow for useful index calculation, these areas were masked. We used a thresholded NDVI image as vegetation mask and the water

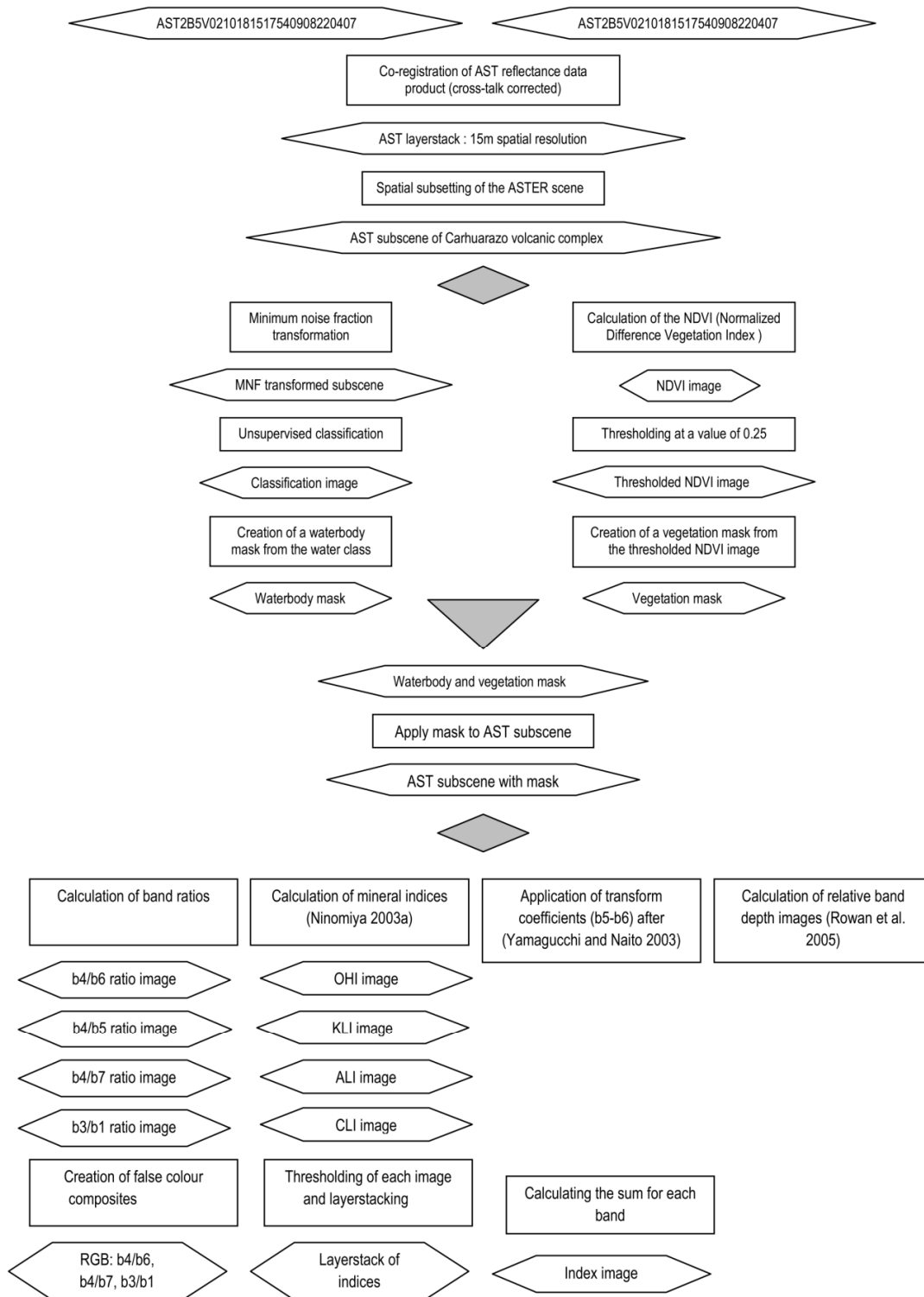


Fig. 3: ASTER processing chart – an overview of the methods described in the text

class of an unsupervised classification on the basis of a MNF (Minimum Noise Fraction) transformed image to mask waterbodies.

#### 4.1.1 Ratio images and mineral indices

In a first step typical ratio images (band4/band5, band4/band6, band4/band7, band3/band1) were calculated using ENVI bandmath and then depicted as RGB false color composites in a first approach of qualitative detection of alteration minerals. ASTER band 5 and 6 show absorption features due to Al-OH bonds caused by clay minerals, alunite and/or muscovite/sericite while band 7 detects Fe-OH features and band 3 and 1 are sensitive to iron oxides (vegetation needs to be masked for analysis). RGB: band4/band6-band4/band7-band3/band1 (Fig. 4) shows alteration zones in yellow to brown while volcanics appear blue and sediments in mixed shades of blue/green. RGB: band4/band5-band4/band6-band4/band7 (Fig.5) is sensitive to absorption features at 2.2  $\mu\text{m}$ , 2.16  $\mu\text{m}$  and 2.26  $\mu\text{m}$  and alteration minerals with Al-OH and Fe-OH absorption features appear in whitish colors.

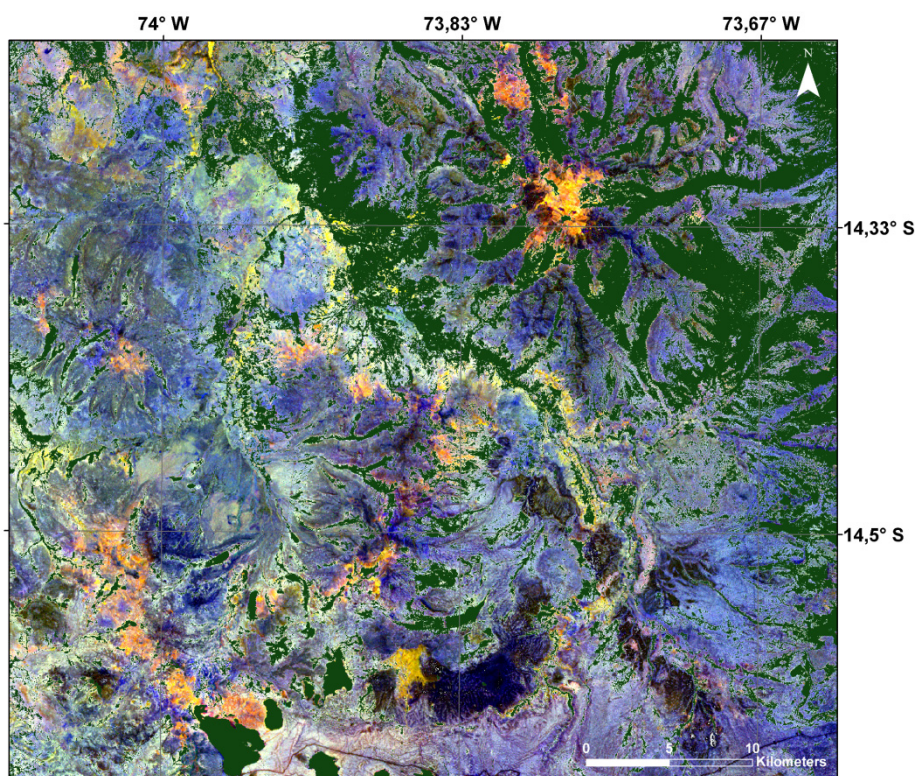


Fig. 4: ASTER RGB: band ratios: 4/6, 4/7, 3/1: Alteration appears yellow while volcanics are blue and sediments appear in mixed colours. Vegetation and waterbodies are masked (green color).

RBD images accentuate the difference between reflectance values of an absorption feature (denominator) and the adjacent higher reflectance (numerator). Two images were calculated (Rowan et al., 2005) and later used in the selection process for representative spectra of alteration zones (see section ‘Matched filter processing in target areas’):

RBD (Al-OH):  $(\text{band } 4 + \text{band } 7) / (\text{band } 6 \times 2)$

RBD (Mg, Fe-OH):  $(\text{band } 7 + \text{band } 9) / (\text{band } 8 \times 2)$

RBD (Al-OH) accentuates absorption features of Al-OH bearing minerals typical for argillic alteration while RBD (Mg, Fe-OH) works likewise for Mg-OH and/or Fe-OH bearing minerals like chlorite or epidote which typically occur in zones of propylitization (Figs. 6 and 7).

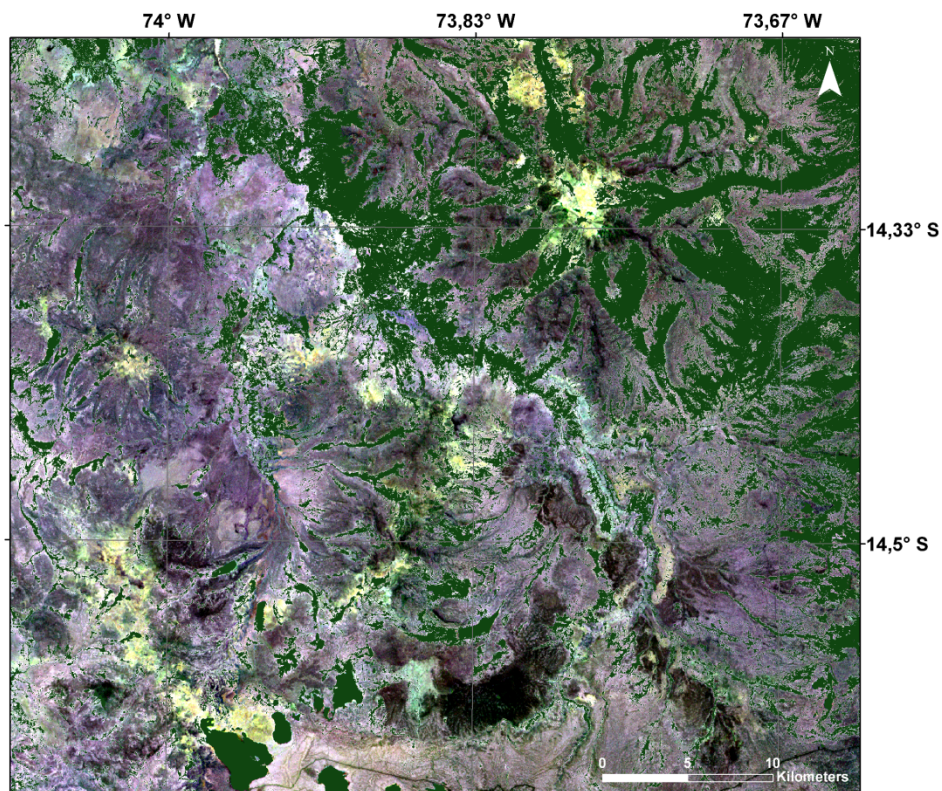


Fig. 5: ASTER RGB: band ratios 4/5, 4/6, 4/7: Whitish areas show absorption at 2.14  $\mu\text{m}$ , 2.2  $\mu\text{m}$  and 2.26  $\mu\text{m}$  corresponding to Al-OH and Fe-OH absorption features. Vegetation and waterbodies are masked (green color).

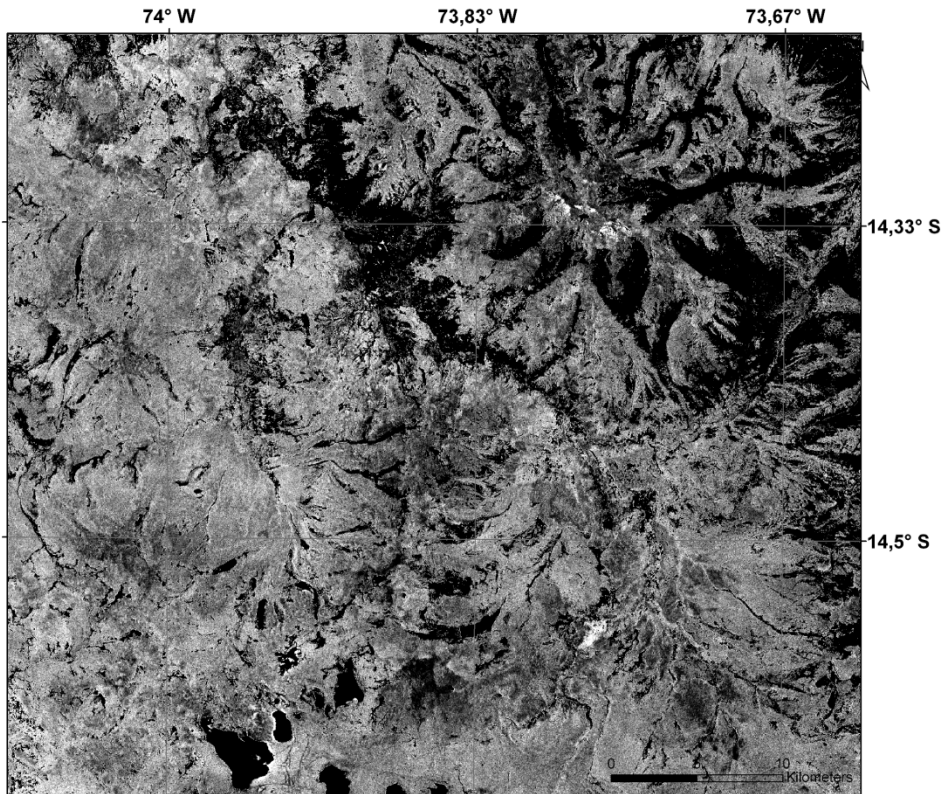


Fig. 6: RBD image for Fe-Mg-Oh (Rowan et al. 2005). Vegetation and water bodies are masked (black color).

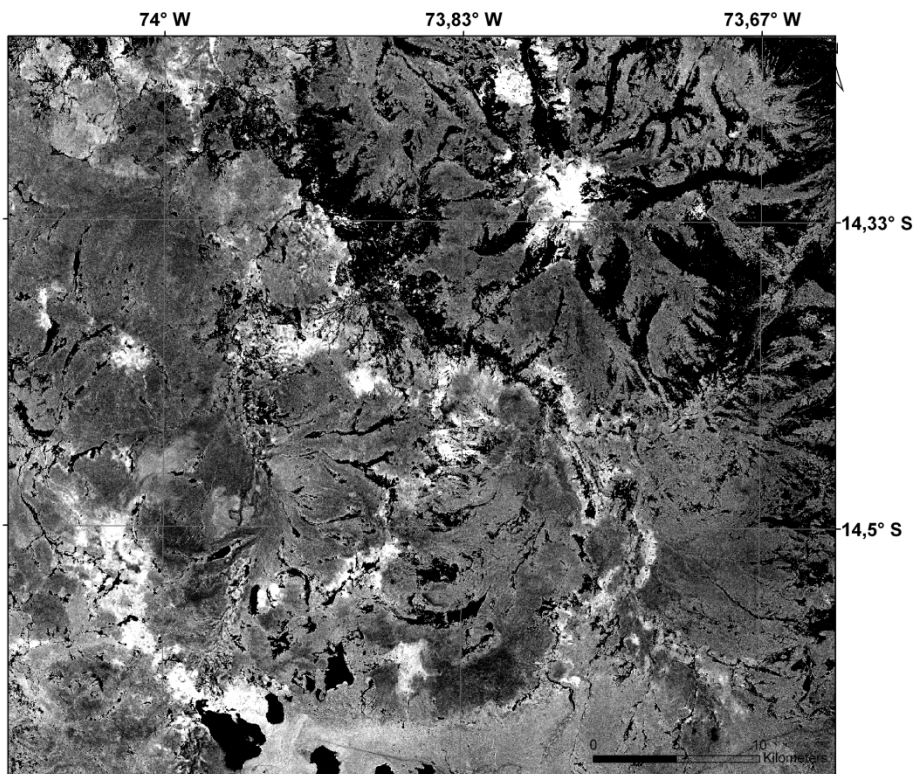


Fig. 7: RBD image for Al-OH (Rowan et al. 2005). Vegetation and waterbodies are masked (black color).



Following the approach proposed by Yamaguchi and Naito (2003), we used AST07 reflectance data for the calculation of alunite, kaolinite and calcite indices. This method and similar approaches have proven successful in Cuprite, Nevada (Rowan et al. 2003, Yamaguchi and Naito 2003) and we will test its validity in this arid region.

The indices proposed by Yamaguchi are based on the assumption that the first component of principal component analysis (PCA) mainly contains information about topography and brightness. Therefore, a first index-image can be determined by applying the transform coefficients to each pixel of each band and summing them up.

Table 1: Transform coefficients for spectral indices after Yamaguchi and Naito (2003)

Spectral index	Band 5	Band 6	Band 7	Band 8	Band 9
Brightness	0,446	0,449	0,453	0,447	0,441
Alunite	-0,694	-0,219	0,562	0,389	-0,048
Kaolinite	0,528	-0,795	0,212	0,174	-0,119
Calcite	-0,087	-0,212	0,322	-0,659	0,64
Montmorillonite	0,138	0,284	-0,134	0,499	-0,796

Higher spectral indices are deviations of each data point from the brightness axis and must be perpendicular to it and orthogonal to each other. Yamaguchi and Naito (2003) defined transform coefficients (see Table 1) for alunite, kaolinite, calcite and montmorillonite according to this principle.

We produced a RGB image for alunite (R), calcite (G) and kaolinite (B) in order to detect areas rich in alunite and kaolinite which are typical alteration minerals found around epithermal ore bodies (argillic alteration) (Fig. 8).

Furthermore we calculated an index image following the method developed by (Zhang et al., 2007) which combines the advantages of mineral indices and PCA. Four mineralogic indices proposed by Ninomiya (2003) were calculated and a PCA transformation was undertaken in order to extract information about mineral locations using the thresholded first PC for mapping. The indices were calculated as follows:

$$\text{OHI} = (\text{band7}/\text{band6}) * (\text{band4}/\text{band6}) \text{ for OH-bearing minerals}$$

$$\text{KLI} = (\text{band4}/\text{band5}) * (\text{band8}/\text{band6}) \text{ for kaolinite}$$

$$\text{ALI} = (\text{band7}/\text{band5}) * (\text{band7}/\text{band8}) \text{ for alunite}$$

$$\text{CLI} = (\text{band6}/\text{band8}) * (\text{band9}/\text{band8}) \text{ for calcite}$$

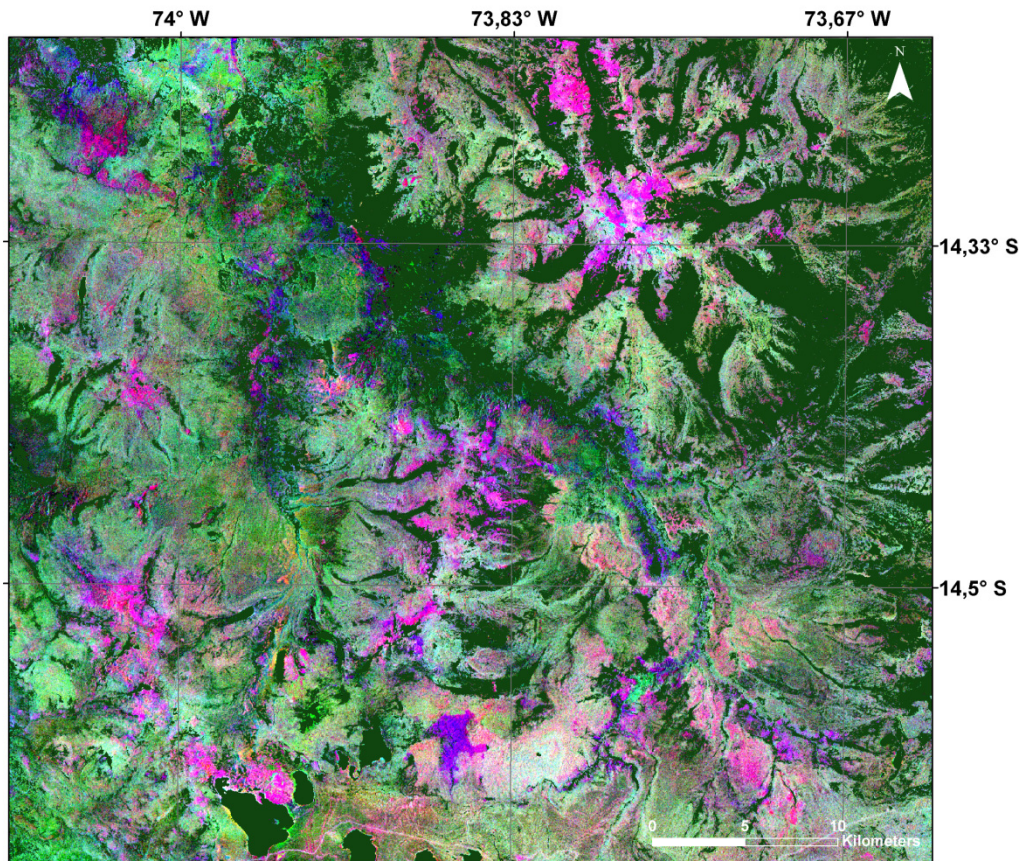


Fig. 8: Spectral index image calculated with transform coefficients proposed by Yamaguchi and Naito (2003). RGB: Alunite index, calcite index, kaolinite index. Regions appearing magenta indicate the presence of alunite and kaolinite. Vegetation and water bodies are masked (green color).

In principle these indices work like the above calculated RBD images and high values in the resulting images correspond to a strong signal of the respective minerals. By using a PC transformation on these images information about mineral variations is lost, but the first principal component reflects areas with the strongest signal for a combination of all the minerals and is a very good indicator for alteration zones. A density slice was performed in order to distinguish high and extremely high values. The resulting two classes are shown in Fig.9 with cyan for very high values and yellow for high values.

The highest values occur in the center of Carhuarazo. The high values near the vegetation mask (green) are due to the residual spectral signal caused by green vegetation. The high values at Carhuarazo and in the south of the scene (little red dots) strongly suggest the presence of argillic alteration and agree with the results shown in Figure 8.

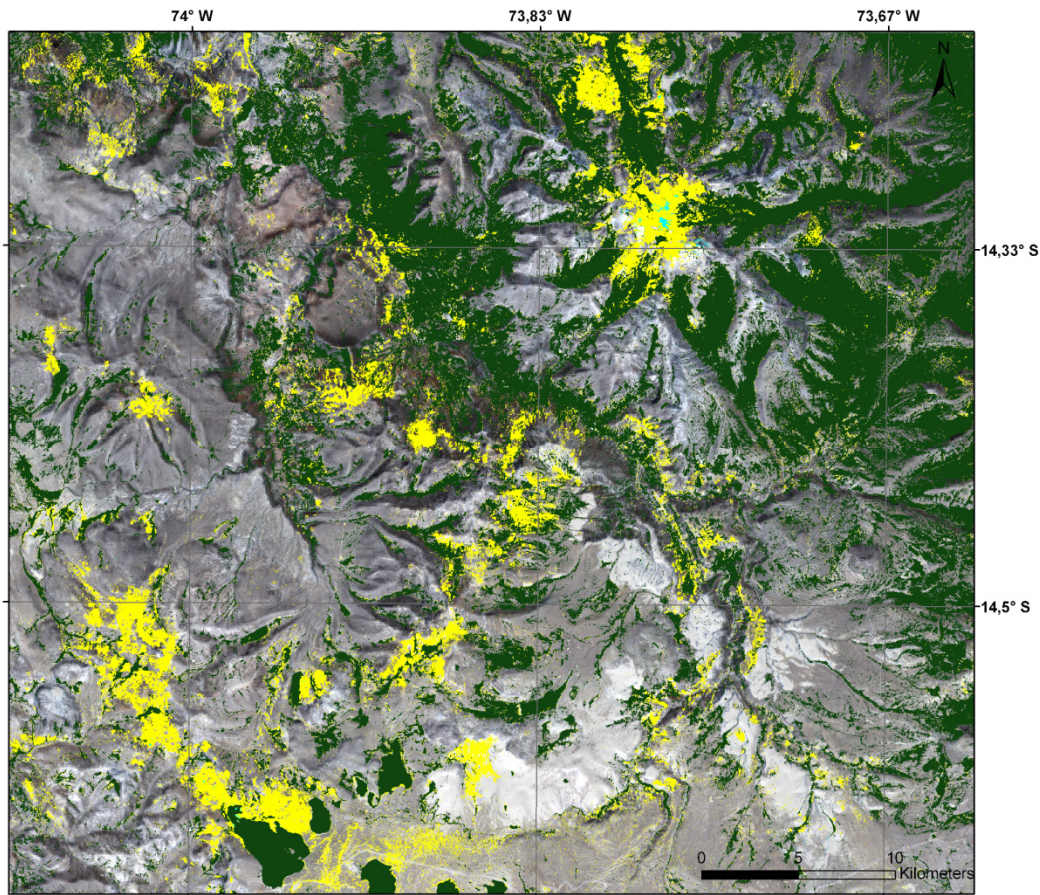


Fig. 9: Thresholded first PC calculated from four mineral indices (OHI, KLI, CLI, ALI) overlain on PC-sharpened Landsat RGB:321 image and ASTER DEM. Vegetation and water bodies are masked (green color).

In summary, the results of the calculated MIs, RBDs and spectral images (e.g. Figs. 4–9) agree very well and give information about the location and the intensity of argillic alteration (Al-OH absorption). The most prominent alteration is found in the center of the Carhuarazo volcanic complex (cyan in Fig. 8 and very high values in Figs. 4, 5 and 7). High values in the calculated band ratios indicate absorption in the spectral range of the denominator and therefore bright areas in Fig. 5 show strong absorption at 2.14, 2.2 and 2.26  $\mu\text{m}$  which is typical for clay minerals. Accordingly, the yellow color in Fig. 4 results from high values in the first (red band) and second (green band) ratio while the third ratio (blue band) has low values. There are no indications for a high abundance of mafic alteration minerals (Fig. 6) and the brighter areas in the center of Carhuarazo are due to anomalous pixel-spectra, probably due to snow/frost patches. In the following we will try to extract more information about the composition of the alteration zones identified in the previous figures by spectral analysis.

4.1.2 VNIR and SWIR Spectral analysis

SWIR data (30m spatial resolution) was spatially registered to the VNIR data (15m spatial resolution) and vegetation and water bodies were masked before further analysis.

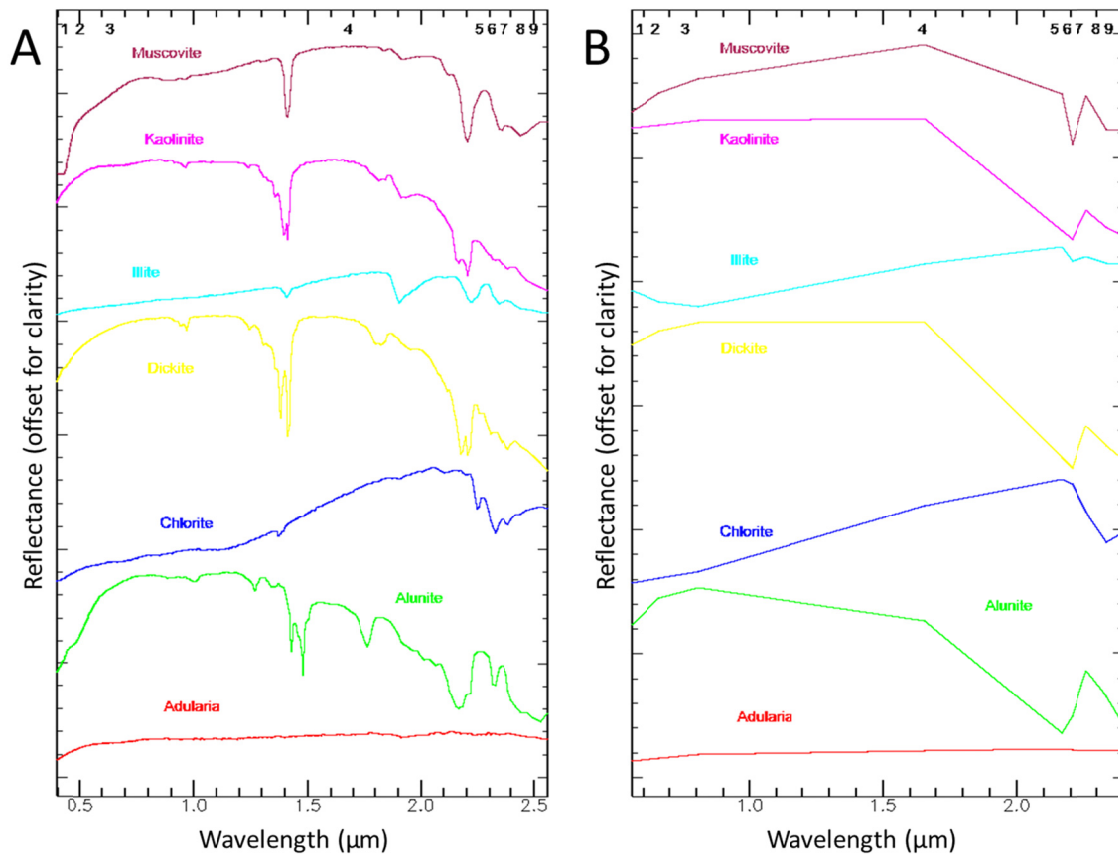


Fig. 10: A: Laboratory spectra of typical alteration minerals and B: resampled to ASTER bands.

In order to visualize subtle spectral differences, a MNF transform was conducted. The MNF transform is a linear transformation that consists of two separate principal components analysis rotations (Green et al. 1988, Boardman and Kruse 1994). The resulting data space can be divided into two parts: one part associated with large eigenvalues and coherent eigenimages and a second part with near unity eigenvalues and noise dominated images. Spectral processing results are improved by just using the coherent portions of the data space. Spectrally different regions appear in bright colors although the image contains no information about the nature of the different materials. This image was used to calculate a pixel-purity-index (PPI) with 20,000 iterations in order to find the spectrally purest or extreme pixels in the scene. The resulting image was helpful in identifying end-members.

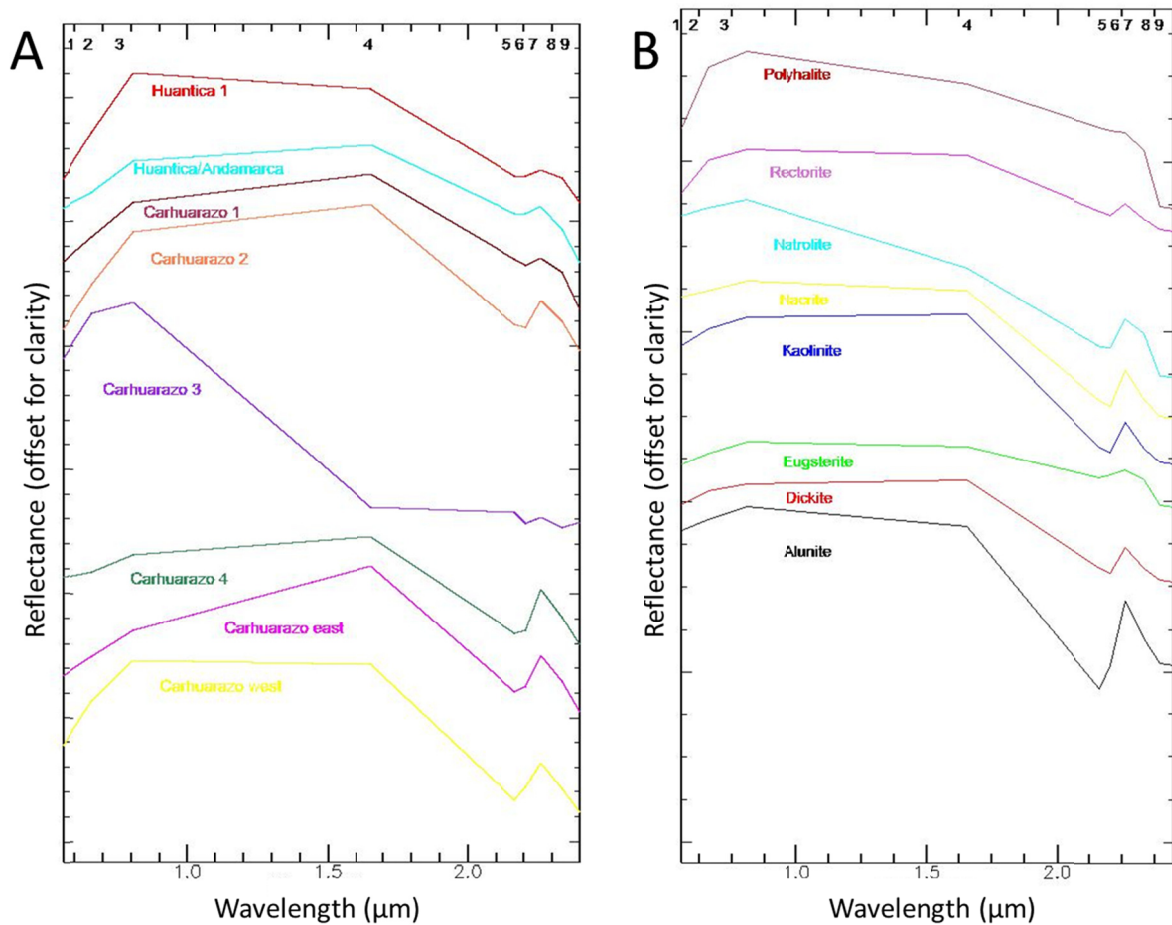


Fig. 11: A: Spectra extracted by PPI, MIs and image interpretation near volcanic centers; B: spectra of minerals discussed in Table 2.

Spectra of some typical alteration minerals found around epithermal ore deposits were selected from USGS spectral library, resampled to ASTER spectral resolution and are shown in Figures 10 A and B. End-member spectra from possible alteration zones which were selected according to the results of PPI calculation, high values in MI and RBD images as well as image interpretation are depicted in Figure 11 A.

Absorption features between 2.17 and 2.22  $\mu\text{m}$  are typical for Al-OH (e.g. alunite, kaolinite) while the absorption features Fe, Mg-OH are around 2.33  $\mu\text{m}$  (e.g. chlorite, epidote, dolomite).

#### 4.1.2.1 Extracting mineralogical information from endmember spectra

As we do not have any data about mineralogical or chemical composition of the rocks and minerals in the area from field work, this approach is based only on spectral information. Three different methods were applied in order to identify dominant minerals in each selected

spectra. This approach should give good results as the spectrally purest pixels in the scene can be considered as endmembers which are dominated by the absorption features of their principal constituent.

Andamarca' are from different locations of the Huantica volcanic complex and show absorption features in ASTER bands 5 (2.16  $\mu\text{m}$ ) and 6 (2.2  $\mu\text{m}$ ) (Al-OH). The 'Carhuarazo 3' spectra show absorption in band 6 (Al-OH) and only weakly in band 8 (Fe, Mg-OH) while the steep slope to band 4 may be due to snow/frost patches in the pixel. 'Carhuarazo east' and 'Carhuarazo 2' display broad band 5 to band 6 absorption while 'Carhuarazo west' only shows a strong band 5 absorption feature (see Table 2).

Pixels always show the spectra of a mixture of different materials but spectrally pure pixels should show absorption features of one dominant component very strongly and thus in a first step we analysed each spectra using the spectral angle mapper (SAM), FFM method and BE using USGS spectral library resampled to ASTER spectral resolution to find the dominant mineral. The maximum deviation in radians tolerated is 0.15 and for FFM a root mean square error of 0.02 and for BE 0.5 (50% of the bands have to match for the mineral to be considered). FFM works very well if there are diagnostic absorption features, which is the case for most alteration minerals while SAM and BM differentiate minerals on the basis of the form of the spectra or the mean band value respectively. It is important to analyze different parts of the spectra which might be diagnostic for a certain mineral. Therefore, we considered the whole spectrum (0.556–2.4  $\mu\text{m}$ ) as well as the subset from 1.6/2.0 to 2.4  $\mu\text{m}$  as many absorption features fall into this range.

For 'Huantica 1' the best fit in FFM is alunite while rectorite, ammonioalunite and eugsterite also score high in SAM and BE and might occur in this environmental setting (see Figs. 11A and B and Table 2). Using only bands 5–9, the results are similar with syngenite scoring high as well. The results for 'Huantica/Andamarca' indicate a mixture of multiple components and alunite, dickite, nacrite score relatively high in FFM while rectorite and eugsterite show good results in BE. Results for band 5–9 are similar.

For 'Carhuarazo 1' dickite, kaolinite, rectorite and polyhalite give the best fit for every method and analysis of band 4–9 indicate kaolinite and dickite as important constituents. Most important minerals for 'Carhuarazo 2' are dickite, kaolinite and nacrite, but natrolite, rectorite and polyhalite score even higher although rectorite rarely occurs in huge deposits (Hanlie et al. 2008) that might be detected at the spatial resolution used in this study. Polyhalite is known to occur in evaporitic sequences rather than in a volcanic environment.

Table 2: Description of the profiles discussed in the text (see Figs. 11 and 12)

Spectra	Characteristics at ASTER spectral resolution
Huantica 1	Absorption features at bands 5 and 6, steep slope from band 3 towards band 1, highest reflectance at band 3
Huantica/Andamarca	Absorption features at bands 5 and 6, moderate slope from band 3 towards band 1, highest reflectance in band 4
Carhuarazo 1	Absorption feature at band 6, highest reflectance in band 4
Carhuarazo 2	Absorption features at bands 5 and 6, highest reflectance at band 4, very steep slope from band 1 towards band 3
Carhuarazo 3	Weak absorption features at band 6 and 8, steep slope from band 3 towards band 1
Carhuarazo 4	Absorption features at bands 5 and 6, highest reflectance values at band 4, moderate slope from band 3 towards band 1
Carhuarazo east	Absorption features at band 5 and 6, highest reflectance at band 4, relatively steep slope from band 4 towards band 3
Carhuarazo west	Absorption feature at band 6, steep slope from band 3 towards band 1, highest reflectance at band 3 and 4
Alunite	Strong absorption feature at band 5, highest reflectance at band 3, moderate slope from band 3 towards band 4
Dickite	Strong absorption feature at band 5, steep slope from band 4 towards band 5, highest reflectance at bands 3 and 4, moderate, convex slope from band 3 towards band 1
Kaolinite	Strong absorption features at band 5 and 6, steep slope from band 4 towards band 5, highest reflectance values at bands 4, 3 and 2, highest reflectance at bands 1 to 4 in comparison to the other minerals discussed
Natrolite	Absorption features at bands 5, 6 and 9, highest reflection value at band 3, moderate slope from band 3 towards band 1, rather low reflectance at bands 4 to 9 in comparison to the other minerals discussed
Polyhalite	Moderate absorption feature at band 5, very low reflectance in band 9, steep slope from band 2 towards band 1, highest reflectance in band 3
Rectorite	Moderate absorption feature at band 5, lowest reflectance of all the discussed minerals, moderate, convex slope from band 3 towards band 1
Nacrite	Strong absorption feature at bands 6 and 5, steep slope from band 4 towards band 5, highest reflectance at bands 3 and 4
Eugsterite	Absorption feature at band 5, highest reflection values at band 4 and 3, slopes from band 3 towards band 1 and from band 4 towards band 6 are not very pronounced

The profile ‘Carhuarazo 3’ is considered because it occurs in many parts around Carhuarazo but is due to snow and frost patches. As areas showing this spectral feature coincide with high values in the Fe, Mg-OH RBD but do not fit the spectra of any mafic mineral in matched filter processing or linear spectral unmixing they will be ignored in further analysis. ‘Carhuarazo 4’ is different from all of the other spectra insofar as natrolite and syngenite, a mineral occurring near volcanic deposits, show best results especially when analysing the spectral subset of 1.6–2.4  $\mu\text{m}$ . Alunite is by far the most important mineral in ‘Carhuarazo east’ and ‘Carhuarazo west’ with natrolite and eugsterite (‘Carhuarazo west’ only) scoring high as well. Many minerals (especially clay minerals) have very similar spectra in ASTER resolution and there are also variations in spectral properties dependent on grain size, trace element content, etc. Therefore, the obtained minerals are likely to represent rather a mineral family than just one particular mineral.

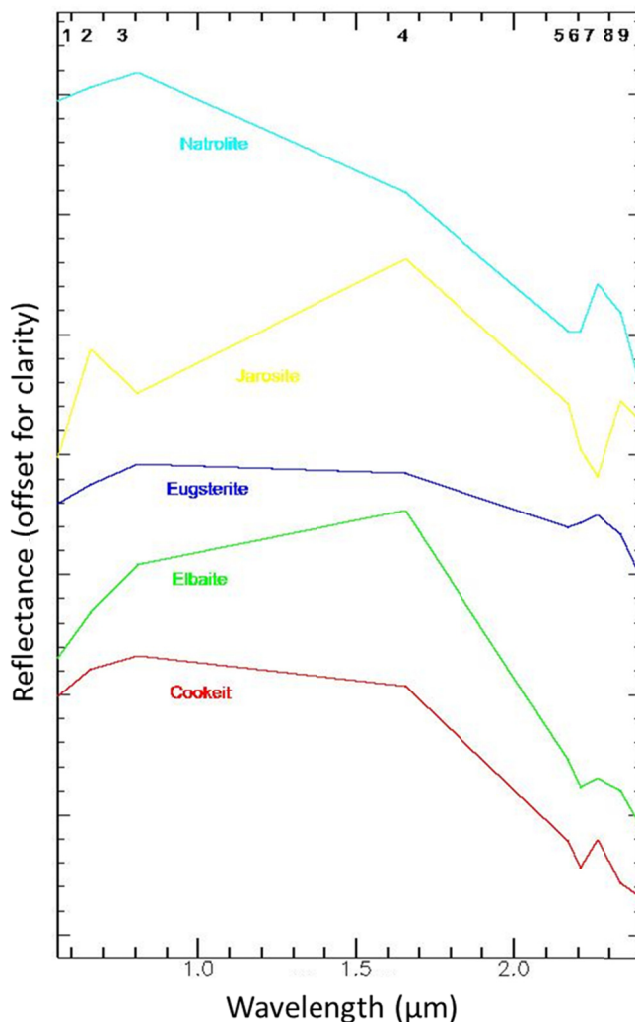


Fig. 12: Spectra of sulfate and other minerals that might occur in a volcanic and/or arid setting (USGS spectral library) resampled to ASTER bands.



#### 4.1.2.2 Matched filter processing in target areas

For further spectral analysis, sub-scenes of the image were selected which showed high values in the above calculated MI and RBD images in order to perform matched filtering using the dominant minerals of the extracted spectra. Matched filtering is a method to find the abundance of the user-defined end-members using a partial un-mixing technique and does not require the knowledge of all the end-members contained in the scene. The region showing high values for the first principal component calculated above (yellow and cyan region in Fig. 9) was selected for further analysis.

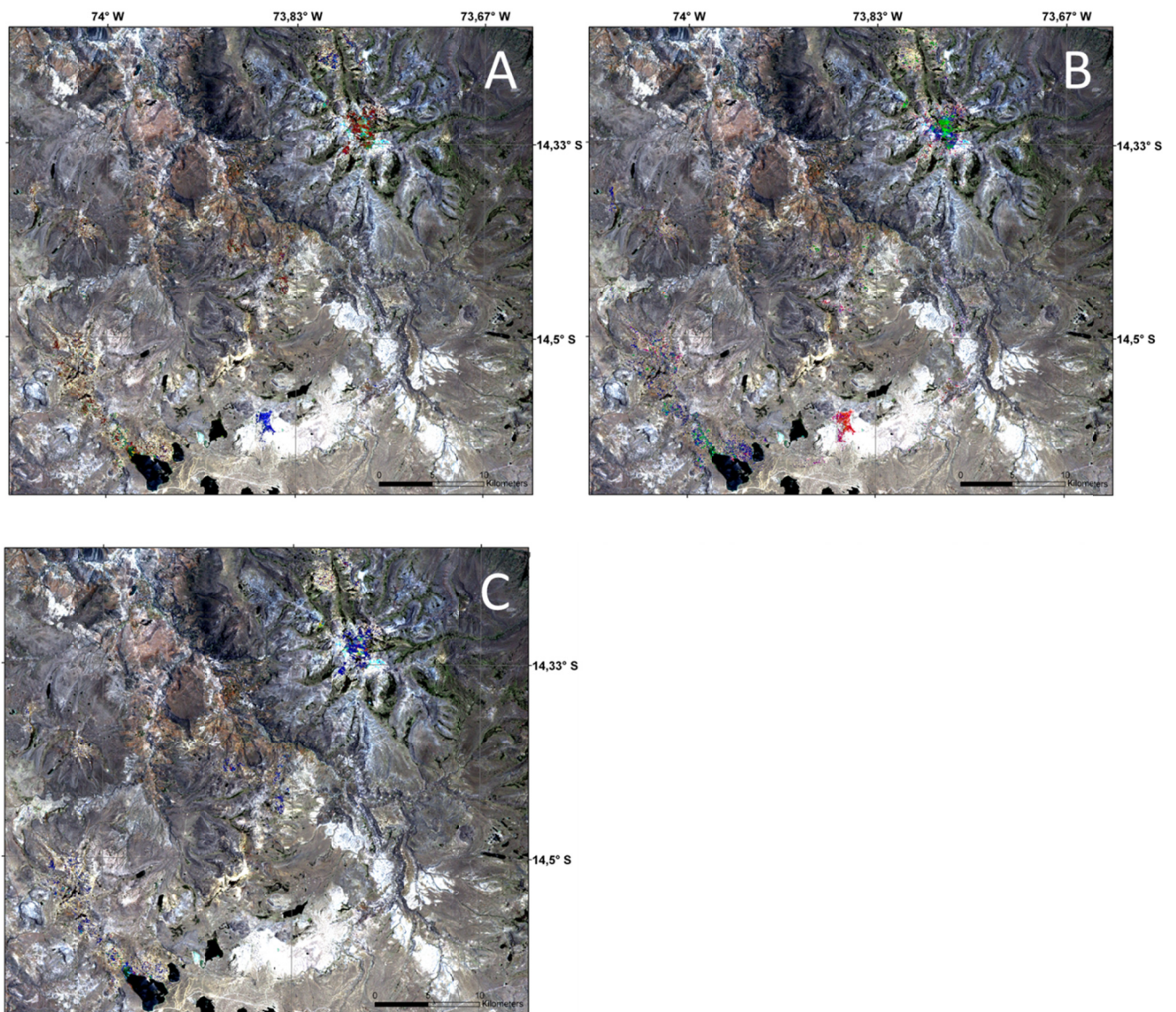


Fig. 13: Matched filter processing results on PC sharpened Landsat true colour image: A: RGB: kaosmectite, nacrite, natrolite, content ranging from 7 to 75, 37 and 29% respectively. B: RGB: eugsterite, nacrite, rectorite, content ranging from 7 to 27, 37 and 89% respectively. C: RGB alunite, dickite, kaosmectite, content ranging from 7 to 26, 21 and 75%, respectively.

It encompasses mainly areas around the volcanic center of Carhuarazo, around Huantica/Andamarca and near the Huantica volcanic complexes. The more spectral end-members (mineral components in our case) are known, the better the method works and a lot of testing is necessary to find the best fit. Using matched filtering with a greater number of possible minerals and then reducing the number to the most probable components gives good results in accordance with MIs and RBDs and a first estimate of mineral abundance can be made.

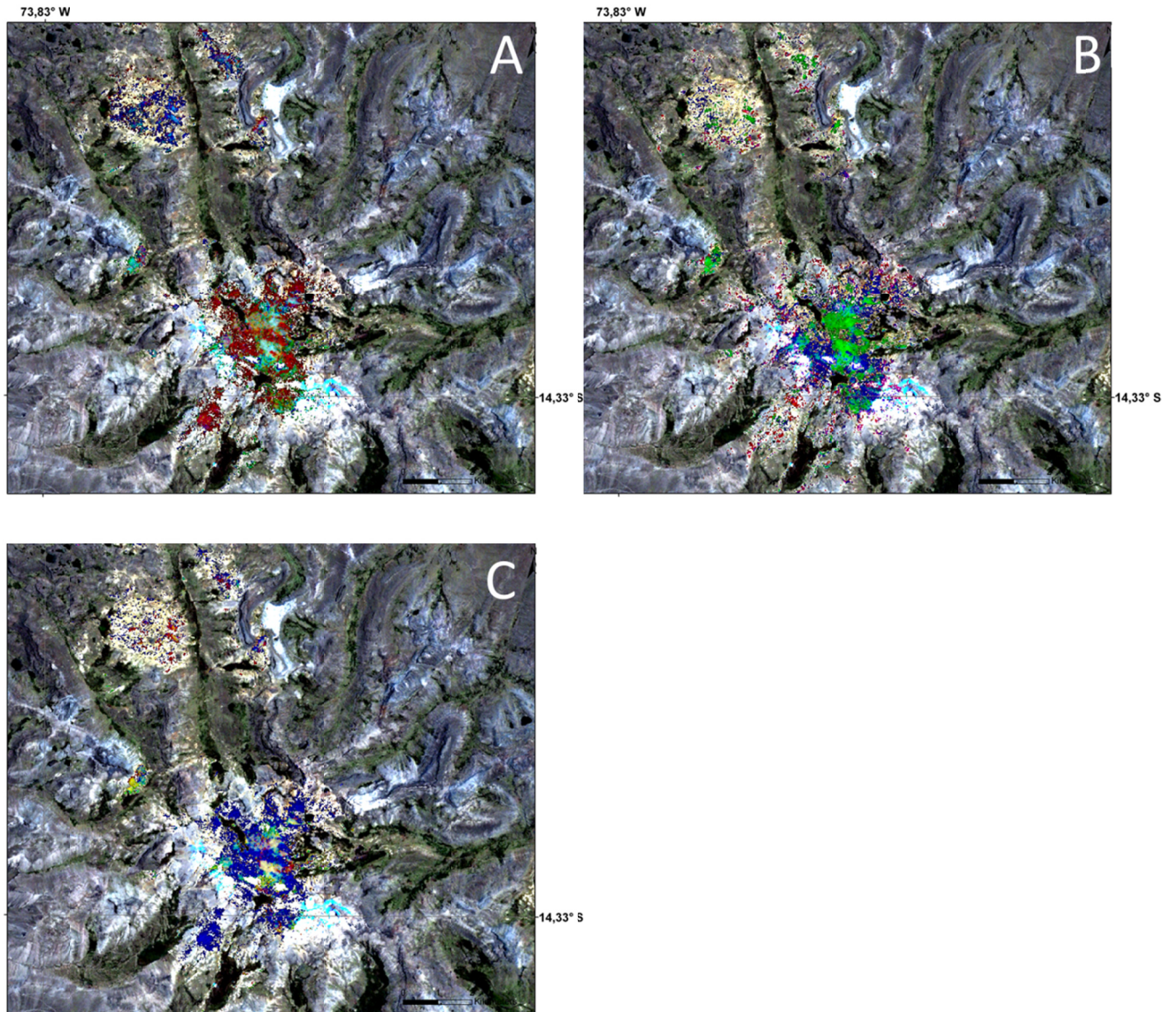


Fig. 14: Matched filter processing results on PC sharpened Landsat true colour image. The images display the volcanic centre of Carhuarazo: A: RGB: kaosmectite, nacrite, natrolite, content ranging from 7 to 75, 37 and 29%, respectively. B: RGB: eugsterite, nacrite, rectorite, content ranging from 7 to 27, 37 and 89%, respectively. C: RGB: alunite, dickite, kaosmectite, content ranging from 7 to 26, 21 and 75%, respectively.

The results for the most important minerals are given in Figures 13 A-C (whole scene) and 14 A-C (subscene of the volcanic center of Carhuarazo).

The percentages given in Figures 13 A–C and 14 A-C are not a measurement for the volumetric or mass (=real) abundance but give the calculated contribution of the spectra of a certain mineral to a mixture of minerals and is therefore a function of the real abundance of the mineral. Matched filter processing confirms the results of MIs and RBDs with respect to intensity of alteration and provides a first estimate of important mineral suites. It is obvious that kaolinite and other aluminous tectosilicates (dickite, nacrite, alunite) dominate in alteration found at the volcanic center of Carhuarazo and in the valleys around the Huantica formation (southeast of the image) while there is one region in the south of the image (red in Figure 13 A, blue in Figure 13 B) that rather seems to locate sulphates (Eugsterite:  $\text{Na}_4\text{Ca}(\text{SO}_4)_3 \cdot 6\text{H}_2\text{O}$ ) and zeolite (natrolite:  $\text{Na}_2(\text{Al}_2\text{Si}_3\text{O}_{10}) \times 2 \text{H}_2\text{O}$ ). Confirming the information gained from the RBD image for mafic minerals we could not detect and map any mafic alteration.

We found no evidence for propylitization (e.g. epidote, chlorite) which is the typical alteration form of andesites near epithermal ore deposits. This might either be due to very small haloes and/or the presence of vegetation and covering sediments near Carhuarazo or because this form of alteration is not present at all. On the contrary, argillization seems to be well developed and can easily be detected.

## 5 Conclusions

---

Ratio images, MIs, RBDs and mineral mapping have been discussed widely and evaluated in well-known regions but literature is sparse or non-existent for spectral analysis of large, relatively unknown regions. In this study, we analysed an area of 2,222 km<sup>2</sup> in Southern Peru using not only MIs, RBDs and ratio images for detection of absorption features (caused for example by Al-OH and Fe, Mg-OH bonds) but also trying to identify single minerals and to give an estimate about relative abundances using matched filter processing. This is a powerful tool to gain information about large areas which can be used in combination with other geological data for the determination of target areas for future fieldwork. The results of MI and RBD calculation leave no doubt about the distribution of altered rocks as well as some information about the nature of mineralization. The RBD image for Al-OH absorption gives very good results while the RBD for Fe, Mg-OH detection shows a very poor response and does not indicate propylitization.

PPI processing combined with the information gained by these methods is a good way to further collect information about the alteration type. The spectra selected with this method

should represent the spectrally purest pixels and therefore absorption features of the dominant mineral should be detectable.

Analyzing each spectra using SAM, BE and FFM with the USGS spectral library as reference resulted in an estimate of minerals present. In addition to alunite, kaolinite, dickite, nacrite and kaolinite which are typical minerals for argilization we found some evidence for subordinate minerals (eugsterite, natrolite and rectorite) which might be present in a volcanic environment but should not be overestimated.

At Huantica/Andamarca natrolite and eugsterite give best results whereas there may only be small amounts of clay minerals present. Above the lake in the extreme southwest of the image reaching northward our results indicate a mixture of clay minerals and sulphates to variable degrees.

The volcanic centre of Carhuarazo is depicted in detail in Figures 14 A-C. Kaolinite and nacrite dominate in the centre together with some alunite and dickite. Some sulphates might be present in small amounts. Natrolite is a hydrated tectosilicate of the zeolite family and is therefore not a very probable candidate for this environmental setting and in higher amounts. As the spectrum is quite similar to the spectra of kaolinite, the detection of this mineral is probably not correct and field evidence is necessary to solve this problem. As clay minerals are also present, complex mixing of different minerals might cause the spectra to be similar to the natrolite spectra.

We found no evidence for propylitization while argilization seems to be well developed and can easily be detected. It is possible that propylitization could not be detected due to vegetation cover or because the alteration is confined to small bands that cannot be mapped at ASTER spatial resolutions.

In summary, we can state that young volcanic structures and argilization can be mapped in unknown regions using ASTER reflectance data and to some degree estimates the probable mineral distribution only relying on spectral information can be made. In order to calibrate the proposed method, detailed ground truth data are necessary and we propose further research following our approach combined with field work as many tertiary volcanic structures are already eroded and cannot be detected by their morphology but might be identified by the presence of alteration assemblages.

Only building a geodatabase in ArcGIS/ArcScene or a similar software allows to further compile, visualize and analyse data. Please find some of our results in video clips produced in ArcScene on our homepage: (<http://www.uni-geochem.gwdg.de/>).

## REFERENCES:

- Boardman, J.W., Kruse, F.A. 1994. Automated spectral analysis: a geological example using AVIRIS data, north Grapevine Mountains, Nevada, ERIM Tenth Thematic Conference on Geologic Remote Sensing. Environmental Research Institute of Michigan, Ann Arbor, p. I-407-I-418.
- Clark, A.H., Farrar, E., Kintak, D.J.L., R.J., Arenas, M.J., France, L.J., McBride, S.L., Woodman, P.L., Wasteneys, H.A., Sandeman, H.A., and Archibald, D.A. 1990. Geologic and geochronologic constraints on the metallogenic evolution of the Andes of southeastern Peru. *Econ. Geol.*, p. 1520-1583.
- De Souza Filho, C.R., Tápia, C.H., Crósta, A.P., and Xavier, R.P. 2003. Infrared spectroscopy and ASTER imagery analysis of hydrothermal alteration zones at the Quellaveco porphyry copper deposit, Southern Peru, ASPRS 2003 Annual Conference Proceedings. Anchorage, Alaska.
- Di Tommaso, I., and Rubinstein, N. 2007. Hydrothermal alteration mapping using ASTER data in the Infiernillo porphyry deposit, Argentina. *Ore Geology Reviews*, v. 32, p. 275-290.
- Earth Remote Sensing Data Analysis Center (E.E.R.S.D.A). 2005. ASTER User's Guide, Part 1., Ver. 4.0.
- Echavarría, L.N., Humphrey, J., Chavez, J., Escobedo, L., Iriondo, A. 2006. Geologic Evolution of the Caylloma Epithermal Vein District, Southern Peru, *Econ. Geol.* 101, 843-863.
- Green, A. A., Berman, M., Switzer, P, and Craig, M.D. 1988. A transformation for ordering multispectral data in terms of image quality with implications for noise removal: *IEEE Transactions on Geoscience and Remote sensing*, v. 26, p. 65-74.
- Hanlie, H., Xiaoling, Z., Miao, W., Yijun, H., Dengwen, D. 2008. Morphological characteristics of (K, Na)-rectorite from Zhongxiang rectorite deposit, Hubei, Central China. *Journal of China University of Geoscience* 19, 38-46.
- Hewson, R.D., Cudahy, T.J., Mizuhiko, S., Ueda, K., and MAuger, A.J. 2005. Seamless geological map generation using ASTER in the Broken Hill-Curnamona province of Australis: *Remote Sensing of Environment*, p. 159-172.
- Mahlburg Kay, S.; Godoy, E; Kurtz, A. 2005. Episodic arc migration, crustal thickening, subduction erosion, and magmatism in the south-central Andes. *GSA Bulletin*, v. 117, no. 1/2. p. 67-88.
- Mahlburg Kay, S., Mpodozis, C., and Coira, B., 1999, Neogene magmatism, tectonism, and mineral deposits of the Central Andes (22° to 33° S latitude). *Geology and Ore Deposits of the Central Andes*, v. 7, p. 27-59.
- Mamani, M., Wörner, G. and Sempere, T., 2009, Geochemical variations in igneous rocks of the Central Andean orocline (13° to 18°S). Tracing crustal thickening and magma generation through time and space. *GSA Bulletin*, v. 122, no. 1/2, p. 162-182.
- Ninomiya, Y. 2003. A stabilized vegetation index and several mineralogic indices defined for ASTER VNIR and SWIR data, *IEEE 2003 International Geoscience and Remote Sensing Symposium (IGRSS'03)*, Volume 3. Toulouse, France, p. 1552-1554.
- Ninomiya, Y., Fu, B., and Cudahy, T. 2005. Detecting lithology with Advanced Spaceborne Thermal Emission and Reflection Radiometer (ASTER) multispectral thermal infrared 'radiance at sensor' data. *Remote Sensing of Environment*, v. 99, p. 127-139.
- Pohl, W.L. 2005. *Mineralische und Energie-Rohstoffe*. Stuttgart, E. Schweizerbart'sche Verlagsbuchhandlung.

- Rosenbaum, G., Giles, D., Saxon, M., Betts, P.G., Weinberg, R.F., and Duboz, C. 2005. Subduction of the Nazca Ridge and the Inca Plateau: Insights into the formation of ore deposits in Peru. *Earth Planet. Sci. Lett.*, p. 18-32.
- Rowan, L.C., and Mars, J.C. 2003. Lithologic mapping in the Mountain Pass, California area using Advanced Spaceborne Thermal Emission and Reflection Radiometer (ASTER) data. *Remote Sensing of Environment*, p. 350-366.
- Rowan, L.C., Mars, J.C., and Simpson, C.J. 2005. Lithologic mapping of the Mordor, NT, Australia ultramafic complex by using the Advanced Spaceborne Thermal Emission and Reflection Radiometer (ASTER). *Remote Sensing of Environment*, p. 105-126.
- Rowan, L.C., Schmidt, R.G., and Mars, J.C. 2006. Distribution of hydrothermally altered rocks in the Reko Diq, Pakistan mineralized area based on spectral analysis of ASTER data. *Remote Sensing of Environment*, p. 74-87.
- Sandeman, H. A., Clark, A. H., and Farrer, E. 1995. An Integrated Tectono-Magmatic Model for the Evolution of the Southern Peruvian Andes (13°-20°S) since 55 Ma. *International Geology Review*, p. 1039-1073.
- Semperé, T., and Jacay, J. 2007. Synorogenic extensional tectonics in the forearc, arc and southwest Altiplano of Southern Peru. *EOS (Transactions, American Geophysical Union)*, v. 88, p. Joint Assembly supplement, abstract U51B-04.
- Tosdal, R.M., Clark, A.H., and Farrar, E. 1984. Cenozoic polyphase landscape and tectonic evolution of the Cordillera Occidental, southernmost Peru. *Geol.Soc.Am.Bull.*, v. 95, p. 1318-1332.
- Wörner, G., Uhlig, D., Kohler, I., and Seyfried, H. 2002. Evolution of the West Andean Escarpment at 18°S (N. Chile) during the last 25 Ma: uplift, erosion and collapse through time. *Tectonophysics*, p. 183-198.
- Yamaguchi, Y., and Naito, C. 2003. Spectral indices for lithologic discrimination and mapping by using the ASTER SWIR bands. *International Journal of Remote Sensing*, v. 24, p. 4311-4323.
- Zhang, X., Pazner, M., and Duke, N. 2007. Lithologic and mineral information extraction for gold exploration using ASTER data in the south Chocolate Mountains (California). *Photogrammetry & Remote Sensing*, v. 62, p.

## MANUSCRIPT II

---

# Mapping patterns of mineral alteration in volcanic terrains using ASTER data and field spectrometry in Southern Peru

Brandmeier, M.<sup>a</sup>, Erasmi, S.<sup>b</sup> Hansen, C.<sup>a</sup>, Höweling, A.<sup>a</sup>, Nitzsche, K.<sup>a</sup>, Ohlendorf, T.<sup>a</sup>, Mamani, M.<sup>c</sup>, Wörner, G.<sup>a</sup>

<sup>a</sup> Georg-August- Universität Göttingen, GZG, Geochemisches Institut, Goldschmidtstr.1, Göttingen D-37077, Germany

<sup>b</sup>Georg-August University Göttingen, Institute of Geography, Goldschmidtstr. 5, D-37077 Göttingen

<sup>c</sup>Pontificia Universidad Católica del Perú, Av. Universitaria 1801, San Miguel, Lima 32, Peru

Published in: JSAES

---

## Abstract

*Because formation of ore deposits is linked to volcanic and post-volcanic processes, an understanding of alteration style in volcanic regions has important applications in economic geology.*

*We use ASTER (Advanced Spaceborne Thermal Emission and Reflection Radiometer) data and field spectrometry for mineral mapping in selected Miocene to Quaternary volcanic areas in Southern Peru to better characterize and understand the Tertiary volcanic evolution in this region. Our goal is to characterize volcanic regions near Puquio (Ayacucho) by correlating areas of intense alteration and related ignimbrite outflow sheets. In particular, we spectrally and mineralogically map different types and intensities of alteration based on remote sensing and ground-truth data.*

*ASTER ratio images, alteration indices and false color composites were used to select ground-training areas for sample collection and field spectrometry. Alteration samples were characterized geochemically, mineralogically and spectrally. Absorption features correlate with chemical properties (e.g. iron content). Hyperspectral data from field spectrometry allow identification of important alteration minerals such as kaolinite and smectite. Alteration mineral assemblages range from silicic to argillic to “zeolite-type”. Using a support vector machine classification (SVM) algorithm on ASTER data, we mapped the different types and intensities of alteration, along with unaltered ignimbrite and lava flows with an accuracy of 80%. We propose a preliminary model for the interpretation of alteration settings, discuss the*

Manuscript II - Mapping patterns of mineral alteration in volcanic terrains using ASTER data and field spectrometry in Southern Peru

*potential eruption sites of the ignimbrites in the region and, propose pH and temperature estimates for the respective classes based on the mineral assemblages identified.*

KEYWORDS: *ASTER, Peru, volcanic structures, mineral detection, spectral analysis, ore deposits, alteration zones*



## 1 Introduction

---

While the large Miocene to Quaternary silicic ignimbrite fields on the Puna-Altiplano plateau of the southern Central Volcanic Zone (CVZ) are very well studied (e.g. De Silva, 1989, De Silva, 1991, Kay et al., 2010, Lindsay et al., 2001, Salisbury et al., 2011, Schmitt et al., 2003, Soler et al., 2007), little is known about the ignimbrites and their eruptive centers in the less arid northern CVZ in Southern Peru. This is due to their older ages, higher rates of precipitation and resultant, somewhat denser vegetation cover, deep valley incision, and weathering in this area compared to the hyper-arid climate and excellent preservation of the southern Altiplano/-Puna ignimbrites and related calderas. Nevertheless, large ignimbrite sheets with estimated volumes that are comparable to Altiplano outflow sheets can be observed, and knowledge about timing, location of eruptive centers, and composition can provide valuable information for the temporal and spatial understanding of the Tertiary evolution of the Andes.

Calderas represent long-lived magmatic systems that may span several millions of years, show prolonged hydrothermal activity, and form mineral deposits related to caldera structures (Rytuba, 1994, Woldegabriel, 1990, Smith and Bailey, 1968, McKee, 1979, Lipman, 1984). Hydrothermal systems are mainly related to post-caldera intrusions and vent complexes along reactivated faults towards the end of a caldera cycle. Our region of interest is located near Puquío (Ayacucho) (Fig. 1). Magmatic activity spans from the eruption of the Nazca ignimbrites > 22 Ma (Roperch et al., 2011, Thouret et al., 2007) to the age of deeply glaciated stratovolcanoes (7 to 9 Ma; Karatson et al., 2012) in the area. Little is known about the location of these calderas and timing of their magmatic and hydrothermal activity. Caldera structures such as ring faults or radial fissures are important in localizing hydrothermal activity, rock alteration, and associated ore deposits. A simplified conceptual model of a caldera system with ignimbrite eruption, reactivated faults, post-caldera volcanism, and hydrothermal alteration is shown in Fig. 1 to further guide the presentation and interpretation of our data. The sketch shows our area of interest in Southern Peru, an elevation profile through the area (black line), and schematic magmatic intrusions that may have driven hydrothermal systems and caused alteration.

Remote sensing data is well suited for geological mapping and mineral exploration in volcanic regions. The advent of the Advanced Spaceborne Thermal Emission and Reflectance Radiometer (ASTER) has led to advances in mineral surface mapping using band ratio images, spectral indices and even, on a subpixel level, spectral

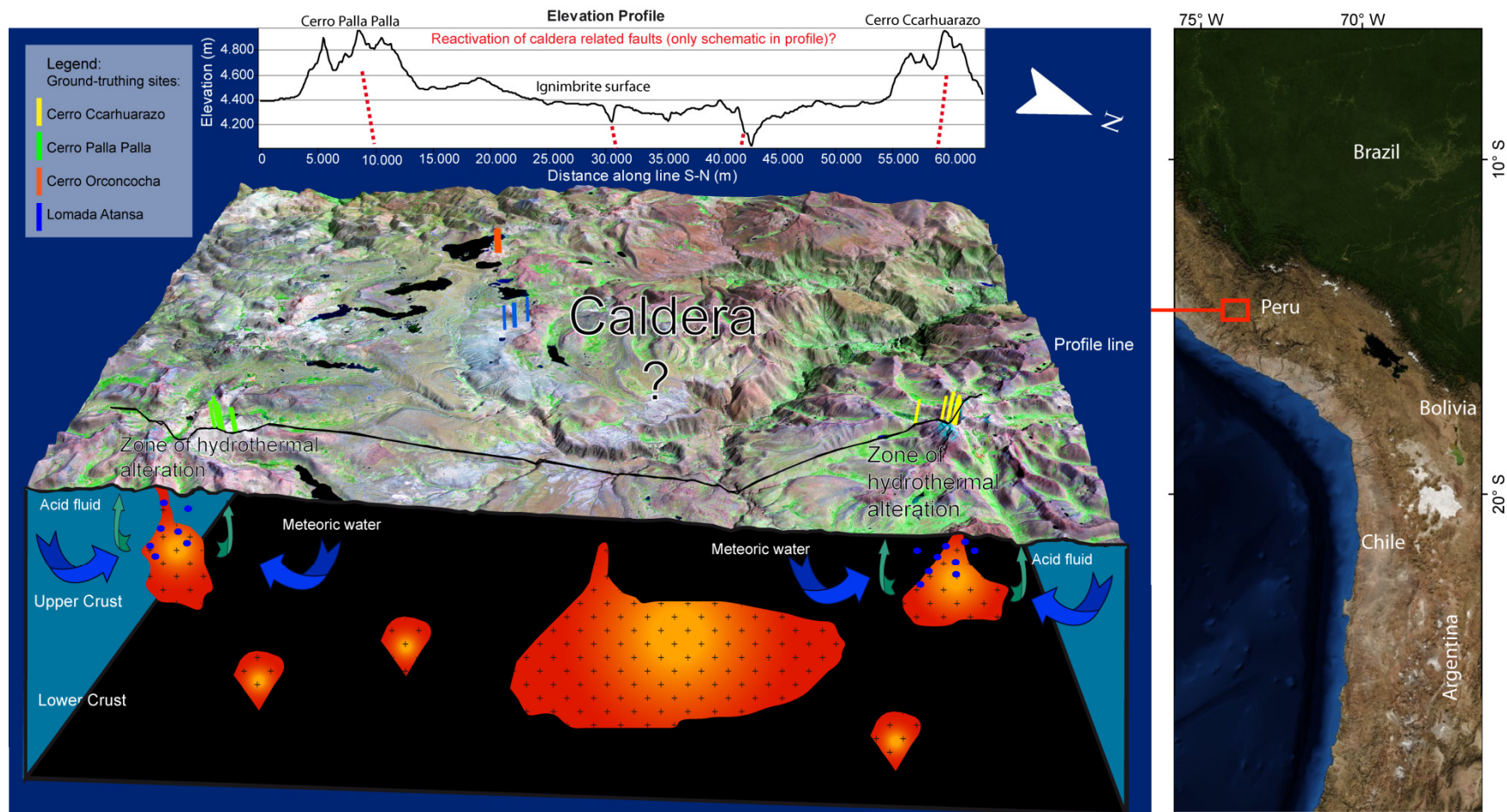


Fig. 1: The area of interest is shown as Landsat (RGB:742) draped on SRTM elevation data ( $z=2$ ) and an elevation profile through the Cerro Palla Palla, the ignimbrite surface and the Cerro Carhuarazo (black line). Ground-truthing sites are shown as 3D features and are also provided as kml file. Underlying the satellite data, a conceptual model is shown: Assuming that the caldera cycle is only part of a larger magmatic episode spanning millions of years, ring fractures of calderas and other tectonic features related with the formation of a caldera can be reactivated and magmatic and hydrothermal activity can continue. Surface processes alter the morphology of the landscape and caldera structures might no longer be visible, but hydrothermal alteration related to reactivated structures can still be detected. The model shows an old magma chamber below the ignimbrite surface and hydrothermal activity close to younger volcanic edifices.

unmixing methods (Ninomiya, 2003a, Rowan et al. , 2006, Sabins, 1999, van der Meer et al., 2012, Pour and Hashim, 2012, Yamaguchi and Naito, 2003 to name but a few).

In this study we use a combination of hyperspectral field spectrometer data, rock sample geochemical analysis and ASTER data in order to (a) characterize alteration patterns related to magmatic and hydrothermal activity in the study area, (b) map the extent of ignimbrites in the same area, (c) apply a classification algorithm on reflectance and emissivity data in order to parameterize our findings within a GIS database. The combined data improve understanding of the relationship between volcanic and tectonic features and to constrain the potential eruption site(s) of the observed ignimbrites.

## 2 Location and Geological setting

---

The study area is located in the Ayacucho province in the northern Central Andes of Southern Peru at an average elevation of more than 4000 m a.s.l. (Fig. 1). The region is located directly at the drainage divide between the Pacific and Atlantic Oceans and forms part of the Andean Cordillera just to the north of the active Central Volcanic Zone. Reconnaissance mapping (geological maps 30-o; INGEMMET, 2001b and 29-o; INGEMMET, 2001a), that covers this area, identifies Miocene to Pliocene ignimbrites and lava flows, intercalated with terrestrial sediments. The volcanic pile overlies thick sequences of sediments derived from the uplift of the Andes at least since 35 Ma (Decou et al., 2013 and reference therein) and the folded pre-Andean basement. Roperch et al. (2011) provide Ar-Ar ages of 13.5 to 20 Ma for two rhyolite samples of the Puquio Formation. Bellón and Lefèvre (1977a,b) dated lavas of the Cerro Carhuarazo at 9.2 +/- 0.5 Ma. The geological map distinguishes four Miocene ignimbrite formations (Huaylillas, Alpabamba, Aniso and Caudalosa), the Pliocene Andamarca (=Sencca) formation and Barroso lavas. Bellón and Lefèvre (1977a,b) provide one radiometric age ( $^{40}\text{K}/^{40}\text{Ar}$ ) of 8.3 Ma of the Andamarca formation in the Urayhuna river valley. Many questions about correlation of the ignimbrites, timing and location of the eruption centers remain unsolved. Major regional tectonic structures of poorly defined age are oriented NW-SE and, to a minor degree, NE-SW and N-S. Some local structures with orientations between N50° and 70°E to E-W also occur that probably correspond to the Quechua 3 event (Guevara, 2001, INGEMMET, 2001b).

A schematic geological map of the study area reproduced from the INGEMMET maps is provided as supplementary material.

### 3 Methods

---

#### 3.1 Alteration Mapping

---

Alteration mapping is an important tool for exploration. Processes and types of alteration and their relation to ore deposits, as well as the tectonic features of caldera settings are widely known and described (e.g. Hedenquist et al., 2000, Rytuba, 1994).

ASTER is a multispectral imaging system on board NASA's TERRA spacecraft, launched in December 1999 that records radiation in 14 spectral bands. Reflected radiation is measured in three bands between 0.52 and 0.86  $\mu\text{m}$  (visible and near infrared - VNIR) and six bands from 1.6 to 2.43  $\mu\text{m}$  (shortwave infrared - SWIR). Emitted radiation is measured in five bands from 8.125 to 11.65  $\mu\text{m}$  (thermal infrared - TIR) (Fujisada, 1995).

In this study we use three different ASTER data products (level 1b radiance at sensor data, cross-talk corrected reflectance data and emissivity data), as well as geochemical and spectral data from ground-truth samples of altered rocks, together with pattern recognition in an ignimbrite-dominated area. A simplified processing chain is illustrated in the following flowchart (Fig. 2).

Four ASTER Level 1B scenes were selected, two each from the same orbital pass in order to facilitate mosaicking. In order to avoid spatial and spectral data gaps along the edges of the images, these were spatially resized before mosaicking. The dark subtraction method was used to correct for atmospheric scattering and crosstalk. The term "crosstalk" in remote sensing refers to the phenomenon where the electrical or optical signals from one SWIR band (especially ASTER band 4) leak to another band (Iwasaki and Tonooka, 2005). With the help of scatterplots for each band combination for areas with very low band values minimum values for each band were extracted. To cross-calibrate the two images (consisting of two scenes each), regions of interest (ROIs) that were representative for different materials that would comprise a reliable band statistic were selected in overlapping areas. A regression line was calculated for the two datasets for each band and the gains and offsets applied to the second image in order to suppress multiplicative effects (such as water vapor in bands 5, 6, 8, 9). The resulting mosaic was tested for radiometric fidelity using ratio images. Remaining scene differences were noted to be changes in vegetation cover between the different times of acquisition. For the crosstalk-corrected reflectance data, only spatial resizing was necessary.

The advantage of the first product is that it allows for proper correction of additive effects before multiplicative operations are applied (Cudahy et al., 2008). The second product is

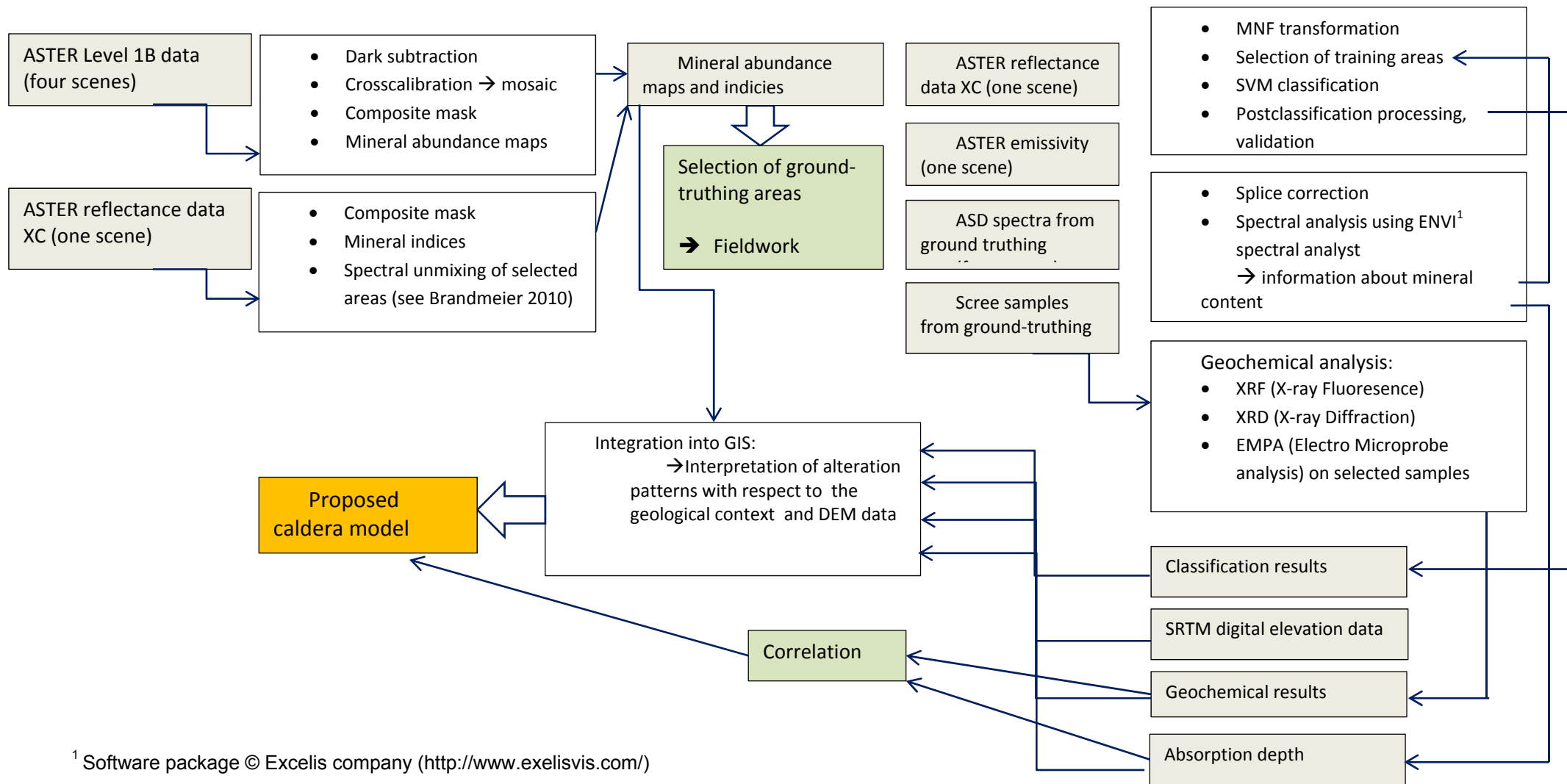


Fig. 2: A simplified processing chain illustrated in a flowchart, see text for further details

already atmospherically corrected and provided as reflectance data. The atmospheric correction algorithm for VNIR is based on a Look-Up Table (LUT) approach that uses results from a Gauss-Seidel iteration of the Radiative Transfer Code (RTC) :

([https://lpdaac.usgs.gov/products/aster\\_products\\_table/ast\\_07xt](https://lpdaac.usgs.gov/products/aster_products_table/ast_07xt))

The next step was the creation of a composite mask for vegetation, water, and shadows. This step was crucial for good results in image analysis later on, and significant interactive testing was needed to choose the proper thresholds for each sub-mask. For vegetation delineation NDVI calculation was used for masking. Water and shadows were masked by thresholding band 4. The scene was free of clouds and therefore no cloud-mask was necessary. Nevertheless, the effect of very thin clouds was observed in some places.

Mineral abundance maps following the approach developed by Cudahy et al. (2008) were derived, spatial and spectral registration, radiometric correction and the composite masking were applied. The empirical method based on the normalized absorption depth of diagnostic spectral features of minerals was adapted to the environmental settings of this study. The basic assumption is that the abundance of a given mineral is proportional to the normalized continuum-depth of a diagnostic absorption feature, where zero abundance equals no absorption (i.e. no mineral present). Given the 9-14 band spectral resolution of ASTER, this method maps mineral groups rather than individual minerals. For example, we produced maps of the contents of iron oxide (hematite, goethite), ferrous iron, opaque minerals (sulfides, carbon, magnetite, Mn-oxides), minerals containing an Al-OH group (illite, muscovite, smectite, kaolinite), Mg-OH and CO<sub>3</sub> groups (calcite, dolomite, magnesite, chlorite), Fe-OH groups (chlorite, epidote, jarosite, nontronite) and of the distribution of advanced argillic alteration (pyrophyllite, alunite and kaolinite). The band ratios used for creating masks and mapping are described in detail by Cudahy et al. (2008). For Al-OH group minerals the spectral range of ASTER bands 5 to 7 was used, for Mg-OH group content ASTER bands 6 to 9 were used, and for ferric oxides and ferrous iron content ASTER bands 3 to 5 were used. The resulting grayscale ratio-images were interactively stretched and color-coded with a rainbow color scale where highest values are shown as red. All these steps were conducted using ENVI<sup>1</sup> software and then converted to GIS compatible GeoTiff format for inclusion to ArcGIS<sup>2</sup> for further analysis. Also included were the mapping results of a previous study using the reflectance data set (Brandmeier, 2010) (PPI calculation, matched filtering). These prior maps derived from level 1B data and from reflectance data were compared and used for identifying spectral anomalies in the field and for selecting regions for ground-truth sample collection.

---

<sup>1</sup> Software package © Excelis company (<http://www.exelisvis.com/>)

<sup>2</sup> Software package © ESRI (<http://www.esri.de/>)

### 3.2 Ground-truthing

---

Four regions of interest were selected as ground truth training sites based on both accessibility and the results of alteration mapping (e.g. anomalies in the Level 1b mineral abundance maps or in mineral indices calculated in (Brandmeier, 2010).

At 52 sites ASD hyperspectral data and samples were measured and collected in order to characterize different alteration settings at (Fig.1): Cerro Carhuarazo, Cerro Chavina (Palla Palla), Lomada Atansa and Cerro Orconcocha (Fig. 3A-E).

Cerro Carhuarazo is a 25 km diameter ca, 9,5 Ma old stratovolcano (Bellón and Lefèvre, 1977) with a strongly epithermally altered center showing anomalies in mineral indices and Al-OH abundances (Brandmeier, 2010, Paz et al. 2000). The second location near Chavina is the Palla Palla volcanic center (Inca and Cayo, 2000) showing strong spectral alteration anomalies in the Al-OH abundance maps. It was sampled along a traverse from the center to the margin of the alteration zone. Lomada Atansa is an ignimbritic surface of the Andamarca ignimbrite formation that showed spectral alteration anomalies and high abundances for natrolite in the spectral unmixing (Brandmeier, 2010). Cerro Orconcocha is part of the Huantica volcanic complex and showed spectral anomalies indicating strong hydrothermal alteration confirmed previously by Guevara (2001).

Spectral measurements were conducted using an ASD FieldSpec3 spectrometer with a spectral range from 350 nm to 2500 nm at a spectral resolution of 3 nm (at 700 nm) and 10 nm (at 1400 nm and 2100 nm) and a sampling interval of 1.4 nm (350-1000 nm) and 2 nm (1000-2500 nm). For each sampling site 5 measurements were taken, each averaged from 30 spectral scans. The data was accumulated as reflectance data after a calibration with a Spectralon Target as reflectance standard. Representative scree/rock samples were collected for chemical and mineralogical analysis and for further spectral measurement using the contact probe with an artificial light source in the laboratory.

Field measurements proved to be difficult as atmospheric conditions at this altitude were rapidly changing, and recalibration of the spectrometer was constantly necessary. ASD reflectance data was imported into ENVI for analysis and splice corrections applied using ViewSpecPro. Spectral libraries were built for each location for (a) field measurements and (b) contact probe measurements and also resampled to ASTER spectral resolution. Spectral analysis using the ENVI spectral analyst tool (algorithms described by Clark et al., 1990, 1987; Clark and Roush, 1984; Kruse et al., 1993) was conducted for all samples separately. Field- and contact-probe measurements were comparable and will be discussed together in the following.

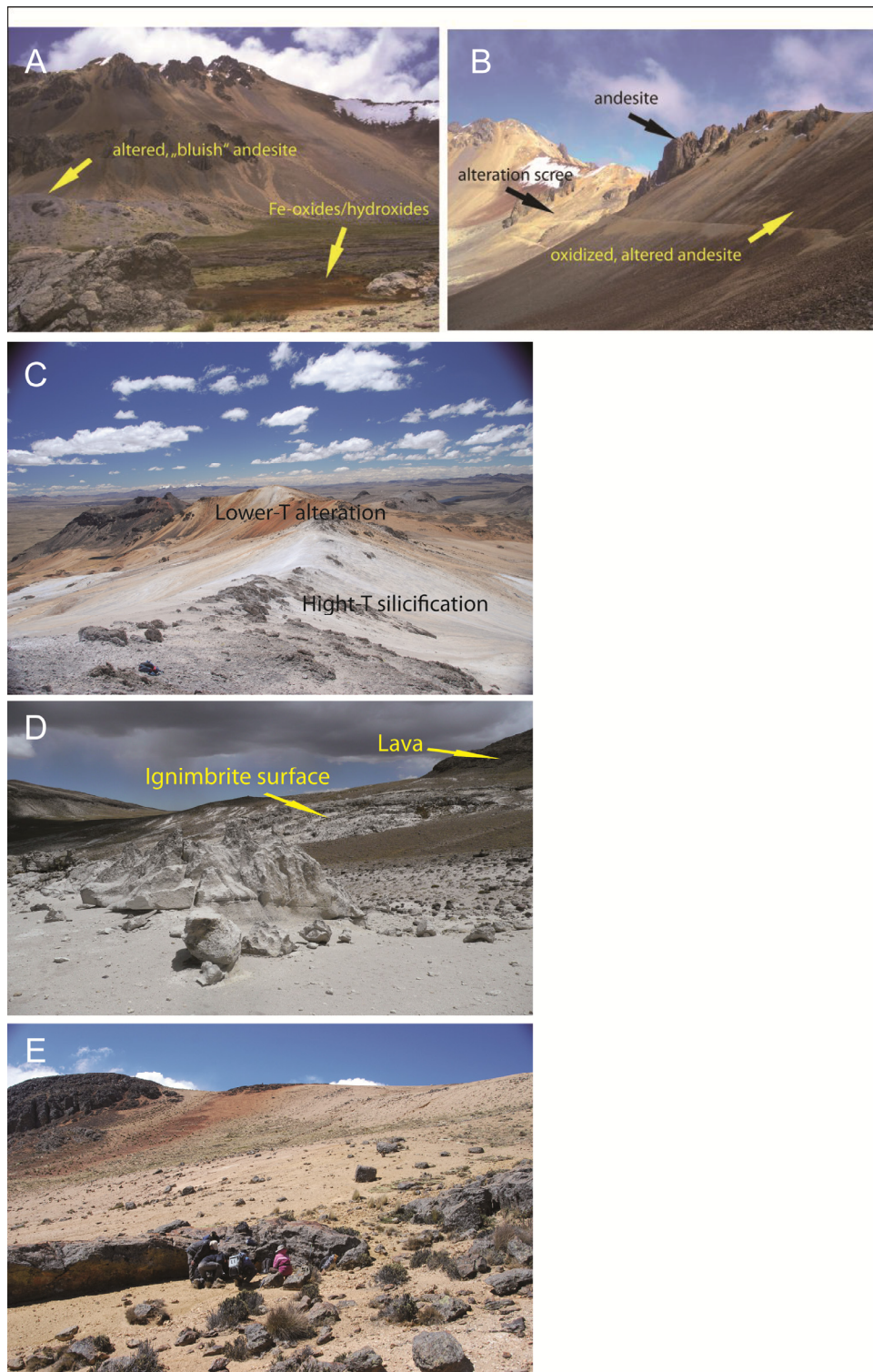


Fig. 3 A-E: Ground-truthing sites: A and B: Cerro Carhuarazo. This ground-truthing site is an epithermally altered volcano (Paz et al. 2000). Alteration debris and altered andesite can be seen. C: Cerro Palla Palla (Chavina). This ground-truthing site is an epithermally altered volcano core (Inca and Cayo, 2000) and was sampled in a traverse across areas with different alteration style. D: Lomada Atansa. This ground-truthing site is an ignimbrite outcrop showing strong anomalies in alteration indices and Pixel purity index (PPI)-calculation (Brandmeier, 2010). E: Cerro Orconccocho. This ground-truthing site showed elevated values for several alteration indices.



Method weights for spectral angle mapper (SAM), spectral feature fitting (SFF) and binary encoding (BE) were equally set to 1 and minimum and maximum values to min. 0.0, max. 0.5 to 0.1 (radians), min. 0.05, max. 0.1 (RMS error) and min. 0.5, max. 0.76 (percentage of bands correctly matched) respectively. These algorithms compare the spectral similarity of a sample spectrum to reference spectra from the USGS spectral library. The principal aims were to (a) identify typical alteration minerals based on the spectra, (b) observe changes in the depth of the absorption features with changes in location, and (c) find a method to distinguish different types of alteration on the basis of ASTER image. Absorption depth for the 2.2  $\mu\text{m}$ , the 2.165  $\mu\text{m}$  and the 0.95  $\mu\text{m}$  absorption features were measured directly from the continuum removed (=normalization to a common baseline) spectra (Clark et al. 1984). Spectral data was exported to Excel and GIS in order to better evaluate the correlation between ASTER remote data and ASD ground-truthing data.

### 3.3 Geochemical analysis

---

#### 3.3.1 X-ray Fluorescence Spectrometry (XRF)

---

Major and trace elements of 35 rock alteration samples and 9 reference samples (unaltered rock) were analyzed by XRF (AXIOS-Advanced, PANalytical). This method allows for routine analysis of rocks, minerals, soils and solid synthetic materials. XRF has the capability to determine all elements of the Periodic Table from B to U.

The samples were prepared for measurement as glass disks. Because the surface and homogeneity of the specimen are essential for the accuracy and precision of the determination, we use a fully automated fusion technique, SGE 21 from Schoeps.

Major elements ( $\text{SiO}_2$ ,  $\text{TiO}_2$ ,  $\text{Al}_2\text{O}_3$ ,  $\text{MnO}$ ,  $\text{MgO}$ ,  $\text{CaO}$ ,  $\text{Na}_2\text{O}$ ,  $\text{K}_2\text{O}$ ,  $\text{P}_2\text{O}_5$ ,  $\text{Fe}_2\text{O}_{3\text{t}}$  given in wt-%) were analyzed using the SSTmAX-4-kW rhodium target X-ray tube for sample excitation. Detection limits vary from 3 to 0.5 ppm for most of the measured trace elements.

#### 3.3.2 Electron Microprobe Analyses (EMPA)

---

Three thin sections of selected samples were carbon-coated and analyzed for zeolites. Furthermore, nine representative sediment grains from each sample with a maximum diameter of 1 mm were picked under a microscope and mounted on glass in resin. The grains were ground, polished and then analyzed. Compositional images (BSE) were taken and major elemental compositions of miscellaneous distinguishable mineral phases were determined using the energy dispersive system attached to the probe (EDX).

Electron Microprobe (EMP) measurements were performed using a JEOL JXA 8900 RL instrument and included low-resolution BSE images for overview, accumulated BSE images as high-resolution imaging method and quantitative wavelength dispersive analyses of alteration minerals. The instrument was run at 15 kV potential and at 10  $\mu\text{m}$  beam diameter. For the thin sections signals for Si, Al, Na, K, Ca, Ba, Mg, Sr and Fe were detected on the five spectrometers, while additionally also the BSE signal was recorded in the COMPO-mode.

Grain mounts were only analyzed qualitatively, as quantitative analysis was not possible due to small grain size, low crystallinity, and mineral instability under the beam.

### 3.3.3 X-ray Diffraction (XRD)

---

We measured 35 powdered samples (clay to silt fraction) with a Philips powder diffractometer at the Dept. for Crystallography in Göttingen. Measuring time was 5 and 15 seconds (day and nighttime measurements respectively) at  $0.2^\circ$  2-theta. Scree samples were dried before measurement at  $110^\circ\text{C}$ .

## 3.4 Classification Mapping of Alteration Patterns

---

The aim of spectral classification was to map ignimbrite outcrops and alteration patterns based on the results from ground-truth samples, correlated spectral measurements and geochemical analysis. For this purpose we tested various methods in order to find the best one for our particular regional, spatial and spectral setting.

The classification method used was the Support Vector Machine Classification algorithm available in ENVI. This algorithm separates classes using a decision surface that maximizes the margin between different classes (optimal hyperplane). Detailed information about this classification algorithm can be found in Boser et al. (1992), Chih-Wei Hsu and Chih-Jen Lin (2003) and Cortes and Vapnik (1995.).

The classification was conducted in two steps using twelve different training sites (ROIs) (see table 1). ROIs were chosen on the basis of detailed fieldwork and represent different alteration settings and lithologies. The nine ASTER reflectance bands (after applying the vegetation suppression algorithm provided in ENVI) were combined with 7 bands of Minimum Noise Fraction (MNF) transformed (Green et al. 1988) reflectance data. The two last eigenchannels were removed for classification as a method of noise suppression. Additionally, the surface emissivity product was used for classification, as thermal infrared provides additional information about silicate minerals present (Hecker et al., 2012). This

data is derived from level 1B radiance at sensor data after atmospheric correction and separation of the emissivity component from kinetic temperature component (Gillespie et al., 1998).

Examples of the spectral characteristics of the respective training areas are given in Fig. 4A and B. Although differences in the nine reflectance bands are not obvious, MNF transformation allows enhancement spectral differences. The addition of these bands increases dimensionality in the dataset although some information might also get lost using MNF bands only. Emissivity data (zoom) shows subtle differences for the respective classes with the “lava” class showing highest values. The composite mask was applied and the SVM classification was started. The penalty parameter was set to 50 and the probability threshold to 0.5. The gamma parameter automatically set by ENVI was not changed. Classes and reference samples for the definition of ROIs are given in Table 1.

As the automatic classification output proved insufficiently accurate, the rule classifier was used to optimize class thresholds. The “Soil/Regolith” class was set to background value. The accuracy of the classification was assessed by calculating a confusion matrix using a second set of ground-truth ROIs that was selected together with the ROIs used for classification but kept apart for quality assessment. The resulting class image was exported to ArcGIS. For the “ignimbrite” class a buffer image was calculated in order to better highlight isolated pixels in the image. The classes defined by the ROIs and separated by this procedure are summarized in Table 1.

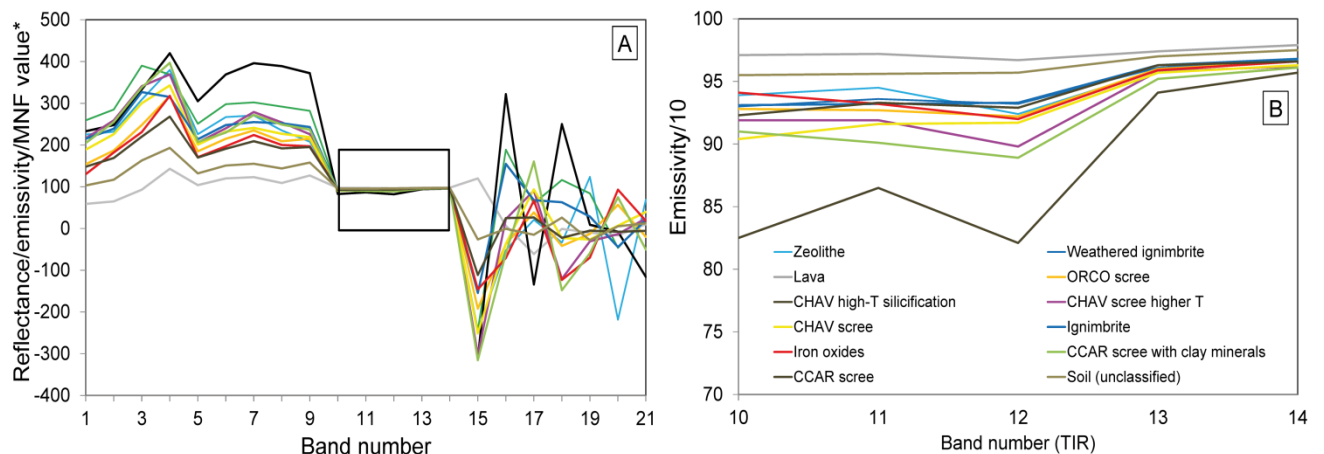


Fig. 4: A: Plot showing examples for the different classes of SVM classification. The first nine bands are ASTER reflectance data (in % multiplied by 10), bands ten to 14 are emissivity data (scale factor 100), bands 15 to 21 are MNF transformed bands that were used to increase dimensionality and to reduce noise. B: Zoom to the emissivity bands (square in Fig. 5 A) in order to highlight spectral differences.

Table 1: Description of ROIs used for classification and reference samples.

Regions of interest for SVM classification

Class	Description	Reference sample*
Zeolithe	Fault zone in ignimbrite at Lomada Atansa with zeolithes	ATAN-11-08, ATAN-11-09, ATAN-11-05
ORCO scree	Alteration at Cerro Orconcocha with a high degree of silicification, clay minerals, iron oxides, rutile	ORCO-11- 10
CHAV scree higher-T	Alteration at Cerro Palla Palla with clay minerals, a high degree of amorphous silica and some oxides	CHAV-11-09, CHAV-11-12
CHAV high-T silicification	Silicified rock at Cerro Palla Palla, up to 99 wt-% SiO <sub>2</sub>	CHAV-11-08, CHAV-11-07, CHAV-11-06, CHAV-11-17
CHAV scree	Alteration scree at Cerro Palla Palla, clay minerals, amorphous silica	CHAV-11-01, CHAV-11-02, CHAV-11-03, CHAV-11-04
Iron oxides	Alteration with dominating iron oxides and clay minerals at Cerro Palla Palla	CHAV11-16, CHAV-11-14
Weathered Ignimbrite	Weathered ignimbrite, some clay minerals	ATAN-11-01
CCAR scree	Alteration scree at Cerro Carhuarazo, amorphous silica, iron oxides	CCAR-11-08, CCAR-11-09
CCAR scree with clay minerals	Alteration at Cerro Carhuarazo, clay minerals, amorphous silica, iron oxides	only spectral indices
Soil/Regolith (unclassified)	Covered to partially covered ground	only validation in the field
Lava	Lava flows and volcanic rocks	only validation in the field
Ignimbrite	Ignimbrite outcrops	only validation in the field

\* training areas were determined using reference samples, spectral indices and ground-truthing experience.

## 4 Results and Discussion

### 4.1 ASTER mineral indices and abundance maps

Mineral abundance maps created using ENVI software highlight volcanic alteration zones. The mapped areas are particularly promising for locating alteration minerals such as kaolinite, smectites or alunite. All digital maps are available upon request from the first author as GeoTIFF or as ArcGIS project. The maps were used, together with geological maps, ground-truth information, DEMs, and geochemical and XRD analysis for geological interpretation and classification.

Data quality was assessed by plotting band ratios derived from ASTER reflectance data against ratios from laboratory ASD hyperspectral data (Fig. 5). Except for samples of iron oxide crusts which are not representative of ASTER 30x30 m pixels, results were generally good. Quality of the mineral abundance maps and indices are different for various reasons.

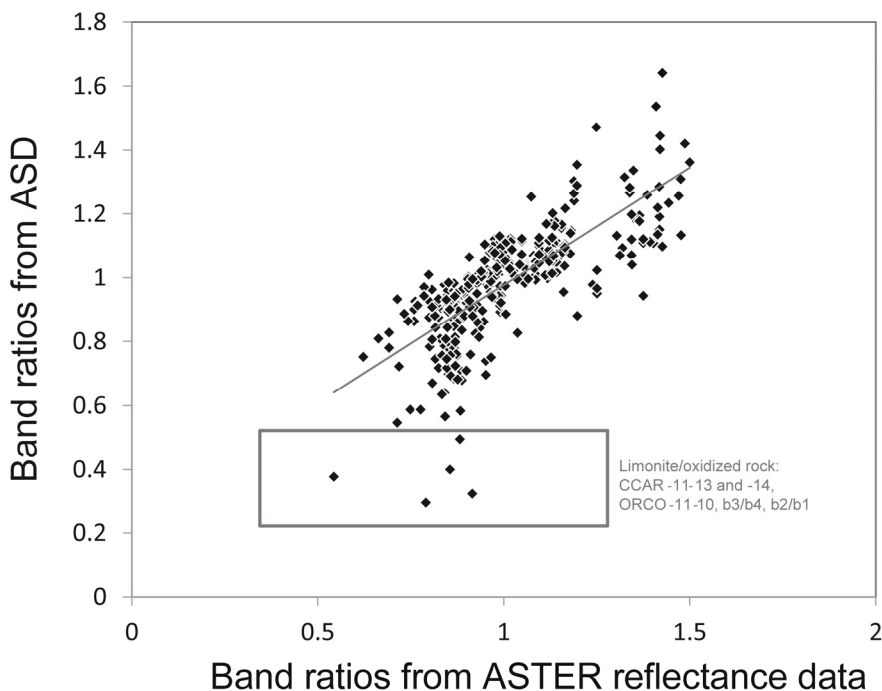


Fig. 5: ASTER Quality assessment. Ratios from ASTER reflectance data are plotted with ASD ratios. Correlation is good except for samples rich in iron oxides that are not representative for an ASTER 30x30 m pixel.

The results can be summarized as follows: We found no proof of propylitization (Mg-OH and Fe-OH group minerals) which would be typical for deeper alteration of porphyry copper and altered mafic intrusions. Mg-OH and Fe-OH content maps also appear to be very sensitive to moisture, shadowed areas, and residual vegetation. This is illustrated in Fig. 6D,

showing the Mg-OH content map overlain on ASTER false color image. High (red) values are considered false positives and delineate steep, shadowed areas.

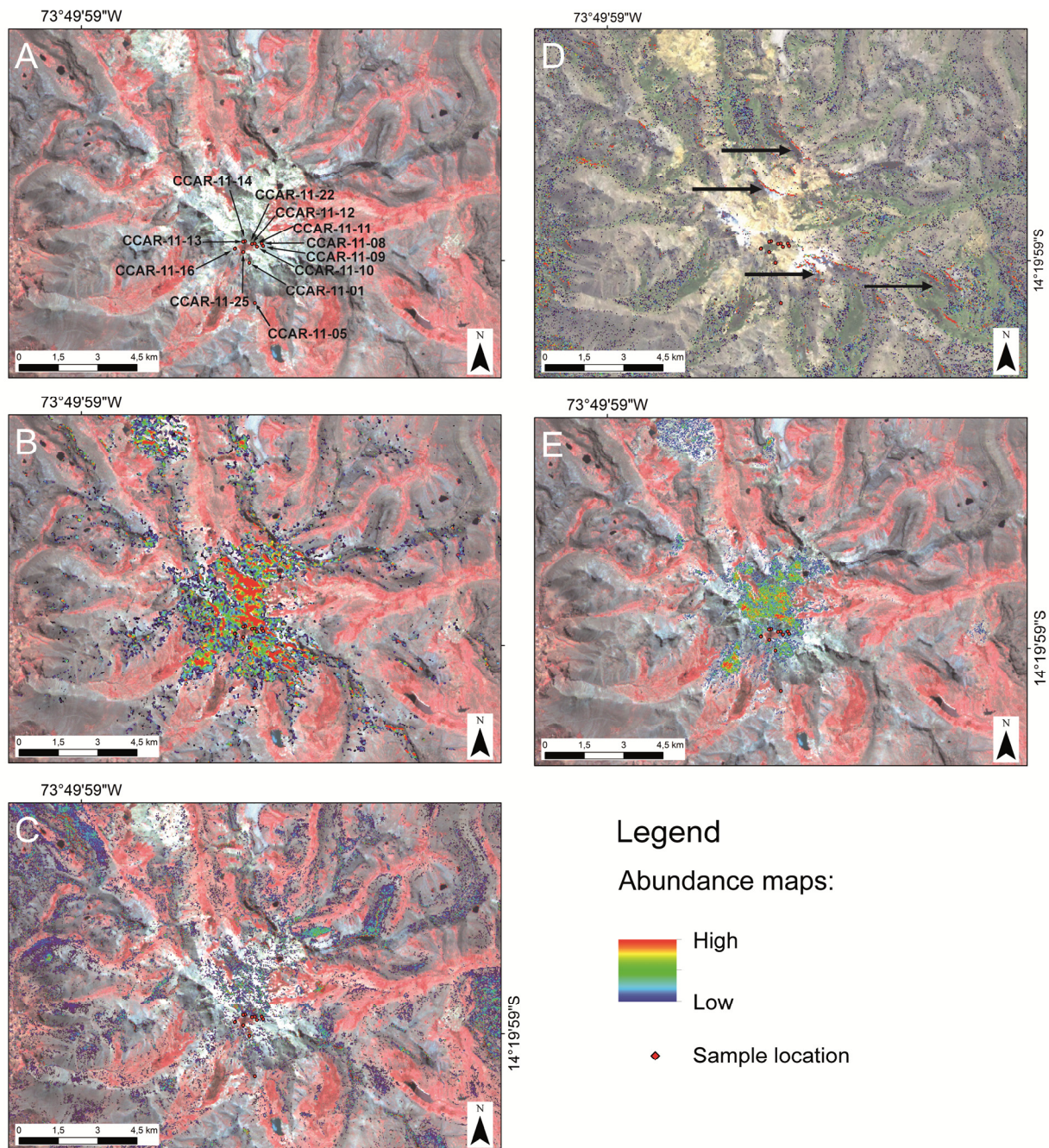


Fig. 6: A: Cerro Carhuarazo (ASTER RGB:321) with sample locations. This subset is an example of results for mineral abundance maps and spectral indices. B: Cerro Carhuarazo subscene with Al-OH abundance map as overlay. Red color means high abundance, blue is low abundance. Al-OH abundance maps are calculated using ASTER band ratio  $(b5+b7)/b6$  with the composite mask applied. C: Cerro Carhuarazo subscene with ferric oxide abundance map as overlay. High contents (red) near the samples in the northern part were confirmed in the field. D: Mg-OH content map overlain on ESRI imagery. High values (red) highlight steep, shadowed areas (black arrows). There is no evidence for propylitization. E: Cerro Carhuarazo subscene with Matched Filtering results for a mixture of kaolinite and smectites as overlay (Brandmeier, 2010). The “Kaosmectite spectra” used for matched filtering is from USGS spectral library.

The high scores of kaolinite and smectite and high values in Al-OH abundance maps are highly correlated and confirmed by our ground-truthing observations. Furthermore, the spectral unmixing results in Brandmeier (2010) of natrolite, kaolinite-group minerals and smectites is supported by ground-truthing and mineral analysis. We thus conclude that our approach and ground-truthing of the ASTER spectral data should result in meaningful mineral distribution maps.

Results for mineral maps and spectral indices will be further discussed in the context of subscene maps for Cerro Carhuarazo (Fig. 6) and Lomada Atansa (Fig. 7). For the first subscene, five different mineral abundance maps are shown in Fig. 6A-E. Fig. 6B shows results for Al-OH mineral group abundance mapping. Anomalies were confirmed in the field and are in accordance with matched filtering results for kaolinite/smectite mixtures (Fig. 6E, Brandmeier, 2010). In comparison to matched filtering results, Al-OH abundance maps are less reliable as they are more sensitive to areas with shadows and moisture. This problem was circumvented following Brandmeier (2010) by (a) using crosstalk-corrected reflectance data instead of level 1b data and (b) using a selected subset for mapping instead of only creating a mask. The drawbacks of Brandmeier's (2010) approach are that 1) the spatial and spectral resolution of ASTER is still not good enough to reliably identify minerals and 2) that the spectral unmixing employed was more time consuming due to the need to identify and isolate suitable spectrally mixing endmembers. This is why matched filtering results shows high values for kaolinite, dickite, nacrite and kaolinite/smectite mixtures, which cannot be distinguished (some are polymorphs of the same mineral) or quantified using ASTER data with limited spectral resolution as compared to hyperspectral data. Nevertheless, these results indicate the general type of alteration and the presence of clay minerals very well (Fig. 6).

Results for ferric oxide content maps following the approach of Cudahy et al. (2008) are shown in Fig. 6C. The high values near the samples in the north of Carhuarazo volcano (CCAR-11-13, CCAR-11-14) were confirmed in the field. This data product proved to be very sensitive to residual, dry vegetation as also observed by Cudahy et al. (2008).

The second example for ASTER mineral mapping is Lomada Atansa, an ignimbrite sheet cut by minor faults, with typical zeolite alteration of the glass-rich ignimbrite rocks. The area (Fig. 7) was chosen according to the results of Brandmeier (2010) based on anomalous high Pixel Purity Index (PPI) values and corresponding Matched Filtering (MF) results. Natrolite MF results are shown in Fig. 7B. Field measurements and electron microprobe (EMP) analysis confirm this finding. Although ASTER spectral resolution could not distinguish natrolite, the different alteration type with minerals of the zeolite group in this ignimbrite setting was successfully mapped.

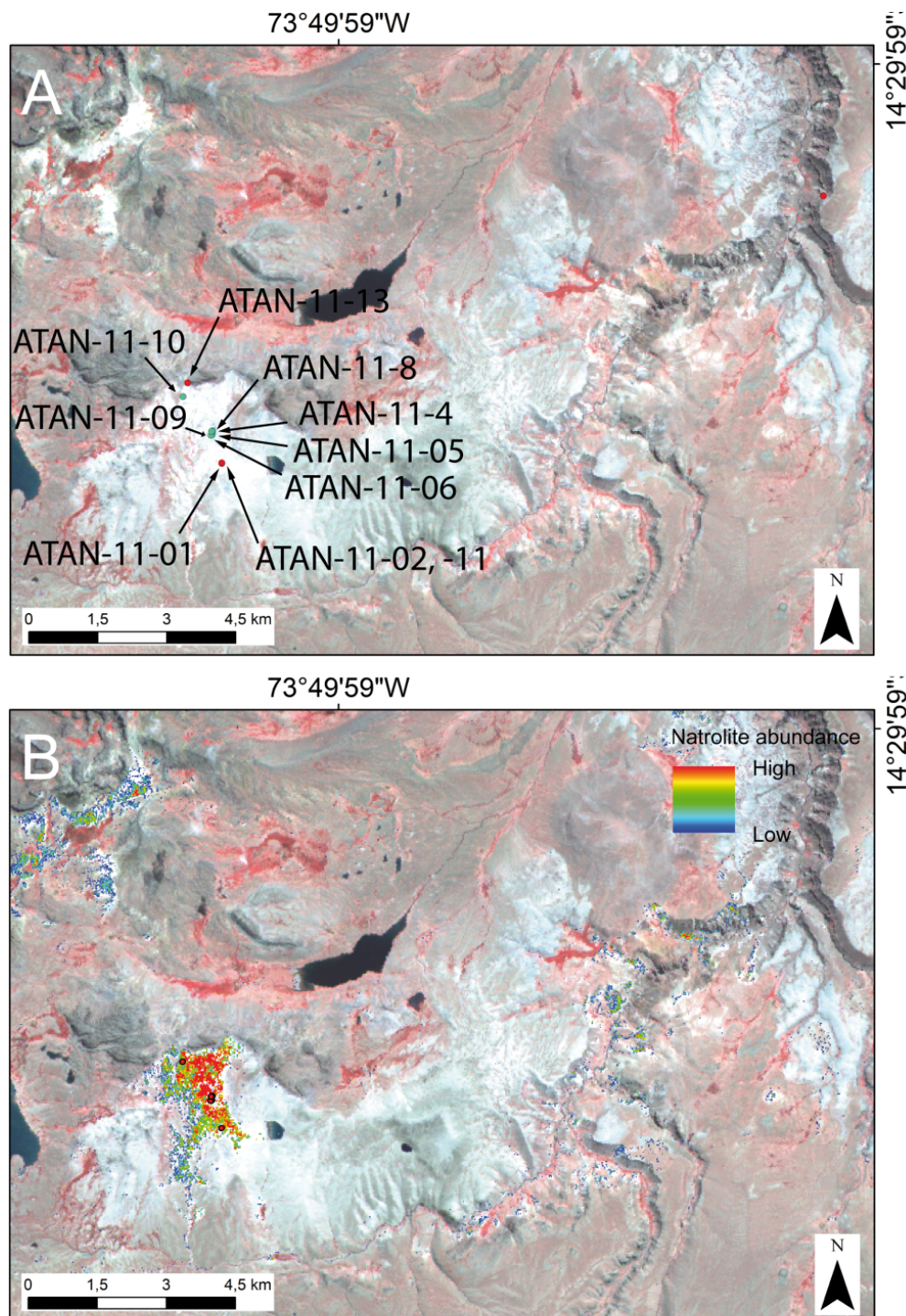


Fig. 7: A: Lomada Atansa with sample locations. This subset will be used to exemplify results for mineral abundance maps and spectral indices. B: MF results for natrolite (Brandmeier, 2010) (1.6% to 19.8% linearly stretched image) overlain on ASTER RGB:321 at Lomada Atansa. The rainbow colors (green: medium abundance to red: high abundance) highlight areas with high abundance of zeolites.



## 4.2 Geochemical analysis- major elements and mineral content (RFA, EMP and XRD)

### 4.2.1 X-ray Fluorescence Spectrometry (XRF)

Results for major elements are given in Table 2 and included in digital kml file format available as supporting online material. Totals include the LOI, but for diagrams values were normalized to 100 % without LOI in order to facilitate comparison of altered samples.

We observe a wide range in SiO<sub>2</sub> (2.88 – 97.69 wt-%), K<sub>2</sub>O (0.05-3.83 wt-%), Na<sub>2</sub>O (0.01-4.95 wt-%) and CaO (0.02-2.92 wt-%) abundances. Especially samples from Cerro Palla Palla (CHAV) and Cerro Orccococha (ORCO) show high values of SiO<sub>2</sub> and low values for the mobile alkali metals Na<sub>2</sub>O and K<sub>2</sub>O and CaO.(CHAV-11-17, CHAV-11-18, ORCO-11-01-1, ORCO-11-01-2). Even relatively immobile elements like Al<sub>2</sub>O<sub>3</sub> and TiO<sub>2</sub> show some variations with extremely low values of Al<sub>2</sub>O<sub>3</sub> and low TiO<sub>2</sub> values for some of the samples (CCAR-11-13 and CCAR-11-14; Table 2). These samples are also very low in SiO<sub>2</sub> and consist mainly of iron (Fe<sub>2</sub>O<sub>3</sub> of 50.42 and 60.26 wt-%). These results will be discussed further in chapter 5.

Table 2: Results of major element determinations, CIA, IOA and absorption depth of selected absorption features.

Lomada- Atansa									
Sample	ATAN-11-01	ATAN-11-03	ATAN-11-04	ATAN-11-05	ATAN-11-08	ATAN-11-10	CCAR-11-01	CCAR-11-03	
rock type*	ai	ai	ai	fb	fb	s	s	s	
SiO <sub>2</sub>	68.49	62.58	64.85	63.98	64.03	65.09	61.80	61.09	
TiO <sub>2</sub>	0.37	0.43	0.34	0.33	0.33	0.33	0.82	0.77	
Al <sub>2</sub> O <sub>3</sub>	16.27	17.07	15.67	14.68	14.69	15.93	17.45	17.99	
Fe <sub>2</sub> O <sub>3</sub> t	1.89	2.41	1.98	1.83	1.83	1.80	5.72	5.19	
MnO	0.08	0.11	0.10	0.09	0.09	0.09	0.03	0.02	
MgO	0.33	0.68	0.53	0.82	0.82	0.39	0.86	0.89	
CaO	1.40	2.15	1.49	2.92	2.92	1.88	0.37	0.34	
Na <sub>2</sub> O	4.95	3.15	3.01	2.19	2.19	4.21	2.66	2.19	
K <sub>2</sub> O	3.83	3.02	3.87	3.01	3.01	3.56	2.90	3.10	
P <sub>2</sub> O <sub>5</sub>	0.06	0.09	0.04	0.02	0.02	0.03	0.29	0.29	
LOI	4.15	7.97	7.91	9.92	9.92	6.45	6.55	7.45	
total	101.82	99.65	99.79	99.78	99.86	99.74	99.46	99.33	
CIA	0.62	0.67	0.65	0.64	0.64	0.62	0.75	0.76	
0,95µm**	0.00	0.01	0.00	0.03	0.02	0.01	0.07		
2,165 µm**	0.02	0.02	0.03	0.00	0.00	0.01	0.04		
2,2 µm**	0.05	0.07	0.12	0.01	0.05	0.10	0.13		
2,2+2,165 µm**	0.06	0.09	0.16	0.01	0.05	0.11	0.17		
IOA	0.07	0.10	0.16	0.04	0.07	0.12	0.24		
Latitude	-73.8563	-73.8584	-73.8585	-73.8583	-73.7335	-73.8642	-73.7733	-73.7733	
Longitude	-14.5791	-14.5735	-14.5737	-14.57284	-14.7093	-14.56604	-14.3344	-14.33442	

\* s= scree, ai= altered ignimbrite, al= altered lava, fb= fault breccia, n.a. : not analyzed, CIA: Chemical Index of Alteration (Nesbit&Young, 1982), \*\* Absorption depth from ASD spectrum in µm, IOA: Index of Absorption

Manuscript II - Mapping patterns of mineral alteration in volcanic terrains using ASTER data and field spectrometry in Southern Peru

Table 2 (continued):

Cerro Carhuarazo								
Sample	CCAR-11-08	CCAR-11-10	CCAR-11-11	CCAR-11-12	CCAR-11-13	CCAR-11-14	CCAR-11-17	CCAR-11-19
rock type*	s	s	s	s	s	s	s	al
SiO <sub>2</sub>	62.40	64.09	47.54	50.43	4.20	2.88	39.34	65.62
TiO <sub>2</sub>	0.85	0.74	0.65	1.02	0.07	0.04	0.57	0.84
Al <sub>2</sub> O <sub>3</sub>	16.40	15.16	13.89	17.82	1.21	0.79	9.75	17.68
Fe <sub>2</sub> O <sub>3t</sub>	4.99	4.17	20.30	12.58	50.42	60.26	34.44	2.45
MnO	0.06	0.18	0.49	0.01	0.00	0.00	0.01	0.01
MgO	1.09	0.75	0.61	0.25	0.01	0.01	0.29	0.29
CaO	0.50	0.46	0.25	0.29	0.22	0.26	0.25	0.06
Na <sub>2</sub> O	1.74	2.61	1.54	0.68	0.05	0.03	1.00	0.65
K <sub>2</sub> O	2.69	3.06	2.10	2.72	0.24	0.11	1.87	3.09
P <sub>2</sub> O <sub>5</sub>	0.36	0.23	0.35	0.47	0.34	0.93	0.30	0.12
LOI	8.42	8.13	11.85	12.17	41.17	29.94	11.22	7.82
total	99.51	99.57	99.57	98.43	97.92	95.25	99.02	98.63
CIA	0.77	0.71	0.78	0.83	0.70	0.66	0.76	0.82
0,95µm**	0.03	0.03	0.16	0.17	0.51	0.55	0.22	0.09
2,165 µm**	0.03	0.03	0.03	0.10	0.00	0.00	0.02	0.11
2,2 µm**	0.09	0.08	0.08	0.11	0.02	0.00	0.06	0.19
2,2+2,165 µm**	0.12	0.11	0.11	0.21	0.02	0.00	0.08	0.30
IOA	0.15	0.14	0.28	0.38	0.53	0.55	0.30	0.39
Latitude	-73.7691	-73.7708	-73.7716	-73.7725	-73.7725	-73.7750	-73.7756	-73.7681
Longitude	-14.3279	-14.3291	-14.3279	-14.3281	-14.3281	-14.3272	-14.3273	-14.3267

\* s= scree, ai= altered ignimbrite, al= altered lava, fb= fault breccia, n.a. : not analyzed, CIA: Chemical Index of Alteration (Nesbit&Young, 1982), \*\* Absorption depth from ASD spectrum in µm, IOA: Index of Absorption

Cerro Chavina								
Sample	CHAV-11-01	CHAV-11-02	CHAV-11-03	CHAV-11-04	CHAV-11-10	CHAV-11-12	CHAV-11-14	CHAV-11-16
rock type*	s	s	s	s	s	al	s	s
SiO <sub>2</sub>	68.06	58.49	58.57	63.46	69.29	61.03	59.48	54.72
TiO <sub>2</sub>	1.06	1.21	1.20	1.04	1.27	0.90	1.01	0.96
Al <sub>2</sub> O <sub>3</sub>	12.18	18.53	12.29	15.78	11.67	15.54	17.14	18.52
Fe <sub>2</sub> O <sub>3t</sub>	5.90	5.24	12.93	6.17	4.49	6.62	6.30	10.32
MnO	0.01	0.01	0.01	0.01	0.00	0.02	0.02	0.01
MgO	0.42	0.87	0.63	0.51	0.37	0.70	0.54	0.32
CaO	0.31	0.41	0.52	0.20	0.26	0.98	1.05	0.94
Na <sub>2</sub> O	0.70	1.79	1.77	0.34	0.42	1.12	1.75	1.23
K <sub>2</sub> O	1.16	1.52	1.31	1.73	1.14	1.73	2.13	1.64
P <sub>2</sub> O <sub>5</sub>	0.32	0.29	0.33	0.31	0.27	0.24	0.26	0.31
LOI	9.22	11.20	9.69	9.36	9.33	10.39	9.60	10.44
total	99.36	99.56	99.26	98.92	98.51	99.25	99.29	99.41
CIA	0.85	0.83	0.77	0.87	0.87	0.80	0.78	0.83
0,95µm**	0.06	0.02	0.16	0.12	0.12	0.10	0.12	0.16
2,165 µm**	0.05	0.05	0.03	0.10	0.11	0.06	0.07	0.11
2,2 µm**	0.10	0.11	0.08	0.16	0.18	0.14	0.16	0.22
2,2+2,165 µm**	0.15	0.17	0.11	0.26	0.28	0.20	0.23	0.33
IOA	0.20	0.19	0.27	0.37	0.40	0.30	0.35	0.49
Latitude	-73.7452	-73.7454	-73.7453	-73.7338	-73.7300	-73.7295	-73.7288	-73.7299
Longitude	-14.7202	-14.7197	-14.7197	-14.7143	-14.7128	-14.7114	-14.7053	-14.7046

\* s= scree, ai= altered ignimbrite, al= altered lava, fb= fault breccia, n.a. : not analyzed, CIA: Chemical Index of Alteration (Nesbit&Young, 1982), \*\* Absorption depth from ASD spectrum in µm, IOA: Index of Absorption

Manuscript II - Mapping patterns of mineral alteration in volcanic terrains using ASTER data and field spectrometry in Southern Peru

Table 2 (continued):

Cerro Orconccocho										
Sample	CHAV-11-17		CHAV-11-18		ORCO-11-01-1	ORCO-11-01-2	ORCO-11-01-3	ORCO-11-03	ORCO-11-05	ORCO-11-06
rock type*	al	s	al	al	al	s	s	s	s	
SiO <sub>2</sub>		97.69	78.14		97.09	86.49	68.83	66.39	69.74	59.46
TiO <sub>2</sub>		1.14	1.22		0.77	0.73	0.72	0.96	0.86	0.86
Al <sub>2</sub> O <sub>3</sub>		0.63	8.85		0.15	8.12	15.18	16.18	13.92	17.11
Fe <sub>2</sub> O <sub>3t</sub>		0.09	2.44		1.22	0.69	7.31	3.32	5.68	4.93
MnO		0.01	0.01		0.04	0.00	0.00	0.02	0.01	0.05
MgO		0.35	0.26		0.01	0.01	0.02	0.87	0.20	1.00
CaO		0.02	0.27		0.02	0.05	0.04	0.25	0.20	0.52
Na <sub>2</sub> O		0.01	0.42		0.01	0.03	0.05	0.23	0.24	0.70
K <sub>2</sub> O		0.05	1.17		0.03	0.06	0.04	1.73	0.47	2.49
P <sub>2</sub> O <sub>5</sub>		0.02	0.18		0.01	0.17	0.14	0.19	0.20	0.25
LOI			6.03		0.59	3.50	7.40	9.69	8.25	12.47
total		100.00	98.99		99.96	99.85	99.74	99.83	99.78	99.83
CIA		0.89	0.83		0.71	0.98	0.99	0.88	0.94	0.82
0,95µm**			0.05					0.08	0.11	0.07
2,165 µm**			0.05					0.09	0.10	0.07
2,2 µm**			0.09					0.20	0.16	0.12
2,2+2,165 µm**			0.15					0.29	0.26	0.19
IOA			0.19					0.38	0.37	0.25
Latitude		-73.7335	-73.7375		-73.9496	-73.9496	-73.9496	-73.95	-73.95	-73.95
Longitude		-14.7093	-14.7185		-14.5939	-14.5939	-14.5939	-14.59	-14.59	-14.60

\* s= scree, ai= altered ignimbrite, al= altered lava, fb= fault breccia, n.a. : not analyzed, CIA: Chemical Index of Alteration (Nesbit&Young, 1982), \*\* Absorption depth from ASD spectrum in µm, IOA: Index of Absorption

Cerro Orconccocho						
Sample	ORCO-11-08	ORCO-11-09	ORCO-11-10	ORCO-11-11	ORCO-11-12	
rock type*	s	s	al	s	al	
SiO <sub>2</sub>		55.64	62.26	65.10	62.02	68.08
TiO <sub>2</sub>		1.02	1.07	1.02	1.13	0.85
Al <sub>2</sub> O <sub>3</sub>		13.33	20.05	14.82	15.88	17.65
Fe <sub>2</sub> O <sub>3t</sub>		16.10	2.92	8.20	7.24	3.08
MnO		0.01	0.01	0.00	0.02	0.00
MgO		0.68	1.00	0.02	0.92	0.03
CaO		0.45	0.07	0.14	0.38	0.06
Na <sub>2</sub> O		0.38	0.31	0.06	0.55	0.04
K <sub>2</sub> O		1.79	3.64	0.16	2.03	0.07
P <sub>2</sub> O <sub>5</sub>		0.25	0.11	0.30	0.26	0.13
LOI		10.00	8.18	9.22	9.24	9.04
total		99.66	99.63	99.04	99.68	99.02
CIA		0.84	0.83	0.98	0.84	0.99
0,95µm**		0.23	0.03	0.51	0.09	
2,165 µm**		0.05	0.09	0.09	0.06	
2,2 µm**		0.12	0.20	0.14	0.13	
2,2+2,165 µm**		0.18	0.29	0.22	0.19	
IOA		0.40	0.32	0.74	0.28	
Latitude		-73.96	-73.95	-73.95	-73.95	-73.95
Longitude		-14.60	-14.60	-14.60	-14.60	-14.60

\* s= scree, ai= altered ignimbrite, al= altered lava, fb= fault breccia, n.a. : not analyzed, CIA: Chemical Index of Alteration (Nesbit&Young, 1982), \*\* Absorption depth from ASD spectrum in µm, IOA: Index of Absorption

#### 4.2.2 Electron Micro Probe (EMP)

---

Zeolites were identified in three thin sections from Lomada Atansa. These minerals are very unstable and easily break down under the electron beam of the EMP. Furthermore crystal size was very small and therefore no quantitative analysis was possible. As zeolites are tectosilicates containing variable degrees of water, totals are very low and EDS results indicate the typical elements (Si, Na, Ca, K, Al) contained in zeolites and therefore semi-quantitative identification possible.

Analysis of the grain mounts proved to be complicated by high contents of amorphous matrix. Compositional images (BSE) and EDX analysis of the nine selected samples indicate kaolinite in sample ORCO-11-01-3 and ORCO-11-01-1 within a siliceous matrix. Sample ORCO-11-01-1 only consists of Si and euhedral quartz can be recognized in BSE image. Samples from Cerro Palla Palla (CHAV-11-10 and CHAV-11-04) contain kaolinite and Fe- and Ti-bearing mineral phases, quartz and barite. Sample ATAN-11-01 from the ignimbrite setting contains relics of feldspar and shows alteration to illite. The matrix is very rich in silica. Samples from Cerro Carhuarazo show high Fe-contents (CCAR-11-14) and feldspar with illite alteration (CCAR-11-19).

#### 4.2.3 X-ray Diffraction

---

X-ray diffraction results are difficult to interpret due to large amounts of amorphous phases that hinder identification of specific mineral phases. However, we identified quartz, feldspar and zeolites in sample ATAN-11-08 and quartz and albite for sample ATAN-11-10 ignimbrite. For Cerro Carhuarazo we identified montmorillonite, quartz and jarosite beside the amorphous phases. Cerro Palla Palla samples contain quartz, albite, kaolinite, illite and montmorillonite (CHAV-11-02, CHAV-11-10) and amorphous silica. Sample ORCO-11-11 contains kaolinite.

#### 4.3 ASD hyperspectral data

---

Results of spectral analysis and mineral groups identified in different samples are given in Table 3. Measured absorption depth for the 2.2  $\mu\text{m}$  Al-OH, the 2.165  $\mu\text{m}$  kaolinite and the 0.95  $\mu\text{m}$  iron absorption features are included in table 2 and provided with sample locations and bulk geochemical data as kml file. Spectra from field measurements and contact-probe measurements are presented together.

Alteration zones at Cerro Orconccochoa are found in Plio- to Pleistocene andesitic lavas that form part of the Barroso formation (Guevara, 2001, INGEMMET, 2001b). Ground truth data at Cerro Orconccochoa comprised eleven sites where spectra were collected and scree samples taken. All spectra show an absorption feature at 2.2  $\mu\text{m}$  although the absorption depth is variable (Fig. 8). A double absorption feature at 2.165  $\mu\text{m}$  and 2.2  $\mu\text{m}$  indicates a mineral mixture involving kaolinite and (probably) smectites (ORCO-11-05; Fig. 8B). By contrast, a single absorption feature at 2.2  $\mu\text{m}$  indicates montmorillonite (ORCO-11-09; Fig. 8C). Absorption at 0.56  $\mu\text{m}$ , 0.67  $\mu\text{m}$  and a deep absorption trough around 0.95  $\mu\text{m}$  (e.g. ORCO-11-11 or ORCO-11-03) should be indicative of goethite (Fig. 8D) or a mixture with nontronite or with jarosite (absorption only at 0.42  $\mu\text{m}$  and 0.96  $\mu\text{m}$ ). Absorption patterns of ORCO-11-08 or ORCO-11-10 can either be explained by goethite (or other iron oxides/hydroxides) or jarosite. In summary, the spectra sampled at Cerro Orconccochoa show mixtures of kaolinite, smectites and iron oxides/hydroxides and/or jarosite.

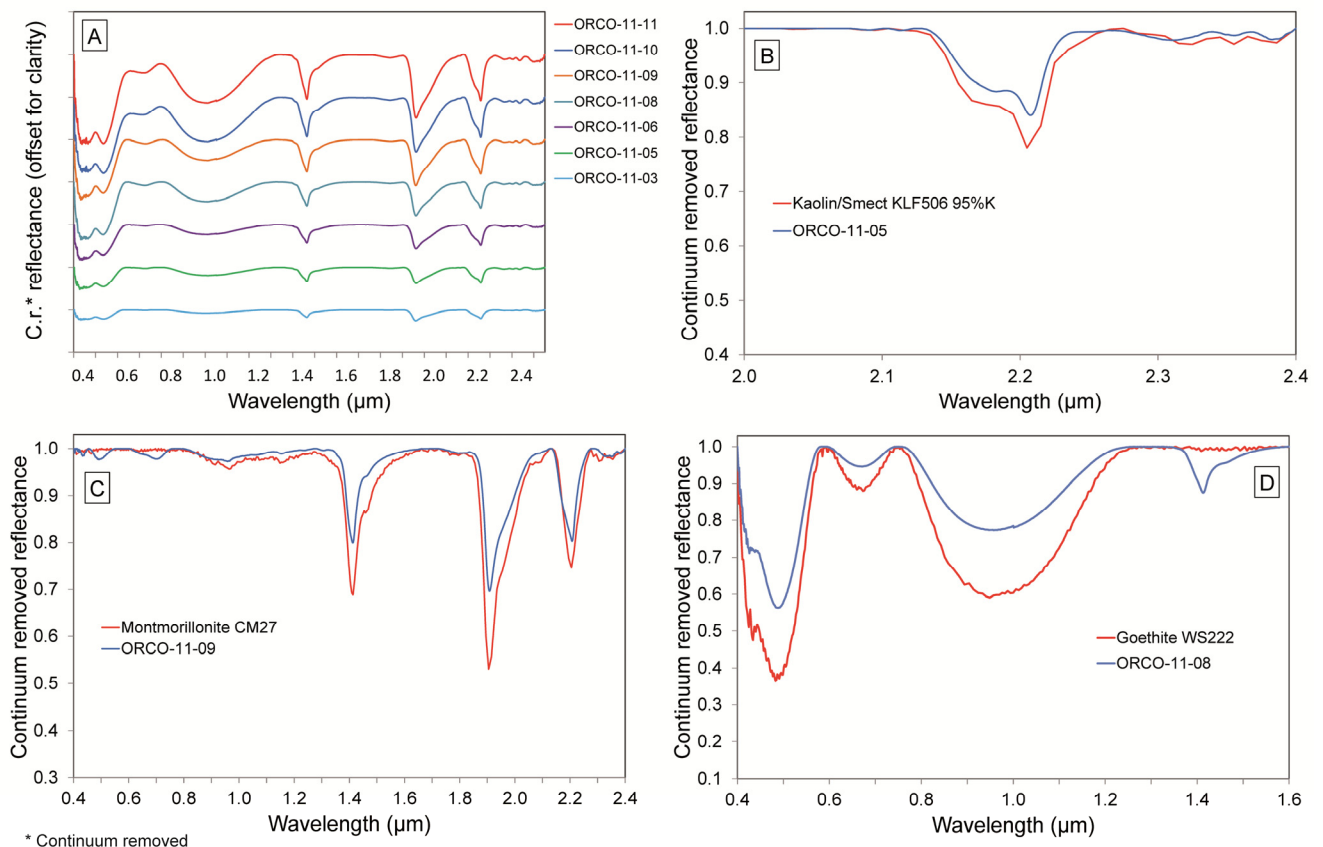


Fig. 8: A: Accumulated mean spectra (30 x 5 measurements) of samples from the different sampling sites at Cerro Orconccochoa measured with the contact probe after drying the samples at 110° for 12 hours. All spectra are continuum removed in order to emphasize changing absorption features. B: Double absorption feature typical of a mixture between kaolinite and smectites. ORCO-11-05 in comparison to USGS spectral library plot. C: ORCO-11-09 plotted with montmorillonite spectrum from USGS spectral library. Spectra are continuum removed. D: Orco-11-08 is shown together with goethite from the USGS spectral library. Absorption caused in this part of the spectrum (0.4  $\mu\text{m}$  to 1.3  $\mu\text{m}$ ) are caused by iron oxides/hydroxides.

The second ground-truthing site, Cerro Palla Palla (near Chavina), is the core of an epithermally altered andesitic volcano (Inca and Cayo, 2000, INGEMMET, 2001b). We sampled along a traverse representing decreasing degrees of alteration from a high-T alteration core with bleached and silicified andesite to low-T altered andesite at the outer volcano flanks (Fig. 3C). A total of 25 mean spectra were analyzed (12 contact probe measurements, 13 field sites; Fig. 9A and B). Ground-truthing took place from 10 am to 2 pm when weather conditions were good with only few passing clouds but strong wind at this high altitude (around 5,000 m).

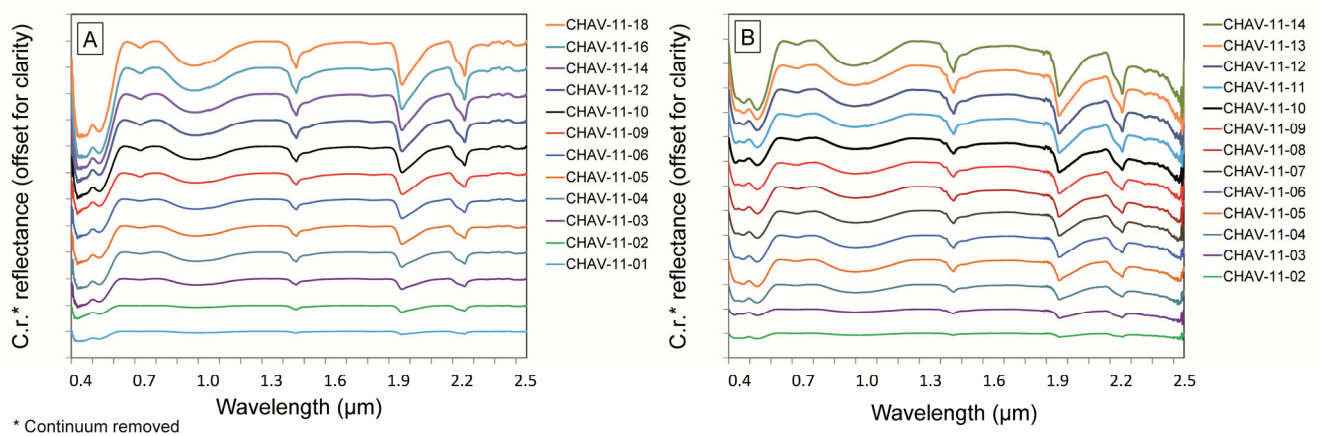


Fig. 9: A: Mean spectra of samples from sites at Cerro Palla Palla (Chav) measured with the contact probe after drying the samples at 110° for 12 hours. All spectra are continuum removed in order to emphasize changing absorption features. B: Mean spectra of the different sampling sites at Cerro Palla Palla measured in the field. All spectra are continuum removed in order to emphasize changing absorption features

Samples from the top of Cerro Palla Palla contain quartz and/or feldspar, minerals that have no diagnostic absorption features in the wavelength region of the spectrometer. Spectral Analyst scores are high for minerals like sanidine, quartz or albite in these high-T altered samples. The very flat spectra of CHAV-11-05, CHAV-11-06 and CHAV-11-09 therefore exclude any other mineral. This is confirmed by geochemical and X-ray diffraction data (see below). CHAV-11-01 and CHAV-11-02 at ca. 1.7 km distance from the summit show absorption features characteristic for smectites and kaolinite (2.2 µm and 2.165 µm respectively) as well and some absorption at 0.95 µm (CHAV-11-01 only) that is caused by minerals hematite and/or jarosite. CHAV-11-04 has strong smectite/kaolinite absorption and scores for barite and jarosite are quite high as well. However, the spectra do not allow unequivocal distinction between these minerals. Samples CHAV-11-10 and CHAV-11-12 contain montmorillonite as well as some Fe bearing minerals (hematite or jarosite). CHAV-11-14 and CHAV-11-16 represent the more distant, red, oxidized alteration zone and show

strong absorption at 0.95  $\mu\text{m}$  indicating high amounts of hematite and other iron oxides. Furthermore clay minerals are present in these low-T altered samples.

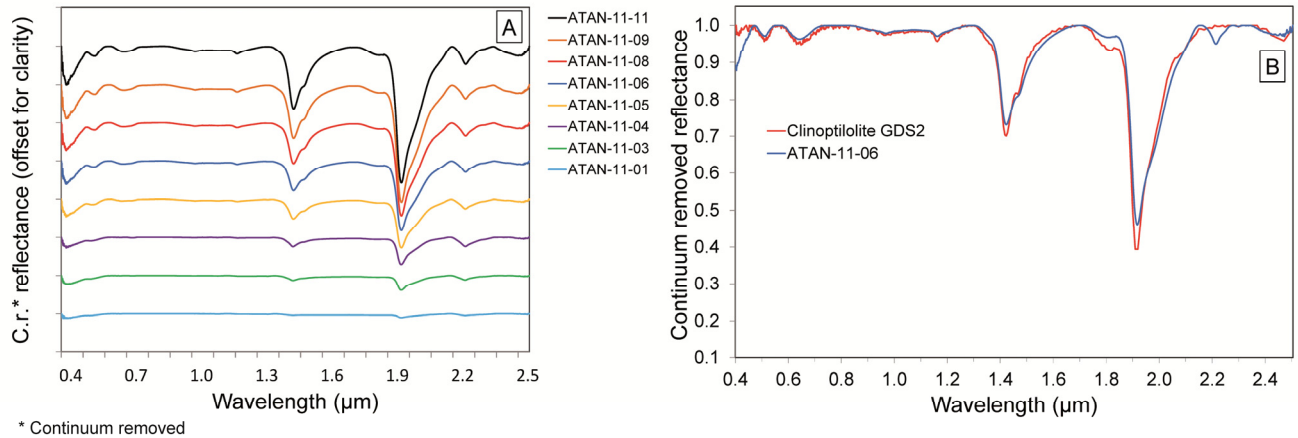


Fig. 10: A: Spectra collected for samples from the different sites at Lomada Atansa measured with the contact probe after drying the samples at 110° for 12 hours. All spectra are continuum removed in order to emphasize changing absorption features. B: Continuum removed spectra of sample ATAN-11-06 compared to Clinoptilolite (a zeolite mineral) from the USGS spectral library. The spectral similarity is very high and therefore the probability for this mineral to be identified positively is very high. Wavelength is given in  $\mu\text{m}$ .

In summary, the samples show gradual changes from silicified samples to samples containing clay minerals and varying degrees of iron oxide enrichment. Minerals like jarosite and barite might be present but cannot be identified unambiguously as the spectral characteristics are not sufficiently diagnostic.

The third location, Lomada Atansa, exposes an altered and/or weathered ignimbrite that is part of the Andamarca Formation (Fig. 3). We took 14 samples, collected spectra from nine field sites and measured eight contact probe spectra (Fig. 10A). Weather conditions were not ideal due to intermittent cloud cover and we had to wait for illumination conditions to stabilize before each measurement. We sampled spectra from 10 am to 1 pm.

ATAN-11-01 was collected from the “fresh” ignimbrite and shows a flat spectrum, indicating volcanic glass or minerals like quartz and feldspars (high scores for microcline). ATAN-11-03 and ATAN-11-04 show deeper absorption at 1.9  $\mu\text{m}$  and 2.2  $\mu\text{m}$ , typical for clay minerals (bonded water and Al-OH absorption). Therefore smectites receive high scores. Otherwise, the spectra look similar to the ignimbrite spectrum. Samples from a conspicuous fault zone within the ignimbrite (ATAN-11-05, -06, -08, -09) show a very different spectrum that matches almost perfectly to zeolite minerals (clinoptilolite, mordenite Fig. 10B). In this zone, no clay is observed since the 2.2  $\mu\text{m}$  absorption feature almost disappears. Other samples (ATAN-11-11, -12) in addition score high for palygorskite, a hydrothermal clay mineral.

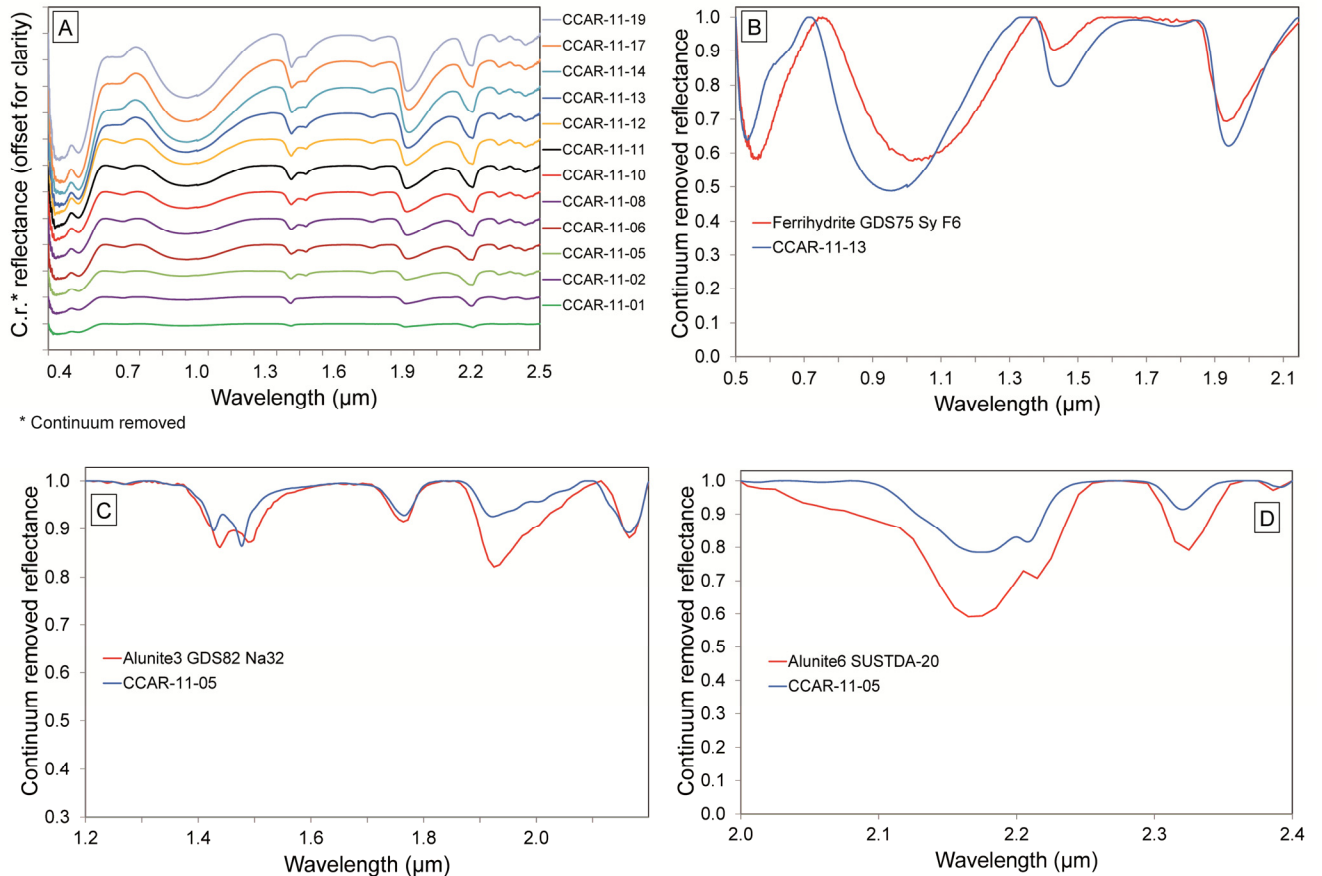


Fig. 11: A: Mean spectra of the different sampling sites at Cerro Carhuarazo measured with the contact probe after drying the samples at 110° for 12 hours. All spectra are continuum removed in order to emphasize changing absorption features. B: CCAR-11-05 is shown together with alunite spectra from the USGS spectral library. The double absorption feature at 1.4 μm is very indicative, together with the absorption pattern at longer wavelength regions (C). C: CCAR-11-05 is shown together with alunite spectra from USGS spectral library. In combination with the absorption feature at 1.4 μm (B), the spectral signature of this sample strongly indicates the presence of alunite. D: Sample CCAR-11-13 is shown together with ferrihydrite spectra from USGS spectral library. It was collected on Cerro Carhuarazo in the environment depicted in Fig. 3 A, left picture. Wavelength is given in μm.

The last ground-truthing site, Cerro Carhuarazo, is an epithermally altered andesitic volcanic complex (INGEMMET, 2001a, Paz et al., 2000). Spectra are shown in Fig. 11. Sample CCAR-11-01 is a yellow scree and spectral analysis shows that some iron oxides (absorption at around 0.9 μm) are present next to quartz and/or feldspars. CCAR-11-02 also has an Al-OH absorption feature (0.2 μm) indicating clay minerals and/or muscovite. Sample CCAR-11-05 was collected near a dike and has a double absorption feature at around 1.4 μm and absorption at 1.75 μm and 2.165 μm are indicative of alunite (Fig. 11C and D). Sample CCAR-11-06 shows stronger iron oxide/hydroxide absorption than nearby sample CCAR-11-05 but only a very weakly developed alunite absorption feature. Samples CCAR-11-08 and CCAR-11-10 show very flat spectra indicating mainly quartz and feldspars. The weak absorption at 2.2 μm might be caused by some illite or clay minerals. Samples CCAR-11-11 and CCAR-11-12 are fine fraction scree samples and contain iron oxides/hydroxides



and/or jarosite (absorption at 0.9  $\mu\text{m}$  and steep slope around 0.5  $\mu\text{m}$ ). Samples CCAR-11-13 and CCAR-11-14 mainly consist of iron oxides/hydroxides (Fig. 11E). There is a deep absorption trough around 0.9  $\mu\text{m}$  and spectral analysis indicates ferrihydrite, goethite and jarosite. Samples CCAR-11-15 and CCAR-11-16 (not shown in Fig. 11, only field measurements) show very flat spectra, typical for fresh volcanic rocks. CCAR-11-16 has a weak absorption feature indicating some illite. Sample CCAR-11-19 contains some clay minerals like montmorillonite (2.2  $\mu\text{m}$  Al-OH absorption).

In summary, Cerro Carhuarazo shows three different sets of spectral patterns: (1) A very flat spectrum for unaltered volcanic rocks, (2) spectral indication of iron oxides/hydroxides and (3) sulfides and spectra indicating some argillic alteration. Furthermore alunite is present in the dike sample (CCAR-11-05).

#### 4.4 Alteration intensity, mineral abundances and whole rock compositions

The depth of an absorption feature is in principle an indicator of the amount of that mineral present, although crystallinity and other factors influence absorption shape and depth as well. Changes in mineralogy and mineral abundances due to variable hydrothermal alteration, thus should be roughly related to whole rock chemical compositions. However, we found that the combined 2.165  $\mu\text{m}$  and 2.2  $\mu\text{m}$  absorption depth, which we take as a measure for the degree of alteration due to clay minerals, is not correlated with chemical index of alteration (CIA; Nesbitt and Young, 1982). Hydrothermal alteration should either lead to passive enrichment (argillitization) or – in case of very alkaline or acid conditions - leaching of  $\text{Al}_2\text{O}_3$  and enrichment of Si (silicification). However, relatively unaltered reference samples (Table 1 in supporting online material - SOM) show similar or even higher  $\text{Al}_2\text{O}_3$  contents compared to altered samples, even though the chemical index of alteration is much higher in the latter. This indicates that leaching of alkalis may be partly balanced by silicification, resulting in constant  $\text{Al}_2\text{O}_3$ . As a result, the measured  $\text{Al}_2\text{O}_3$  contents are poorly correlated with indices of alteration. In contrast, we found evidence for more or less intense silicification (rather than argillitization) where the sensitivity of the ASD measurements, even at low abundances of clay minerals, shows significant spectral features in the combined 1.165  $\mu\text{m}$  and 2.2  $\mu\text{m}$  absorption depth.

Correlation between the 0.95  $\mu\text{m}$  Fe-OH absorption feature and measured  $\text{Fe}_2\text{O}_3$  is linear with an R-squared of 0.94 for the CCAR samples where  $\text{Fe}_2\text{O}_3$  contents range from 5 wt-% to 60 wt-% (Fig. 12). ATAN samples are low in iron and show no absorption features for Fe-OH. Pervasive iron enrichment as well as the formation of crusts and desert varnish is most intensive on Cerro Carhuarazo. The ORCO sample that shows deep absorption but only low

Fe<sub>2</sub>O<sub>3</sub> content is a sample with only a thin layer of desert varnish on an otherwise relatively Fe-poor altered andesite. Therefore, in this case, the measured absorption depth reflects the iron content of the surface varnish and not the whole-rock. This effect was also found by Rivard et al. (1992) for varnished desert pavements in Egypt.

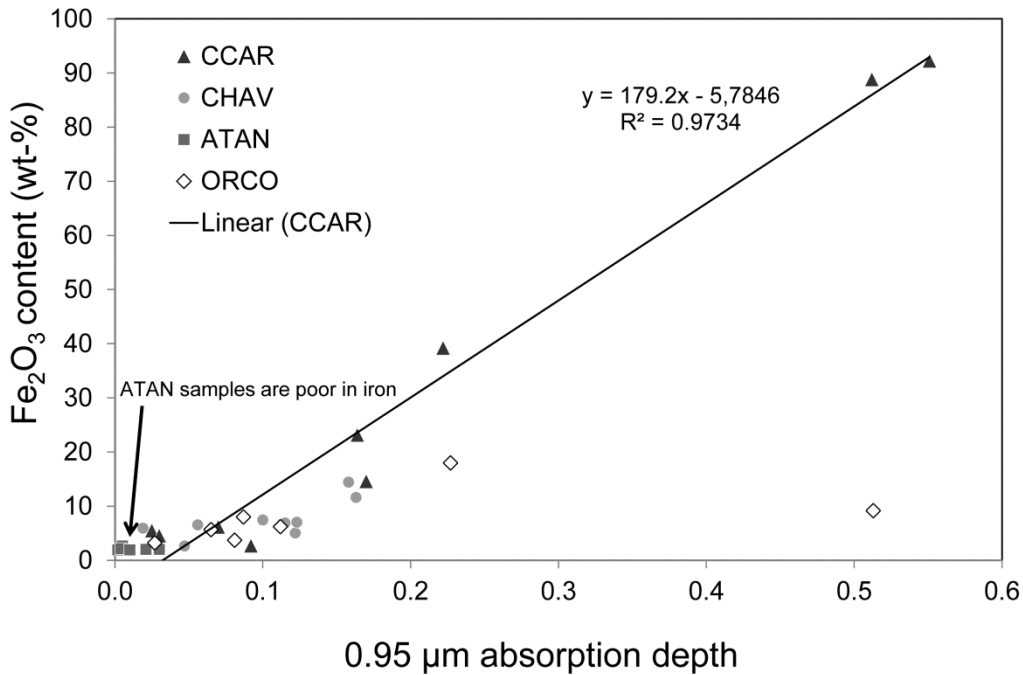


Fig. 12: Fe<sub>2</sub>O<sub>3</sub> content versus 0.95 μm iron absorption feature. There is a correlation for most samples, exemplified here by Cerro Carhurazo. The trend observed for these samples is exponential considering all samples. Lomada Atansa samples show no correlation due to an extremely low iron content. The outlier (ORCO-11-10) is an oxidized rock where the high iron content is only concentrated in a thin crust. This is why the total iron content in whole rock measurement is low whereas the Fe-absorption feature is very strong.

In order to quantify the degree of alteration based on these spectral characteristics we define the index of alteration (IOA) which is composed by the addition of absorption depths at 2.2 μm, 2.165 μm, and 0.95 μm of the continuum removed spectrum. This IOA we compare to the CIA in Fig. 13. Samples with crusts of iron hydroxides show too high values of the index of absorption and are excluded from the logarithmic correlation.

This correlation seems to hold for igneous rocks undergoing argillic alteration, iron oxide enrichment and zeolitization. In case of strong leaching and silification the index of absorption would go to zero (only SiO<sub>2</sub> left) and the index of alteration would go to 1. Therefore this method cannot be applied to silicified samples or alteration that results in extreme (iron crusts) Fe- enrichment. We thus define two separate spectral parameters (Fe-OH-0.95 and IOA) that cover most of the alteration characteristics observed in the spectral data.

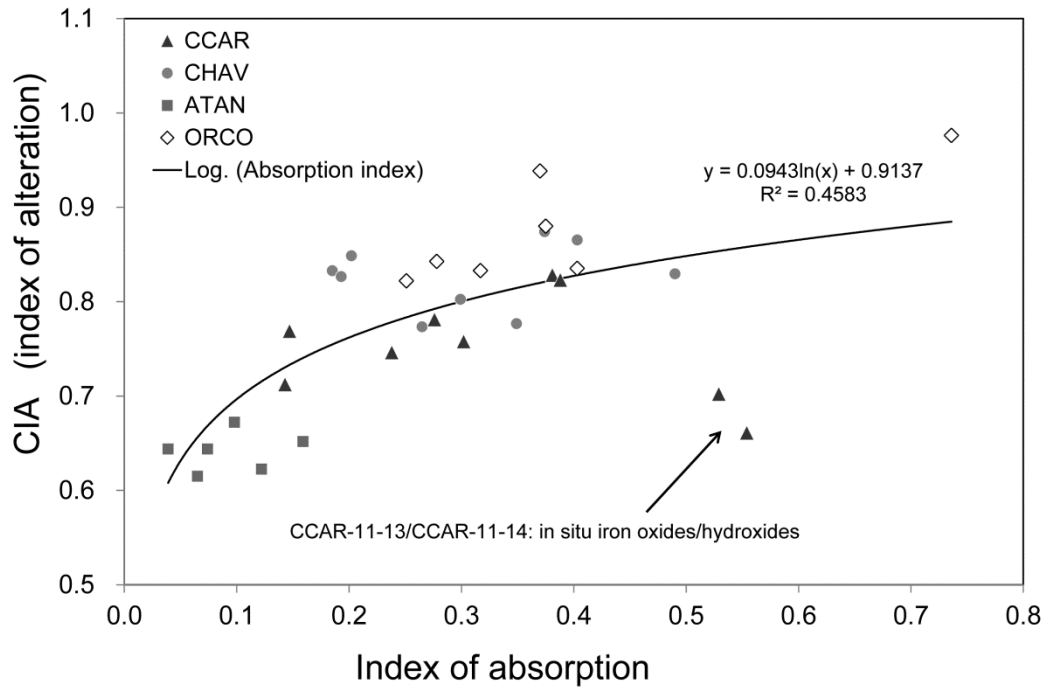


Fig. 13 The Index of absorption (IOA as defined in the text) is plotted against the Chemical Index of Alteration (CIA = molar  $\frac{Al_2O_3}{Al_2O_3+K_2O+NaO+CaO}$ , (Nesbitt and Young, 1982). Correlation can be found for samples with clay minerals and iron-oxides. This correlation is not valid for extremely leached samples or iron oxide/hydroxide crusts (CIA = 1, IOA= 0).

#### 4.5 Classification and alteration mapping using ASTER reflectance and emissivity data

The distribution of ignimbrites and lava flows with different alteration intensities and types was mapped using ASTER reflectance and emissivity as a basis for classification. The results are included in the ArcGIS database, and the different classes that were used are shown in Table 1.

The overall classification accuracy was 80% and classes showing lowest accuracy values are those being very similar in terms of alteration spectral signature (see Table 3). The ignimbrite mesas (such as Lomada Atansa in Fig. 14C and D) were mapped well using the “ignimbrite” spectral signature and are surrounded in the south by zones of intense alteration in younger volcanos. The alteration gradient from the core of volcanos (especially Cerro Palla Palla in Fig. 14 B) was mapped very well from core to the unaltered volcano flanks by the “CHAV high-T silicification” spectral signature to the various “scree” spectral signatures. A fractured zone within the ignimbrites was mapped using the “zeolite” spectral signature containing altered volcanic glass with minerals of the zeolite group. The quality of the classification is not homogeneous for all classes and will be discussed further in the section.

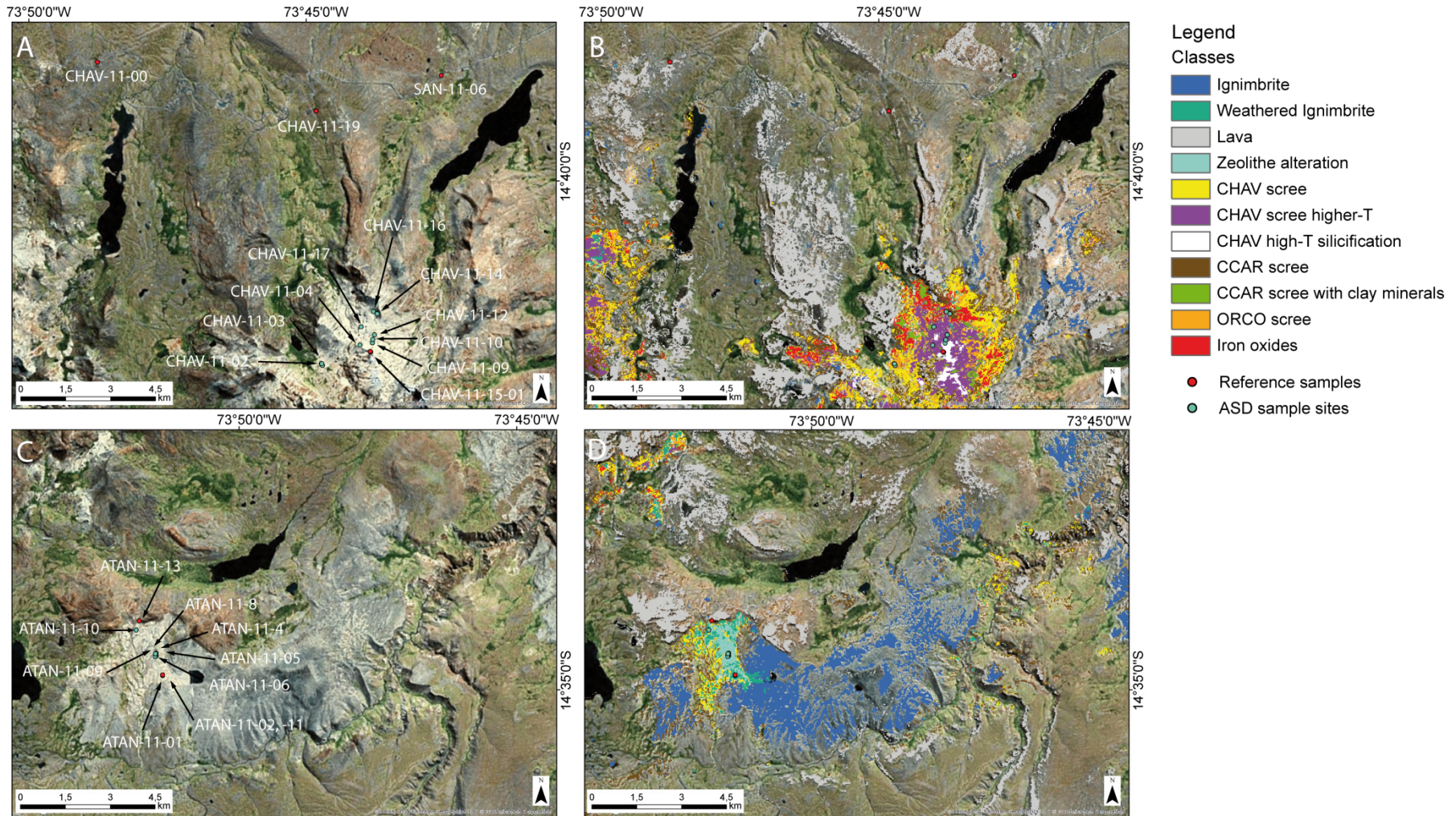


Fig. 14: A: Sample location map for Cerro Palla Palla (CHAV). Green dots: Alteration samples. Red dots: Reference and dating samples. ESRI Imagery overlain on SRTM derived hillshade image ( $z=2$ ). B: Support vector machine classification results for the area around Cerro Palla Palla. Classification results are overlain on ESRI imagery and SRTM derived hillshade image ( $z=2$ ). C: Sample location map for Lomada Atansa. D: Support vector machine classification results for the area around Lomada Atansa. Classification results are overlain on ESRI imagery and SRTM derived hillshade image ( $z=2$ ).

Omission error for “CHAV alteration”, for example, can be explained by the very similar alteration type with “CHAV debris” and the gradual transition between the two classes. Omission for the “lava” class is due to a very strict threshold applied here. This was necessary, as this class tends to include wet, shadowed and sparsely vegetated ground. The ignimbrite class omission is due to humid ground and a strict threshold is necessary to avoid commission of weathered lava which is spectrally very similar.

As classification was conducted with the aim of positively identifying ignimbrite surfaces, this class shows low commission but high omission. Commission using less strict thresholding increases rapidly as dacitic lava is included into this class. As can be seen at Lomada Atansa (Fig. 14C and D), ignimbrite weathering also leads to the occurrence of clay minerals. This is why we also find the “CHAV scree” class where we should expect only ignimbrite. Such transitions from “zeolite” to “weathered ignimbrite” to “CHAV scree” classes make positive identification of ignimbrite surfaces difficult. At the valley flanks west of Cerro Carhuarazo the “zeolite” class captures correctly the ignimbrite sheets and/or other altered magmatic rocks. The mapping of the “zeolites” class at Lomada Atansa gives very good results with a user accuracy of 100%. This result was achieved by selecting the training areas on the basis of fieldwork and pixel-purity-index interpretation. Another important result is the distinction between the “silicification” class at the summit of Cerro Palla Palla (CHAV) from the more argillic to oxidized (Fe-oxides) regions on the same volcano. However, here are pixels misclassified as ignimbrite in the shadow of clouds at the very top of the volcano. Comparing this finding to Fig. 4 it is obvious that the reduced reflectance of these ignimbrites changes the spectrum closer to the lava signature and leads to this misclassification.

Many pixels are classified as “CAV debris” and this is a good result since this alteration type with clay minerals is typical in general for all epithermally altered volcanoes (Inca and Cayo, 2000; Paz et al. 2000; and own ground truthing). The same is true for the alteration of Cerro Carhuarazo (“CCAR scree with clay minerals”) that can be traced on Cerro Palla Palla and other, similar locations. Furthermore, the alteration style of Cerro Orconcocha can be found in various locations that are also confirmed in a study by Guevara (2001). The signature of the alteration scree is very similar for all three volcanoes (Fig. 4). The parts of Cerro Palla Palla that are characterized by iron oxides were also classified correctly. The general trend from silicification to argillic and argillic-iron oxide alteration along the thermal gradient from the center of Palla Palla to the rim is captured and mapped very well (Fig. 14 A and B).

Table 3: Classification accuracy

Confusion matrix for Support Vector Machine Classification				
Class	Producer Accuracy (Percent)	User		
		Accuracy (Percent)	Accuracy (Pixels)	
Zeolithe	76.92	100	10/13	10/10
ORCO alteration	60.24	83.33	50/83	50/60
CHAV scree higher-T	59.21	84.91	45/76	45/53
CHAV high-T silicification	87.93	100	51/58	51/51
CHAV scree	83.33	25.64	10/12	10/39
Iron oxides	86.96	100	20/23	20/20
Weathered Ignimbrite	90.63	65.91	29/32	29/44
CCAR scree	84	89.36	42/50	42/47
CCAR scree with clay minerals	100	37.04	10/10	10/27
Soil/Regolith (unclassified)	100	79.26	172/172	172/217
Lava	77.44	100	127/164	127/127
Ignimbrite	61.29	86.36	19/31	19/22
Overall Accuracy	(585/724)	80.80%		
Kappa Coefficient	0.7755			

In summary, the classification algorithm distinguishes between highly silicified regions in the volcanic core (“CHAV high-T silicification”), areas with argillic alteration, silicification and iron oxides to variable degrees (“ORCO alteration”, “CCAR scree”, “CCAR scree with clay minerals”, “CHAV scree”), areas with dominating iron oxides (“iron oxides”), ignimbrite outcrops, lava and “zeolite alteration”. The differences between the “scree” classes lies in the amount of iron oxides and clay minerals and the amount of silicification. This can be seen in different absorption depth for different samples, in the geochemical data and in Fig. 4. Therefore, on each epithermally altered volcano, we find all scree classes represented. This shows the similarity style of alteration on all volcanic centers and the gradual change from silicification to areas with increasing amount of clay minerals and iron oxides.

## 5 Discussion

### 5.1 Chemical effects and styles of alteration

Our analysis shows that the results of the spectral analysis of our ground-truth areas in the field, laboratory spectral measurements on sampled material, as well as geochemical analysis results are mutually consistent (Table 4). Alteration styles were identified and

mapped successfully by combining these approaches in interpreting the ASTER spectral data. We will now link these different styles of alteration to bulk geochemical changes in major and trace element composition of the altered volcanic rocks.

Hydrothermal alteration results in changes of major element contents that becomes apparent in a plot of  $K_2O$  and the chemical index of alteration (CIA) versus  $SiO_2$  (Fig. 15, 16). While magmatic differentiation should lead to an increase in  $K_2O$  with an increasing  $SiO_2$  content, hydrothermal fluids leach potassium preferentially to other oxides ( $Al_2O_3$ ) that remain or can even be actively enriched ( $SiO_2$ ) in the process. At the same time the CIA increases with mobilisation and decreasing contents of Na, Ca and K. Only under extremely acid or alkaline conditions Al becomes also mobile (Hay and Sheppard, 2001) and under these conditions the CIA loses its measure for alteration. Andesite from Cerro Orconccochoa and Cerro Palla Palla show high degrees of leaching and silicification, where we observe silicification up to almost 100%  $SiO_2$  (Fig. 15).

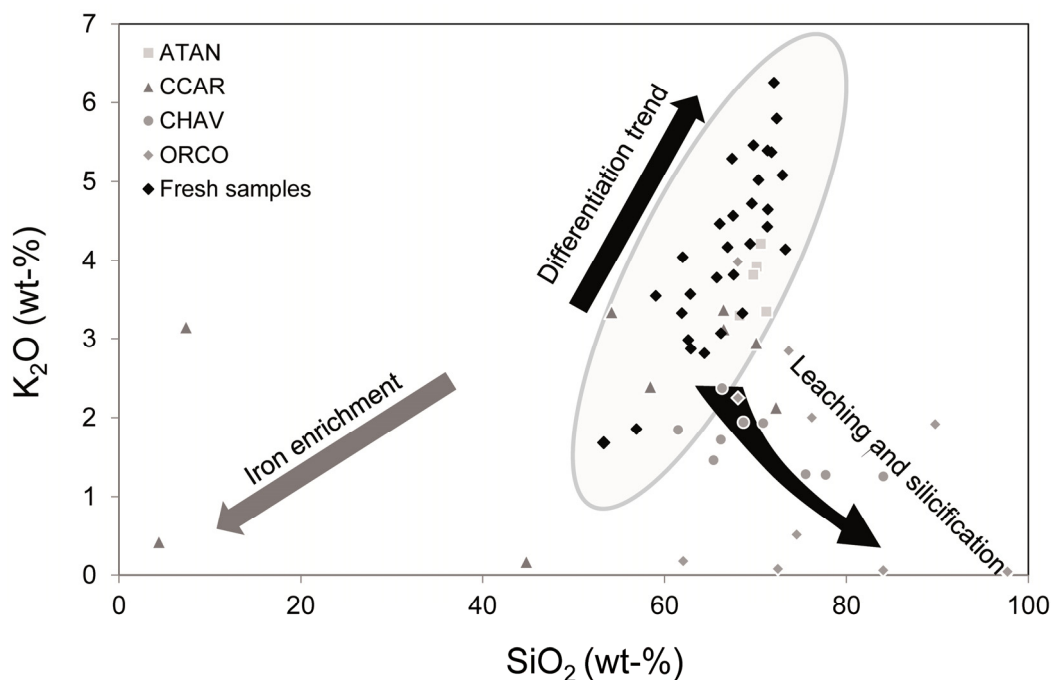


Fig. 15: Element variation plot for  $SiO_2$  (wt-%) versus  $K_2O$  (wt-%). Arrows show trends defined by differentiation, iron enrichment, silicification and hydrothermal leaching. Fresh Ignimbrite and lava samples collected in the same area are plotted together with alteration samples. Samples from Cerro Palla Palla and from Cerro Orconccochoa show strong leaching and silicification while samples from Lomada Atansa and Cerro Carhuarazo are closer to the differentiation trend or show iron enrichment.

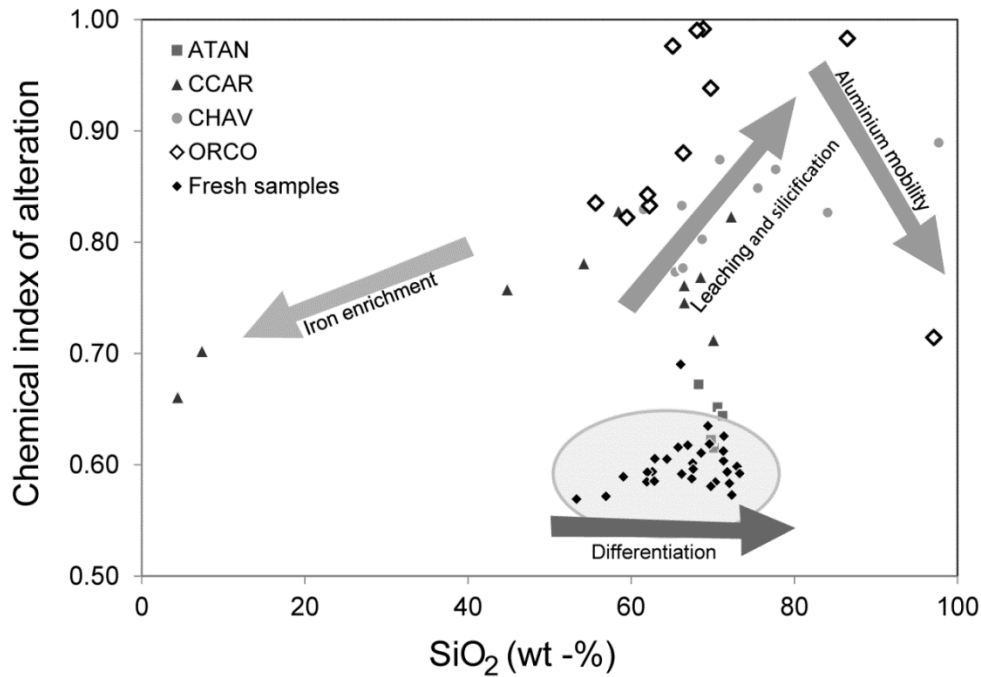


Fig. 16: This diagram shows the Chemical index of alteration (Nesbitt and Young, 1982) plotted against SiO<sub>2</sub>. Fresh samples are shown in yellow for comparison. Different processes are shown with arrows. Hydrothermal alteration first leaches the rock of alkaline elements and active SiO<sub>2</sub> enrichment occurs. Under extremely acid or alkaline conditions aluminium becomes mobile and the CIA decreases.

According to Corbett and Leach (1997), the formation of alteration minerals is determined by a number of variables that can be grouped into seven main categories (Browne, 1978): temperature, fluid chemistry, concentrations, host rock composition, kinetics of reactions, duration of activity or degree of equilibrium and permeability. SiO<sub>2</sub> contents of unaltered volcanic rocks in our study area range from about 53 weight-% to 73 weight-% (29 lava and ignimbrite pumice samples). Temperature and fluid chemistry have the strongest influence on the style of hydrothermal alteration, although all of the stated factors are somewhat interdependent. In a diagram that was derived from a data compilation by Corbett and Leach (1997), fluid pH and temperature were used to show stability ranges for common hydrothermal alteration minerals. Although the stability ranges can change due to other factors, the diagram in his study serves as a good approximation for stability ranges here.

Characterizing our own results accordingly, we observe mostly silica group minerals grading to kaolinite/illite group minerals. Highest temperatures and lowest pH occur on top of Cerro Palla Palla (spectral class "CHAV-high-T silicification") and on Cerro Orconchocha (spectral class "ORCO alteration"). Silica group minerals indicate a fluid pH lower than 2 (Stoffregen, 1987). We attribute the very high content of amorphous silica to the fact that hydrothermal fluids must have been highly acidic and oversaturated with respect to SiO<sub>2</sub>. Local hydrothermal alteration recognized in the Incapacha project, a detailed study of Cerro Incapacha and surroundings in the SW of our area (Guevara, 2001) was described as silicic



to advanced argillic and confirms our findings. With increasing pH and decreasing temperature, alunite, and clay minerals: first kaolinite at pH 3-4,  $T < 200-150^{\circ}\text{C}$  and then illite/smectites (pH 4-5,  $T < 100-200^{\circ}\text{C}$ ) become stable mineral phases (Corbett and Leach, 1997). Using spectral classification on ASTER data, we can visualize these changing conditions and stability ranges.

SVM classification identifies zones of silicification that are critical for exploration (Hedenquist et al. 2000) and that are not easily captured by simple and often-used ratio-images. The iron absorption feature normally cannot be seen clearly in ASTER data but the deep trough of the feature still affects ASTER band 3 and band 1 is pulled down by the iron absorption as well. Therefore, a high content of iron can be distinguished because the ASTER spectrum has high ratios for band 2/ band 1 and band 3/ band 2 ("iron oxides" in Fig. 4) and is captured by the classification algorithm. The five bands in the SWIR centered around  $2\ \mu\text{m}$  to  $2.5\ \mu\text{m}$  catch important absorption features of clay minerals. Zeolite absorption features are centered at  $1.4\ \mu\text{m}$  and  $1.9\ \mu\text{m}$  and cannot be detected by ASTER due to atmospheric absorption. Nevertheless, the form of the spectrum from bands 3 to 9 is very pronounced with low reflection of band 3 and 9 and high reflection values for bands 4, 6 and 7 (Fig. 4). This allows distinction of this alteration class in our scenes and is in accordance with pure zeolite spectra from USGS spectral library resampled to ASTER spectral resolution.

Results from geochemical, spectral analysis and classification allow the following observations: 1) We identify areas (stratovolcanos) that show hydrothermal alteration typical for high temperatures and low pH values ( $< 2$ ) and areas with higher pH values (4-5) and argillic alteration. The zonation around a silicic high-T alteration core is striking. 2) There are large areas covered with ignimbrites that are surrounded by the altered volcanic structures. 3) The Andamarca formation is cut by minor faults with zeolitic alteration (pH neutral to alkaline for zeolite stability).

Table 4: Comparison of geochemical and spectral results

Results from ASD spectral analysis, geochemical and mineral sensitive methods (GMS) for the different alteration classes\*

Alteration mineral group**	Zeolithe alteration	weathered ignimbrite	CCAR scree	CCAR scree with clay minerals	CHAV scree
Silica group minerals ASD	x		x	x	x
Alunite group minerals ASD					
Kaolin group minerals ASD					x
Illite group minerals ASD		x	x	x	x
Calc-silicate group ASD	x				
Silica group minerals GMS			x	x	x
Alunite group minerals GMS	x				
Kaolin group minerals GMS					x
Illite group minerals GMS		x			x
Calc-silicate group GMS	x				

\* Samples used to define the class are given in tab n.a.: samples not analyzed

\*\* mineral groups after Corbett&Leach, 1997

Alteration mineral group**	CHAV scree higher-	CHAV high-T silicification	ORCO alterat	Iron oxides
Silica group minerals ASD	x	x	x	x
Alunite group minerals ASD				
Kaolin group minerals ASD			x	x
Illite group minerals ASD			x	x
Calc-silicate group ASD				
Silica group minerals GMS	x	x	x	x
Alunite group minerals GMS				
Kaolin group minerals GMS			x	
Illite group minerals GMS				x
Calc-silicate group GMS				

## 5.2 Can calderas be identified by use of ASTER spectral mapping?

---

Based on the extensive hydrothermal systems that were active in the region, combined with the observation of the large ignimbrite sheets we may expect a buried and overprinted caldera structure - or multiple nested calderas - in the region. Guevara (2001) proposed a "Incapacha-Yauri" caldera (see Fig. 17) but this study did not provide clear evidence for such a structure. Furthermore, we observed more than one ignimbrite sheet representing probably different ages (Roperch et al., 2011; and our own unpublished data) and younger lava flows coming from Cerro Chavina and Cerro Carhuarazo (Barroso group) (INGEMMET, 2001b) that might cover parts of the older Andamarca ignimbrites and their caldera structures.

The regional ignimbrite surface of the Miocene to Pliocene Andamarca Formation (INGEMMET, 2001a) is tentatively correlated based on our own field work. Combined with DEM data this shows a decrease in elevation from Lomada Atansa (4550m) towards the North into the valley west of Cerro Carhuarazo where they underly at c. 4000 m this 9.5 Ma old stratovolcano. Ignimbrites also fill the Uralla valley to the N at 2900 m elevation near Aucara. The region in between is occupied by a deeply eroded and altered massif (5812m) of volcanic and volcanoclastic sequences, including irregularly layered ignimbrites. This region correlates with the location of the proposed Incapacha-Yauri caldera of Guevara (2001). Fig. 17 is a preliminary model showing classification results draped on Landsat ETM+ RGB: 742 imagery and SRTM (Shuttle Radar Topography Mission) DEM (Digital Elevation Model) covering (z=2) the presumed caldera region and part of its ignimbrite outflow sheets. A sketch map of the potential eruption sites for the ignimbrites based on our findings and Guevara's (2001) interpretation of the Incapacha mining prospect is shown in white. The region delineated by strong hydrothermal alteration and morphologic features (incision by rivers) might indicate an overprinted caldera rim. Assuming that the younger stratovolcanoes and outflow sheets now cover former caldera structures that were favorable for passageways for magma and hydrothermal fluids, the southern caldera border should be located even more to the south as proposed by Guevara (2011). Taking into consideration that there are ignimbrite sheets of different ages, we assume rather nested or reactivated calderas as a source for the respective ignimbrites. In order to give a chronologic frame to ignimbrite sheets, caldera centers and associated hydrothermal activity, dating of the respective units was necessary.

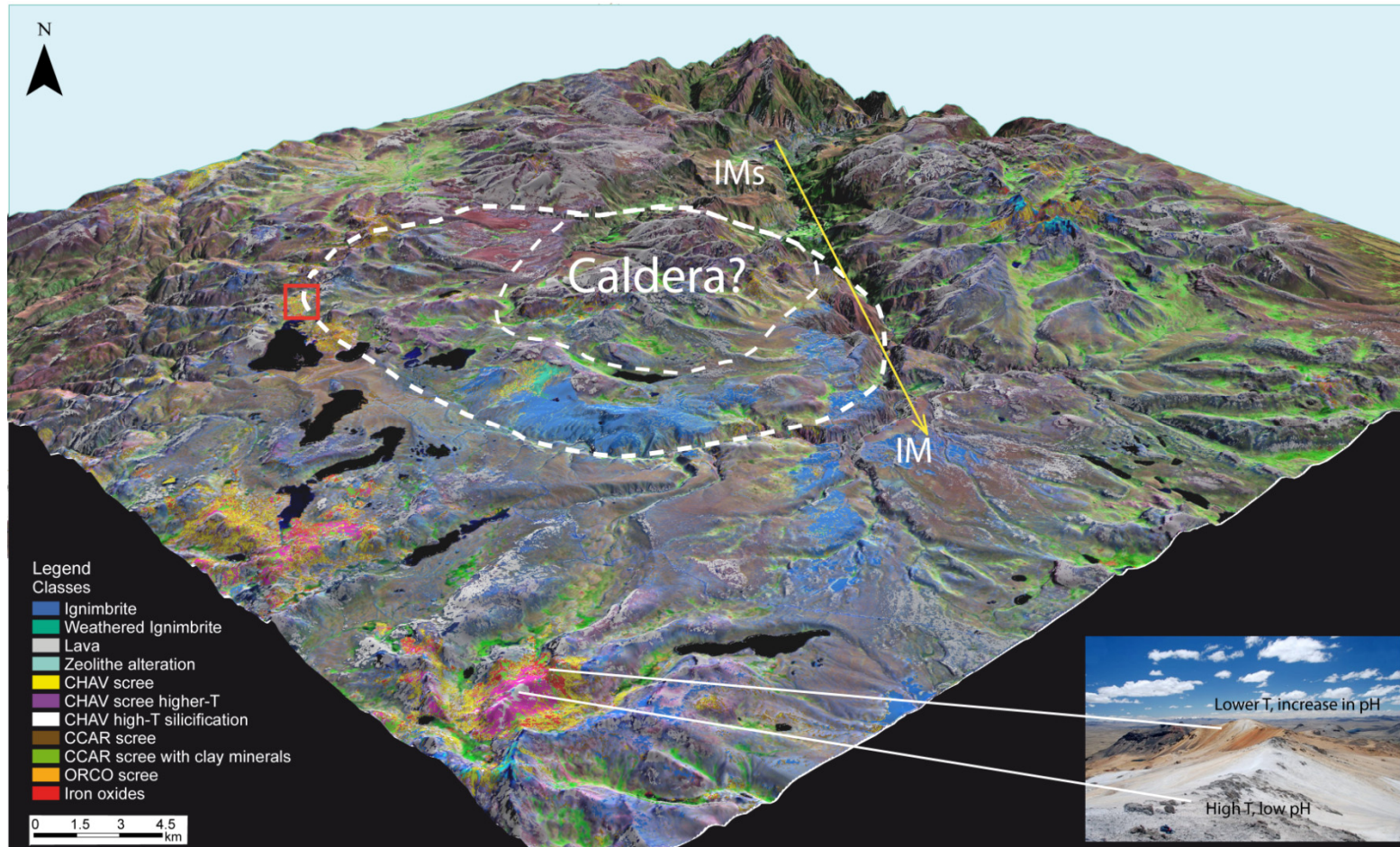


Fig. 17: SVM classification results overlain on Landsat ETM+ 521 image and SRTM digital elevation data ( $z=2$ ). The outer white line delineates the Incapacha caldera proposed by Guevara 2001, the inner white line the caldera location more probable based on this study. The red square is the region studied in the thesis of Guevara (2001). DEM data shows an increase in elevation upvalley (yellow arrow), meaning the ignimbrites form a surface higher in elevation than the ignimbrites we observed along the two marked mesas (IMs = ignimbrite mesas) to the north. Alteration (argillic and silicification) in the region of the Incapacha-project delineates possible borders of a former caldera. Nevertheless, the sketch-map proposed by Guevara (2001) and redrawn in this model and our proposed eruption site for the ignimbrites still has to be confirmed in the field and by radiometric dating of the respective ignimbrites (work in progress). The N-S trending alteration (zeolite alteration) in the Andamarca formation is probably due to minor, N-S trending faults in the region. The other observed faults trend NW-SE (Andean direction) and NE-SW. Strong alteration on the surrounding volcanoes (high temperatures and low pH) indicate strong hydrothermal systems.

## 6 Summary and conclusions

---

ASTER data can be used in several ways to map alteration patterns. The application of mineral maps and spectral indices using ASTER reflectance data gives good results in our study area (Brandmeier, 2010). The method presented by Cudahy et al. (2008) on ASTER level 1b data for Al-OH mineral group abundance maps was used for the selection of our ground-truth sites. Applying a combination of hyperspectral field spectrometry data with chemical analysis allows us to characterize and map different alteration settings.

SVM classification was originally developed for hyperspectral data but proved to give very good results using ASTER SWIR reflectance and TIR emissivity data as well, especially with an increase of dimensionality by use of MNF transformed data. The selection of good training sites was crucial for the quality of classification. Ground-truth sample collection and spectral measurements, pixel-purity index calculation and the calculated mineral indices and mineral abundance maps were used for this process.

Classification allowed us to map the silicic core of Cerro Palla Palla, which was not easily captured by ratio images and helped us to visualize different types and patterns of alteration. We further mapped zones of argillic alteration and regions with high contents of iron oxides/hydroxides at surface level at Cerro Orconcocha and the Miocene Carhuarazo stratovolcano and zeolitic alteration in a fault zone within an ignimbrite. The distinction between unaltered ignimbrites and lava flows still poses a problem using ASTER data with such limited spectral resolution (i.e. 9 bands compared to hundreds for hyperspectral data) because the spectral similarity is very high for shadowed areas. Nevertheless, the overall accuracy of the classification is 80% and results provide robust information about the type and distribution of altered rocks in the region.

The combination of ASTER reflectance data, field spectrometry data and geochemical analysis is a powerful tool for mapping and interpreting alteration patterns in arid areas. Data from field spectrometry measured on the ground, combined with laboratory analyses (chemical and mineralogical) define a correlation between the Chemical Index of Alteration (CIA) and spectral features proposed here to identify alteration zones (IOA). However, this correlation is not valid for extremely leached and silicified samples of altered rocks with Fe-hydroxide-rich crusts.

Mineral assemblages derived and mapped using ASD spectra indicate different styles and intensities of alteration, which allows estimates on pH and temperature conditions in altered zones (Corbett & Leach, 1997) of our study area. Relations to caldera structures and

the correlation of these with ignimbrite sheets, however, remain speculative and must await further mapping and - in particular - radiometric dating.

## ACKNOWLEDGEMENTS

*This work was supported by the German Science Foundation (DFG-grant Wo 362-43-1). We gratefully acknowledge Dr. G. Hartmann for providing help with RFA analysis, Dr. H. Klein for help with XRD analysis and Dr. A. Kronz for support at the microprobe. The DAAD-Promos programme and the Universitätsbund Göttingen provided student travel funds that allowed masters students (Christian Hansen, Andres Höweling, Kai Nitzsche, Tammo Ohlendorf) of the Geowissenschaftliche Zentrum (GZG, Universität Göttingen) to participate in this study as part of our Earth Science curriculum (Geochemie-Projekt M.Geol.122).*

## REFERENCES:

- Bellón, H., Lefèvre, C. Données géochronométriques sur le volcanisme andin dans le Sud du Pérou: implications volcanotectoniques. *CR Acad Sci.* 1977a. 283: 1-4.
- Bellón, H., Lefèvre, R. Spectre d'âges radiométriques du volcanisme cénozoïque du Pérou central (région de Castrovirreyna–Ayacucho–Nazca). *Réunion Annuelle des Sciences de la Terre.* 1977b. 5 (58 pp.).
- Boser, B.E., Guyon, I., Vapnik, V. A training algorithm for optimal margin classifiers. *Fifth Annual Workshop on Computational Learning Theory: ACM Press;* 1992. p. 144-52.
- Brandmeier, M. Remote sensing of Carhuarazo volcanic complex using ASTER imagery in Southern Peru to detect alteration zones and volcanic structures – a combined approach of image processing in ENVI and ArcGIS/ArcScene. *Geocarto International.* 2010. 25: 629-48.
- Browne, P.R.L. Hydrothermal alteration in active geothermal fields. *Annual Reviews in Earth and Planetary Sciences.* 1978. 6: 229-50.
- Castillo, J., Barreda, J., Vela, C. Geología de los cuadrángulos de Laramate y Santa Ana. In: *INGEMMET, editor. Lima: INGEMMET;* 1993.
- Chih-Wei Hsu, C., Chih-Jen Lin. A practical guide to support vector classification. Taiwan: Department of Computer Science, National Taiwan University; 2003.
- Clark, R.N., Gallagher, A.J., Swayze, G.A.. Material absorption band depth mapping of imaging spectrometer data using the complete band shape least-squares algorithm simultaneously fit to multiple spectral features from multiple materials. *Third Airborne Visible/Infrared Imaging Spectrometer (AVIRIS) Workshop: JPL Publications;* 1990. p. 176-86.
- Clark, R.N., Lucey, P.G., 1984. Spectral properties of ice-particulate mixtures and implications for remote sensing: 1. Intimate mixtures. *Journal of Geophysical Research: Solid Earth (1978–2012)* 89: 6341-6348.
- Clark, R.N., King, V.V., Gorelick, N.S. Automatic continuum analysis of reflectance spectra. *Third AIS workshop. Pasadena: JPL Publications* 1987. p. 138-42.
- Clark, R.N., Roush, T.L.. *Reflectance spectroscopy: quantitative analysis techniques for remote sensing applications.* Washington, DC, ETATS-UNIS: American Geophysical Union; 1984.
- Corbett, G., Leach T. Southwest Pacific rim gold-copper systems: Structure, alteration, and mineralization. *Short course manual.* 1997.
- Cortes, C., Vapnik, V. Support-vector network. *Machine learning.* 1995. 20: 273-97.
- Cudahy, T., Jones, M., Thomas, M., Laukamp, C., Caccetta, M., Hewson, R., et al. *Next Generation Mineral Mapping: Queensland Airborne HyMap and Satellite ASTER Surveys 2006-2008.* CSIRO Exploration and Mining Report P2007/364: CSIRO. 2008.
- Decou, A., von Eynatten, H., Dunkl, I., Frei, D., Wörner, G. Late Eocene Andean uplift inferred from detrital zircon fission track and U-Pb dating of Cenozoic siliciclastic forearc sediments (15–18°S). 2013. *Journal of South American Earth Sciences* 45: 6-23
- De Silva, S. The origin and significance of crystal-rich inclusions in pumice from two Chilean ignimbrites. *Geol Mag.* 1989. 126:159-75.
- De Silva, S. Styles of zoning in central Andean ignimbrites ; insights into magma chamber processes. *The Geological Society of America Andean Magmatism and Its Tectonic Setting.* 1991. 265:217-31.

- Fujisada, H. Design and performance of the ASTER instrument. Proceedings of SPIE, the international society for optical engineering. 1995. p. 16-25.
- Gillespie, A., Rokugawa, S., Matsunaga, T., Cothorn, J.S., Hook, S., Kahle, A.B. A temperature and emissivity separation algorithm for Advanced Spaceborne Thermal Emission and Reflection Radiometer (ASTER) images. IEEE Transactions on Geoscience and Remote Sensing. 1998. 36: 1113-26.
- Green, A. A., Berman, M., Switzer, P., and Craig, M. D. A transformation for ordering multispectral data in terms of image quality with implications for noise removal: IEEE Transactions on Geoscience and Remote Sensing, 1988. 26, no. 1: 65-74.
- Guevara, J.E.A. Geología y exploración del proyecto aurífero epitermal Incapacha (Puquio-Ayacucho-Peru). Lima: Universidad Nacional de Ingeniería; 2001.
- Hay, R.L, Sheppard, R.A. Occurrence of Zeolites in Sedimentary Rocks: An Overview. Reviews in Mineralogy and Geochemistry. 2001. 45:217-34.
- Hecker, C., Dilles, J.H., van der Meijde, M., van der Meer, F.D. Thermal infrared spectroscopy and partial least squares regression to determine mineral modes of granitoid rocks. Geochemistry Geophysics Geosystems. 2012: 13.
- Hedenquist, J.W., Arribas, A.R., Gonzalez-Urien, E. Exploration for Epithermal Gold Deposits. SEG Reviews 2000. p. 245-77.
- Inca, P., Cayo, E. Geología y mineralización del yacimiento epitermal Palla Palla Ayacucho-Perú. In: Perú SGd, editor. X Congreso Peruano de Geología. Lima: Sociedad Geológica del Perú; 2000. p. 81.
- INGEMMET. Mapa geológica del cuadrángulo de Querobamba. Lima: INGEMMET; 2001a.
- INGEMMET. Mapa Geológico del cuadrángulo de Chavina. Lima: Instituto Geológico Minero y Metalúrgico. 2001b.
- Iwasaki, A., Tonooka, H. Validation of a crosstalk correction algorithm for ASTER/SWIR. Geoscience and Remote Sensing, IEEE Transactions on. 2005. 43: 2747-51.
- Karátson, D., Telbisz, T., Wörner, G. Erosion rates and erosion patterns of Neogene to Quaternary stratovolcanoes in the Altiplano plateau (Central Andes): a SRTM DEM based analysis. Geomorphology; 2011; 139-140: 122-135
- Kay, S., Coira B., Caffè, P.J., Chen, C-H. Regional chemical diversity, crustal and mantle sources and evolution of central Andean Puna plateau ignimbrites. Journal of Volcanology and Geothermal Research. 2010. 198: 81-111.
- Kruse, F.A., Lefkoff, A.B., Boardman, J.W., Heidebrecht, K.B., Shapiro, A.T., Barloon, P.J. The spectral image processing system (SIPS)—interactive visualization and analysis of imaging spectrometer data. Remote Sensing of Environment. 1993. 44: 145-63.
- Lindsay, J.M., De Silva, S., Trumbull, R., Emmermann, R., Wemmer, K. La Pacana caldera, N. Chile: a re-evaluation of the stratigraphy and volcanology of one of the world's largest resurgent calderas. Journal of Volcanology and Geothermal Research. 2001. 106: 145-73.
- Lipman, P.W. The roots of ash flow calderas in western North America: Windows into the tops of granitic batholiths. Journal of Geophysical Research: Solid Earth. 1984. 89: 8801-41.
- McKee, E.H. Ash-flow sheets and calderas: Their genetic relationship to ore deposits in Nevada. Geological Soc Am Special paper. 1979. 180: 205-211.



- McLaughlin, D.H. Geology and Physiography of the Peruvian Cordillera Department of Junin and Lima. Geol Soc Am Bull. 1924. p.35.
- Nesbitt, H.W., Young, G.M. Early Proterozoic climates and plate motions inferred from major element chemistry of lutites. Nature. 1982. 199: 715-7.
- Ninomiya, Y. A stabilized vegetation index and several mineralogic indices defined for ASTER VNIR and SWIR data. IEEE 2003 International Geoscience and Remote Sensing Symposium IGRSS'03. Toulouse, France. 2003a. p. 1552-4.
- Paz J, Miranda, M, Vidal C. Geología y mineralización del yacimiento epitermal Ccarhuaraso Ayacucho-Perú. X Congreso Peruano de Geología. Lima: Sociedad Geológica del Perú; 2000. p. 87.
- Pour, A.B., Hashim, M. The application of ASTER remote sensing data to porphyry copper and epithermal gold deposits. Ore Geology Reviews. 2012. 44: 1-9.
- Rivard, B., Arvidson, R., Duncan, I., Sultan, M., El Kaliouby, B. Varnish, sediment, and rock controls on spectral reflectance of outcrops in arid regions. Geology 20. 1992. 295-298.
- Roperch, P., Carlotto, V., Ruffet, G, Fornari, M. Tectonic rotations and transcurrent deformation south of the Abancay deflection in the Andes of Southern Peru. Tectonics. 2011. p. 30.
- Rowan, L.C, Schmidt R.G., Mars J.C. Distribution of hydrothermally altered rocks in the Reko Diq, Pakistan mineralized area based on spectral analysis of ASTER data. Remote Sensing of Environment. 2006. 74-87.
- Rytuba, J.J. Evolution of volcanic and tectonic features in caldera settings and their importance in localization of ore deposits. Economic Geology. 1994. 89: 1687-96.
- Sabins, F.F. Remote sensing for mineral exploration. Ore Geology Reviews. 1999. 14: 157-83.
- Salisbury, M.J, Jicha, B.R, de Silva SL, Singer BS, Jimenez NC, Ort MH.  $^{40}\text{Ar}/^{39}\text{Ar}$  chronostratigraphy of Altiplano-Puna volcanic complex ignimbrites reveals the development of a major magmatic province. Geol Soc Am Bull. 2011. 123: 821-40.
- Schmitt, A.K, Lindsay, J.M., De Silva S., Trumbull, R.B. U-Pb zircon chronostratigraphy of early-Pliocene ignimbrites from La Pacana, north Chile: implications for the formation of stratified magma chambers. Journal of Volcanology and Geothermal Research. 2003. 120: 43-53.
- Smith, R.L, Bailey, R.A. Resurgent cauldrons. Geological Society of America Memoir. 1968. 116: 613-662.
- Soler, M.M., Caffee, PJ, Coira, BL, Onoe, AT, Kay SM. Geology of the Vilama caldera: A new interpretation of a large-scale explosive event in the Central Andean plateau during the Upper Miocene. Journal of Volcanology and Geothermal Research. 2007. 164: 27-53.
- Stoffregen, R. Genesis of acid-sulfate alteration and Au-Cu-Ag mineralisation at Summitville, Colorado. Econ Geol. 1987. 82: 1575-91.
- Thouret, J.C, Wörner, G., Gunnell, Y., Singer B., Zhang X., Souriot T. Geochronologic and stratigraphic constraints on canyon incision and Miocene uplift of the Central Andes in Peru. Earth and Planetary Science Letters. 2007. 263: 151-66.
- Van der Meer, F.D., van der Werff, H.M.A., van Ruitenbeek, F.J.A., Hecker, C.A., Bakker W.H., Noomen M.F. Multi- and hyperspectral geologic remote sensing: A review. International Journal of Applied Earth Observation and Geoinformation. 2012. 14: 112-28.
- Yamaguchi, Y., Naito C. Spectral indices for lithologic discrimination and mapping by using the ASTER SWIR bands. International Journal of Remote Sensing. 2003. 24: 4311-23.

Manuscript II - Mapping patterns of mineral alteration in volcanic terrains using ASTER data and field spectrometry in Southern Peru

Woldegabriel, G. Hydrothermal alteration in the Valles caldera ring fracture zone and core hole VC-1: evidence for multiple hydrothermal systems. *Journal of Volcanology and Geothermal Research*. 1990. 40: 105-22.

## MANUSCRIPT III

---

# Age and distribution of Neogene ignimbrites in Southern Peru as tracers for uplift, erosion and changes in the Andean drainage divide between the Pacific and Atlantic Oceans

Brandmeier, M<sup>a</sup>, Mamani, M<sup>b</sup>, Jicha, B<sup>c</sup>, Wörner, G<sup>a</sup>

<sup>a</sup> Georg-August-Universität Göttingen, GZG, Geochemisches Institut, Goldschmidstr.1, Göttingen D-37077, Germany

<sup>b</sup> Pontificia Universidad Católica del Perú, Av. Universitaria 1801, San Miguel, Lima 32, Peru

<sup>c</sup> University of Wisconsin-Madison, Department of Geoscience, 1215 W. Dayton St., Madison, WI 53706, USA

In preparation

---

## Abstract

*In this study we present 31  $^{40}\text{Ar}^{39}\text{Ar}$  ages of ignimbrites and related lava samples from three major valleys draining to the Amazon River and one valley west of the present drainage divide in Southern Peru. We combine these with drainage and DEM analysis and present a new stratigraphy for the western side of the drainage divide. We discuss timing, extent and possible eruptive centers for the ignimbrites and propose a “Santa Ana Caldera” with an age of ~5 Ma and a diameter of ~20 km. Ignimbrite ages correspond to the ~20 Ma (Nazca age) and four age ranges within the “Formación Andamarca”: 14 Ma ignimbrites (Andamarca 1), 7.5-9.5 Ma (Andamarc 2), 5-6.5 Ma (Andamarca 3) and 3.5-4 Ma (Andamarca 4).*

*Based on the position of the samples in the valleys, we found a minimum incision of ~300 m prior to 14 Ma, of ~500-800 m after ~6 Ma (in the Río Caracha valley and the Río Visca valley) and renewed incision after ~3.8 Ma of 200 to 300 m. For the Visca valley, we know of at least one additional event (~9.4 Ma) that filled the valley and cannot be quantified in terms of re-incision. Causes for incision and changes in incision rates are uplift (mainly between 14 Ma to 3.8 Ma) and a change in climate and drainage system with related base-level changes.*

*There are several processes that change incision and drainage over time – and are linked to one another in complex ways: Uplift of the Andes affects precipitation patterns and triggers incision. Incision and removal of material itself also triggers uplift and climatic effects. Feedbacks have to be considered on a global scale (for example, the closure of the Central American Seaway and intensified upwelling of the Humboldt current are discussed as cause for the switch to hyper-aridity in the Atacama desert).*

*Our findings agree with an increase of erosion rates and headwater erosion found by other authors in the Eastern Cordillera at 15-10 Ma that would have shifted the drainage divide in a westerly direction. Drainage analysis and the position of the ~9.4 Ma ignimbrite in the Río Visca valley argue for river capture occurring prior to 9 Ma and changing the drainage direction of that valley. In this valley, incision started earlier than in the other valleys with the basal ignimbrite having an age of 14 Ma.*

*Uplift on the order of 2,000-3,500 m found on the Altiplano and Eastern Cordillera since ~10 Ma are reflected by river incision of at least 1 km during that time, with at least one more phase of incision (9-6 Ma) that cannot be quantified. Re-incision of 200-300 m occurred after 3.8 Ma is probably related to the wetter climate and glaciation history of the area*

*Comparing the stratigraphic record of the three valleys east of the drainage divide to the one valley west of it and stratigraphies found by other authors for the western escarpment, we found that the 20 Ma Nazca age (and probably the 14 Ma age) are completely absent on the eastern part of the drainage divide. This striking difference argues for either very directional deposition model of these ignimbrites, or high rates of incision and denudation towards the east, whereas the plateau-forming Nazca and Huaylillas ignimbrites are so well preserved on the western escarpment. We argue that this is due to uplift caused by the arrival of the Nazca ridge at that latitude after ~12 Ma, accompanied by a change in precipitation toward more humid conditions on the eastern side of the orogen.*

**KEYWORDS:**  $^{40}\text{Ar}/^{39}\text{Ar}$  dating, Peru, ignimbrites, river incision

## 1 Introduction

---

The Altiplano-Puna region of the Andes is one of the best studied volcanic regions in the world with a crustal thickness of more than 70 km (Allmendinger et al., 1997; Baker and Francis, 1978; Beck et al., 1996; De Silva, 1989a; De Silva, 1989b; Francis and Rundle, 1976; James, 1971; Kay-Mahlburg et al., 1991; Kay et al., 2010; Salisbury et al., 2011; Wörner, 2002). Timing, distribution, geochemistry and caldera source of the main ignimbrites are relatively well understood for the southern Altiplano-Puna region (Kay et al., 2010; Salisbury et al., 2011). In contrast, the area north of the Atacama Basin and, in particular north of the Arica bend (approximately 13°S to 15°S) is less well studied apart from sparse radiometric dating. However, this region encompasses the central and northern Altiplano and is of great interest for our understanding of the Andean orogeny. The region has a less arid climate and a higher rate of weathering and erosion and therefore has been much less accessible. However, while preservation of entire ignimbrite sheets is not as good as in the south and vegetation cover and the glacial history of the area (Forbiger, 2008) hinder mapping of the extent of ignimbrites, deep canyon incision exposes a regional stratigraphy that can be used to constrain timing of uplift and erosion (Thouret et al., 2007 and references herein). Whereas in the southern and central Andes Neogene ignimbrites were deposited on the Altiplano and, partially, on the western Andean slope to the Pacific, to the north of the Canon Cotahuasi (15°S) in Southern Peru, ignimbrites were also deposited to the north-east of the present water divide into rivers that belong to the Amazon drainage. Therefore, these ignimbrites may hold important information on the incision history of the valley systems on the eastern Amazonian side that can be compared to the western slope of the Central Andes.

From this region, we report 31 new  $^{40}\text{Ar}/^{39}\text{Ar}$  age determinations of ignimbrite and lava samples collected in a geomorphological context. This new ignimbrite chronology is combined with scattered existing age data and used, together with drainage patterns and river profiles, to better constrain the Neogene uplift, erosion, and drainage history of the northern Central Andes.

## 2 Methods

---

### 2.1 Sample collection

---

The goal of this study is to establish a regional stratigraphy for Neogene ignimbrites to better constrain the morphological evolution of the part of the northern Central Andes that straddles the continental drainage divide. Our objectives for sample collection were to (a) find samples that were least affected by weathering or alteration and (b) to get dating samples from all major ignimbrite sheets in different valley cross-sections (Urayama Valley, the valleys of the Río Mayobamba, the Río Soras and the Río Caracha (Fig. 1)). Ideally, we collected stratigraphically related ignimbrite (and some lava) samples in different morphological positions (plateaus, mesas, valley fills). Geological mapping of ignimbrite units in the field was, however, not our goal. Regional mapping and stratigraphic correlation of individual outflow sheets based on field work is difficult because of inaccessibility and because vast parts of the area are covered by glacial till or fluvio-glacial deposits. Ignimbrites are also dissected and separated by deep valleys and single outflow sheets may regionally change from plateau-forming to valley-filling depending on their age and underlying morphology. However, wherever possible, we traced their distribution, using geological maps provided by INGEMMET in addition to our own observations in the field, to obtain an estimate of the minimum extent of each ignimbrite.

### 2.2 $^{40}\text{Ar}/^{39}\text{Ar}$ Geochronology

---

Target phases for geochronology were sanidine or plagioclase (for samples lacking sanidine). Whole rock/pumice samples were crushed, wet sieved, and the 250  $\mu\text{m}$  to 500  $\mu\text{m}$  fraction was selected for mineral separation. After magnetic separation, crystals were cleaned in tepid HF for 10 minutes, rinsed with distilled water, put into an ultrasonic bath for one hour, and leached with HCl for another 10 minutes. After rinsing with distilled water and drying, single crystals (200-300 per sample) were hand-picked using a binocular microscope and put on a double-sided tape for Raman Spectroscopy. Identification of pure sanidine was done using LabSpec5 by measuring the distance between two peaks in the interval of 450 - 540  $\text{cm}^{-1}$  Raman Shift (Bendel and Schmidt, 2008). After a baseline correction, peaks were fitted and the value for peak-distance was calculated. Crystals with peak distances above 37  $\text{cm}^{-1}$  were classified as sanidine, crystals falling below that value as plagioclase. Quartz and

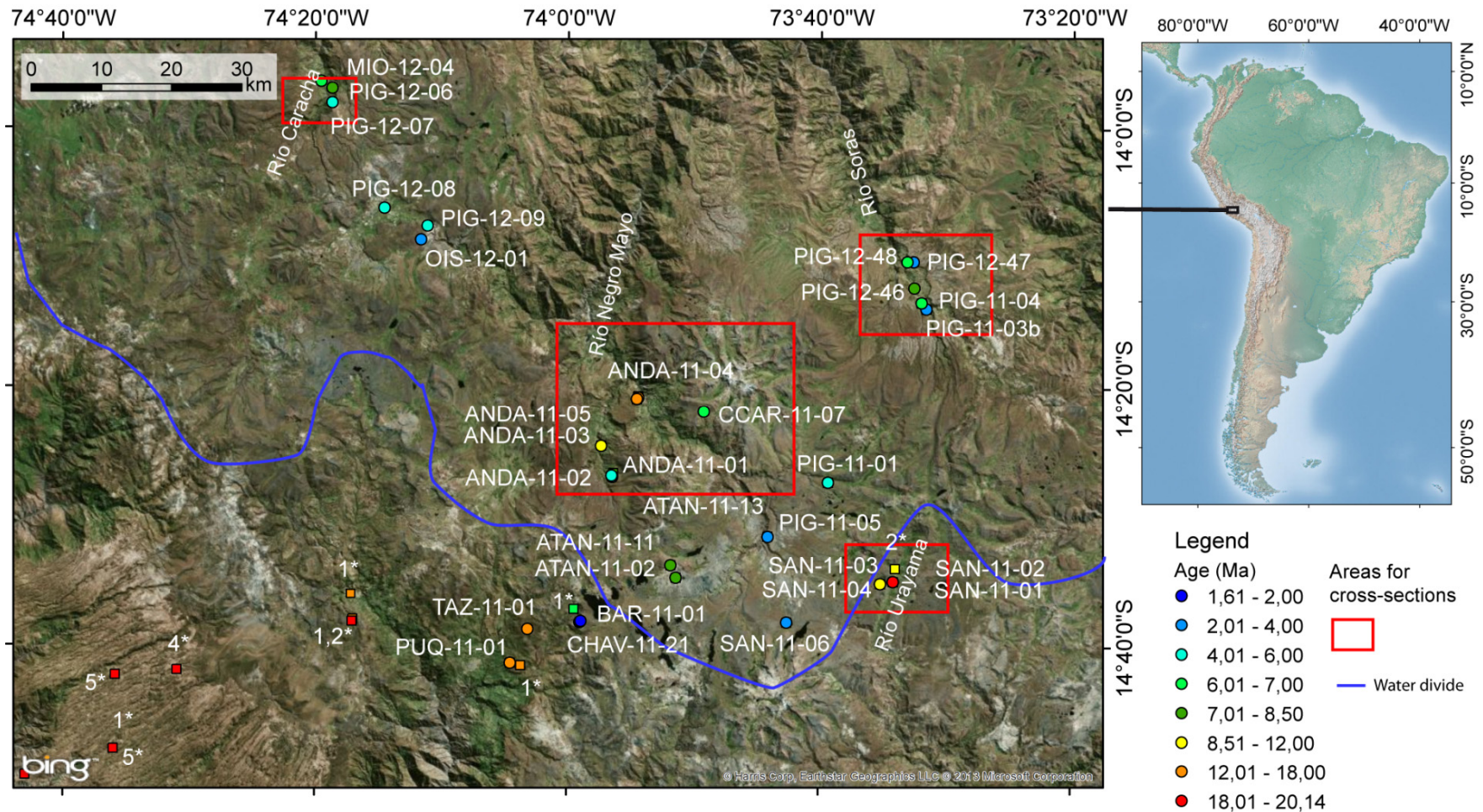


Fig. 1: Sample location map. Note the four river valleys (Areas highlighted in red) that will be discussed in the following. Squares represent samples from literature. 1: Roperch et al. (2011), 2: Bellón & Lefèvre (1977), 4: Thouret et al. (2007).

glass were also identified by their specific Raman spectra. The identified sanidine or plagioclase crystals were then individually picked, cleaned using PE Acetone and air-dried.

Our samples were irradiated together with the 28.201 Ma Fish Canyon Tuff sanidine (FCs) standard (Kuiper et al., 2008) for 4 h at the Oregon State University TRIGA-type reactor in the Cadmium-Lined In-Core Irradiation Tube. At the University of Wisconsin Madison Rare Gas Geochronology Laboratory, plagioclase/sandine were incrementally heated using either a 25 W CO<sub>2</sub> laser or a resistance furnace. For laser experiments, ~40 mg of feldspar was placed in wells and incrementally heated in several steps. Each step was followed by an additional 15 min for gas cleanup. The gas was cleaned during and after the heating period with two SAES C50 getters, one of which was operated at ~450°C and the other at room temperature. Blanks were analyzed after every second laser heating step, and were less than  $4 \times 10^{-17}$ ,  $3 \times 10^{-19}$ ,  $6 \times 10^{-20}$ , and  $2 \times 10^{-19}$  mol for <sup>40</sup>Ar, <sup>39</sup>Ar, <sup>37</sup>Ar, <sup>36</sup>Ar, respectively. Signal to blank ratios for both <sup>40</sup>Ar and <sup>36</sup>Ar varied from ~15 to >200 for each heating step. Ten to twenty mass discrimination measurements via automated analysis of air pipettes were made prior to, and following each incremental heating experiment and encompass the range of <sup>40</sup>Ar observed for the samples. Measured <sup>40</sup>Ar/<sup>36</sup>Ar ratios of atmospheric argon were normalized to <sup>40</sup>Ar/<sup>36</sup>Ar = 295.5 ± 0.5 (Steiger and Jäger, 1977) and the discrimination was calculated using a linear law relationship.

Argon isotope analyses were done using a MAP 215e50, and the isotope data were reduced using ArArCalc software version 2.5 (<http://earthref.org/ArArCALC/>). Ages were calculated from the blank-, discrimination- and decay-corrected Ar isotope data after correction for interfering isotopes produced from potassium and calcium in the nuclear reactor. Analyses of Fe-doped KAlSiO<sub>4</sub> glass following the 2008 refuel of the Oregon State reactor yield (<sup>40</sup>Ar/<sup>39</sup>Ar)<sub>K</sub> = (5.4 ± 1.4) × 10<sup>-4</sup> and (<sup>38</sup>Ar/<sup>39</sup>Ar)<sub>K</sub> = (1.210 ± 0.002) × 10<sup>-2</sup> (Table 1). For the reactions on calcium, we adopt the production ratios of Renne et al. (2013): (<sup>36</sup>Ar/<sup>37</sup>Ar)<sub>Ca</sub> = (2.650 ± 0.022) × 10<sup>-4</sup>; (<sup>38</sup>Ar/<sup>37</sup>Ar)<sub>Ca</sub> = (1.96 ± 0.08) × 10<sup>-5</sup>; (<sup>39</sup>Ar/<sup>37</sup>Ar)<sub>Ca</sub> = (6.95 ± 0.09) × 10<sup>-4</sup>. The age uncertainties reported in Table 1 reflect analytical contributions only at the 2σ level; the decay constants used are those of (Min et al., 2000).

### 2.3 Stratigraphy and DEM analysis

---

Four major valleys (Río Urayama, Río Visca/ Mayobamba, Río Soras and Río Caracha ) were sampled and studied in the field (red squares in Fig. 1).

Cross-sections of these major valleys were derived from ASTER (Advanced Spaceborne Thermal Emission and Reflection Radiometer) digital elevation data in order to illustrate the stratigraphic position of our samples. Data were downloaded from USGS global Data



Explorer and a mosaic for the region of interest was created in ENVI<sup>1</sup>. Profiles were then derived using ArcGIS<sup>2</sup> 3D spatial analyst functions. Sample locations and units observed in the field were projected according to elevation into the profile to establish a geochronological model for the respective location.

Drainage analysis was conducted in RiverTools<sup>3</sup> using a d8 algorithm and imported back into GIS. The continental drainage divide watershed was digitized and surface elevations for Pre-Paleogene rocks were derived using mapped outcrops of old strata and satellite imagery to crop the DEM for visualizing present surface morphology of these rocks with respect to younger strata. This was done in order to better understand the geomorphologic evolution and incision history of the area.

### 3 Results

---

#### 3.1 <sup>40</sup>Ar/<sup>39</sup>Ar Geochronology and Stratigraphy

---

Summarized <sup>40</sup>Ar/<sup>39</sup>Ar results for 31 samples are given in Table 1 - complete data for sanidine and plagioclase incremental heating and total fusion experiments are in the Electronic appendix. One sample (MIO-12-04) gave a discordant spectrum and an age near 7 Ma. According to the available geological maps (INGEMMET, 2001a, b), most of the sampled ignimbrites are mapped as the Pliocene “Formación Andamarca” with no radiometric age data. We will propose a new stratigraphic framework for the area and put it into context with stratigraphies established for areas to the south (Delacour et al., 2007; Lebti, 2006; Noble et al., 1984; Quang, 2005; Roperch et al., 2006; Thouret et al., 2007; Tosdal et al., 1981).

According to the geological map, the Pliocene Andamarca Formation belongs to the Lower Barroso group (Asociación Lagesa, 1996; INGEMMET, 2001a) and is dominated by pyroclastic rocks. The upper Barroso Formation, by contrast, comprises mostly lava flows and volcanic edifices such as the 6.14 ± 0.09 Ma old Cerro Ccarhuarazo (CCAR-11-07) in the study area. Our new data show that such a simple distinction based on lithology (pyroclastic rocks vs. lavas) is an oversimplification and may not be useful for stratigraphic orientation. Some of our samples come from areas mapped as Quaternary fluvio-glacial sediments (e.g. PIG-12-08), and some belong to local volcanic centers like the Pliocene Jello

---

<sup>1</sup> Software package © Excelis company (<http://www.exelisvis.com/>)

<sup>2</sup> Software package © ESRI (<http://www.esri.de/>)

<sup>3</sup> Software package © RiverTools<sub>TM</sub> ([www.rivertools.com](http://www.rivertools.com))

Table 1: Summary <sup>40</sup>Ar/<sup>39</sup>Ar data\*

Incremental heating				K/Ca total	Total Fusion Age (Ma) ±			Isochron Age (Ma) ± 2σ				
Sample #	Sample type	Position in Stratigraphy	Material		2σ	<sup>40</sup> Ar/ <sup>36</sup> Ar <sub>i</sub> ± 2σ	MSWD	6.11	± 0.13			
CCAR-11-07	lava	lava flow Carhuarazo	plagioclase	0.187	6.16	± 0.10	310.19	± 54.96	0.71	6.11	± 0.13	
TAZ-11-01	lava	lava flow	plagioclase	0.023	16.33	± 0.53	300.01	± 12.73	0.18	16.28	± 0.50	
OIS-12-01	dome lava	dome in Santa Ana caldera	matrix	0.106	2.92	± 0.03	270.67	± 26.08	0.53	2.97	± 0.11	
continued:												
Sample #	N	<sup>39</sup> Ar %	MSWD	Plateau Age (Ma) ± 2σ		Location						
						Longitude	Latitude	Elevation				
CCAR-11-07	8 of 8	100	0.65	6.14	± 0.09	-73.82	-14.37	4268				
TAZ-11-01	8 of 8	100	0.23	16.35	± 0.45	-74.05	-14.65	4085				
OIS-12-01	7 of 12	44.29	0.95	2.87	± 0.04	-74.19	-14.14	4070				
Crystal fusion					K/Ca total	N	MSWD	Plateau Age (Ma) ±		Location		
Site	Sample #	Sample type	Position in stratigraphy	Material				2σ	Longitude	Latitude	Elevation	
Urayama valley	SAN-11-06	vitrophyric ig.**	top ignimbrite	sanidine	18.04	18 of 18	1.16	3.85 ± 0.02	-73.71	-14.64	4475	
	SAN-11-04	pumice-rich ig.	below lahar	sanidine	49.71	15 of 15	1.36	6.16 ± 0.04	-73.59	-14.59	4400	
	SAN-11-03	pumice-rich ig.	above SAN-11-02	sanidine	34.31	14 of 15	0.85	9.14 ± 0.08	-73.59	-14.59	4355	
	SAN-11-02	massive, welded ig.	below SAN-11-03	sanidine	41.08	15 of 15	0.87	9.05 ± 0.04	-73.57	-14.58	4348	
	SAN-11-01	pumice flow	lowermost ignimbrite	plagioclase	0.12	15 of 15	0.40	20.14 ± 0.11	-73.57	-14.58	4261	
Sorras valley	PIG-12-47	grey massive ig.	top ignimbrite	sanidine	8.280	15 of 15	0.81	3.85 ± 0.03	-73.54	-14.17	3652	
	PIG-11-03	grey non-welded ig.	top ignimbrite	sanidine	14.95	16 of 16	0.76	3.83 ± 0.03	-73.53	-14.23	3637	
	PIG-12-46	white bulk ig.	one of middle ig. sheets	sanidine	23.585	12 of 13	0.97	6.19 ± 0.03	-73.55	-14.17	3600	
	PIG-11-04	pumice sample	one of middle ig. sheets	sanidine	49.71	15 of 15	1.36	6.16 ± 0.04	-73.59	-14.59	3457	
	PIG-12-48	white bulk ig.	base ignimbrite	plagioclase	0.095	12 of 12	0.48	7.83 ± 0.08	-73.54	-14.20	3310	
Visca/Mayob. valley	ANDA-11-02	brown massive ig.	topmost ig.	sanidine	17.20	16 of 16	0.80	3.86 ± 0.03	-73.94	-14.45	4055	
	ANDA-11-01	pumice sample	pumice below ANDA-11-02	plagioclase	0.170	10 of 10	0.92	5.61 ± 0.06	-73.94	-14.45	4020	
	ANDA-11-03	white non-welded ig.	one of middle ig. sheets	sanidine	48.1	13 of 13	0.42	9.43 ± 0.07	-73.96	-14.41	3518	
	ANDA-11-04	pumice sample	one of middle ig. sheets	plagioclase	0.18	7 of 10	1.19	9.51 ± 0.10	-73.91	-14.35	3664	
	ANDA-11-05	white pumice-rich ig.	one of base ig. sheets	sanidine	44.31	14 of 16	0.54	13.99 ± 0.04	-73.91	-14.35	3600	
	ANDA-11-06	redish non-welded ig.	base ig.	sanidine	26.2	18 of 18	0.82	14.09 ± 0.05	-73.91	-14.35	3364	
Caracha valley	PIG-12-07	vitrophyr	top ig., outflow Santa Ana	plagioclase	0.168	10 of 10	0.45	5.96 ± 0.08	-74.31	-13.97	3800	
	MIO-12-04	lava flow	one of ca. 3 flows	plagioclase				ca. 7	-74.33	-13.94	3677	
	PIG-12-06	redish bulk ig.	top of lowermost ig.	plagioclase	0.073	9 of 12	1.19	8.39 ± 0.10	-74.31	-13.95	3500	
Santa Ana	PIG-12-09	white tuff	intra-caldera tuff	plagioclase	0.041	12 of 12	1.19	5.42 ± 0.26	-74.19	-14.13	4001	
	PIG-12-08	tuff/pumice	intra-caldera	plagioclase	0.084	11 of 12	0.93	5.51 ± 0.19	-74.24	-14.10	4030	
	PIG-12-07	vitrophyr	base of ig., outflow/top Caracha	plagioclase	0.168	10 of 10	0.45	5.96 ± 0.08	-74.31	-13.97	3800	
Lomada Atansa	ATAN-11-02	white non-welded ig.		sanidine	4.26	10 of 12	0.68	7.94 ± 0.09	-73.86	-14.58	4409	
	ATAN-11-11	white non-welded ig.		sanidine	3.81	19 of 19	1.55	8.25 ± 0.04	-73.86	-14.58	4400	
	ATAN-11-13	lava sample		plagioclase	0.05	8 of 8	0.97	8.07 ± 0.16	-73.86	-14.56	4560	
other	PIG-11-05	grey massive ig.	top of valley east of Lomada Atansa	sanidine	16.84	10 of 13	0.89	3.80 ± 0.04	-73.74	-14.53	4324	
	BAR-11-01	lava sample		plagioclase	0.07	13 of 13	1.34	6.34 ± 0.13	-73.98	-14.64	4358	
	CHAV-11-21	pumice sample		plagioclase	0.18	10 of 10	7.40	1.61 ± 0.26	-73.98	-14.64	4325	
	PIG-11-01	vitrophyric ig.	S-W from Carhuarazo, top ig.	sanidine	76.69	6 of 10	1.16	5.96 ± 0.11	-73.66	-14.46	4384	
	PUQ-11-11	massive grey ig.	Puquio ignimbrite	plagioclase	0.33	8 of 8	0.65	13.06 ± 0.07	-74.08	-14.69	3706	

All ages are relative to 28.201 Ma for the Fish Canyon sanidine standard (Kuiper et al., 2008) using Min et al. (2000) decay constant. \* Sample details as electronic appendix (GIS database & additional master table in excel format).\*\* ig. =ignimbrite

Jaso volcanic center (OIS-12-01) or the Pliocene Yactocinco formation (PIG-12-47, PIG-12-46). In the following will present four cross-sections through major river valleys (Río Negromayo, Río Soras, Río Urayuma and Río Caracha) with dated samples projected into the profile.

The valleys were selected for accessibility, an abundance of ignimbrites in stratigraphic sections and an exposed basement to constrain the age of the valleys as well as the age of the oldest ignimbrites in the region.

### 3.1.1 Urayama valley

---

Access to the Río Urayuma valley is via the main road between Puquio and Abancay. It is an ideal location for sampling most major ignimbrite sheets contained within the Andamarca Formation and is the only section located to the west of the drainage divide. A map and a stratigraphic model are shown in Fig. 2. The bottom of the valley comprises terrestrial sediments derived from older underlying intrusive rocks. The oldest pyroclastic deposit overlying this “basement” is a  $20.14 \pm 0.11$  Ma pumice flow. This age corresponds to the Nazca ignimbrites (K-Ar ages from Bellón (1977): 21.6 Ma, Noble et al (1979):  $20.5 \pm 0.6$  Ma, to  $23.3 \pm 0.7$  Ma; Ar-Ar ages from: Thouret et al. (2007):  $22.16 \pm 0.34$  Ma to  $24.43 \pm 0.17$  Ma) forming significant part of the western escarpment of the Andes in the region. Covering this ignimbrite are layers of ash, reworked tephra and another, brown and massive ignimbrite with an age of  $9.04 \pm 0.04$  Ma (SAN-11-02). Between these two sheets, 10 Ma of erosion and sedimentation are represented by approximately 50 m of reworked tephra and sediments (Figs 2 and 3). The 9 Ma eruption produced a pumice-rich pyroclastic flow (SAN-11-03) that stratigraphically overlies SAN-11-02. Another period of sedimentation, erosion and volcanism with lahars is recorded in the stratigraphy. At  $6.16 \pm 0.04$  Ma, SAN-11-04, a pumice-rich ignimbrite erupted, probably regionally related to adjacent volcanic centers. The youngest ignimbrite underlying glacial till, is a  $3.85 \pm 0.02$  Ma old pyroclastic flow with a thickness of around 1 to 3 m that forms a low angle shield of the Pampa Huamanpirca plateau. This ignimbrite is conspicuous because it is entirely composed of densely welded pumices and ash, forming thin black vitrophyr sheets. Similar ignimbrites of similar age and of similar texture are found throughout the region.

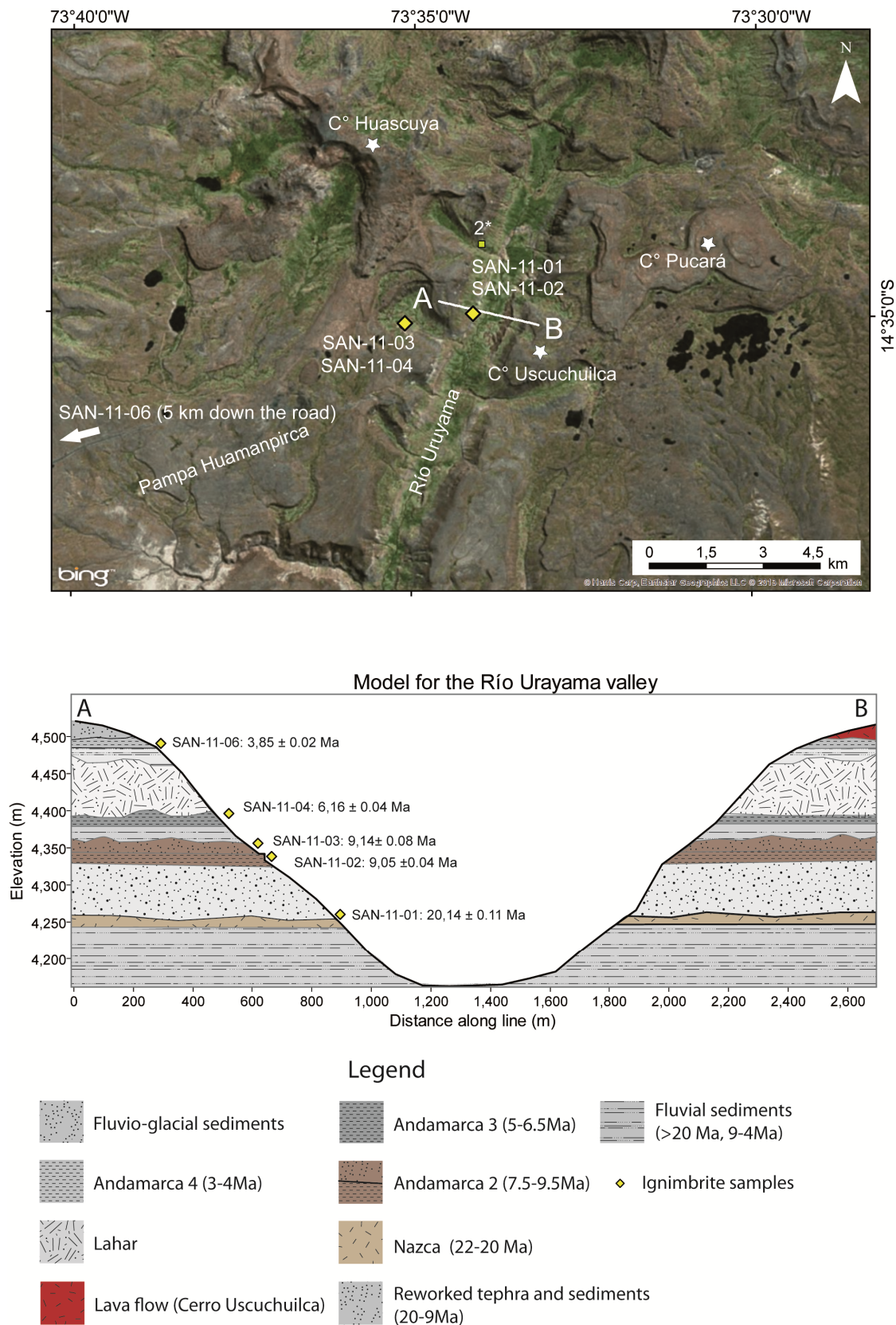


Fig. 2: Map showing a cross-section through the Río Uruyama valley. Elevation data derived from ASTER global DEM. Samples and stratigraphy are projected schematically, according to elevation, into the profile to serve as a chronological model. \*: Samples from Bellón & Lefèvre (1977): K-Ar ages of 8.3 Ma and 9.2 Ma on wholerock and biotite respectively. Vertical exaggeration (z) ~ 2.4.

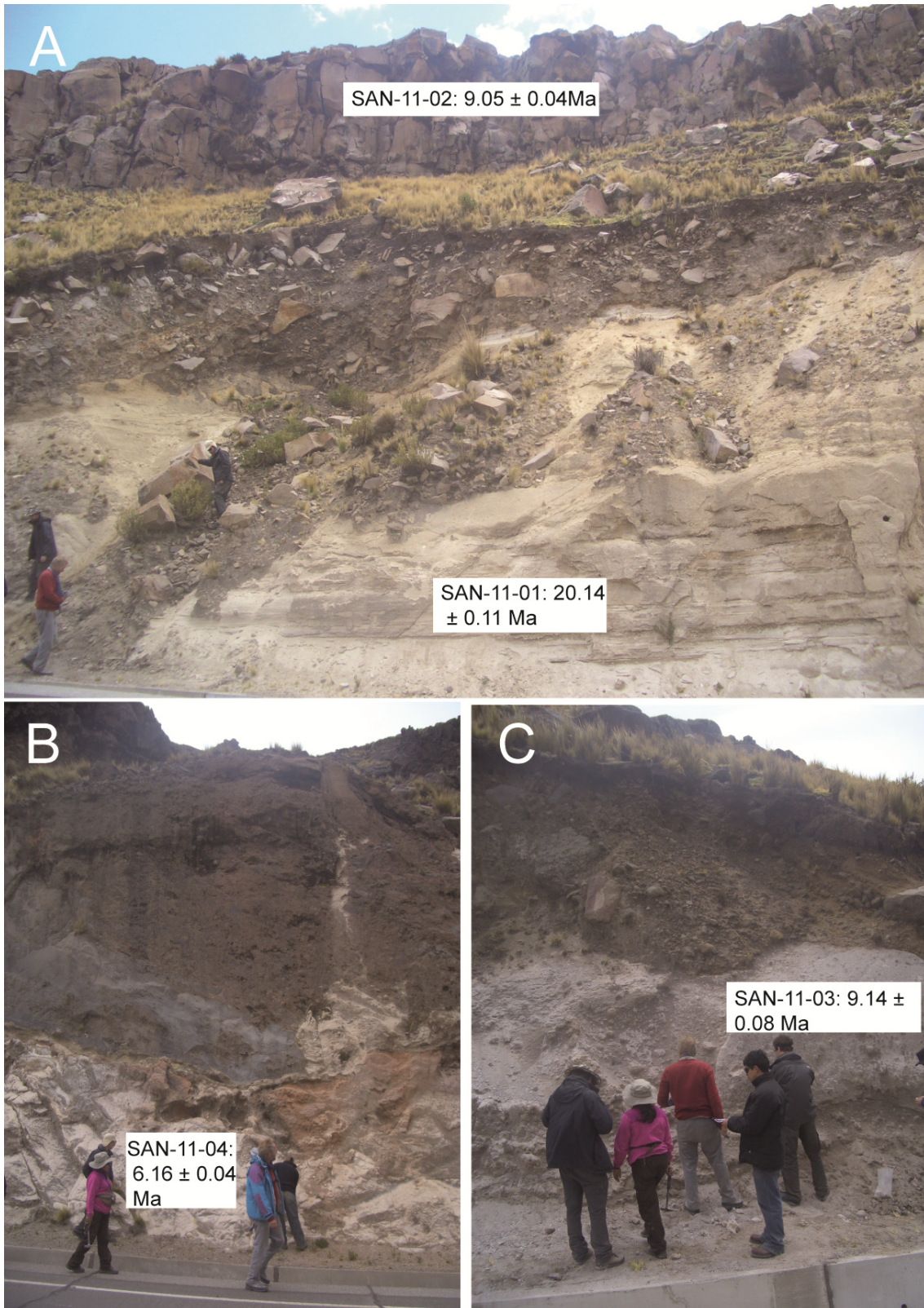


Fig. 3: Photographs showing the different ignimbrite units sampled along the Río Urayama valley. A: Lowermost units of  $20.14 \pm 0.11$  Ma and  $9.04 \pm 0.04$  Ma. Note that SAN-11-01 was taken from a thin (20 cm) pumice flow between the two sediment layers. B: Contact of the lahar with the  $6.16 \pm 0.04$  Ma pumice flow; C: Upper part of the  $9.18 \pm 0.08$  Ma ignimbrite.

### 3.1.2 Río Soras valley

The Río Soras valley is located in the northeast of the study area. We took five samples from the base, middle section and top of the valley. Sample locations and a chronological model are shown in Figs. 4 and 5.

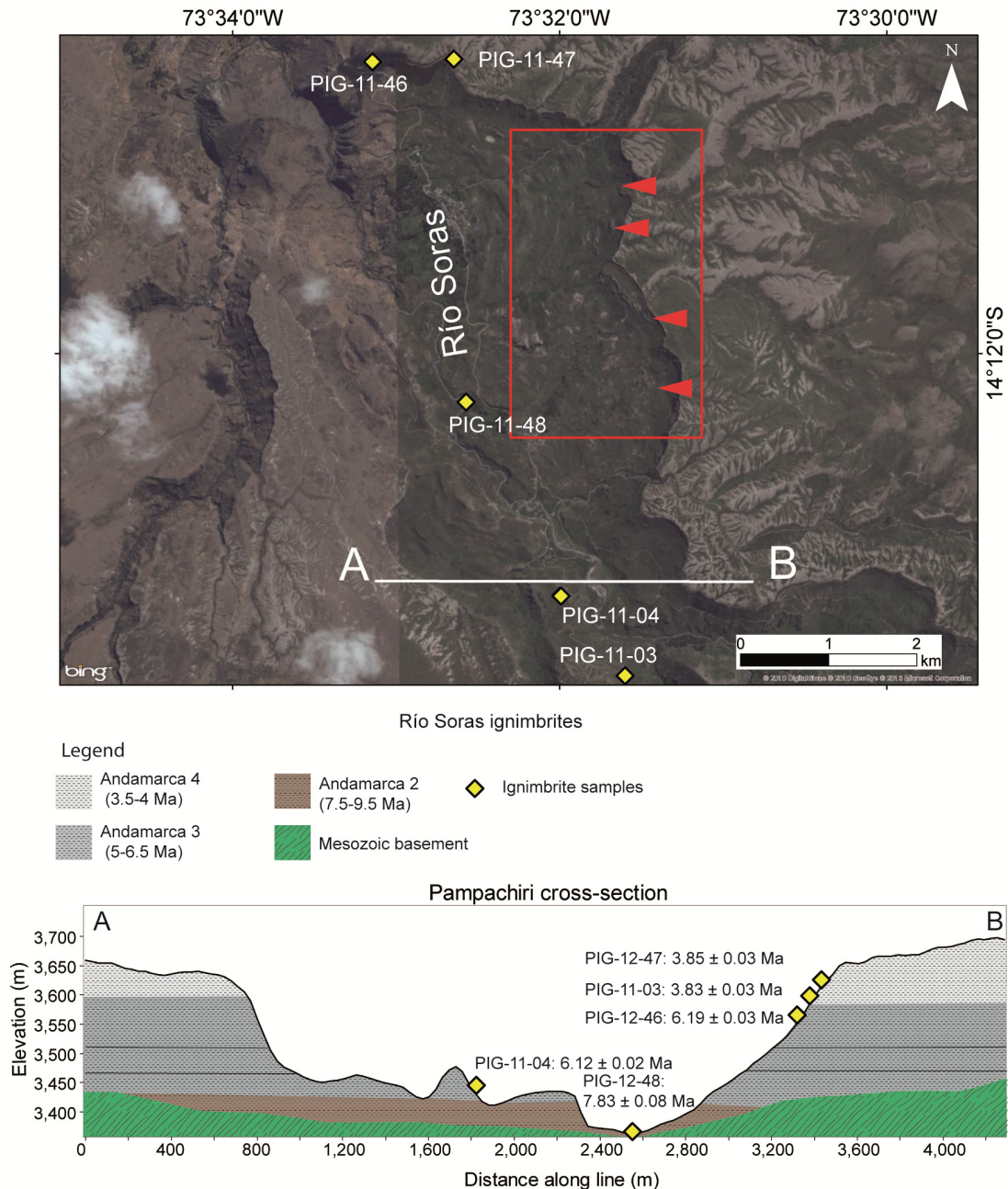


Fig. 4: Sample and profile location map and geochronological model for the Río Soras valley. Samples and stratigraphy are projected schematically, according to elevation, into the profile to serve as a chronological model. The top ignimbrite was dated at  $3.85 \pm 0.03$  Ma and the pumice-rich ignimbrite at the valley floor at  $7.83 \pm 0.08$  Ma. The age of the middle section is around 6.1 Ma. The apparent discrepancy in ages (PIG-11-04 and PIG-12-46) is likely due to long-distance projection into the plane of the section. Red square and arrows show an area of landslides. PIG-11-04 however, is not part of a landslide, but part of the topography still not eroded away by the river. Vertical exaggeration (z) is  $\sim 2.6$ .

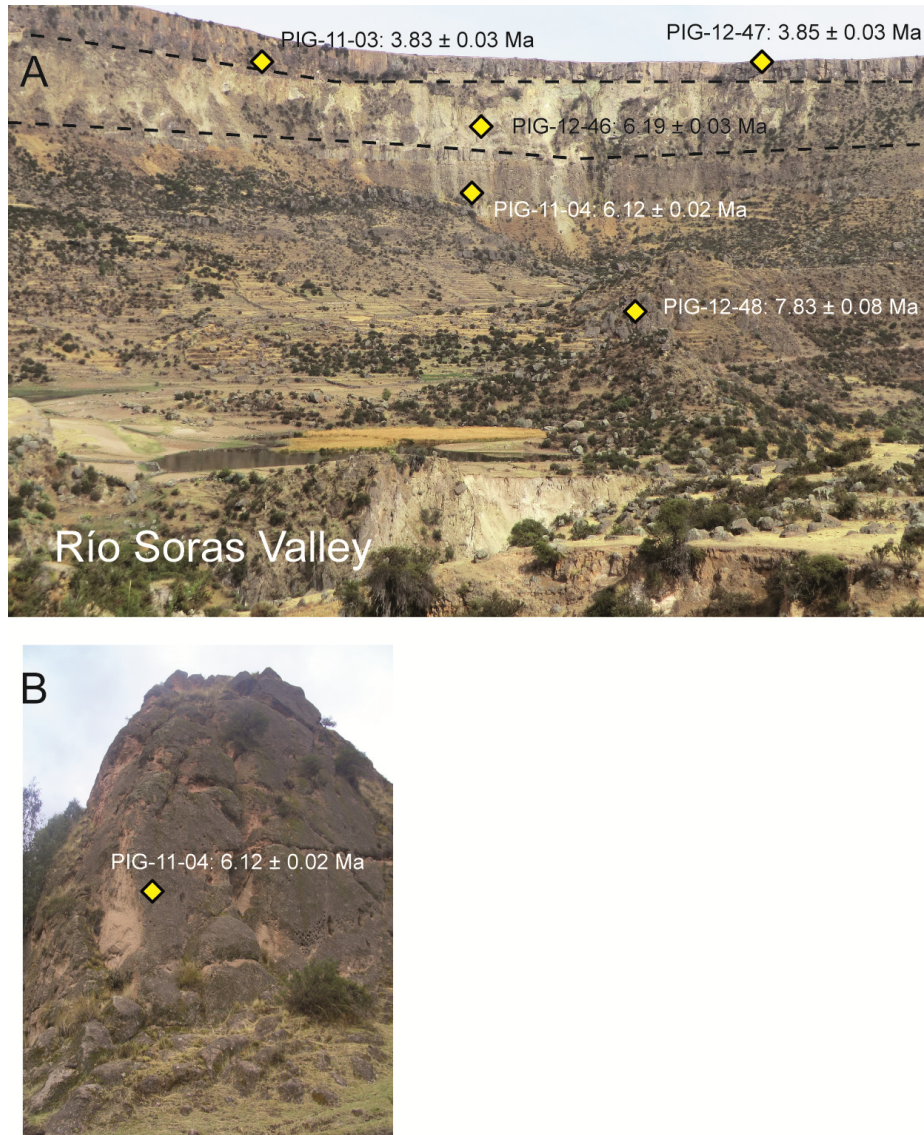


Fig. 5: A: View into the Río Soras Valley. The mesa-forming top ignimbrite was dated at 3.8 Ma. The middle ignimbrite sheets represent the Andamarca 3 ignimbrites. The oldest ignimbrite covers the Mesozoic basement and has an age of 7.83 Ma (Andamarca 2) B: Close-up of the pumice-rich Andamarca 3 ignimbrite. In A, samples are, for illustrational purpose, shown in the units they belong to, not the exact location they were taken.

We dated the massive plateau-forming, top ignimbrite at  $3.85 \pm 0.03$  Ma. The middle ignimbrite is a rose to white colored, pumice-rich unit (PIG-11-04, PIG-12-46) that gave ages of  $6.12 \pm 0.02$  and  $6.19 \pm 0.03$  Ma, respectively. The lowermost, whitish, pumice-bearing ignimbrite (PIG-12-48) overlies Mesozoic quartzite and has an age of  $7.8 \pm 0.08$  Ma.

### 3.1.3 Río Visca/Mayobamba valley

---

Three cross-sections of the Río Visca and Mayobamba valley (in the following we will refer to this valley as Visca valley) are shown in Fig. 6. On the basis of our new age data, we recognize four ignimbrites within these valleys: a 14 Ma ignimbrite (ANDA-11-05:  $13.99 \pm 0.04$  Ma, ANDA-11-06:  $14.09 \pm 0.05$  Ma), recognized as plateau-forming “Huaylillas ignimbrite” in Southern Peru (Thouret et al., 2007), commonly covering the old, Mesozoic landscape or terrestrial sediments derived thereof (Figs. 6 and 7). A second ignimbrite (Andamarca 2) has an age of 9 Ma. (ANDA-11-04:  $9.51 \pm 0.10$  Ma) and covers the older ignimbrites.

Between 6.5 and 5 Ma, lava flows (Cerro Ccarhuarazo: CCAR-11-07:  $6.11 \pm 0.13$  Ma) and local pyroclastic flows (ANDA-11-01 pumice sample:  $5.61 \pm 0.06$  Ma) followed. Finally, a  $3.86 \pm 0.03$  Ma thin, vitrophyric ignimbrite forms the uppermost lid and the mesas adjacent to the valley (Andamarca 4). This age was also found in surrounding areas for similar (vitrophyric) ignimbrite sheets (e.g. PIG-11-05, SAN-11-06, PIG-12-47). However, from their distribution, the mesa- and plateau-forming ignimbrites cannot possibly belong to a single sheet. They are observed in regional basins, separated by ridges and edifices of older volcanics. Therefore, they could represent a series of eruptions from different centers of very similar age and style.



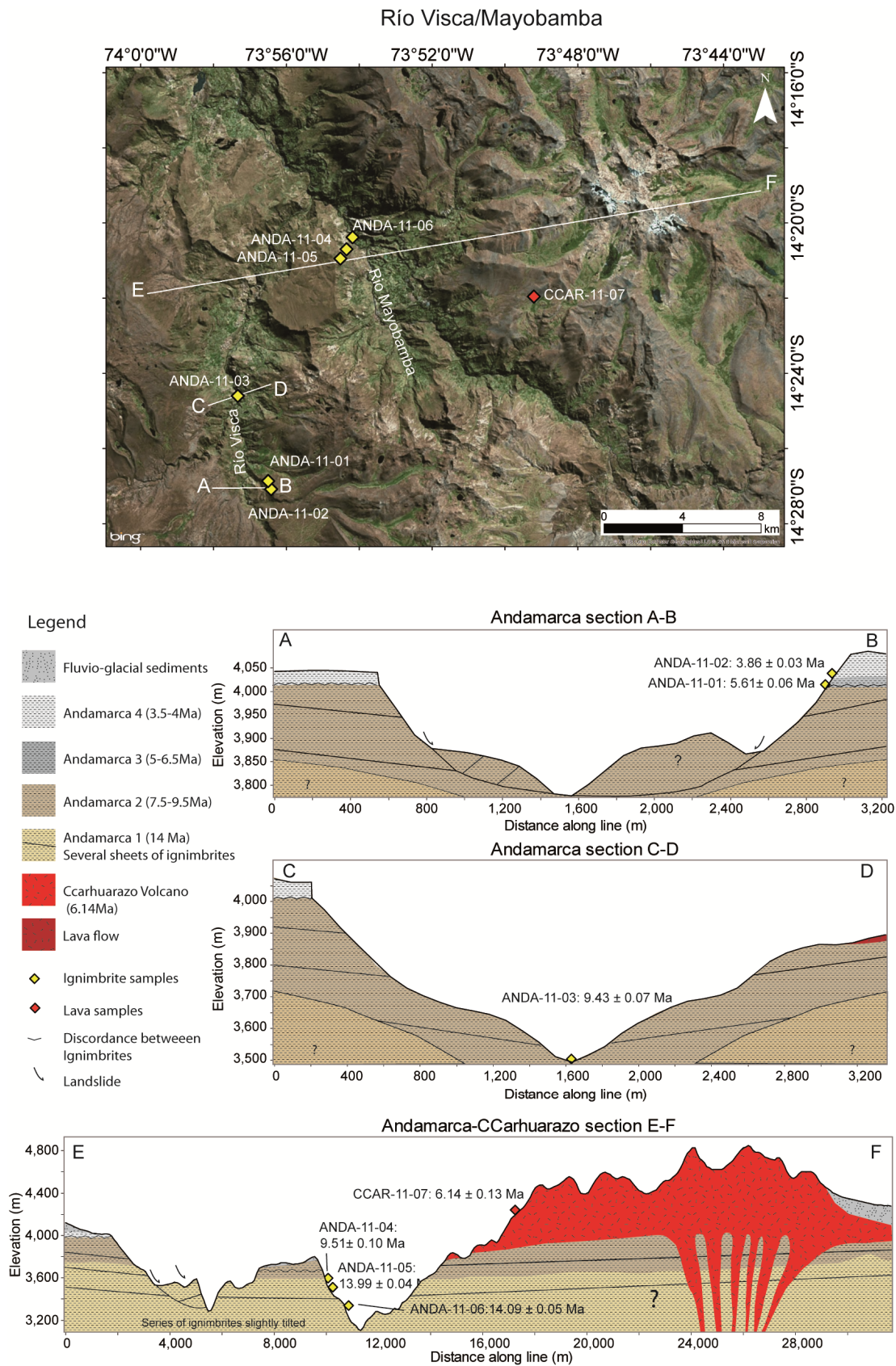


Fig.6: Map showing the three cross-sections through the Río Visca and Mayobamba valleys. Elevation data derived from ASTER global DEM. Samples and stratigraphy are projected schematically, according to elevation, into the profile to serve as a chronological model. Vertical exaggeration (z): A-B: ~2.5; C-D: ~1.6; E-F: ~4.3.

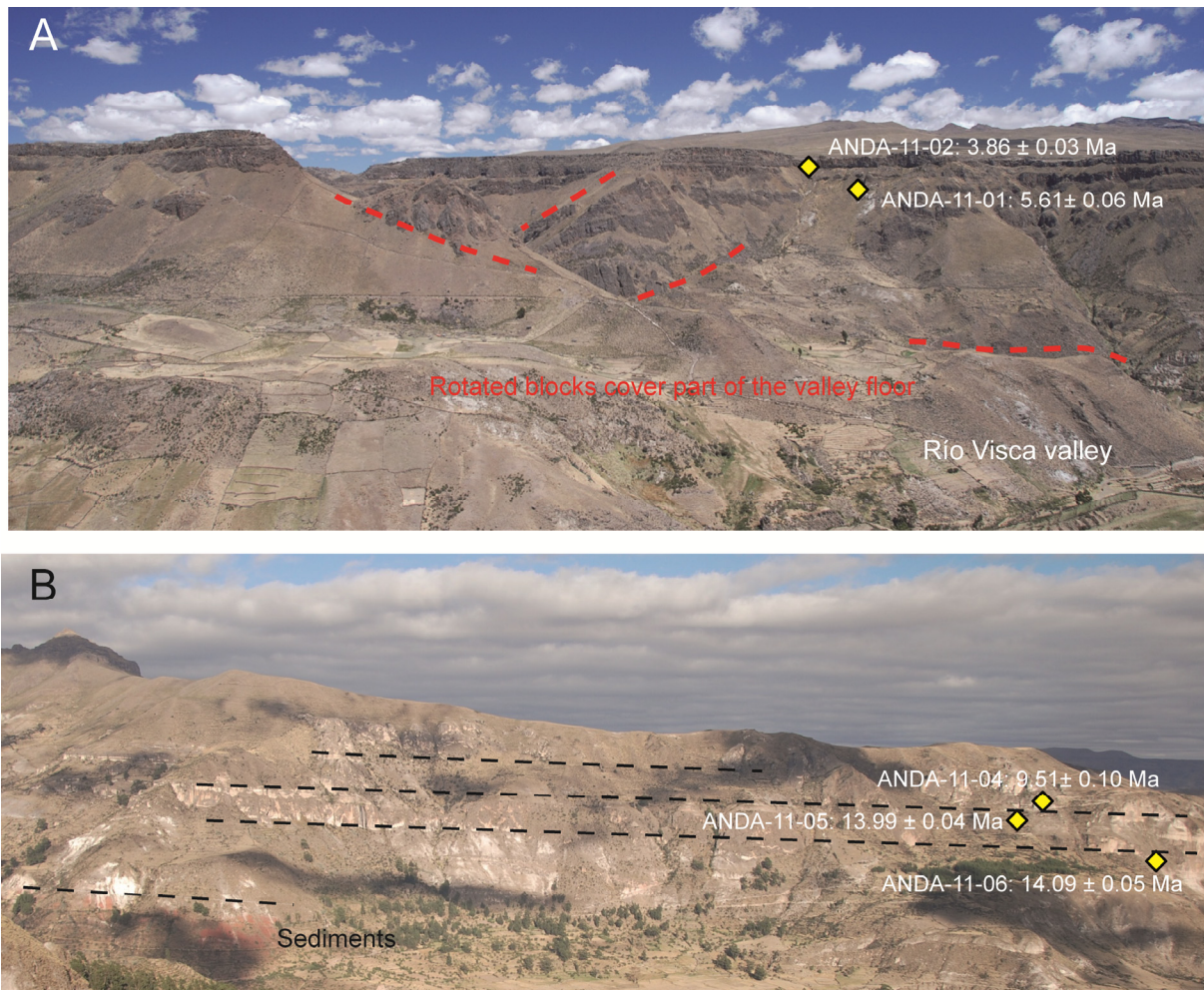


Fig.7: A: View of the Río Visca valley (view to east). Samples were taken from the opposite valley flank. The vitrophyric, 3.8 Ma top ignimbrite forms a mesa and the pumice flow (5.6 Ma) can be distinguished just below. The valley bottom is covered with large fractured and rotated slide blocks that collapsed from the valley walls B: View from Ccarhuarazo toward the east into the Río Mayobamba valley. Above sediments, our sample locations are shown. Several ignimbrite sheets erupted at 14 Ma and formed an ignimbrite plateau.

### 3.1.4 Río Caracha valley

The valley of the Río Caracha is located in the northwest of the study area. It is deeply incised into tilted Mesozoic quartzites covered by volcanoclastic sediments that occur below and are intercalated with a series of ignimbrites and lava flows (Figs. 8 and 9). In the satellite imagery, huge landslides from the valley sides into the valley can be observed (red arrows in Fig. 9) and make the interpretation of stratigraphic positions more difficult.

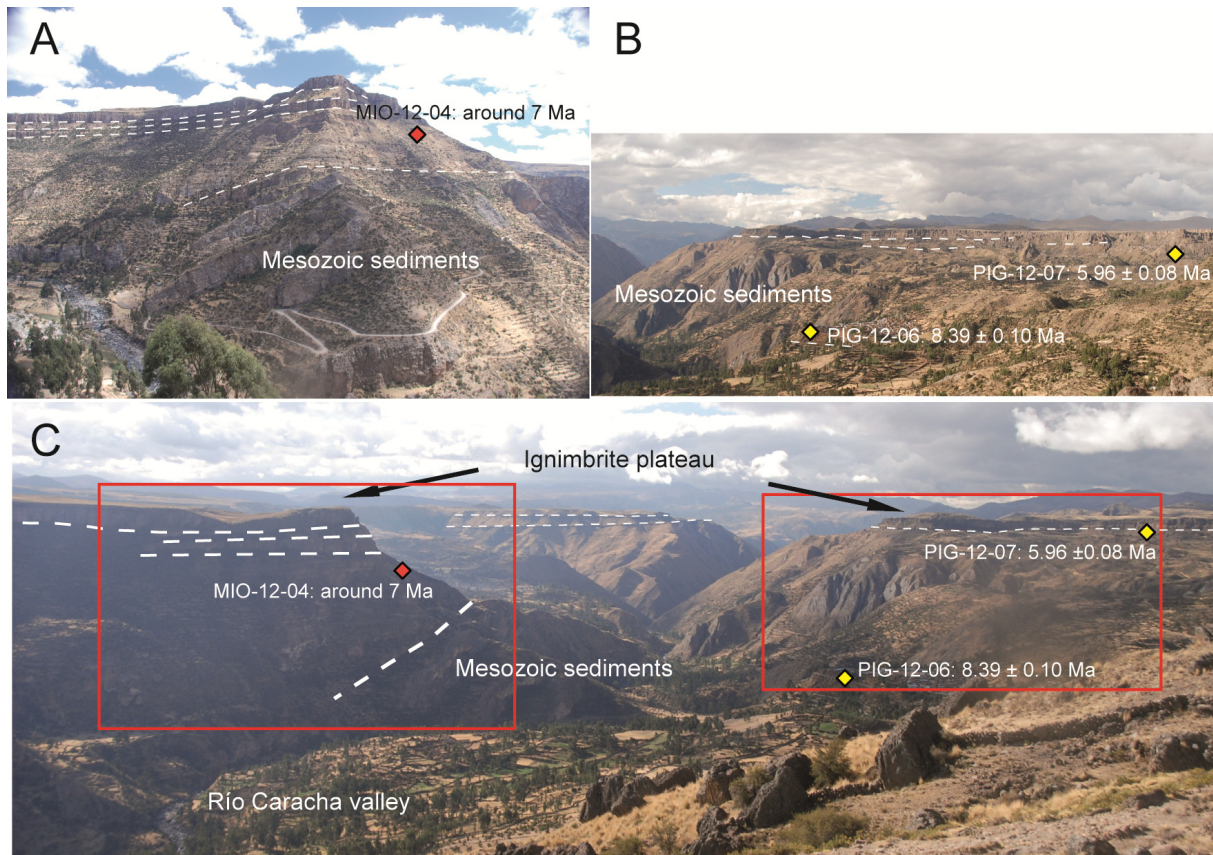


Fig.8: Photographs from the Río Caracha Valley. A and B are close-ups from both valley-flanks (red squares in C). The oldest ignimbrite overlying the Mesozoic sediments has an age of  $8.39 \pm 0.10$  Ma. A series of ignimbrites and lava flows (MIO-12-04) form the middle part of the profile. The youngest ignimbrite (PIG-12-07) has an age of  $5.96 \pm 0.08$  Ma and forms the plateau shown in C.

A cross-section of this valley is shown in Fig. 9. We dated the non-welded, pumice-rich ignimbrite (PIG-12-06) that directly overlies the deeply incised older basement of tilted, Mesozoic sediments at  $8.39 \pm 0.10$  Ma. A sequence of volcanoclastic sediments and a second sheet of ignimbrite cover the basal ignimbrite, together with at least three lava flows (MIO-12-04). The top series of ignimbrites consists of several distinct sheets. Our samples from this series are from both sides of the valley. Dating a sample from the top series on the northern valley rim above the lava section did not give a reliable age due to its high xenocryst content. PIG-12-07, a vitrophyric ignimbrite from the top of the southern side of the valley gave a reliable sanidine age of  $5.69 \pm 0.08$  Ma.

Río Caracha ignimbrites

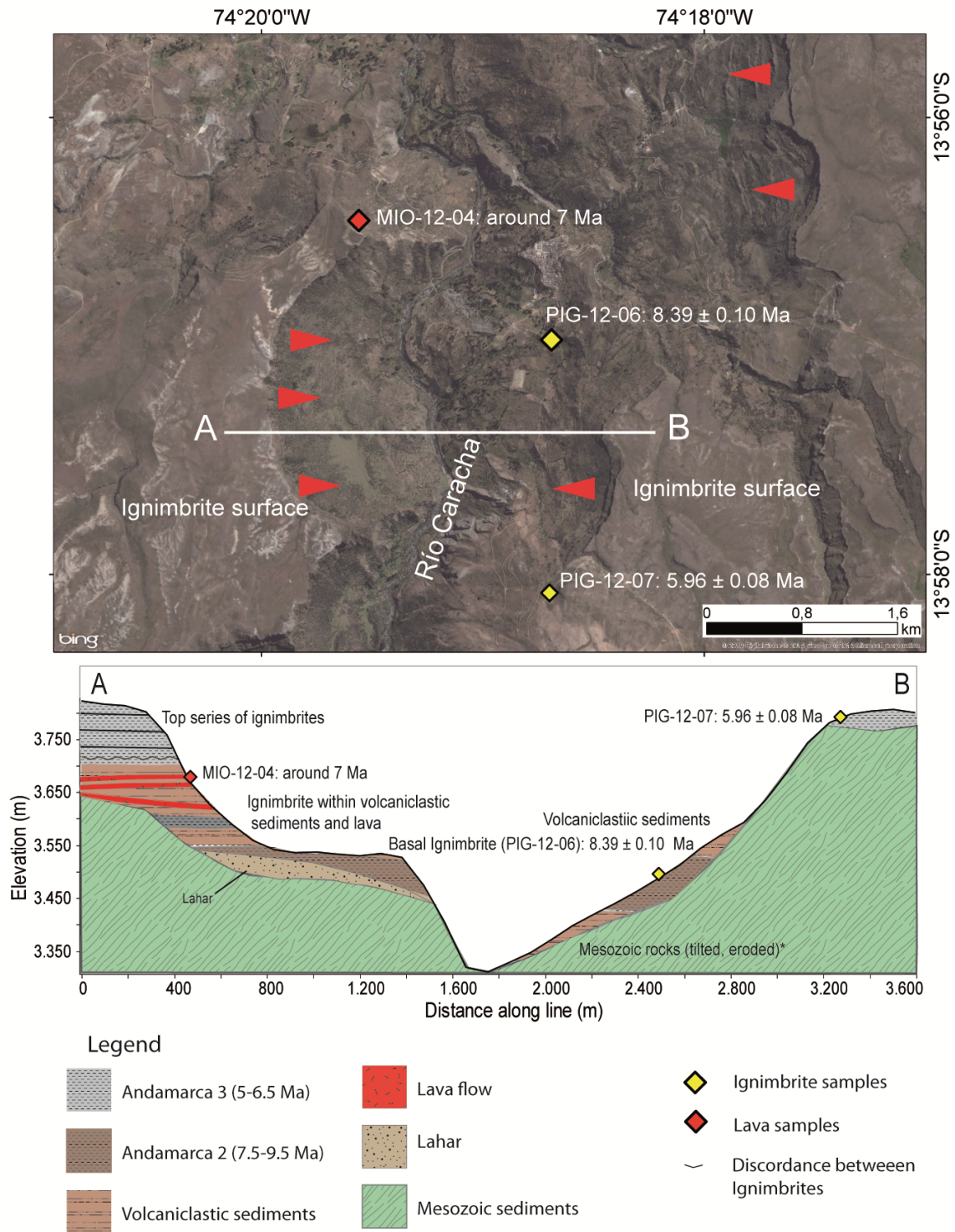


Fig.9: Map showing the three cross-sections through the Río Caracha valley. Elevation data is derived from ASTER global DEM. The section shows a geochronological model for the magmatic history of the area. Red arrows indicate landslides. Vertical exaggeration (z) is ~2.

### 3.1.5 Santa Ana Caldera

---

Further to the southeast of the Río Caracha valley, we sampled air fall pumices from the margin of a circular structure that we interpret to be the source caldera for the youngest Caracha Ignimbrites. We are able to trace the top ignimbrites from the southern margin of the Caracha valley to the proposed caldera (Fig. 10) and found the same age range of approximately 5.4-5.9 Ma for the intra-caldera fill and the outflow sheet. Only the dome that marks the center of the caldera (OIS-12-01) gives a much younger age of  $2.87 \pm 0.04$  Ma. Fig. 10 shows sample locations and a model for the “Santa Ana Caldera” based on field observations, dated samples and results from drainage analysis.

This caldera has not been previously described and the central dome and lava flows in vicinity of the caldera are described as “Centro volcánico Jello Jasa” on geological maps. The pyroclastic units are mapped as “Fm. Castrovirrena”. Several observations argue for the existence of a caldera: The area around the dome (Fig. 10) is completely filled with pyroclastics that are deeply incised by the river (also shown in Fig. 10). We interpret this unit as intra-caldera ignimbrite. The same age was found for a thin, partly vitrophyric ignimbrite (PIG-12-07) that can be traced to the Río Caracha valley and forms the topmost ignimbrite there. The age and distribution of this ignimbrite indicate that it is related to the air fall unit within our proposed caldera. Furthermore, DEM analysis and interpretation of the satellite imagery argue for the structure being a caldera with a diameter of around 20 by 13 km. The overall morphology argues for a nested caldera, including the lava flows and valley on the western side. We cannot identify a comparable intra-caldera ignimbrite in the western valley and the nature of the morphology remains speculative. Detailed mapping is needed to further clarify the nature of this eruptive center.

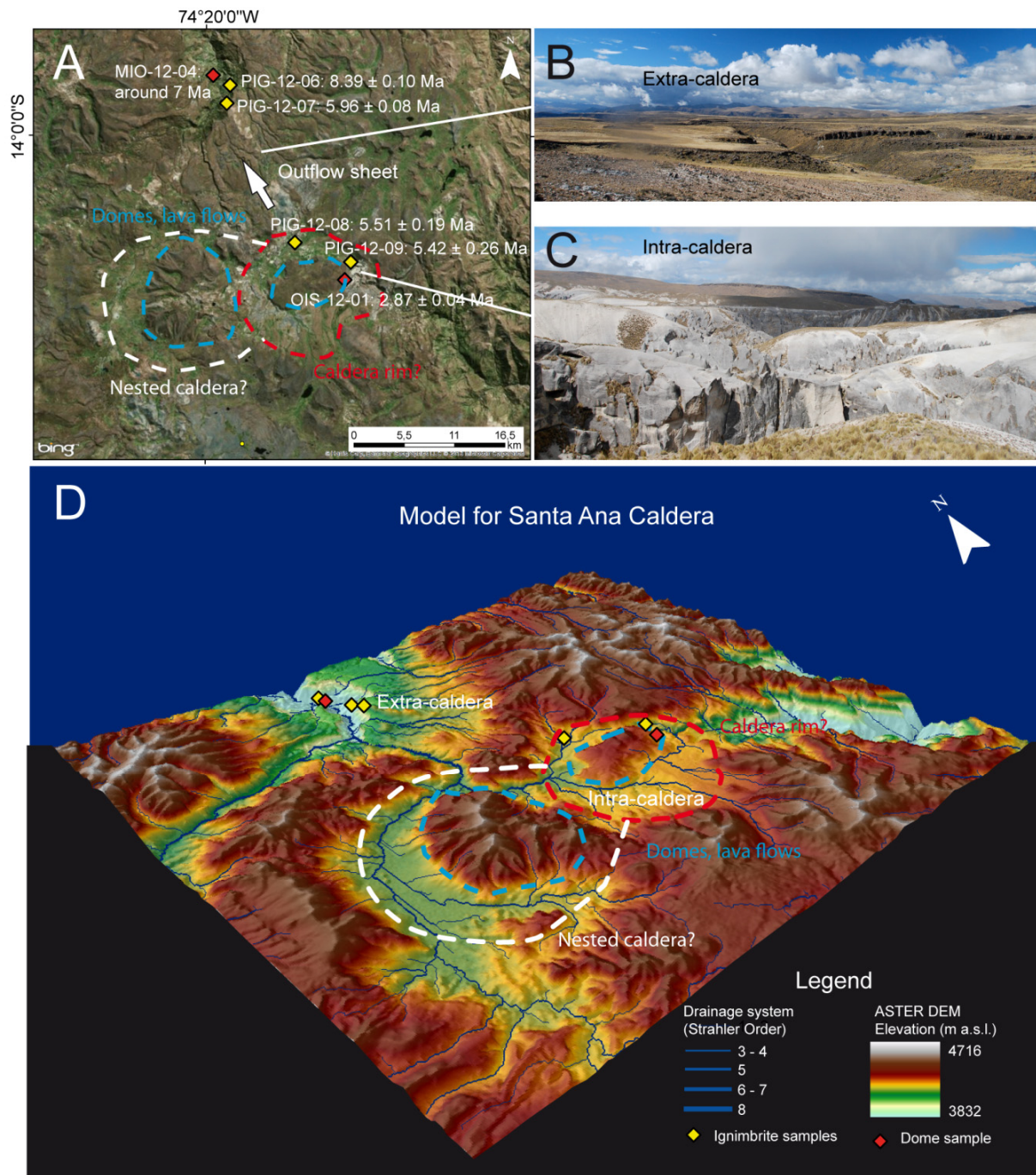


Fig.10: Model for a proposed "Santa Ana Caldera" as a source for the Río Caracha ignimbrites. A: Map of the area with sample locations. B: View of the outflow sheets. C: Caldera-filling ignimbrites. D: ASTER DEM model. z=2. Drainage network obtained with RiverToolsTM. Caldera outline (dashed red line) is based on field observations, interpretation of satellite imagery and DEM analysis. Note almost radial drainage network around the central dome. The morphology even suggests a nested caldera (white dashed line). For further information, please refer to the text.

## 3.2 Ignimbrite distribution, timing and implications for uplift, erosion and geomorphologic evolution

---

### 3.2.1 General considerations

---

Uplift that produces topographic gradients results in increased erosion and orographic barriers that change precipitation patterns. With their North-South orientation, the Andes are a special case of climate-modifier with an arid to hyper-arid climate along the Pacific coast and a humid climate in the Amazon region.

The uplift history of the Andes is still a controversial topic (e.g. Ehlers and Poulsen, 2009; Ghosh et al., 2006; Gregory-Wodzicki, 2000; Hartley, 2003; Lamb and Davis, 2003; Mulch et al., 2010; Thouret et al., 2007 to name but a few).

As Gregory-Wodzicki (2000) stresses, the Andes are not a single entity and timing of uplift is not constant but very likely changes from north to south and east to west. Furthermore, paleoelevation estimates from different methods all have uncertainties and errors as discussed in detail by Gregory-Wodzicki (2000). Indicators for paleoelevations used range from crustal deformation, marine facies, geochemistry of volcanic rocks, climate from fossil floras, erosion rates, erosion surfaces, fission-track ages to rates or terrigenous flux and were reviewed by Gregory-Wodzicki (2000). All methods are based on certain assumptions and data should be interpreted with care. For example, estimates derived from stable isotope ratios in precipitation could be affected due to the rise of the Andean Plateau causing changes in parameters like temperature, vapor source and precipitation (Ehlers and Poulsen, 2009). However, understanding the development of the Central Andean plateau (as defined by Allmendinger et al., (1997) is crucial to evolutionary models of Andean geodynamics and climate patterns (Schildgen et al., 2007). It is currently accepted, that Eocene deformation of the Central Andes (Incaic deformation) affected the Western Cordillera, some local regions of the foreland basins (Jordan et al., 1997; Lamb and Hoke, 1997; Sempere et al., 1997) and then shifted to the east. Compression in the Altiplano-Eastern Cordillera started in the Oligocene (between 25 and 29 Ma) and continued until 10-6 Ma (Allmendinger et al., 1997; Jordan et al., 1997; Lamb and Hoke, 1997; Sempere et al., 1990) and the foreland east of the Subandean area. Deformation in the Subandean zone and the foreland basin started around 10-6 Ma. Compression, unlike traditionally thought (e.g. Mégarid, 1984; Sébrier et al., 1988), was probably rather continuous, creating a fold-thrust belt and foreland-basin system that migrated eastward (e.g. Gregory-Wodzicki, 2000; Jordan et al., 1983; Jordan et al., 1997; Sempere et al., 1997).

In Southern Peru, Thouret et al. (2007) found valley incision of the Cotahuasi and Ocoña canyons starting at around 9 Ma, which they interpreted to have been caused by continued uplift since 13 Ma. Re-incision after 3.8 Ma could not be directly related to an increase in uplift rate (Thouret et al., 2007). It might also be linked to a significant climate change to hyperaridity in the Atacama desert (4-3 Ma) that was probably related to global climate cooling, supported by intensified upwelling of the Humboldt Current generated by the closure of the Central American Seaway (Hartley, 2003). Evidence for the glaciation of parts of Southern Peru was presented in detail by (Forbiger, 2008).

With our new chronological data and DEM analysis, we put some new constraints on the geomorphologic evolution of Southern Peru.

### 3.2.2 Timing and extent of ignimbrites

---

Fig. 11 shows the extent of our newly dated ignimbrites and proposed caldera locations. Fig. 12 shows stratigraphic sections from the western margin of the Central Andes here (Thouret et al., 2007) and references herein) together with our own results from the east of the present major drainage divide between the Atlantic and Pacific Oceans.

In general, ages of ignimbrites range from 20 Ma covering the Pre-Paleogene basement to 3.8 Ma. The 24-20 Ma age of the Nazca ignimbrites are restricted to the western escarpment and western part of the study area (Fig. 11). At around 13-14 Ma, another major phase of ignimbrite volcanism occurred, producing the Puquio and Andamarca 1 ignimbrites. Between 7.8 to 9.5 Ma, ignimbrite eruptions filled all valleys considered in this study. In the Soras and Caracha valleys, they cover the Mesozoic basement, in the Visca valley, they overly the 14 Ma old ignimbrite sheets.

The 3 to 5 Ma (Andamarca 3, 4) ignimbrites cover large parts of the study area. Due to the glacial history of the region (Forbiger, 2008) and vegetation cover, it is difficult to quantify the extent and volume of the ignimbrites or the eruptive center (Brandmeier et al., 2013). In the following, we will discuss distribution and, where possible, flow directions of the respective ignimbrites to better constrain the location of eruptive centers.

The Andamarca 4 ignimbrites (3.5-4 Ma) are a series of rather local, but largely coeval plateau- and mesa-forming ignimbrites. The vitrophyric ~3.8 Ma ignimbrites north of the Cerro Palla Palla are very likely related to this volcano. They flows down the valley south of the Ccarhuarazo and form the Pampa Huamanpirca (see Fig. 2). We dated two lava samples of the volcano that did not yield plateau ages but are very likely between 2-3 Ma and 3-4 Ma. The vitrophyric ignimbrite of the Río Visca valley probably corresponds to the other



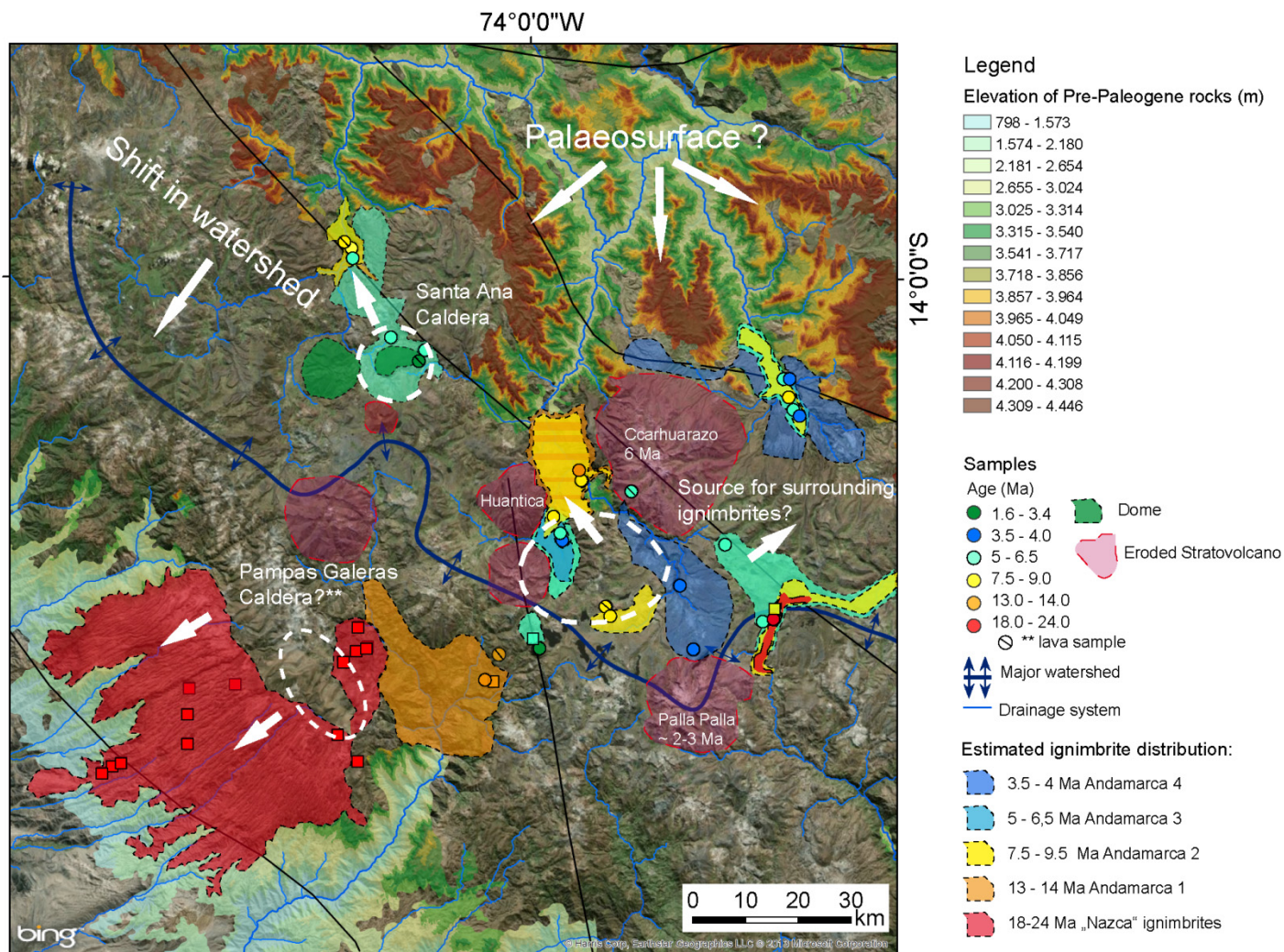


Fig.11: Map showing the distribution of our newly dated ignimbrites, proposed source calderas as well as results from DEM analysis (ASTER global DEM). Pre-Paleogene rocks possibly represent a Palaeosurface and the major drainage divide. (Circled samples: this study; squared samples: literature data: Noble et al. (1979); Roperch et al. (2011); Thouret et al. (2007); Bellón & Lefèvre (1977)). \*\*: proposed calderas by Noble et al. (1979) and references herein. The Pampas Galeras Caldera was proposed as source for the Nazca ignimbrites (Noble et al., 1979). For discussion of the source of the ignimbrites identified in this study, refer to the text.

ignimbrite, though the eruptive center might be different (we have no age information for the Huantica volcano). In the Río Soras valley, the ignimbrite is not welded and forms a plateau on both sides of the valley. To the north, it disappears where basement rocks form the modern topology (Fig. 11). The eruptive center for these ignimbrites is probably located to the south/south-east as derived from the flow direction into the valley. Their extent in the study area is at least 700 km<sup>2</sup>.

The Andamarca 3 ignimbrites (5-6.5 Ma) of the Urayama, Soras and Visca valleys are also rather local and coeval to the Ccarhuarazo and very likely other volcanos in the area that are not dated. The topmost ignimbrite of the Caracha valley, on the other hand, most likely erupted from the Santa Ana caldera described in section 4.4.1.5. It can be traced from the caldera rim to the valley with an age of  $5.96 \pm 0.08$  Ma of the outflow sheet and  $5.51 \pm 0.19$  Ma and  $5.42 \pm 0.26$  Ma for the intra-caldera tuff. This age was found for explosive and effusive volcanism throughout the area. The areal extent of all dated units of this age (including the Ccarhuarazo) is around 3,000 km<sup>2</sup>.

The Andamarca 2 ignimbrites (7.5-9.5 Ma) are widely distributed in the study area. The ~ 9 Ma age is found in the Visca and Urayama valleys as non-welded ignimbrite with small pumices (ANDA-11-05, SAN-11-03) and as a massive, grey ignimbrite (SAN-11-02). It is hard to tell the flow direction for those ignimbrites as the topography was completely different at that time and we do not have enough samples to better constrain elevation levels of the respective ignimbrite sheets. However, the base of this ignimbrite in the Visca valley is ~ 100 m higher in elevation more to the north than to the south. This argues for a flow direction toward the south (or at least not northward), assuming the ignimbrite did not flow uphill as can happen during high-energy eruptions. We will come back to that observation in the next section.

The ~8 Ma old ignimbrites crop out south of the Ccarhuarazo, and at the base of the Caracha and Soras valleys where they cover the Mesozoic basement. For these ignimbrites, flow directions cannot be determined as the Paleotopography at that time was very different from now and ignimbrites (especially large volume ignimbrites) can completely cover topography and even flow uphill. There is no trace of the eruptive center of these ignimbrites due to overprinting of the landscape by younger volcanos and ignimbrites, which themselves are modified by glaciation (Forbiger, 2008). Brandmeier et al. (2013), based on alteration mapping results and a study by (Guevara, 2001), suggested a buried eruptive center south of the Ccarhuarazo for ignimbrites in the area. A dated lava sample (ATAN-11-13) just above the ignimbrite outcrop is coeval with the ignimbrites and one center is probably located south of the younger Ccarhuarazo.

Manuscript III - Neogene ignimbrite pulses in Southern Peru as tracers for uplift, erosion and changes in the major water divide between Pacific and Atlantic Oceans

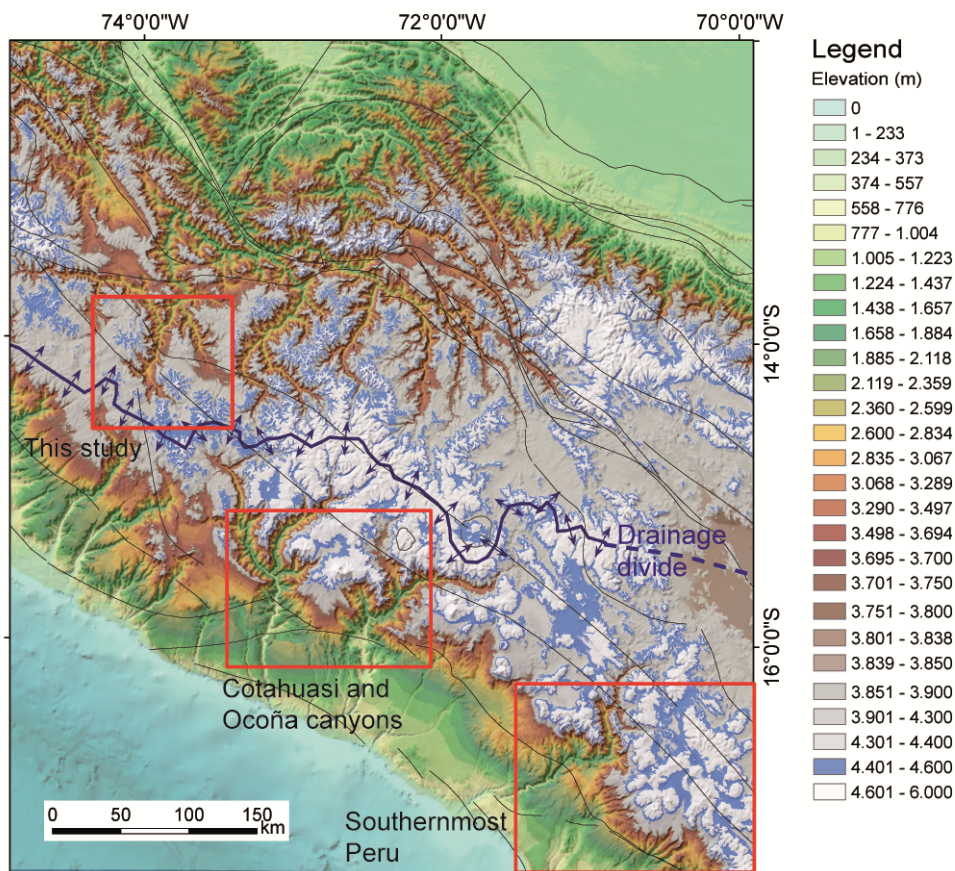
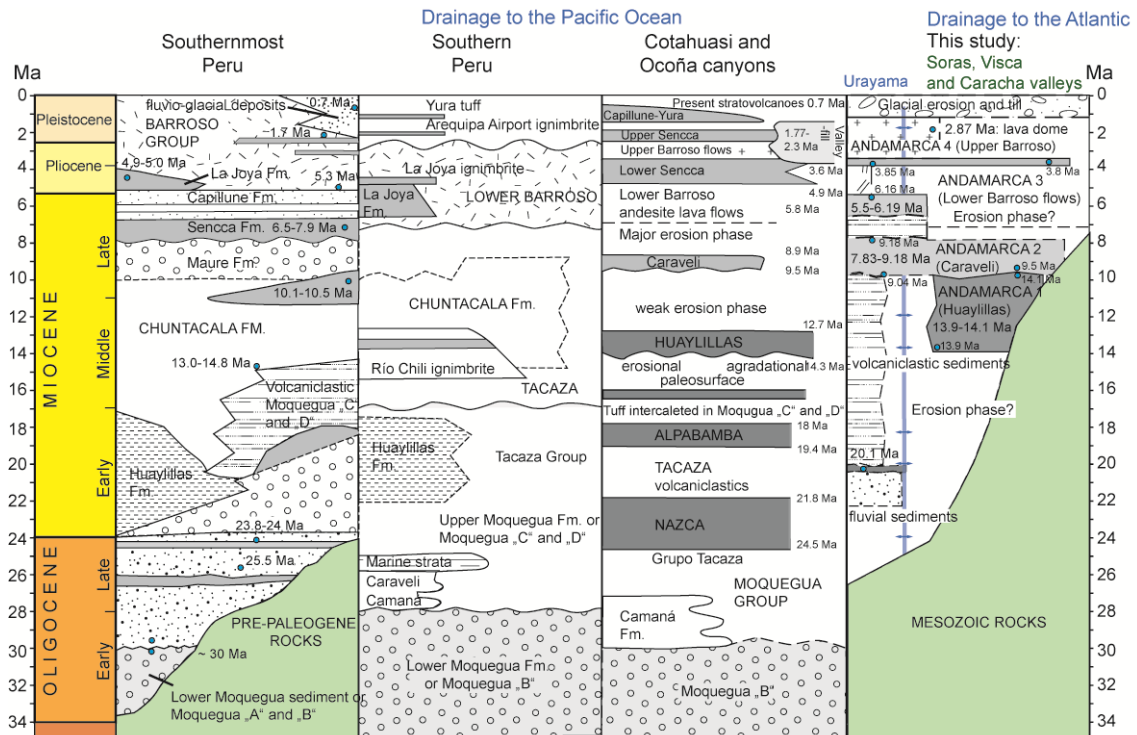


Fig.12: Composite stratigraphic scheme collated for southernmost Peru after Quang et al. (2005), Roperch et al. (2006), Southern Peru (Tosdal et al., 1981; Noble et al., 1984; Sébrier et al., 1988; Paquereau-Lebti et al., 2006), the area of the Cotahuasi, Ocoña, and Colca canyons (Thouret et al., 2007, Paquereau-Lebti et al., 2006; Delacour et al., 2007) and this study highlighting the significance of syn-uplift ignimbrites (dark gray, third column) and syn-incision ignimbrites (light grey, third column). Wavy lines indicate periods of erosion and/or tectonic phases and dashed lines are angular unconformities. In contrast to the above stratigraphies, this study examines an area on the east of the major drainage divide (derived from the Soras, Visca and Caracha valleys) compared to one valley (Urayama valley) just to the west of the drainage divide derived from drainage analysis. The most striking observation is the absence of the Nazca and Alpbamba ignimbrite ages in the three valleys east of the drainage divide. Stronger river incision since at least 9 Ma years shifted the drainage divide towards the Atlantic Ocean, thus cannibalizing the drainage on the south-western flank of the Altiplano and Andean slope.

The Andamarca 1(13-14 Ma) ignimbrites are very prominent in the Río Visca valley and around Puquio. In the Río Visca valley, they form escarpments of several hundreds of meters. This argues for rather large-volume eruptions at 14 Ma. However, uplift of the Western Cordillera occurring after 10 Ma was significant (Schildgen et al., 2007; Thouret et al., 2007) and the Paleotopography at that time is hard to reconstruct. The level of preservation and thickness of these ignimbrites argues for proximity to the center but no convincing evidence for the location of a caldera exists.

The Nazca ignimbrites and the Pampas Galeras collapse caldera were described in detail by Noble et al. (1979). He mapped the caldera (unpublished) and describes evidence from the field. His observation that eruptive centers of felsic volcanic rocks of latest Oligocene to early Miocene age tend to be located near the eastern margin of the coastal batholith is confirmed by the lack of ignimbrites of that age in the valley in the east of the study area.

### 3.2.3 Constraints of uplift, erosion and morphological evolution on the eastern Andean margin

---

Tilted Mesozoic basement or intrusive rocks and their detritus form the base of all of the valleys described in this study. The Nazca ignimbrites, so prominent on the western Andean slope (Fig. 11), are represented merely by a thin ash layer covering fluvial sediments in the Urayama valley. In the other valleys, the basement is unconformably covered by either 14 Ma Ignimbrites (Andamarca 1 or Huaylillas), or by 7.8 to 9.5 Ma ignimbrites (Andamarca 2 or Caraveli).

These basal ignimbrites are the earliest record of valley incision as they filled the old topography created in the Mesozoic rocks. The 14 Ma ignimbrite age is only present in the Río Visca valley, reaching from around 3,300 m a.s.l. to around 3,600 m a.s.l. In the Río Soras and Río Caracha valleys, we found no evidence for this ignimbrite. Here, the Mesozoic rocks are covered by the younger Andamarca 2 ignimbrites. As the 14 Ma ignimbrites are very prominent in the Río Visca valley, this argues for a proximal source. The absence of this

age in the other valleys either means, that they never reached that far, or that they were completely eroded by the time the Andamarca 2 ignimbrites were deposited. Those latter ignimbrites, in the Río Visca valley, are found at elevations of around 3,600 m which is 100-200 m higher than in the other valleys (compare Figs. 9 and 4). These sections are located around 20-30 km to the north of the Río Visca sections considered (Fig. 1). Fig. 13 shows an example for an along-river profile with the elevation of the Pre-Paleogene basement. The present-day river gradient is clearly dipping to the north, although the average elevation of these rocks increases towards the north (Fig. 11). This argues for the presence of deeply incised valleys cutting north by the time that the Andamarca 2 ignimbrites (and Andamarca 1 ignimbrites) were erupted and filled these valleys. For the Río Visca valley, this means ~300 m of incision into the Pre-Paleogene rocks prior to 14 Ma (this corresponds to the thickness of the 14 Ma ignimbrite sheets observed). With this and the following estimates, one has to be aware, that we can only consider what remains of the original sheets and that estimates are minimum estimates. We cannot know what happened between 14 Ma and 9 Ma. The ~9.4 Ma ignimbrites are at an elevation of 3,500 m in section C-D, while the contact with the 14 Ma ignimbrites was found at 3,600 m in section E-F (Fig. 6), farther downstream. This argues for a flow direction toward the south for the 9 Ma ignimbrites. However, this is not reliable proof for flow direction as ignimbrites can also overcome topographic obstacles. However, it still is an important observation as it might indicate differences in the drainage system at that time.

In the Río Caracha valley, Mesozoic sediments can be observed at 3,600 m, indicating valley incision prior to the basal ignimbrite of at least 100 m (thickness of the ignimbrite ~100 m). There is no indicator to constrain incision between the oldest valley-fill and the most recent one (Andamarca 3 and Andamarca 4 respectively). Re-incision can therefore only be restricted to ~500 m for the Caracha valley after around 6 Ma, assuming the valley was completely filled, which is the age of the top ignimbrite. For the Río Soras valley, around 350 m of incision are observed after 3.85 Ma and for the Río Visca valley, ~800 m after around 6 Ma (age of the Ccarhuarazo flow that does not flow over the edge of the valley, Fig. 6, section E-F) and ~300 m after 3.86 Ma which is the age of the youngest ignimbrite (Fig. 6, section A-B). The estimate based on the Ccarhuarazo flow is a bit arbitrary as the glacial history of the area has modified the morphology and the possibility of the valley existing prior to 6 Ma is likely.

In summary, we observe a minimum incision of ~300 m prior to 14 Ma, of ~500 m after ~6 Ma (in the Río Caracha valley and probably the Río Visca valley) and renewed incision

after ~ 3.8 Ma of 200 to 300 m. For the Visca valley, we know of at least one additional event (~9.4 Ma) that filled the valley and cannot be quantified in terms of re-incision.

So far, we have not discussed the Río Urayama valley because it is a special case right on the western side of the drainage divide and therefore serves for directly comparing the incision history for the respective drainage settings. We now address these results together with the findings of other authors for the western part of the drainage system. Elevation of the valley floor of the Urayama valley is higher than the top of the other valleys as the section is located almost on top of the drainage divide. The valley must have existed prior to ~20 Ma which is the age of the base ignimbrite. Minimum incision after ~3.85 Ma is ~ 300 m, similar to the values observed in the other valleys.

Estimates of Paleoelevation of the Western Cordillera agree, that no more than half of the modern topography was reached by 25 Ma and in the Altiplano and Eastern Cordillera 25-30% only by 20 Ma and 14 Ma respectively (Gregory-Wodzicki, 2000). Valley incision prior to 14 Ma is therefore probably due to surface uplift prior to that time. In comparison, (Thouret et al., 2007) found incision on the western escarpment of the Cordillera only starting at ~ 9 Ma with a delay of ~ 4 Ma after continued uplift since 13 Ma. The main phase of incision occurred between 9 Ma and ~ 3.8 Ma with the younger ignimbrite located close to the present valley floor of the Cotahuasi canyon (Thouret et al., 2007). In contrast, the 3.8 Ma ignimbrites east of the drainage divide cap the major valleys, are underlying the glacial sediments of the Pampa Huamanpirca (Fig. 2) and put an age constraint on the re-incision of the valleys. The main phase of incision observed by (Thouret et al., 2007) agrees with our observations in the Caracha and the Río Visca valleys with around 500 m and 800m of incision after ~6 Ma respectively. The most important differences observed are therefore: Incision in the Río Visca valley started prior to 14 Ma while in the Río Soras and Río Caracha valleys, it started prior to ~7.8 Ma and ~8.4 Ma respectively. Incision depth in the Río Caracha valley was at least 100 m. The main incision phase observed for the Cotahuasi and Ocona canyons is also reflected in our study area, although in a lower magnitude and with a 3 Ma delay: The ~2 km of incision between 9 Ma and 3.8 Ma observed by (Thouret et al., 2007) contrast with 500-800 m of incision between ~6 Ma and 3.8 Ma. This and the delay observed, however, are probably due to a lack of data to better constrain the period between ~9 Ma and 6 Ma in our valleys.

The most striking difference is the absence of widespread ignimbrite deposits of Nazca age and to some degree 14 Ma age. This suggests that the older ignimbrites that are so prominent on the Western escarpment either (a) did not occur in the east of the Western Cordillera, or (b) that enhanced erosion and denudation due to uplift and increased

precipitation on the eastern flank of the Andes (Mulch et al., 2010) and references therein) removed all evidence of this event. Surface uplift of 2,000 to 3,500 m of the Altiplano and Eastern Cordillera since 10 Ma (Gregory-Wodzicki, 2000) and a subsequent change in precipitation at around 9 Ma (Ehlers and Poulsen, 2009; Mulch et al., 2010) together with exhumation rates of  $0.17 \text{ km Ma}^{-1}$  between 22-15 Ma in the Western Cordillera (Ruiz et al., 2009), implying around 1.2 km of material removed during that time, argue for the second scenario. We therefore argue that uplift, probably influenced by the arrival of the Nazca ridge at ~12 Ma at these latitudes (Hampel, 2002), accompanied by an increase in precipitation on the eastern side of the Andes led to high erosion and denudation rates stripping the basement blank of the 20 Ma and 14 Ma ignimbrites observed on the dry, western escarpment.

Discussing incision rates and differences on both sides of the present drainage divide, we need to know more about the transport mechanism and depositional environment. Information gained from the river network, river profiles and depositional record will be used to better constrain the morphological evolution of the area. We already mentioned that the ~9.4 Ma ignimbrite in the Río Visca valley is found at higher elevations on the section more downstream of the present river (Fig. 7). Fig. 13 shows the present-day drainage network and a river profile along that valley. Headwater erosion of the rivers draining the Eastern Cordillera (Mulch et al., 2010) shifted the drainage divide in a westerly direction and changed the drainage system during the late Miocene. In agreement to that scenario, drainage in the High Plateau province of central Peru was internal until latest Neogene time, and changed by headward erosion of the Río Mantaro opening up the Ayacucho basin (Wise and Noble, 2008) in the late Pliocene. This means, that valleys now draining to the Amazon basin, were probably captured during the late Miocene/Pliocene as indicated by the ~9.4 Ma ignimbrite flow direction and the sudden turn in direction of the upstream Río Visca (red square in Fig. 13).

Provenance analysis of the sediment record gives further information about Paleodrainage. Noble et al. (1979) describe the Nazca Group as resting on a major erosional surface cut in rocks of the Coastal batholith and older units (post-Incaic unconformity after Noble et al., 1979 and references therein). The lower part of the group consists of conglomerates, probably of Eocene age, which correlate with the Moquegua Formation in southernmost Peru (Decou et al., 2013, 2011), while the upper part is formed by the Nazca ignimbrite sheets. The depositional surface below the ignimbrites represents

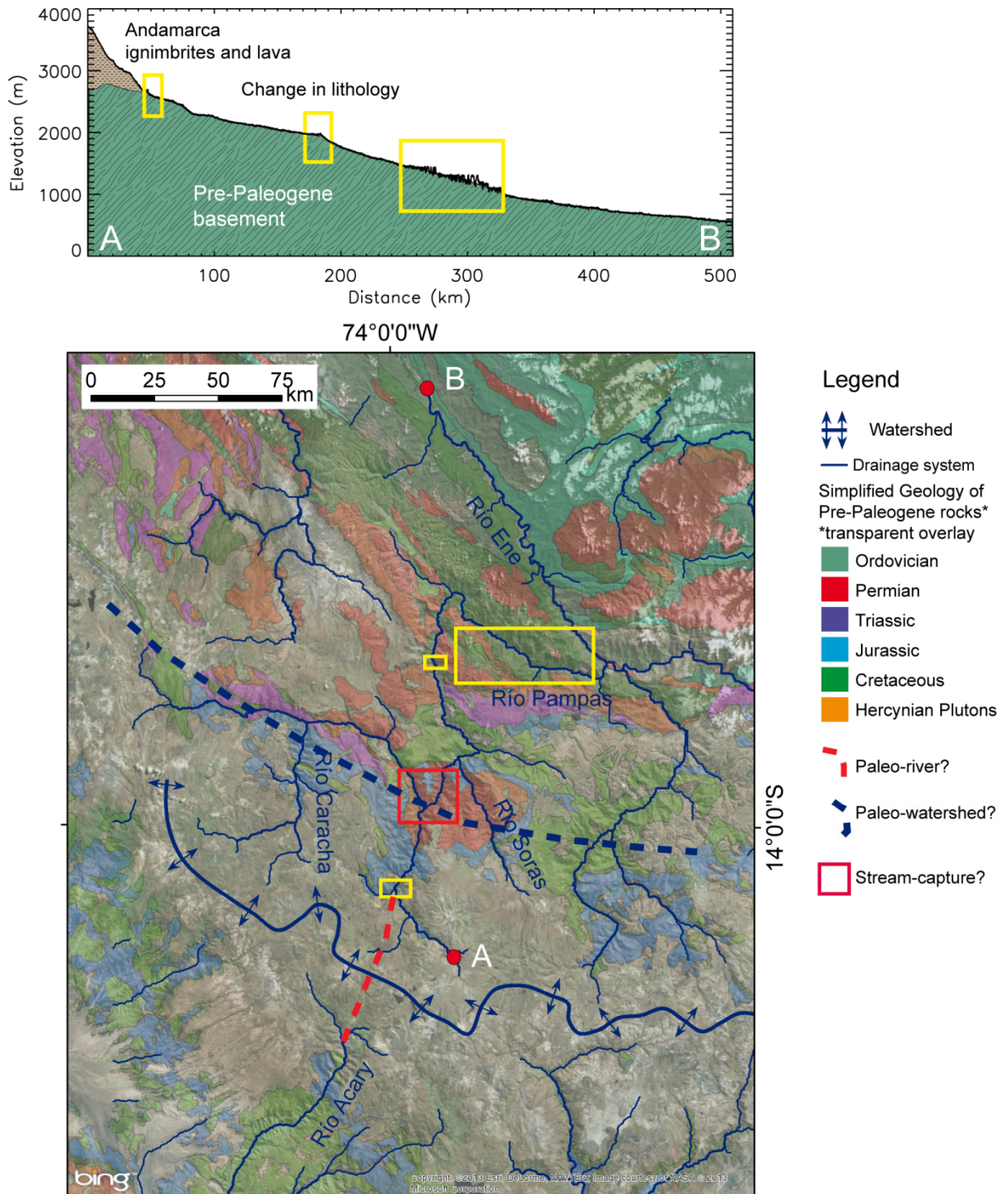


Fig.13: Present drainage system and pre-Paleogene rocks. The above profile shows the typical form of the rivers draining the area toward the Amazon (Río Ene), with headwater erosion incising into the Neogene volcanics overlying mainly Mesozoic rocks. For more details refer to the text. The small yellow squares highlight points in the profile, where a change in lithology (ignimbrite-basement and plutonic rock-tilted Mesozoic basement) occurs. The big yellow square shows the location of the strange profile zig-zag in the map. This might be due to the resolution of the ASTER DEM in this area of low gradient, curved river and relatively steep valley flanks.

the top of a large Tertiary sedimentary wedge that can be traced along the Pacific fore-arc side of the Andean orogen. This sedimentary wedge is the result of uplift and erosion of the



Central Andes and ranges in age from >45 Ma to c. 10 Ma (Decou et al., 2013, 2011). Provenance studies indicate a change in provenance around 35 Ma from the Eastern to the Western Cordillera (Decou et al., 2013, 2011). This change was due to uplift and a re-orientation of the drainage system that is still ongoing in terms of headwater erosion of the rivers draining to the Amazon basin.

If, as suggested by the ~9 Ma ignimbrite in the Río Visca valley and the drainage pattern, this valley was captured by headwater erosion around that time, this means that incision at the western side of the drainage divide already started prior to 14 Ma (age of the oldest ignimbrite in this valley) and therefore somewhat earlier than suggested by Thouret et al. (2007).

#### 4 Summary and Conclusions

---

We provide 31  $^{40}\text{Ar}/^{39}\text{Ar}$  ages of ignimbrites and some related lava samples from four major valleys in Southern Peru and propose a new stratigraphy for the valleys draining to the Amazon river in comparison to the western drainage system. Together with drainage and DEM analysis, we use this data to better constrain the uplift and erosion history of the area and major changes in the drainage system during the late Miocene.

There are several reasons for the change of incision and drainage over time, with processes being linked to each other in a complex way. Uplift of the Andes affects precipitation pattern (Ehlers and Poulsen, 2009) and triggers incision (Schildgen et al., 2007; Thouret et al., 2007 to name but a few). Incision and removal of material itself also triggers uplift and climatic effects and causes have to be considered on a global scale (for example, the closure of the Central American Seaway and intensified upwelling of the Humboldt current are discussed as cause for the switch to hyper-aridity in the Atacama desert (Hartley, 2003)). The complex relationships between different causes and effects have to be kept in mind when interpreting data. For our study area, based on the discussion above, we propose the following evolutionary model from Miocene to recent:

Prior to the deposition of the Nazca ignimbrites, erosional debris was transported toward the Pacific, similar to what was described by Decou et al. (2011,2013) for the Moquegua group of Southern Peru. Evidence from drainage analysis and the position of the ~ 9.4 Ma ignimbrite in the Visca valley argue for incision of the Acary valley prior to 14 Ma as the Visca valley - now draining east - was probably only captured by headwater erosion prior to 9 Ma (Fig. 13) and until then might have been the upstream part of the Acary valley. If this was the case, incision would have started 4 Ma earlier than found for the Cotahuasi valley by Thouret

et al. (2007). Evidence from the Soras and Caracha valleys further to the east suggests incision prior to ~ 8 Ma and therefore later than on the western escarpment. Further evidence is needed from the Acary valley to confirm one or the other scenario.

Uplift of around 2 km between 9 Ma and 3.8 Ma observed by Thouret et al. (2007) contrast with 500-800 m of incision between ~ 6 Ma and 3.8 Ma in the valleys draining to the east. The difference in magnitude might be due to the lack of data to better constrain the period between 9 and 6 Ma in these valleys. Widespread volcanism occurring between 2 and 6 Ma (e.g. Palla Palla, Carhuarazo) modified the topography and probably also led to changes in the drainage system, possibly further blocking drainage to the west as also evident in provenance analysis from the Moquegua group (Decou et al., 2013).

The most recent morphological element in the area are a series of rather local, but largely coeval plateau- and mesa-forming ignimbrites with ages of ~3, 8 Ma. They form the top of almost each succession of ignimbrites in the incised valley and also cover the flat-lying areas in the basins between the major stratovolcanoes. The glacial morphology described by Forbiger (2008) suggests an even younger age of these valleys, at least in their upper reaches.

In summary, we observe a minimum incision of ~300 m prior to 14 Ma, of ~500-800 m after ~6 Ma (in the Río Caracha valley and the Río Visca valley) and renewed incision of 200 to 300 m after ~3.8 Ma. For the Visca valley, we know of at least one more event (~9.4 Ma) that filled the valley and cannot be quantified in terms of re-incision. Causes for incision and changes in incision rates are uplift (mainly 14 Ma to 3.8 Ma) and a change in climate and drainage system with related base-level changes. Our findings agree with an increase of erosion rates in the Eastern Cordillera at 15-10 Ma (Gregory-Wodzicki, 2000) that would have changed the drainage pattern. Uplift in the order of 2000-3500m in the Altiplano and Eastern Cordillera since ~10 Ma (Gregory-Wodzicki, 2000; Thouret et al., 2007) are confirmed by river incision of at least 1 km during that time, with at least one more phase of incision (9-6 Ma) that cannot be quantified.

Comparing the stratigraphic record of the three valleys east of the drainage divide to the one valley to the west and stratigraphies found by other authors for the western escarpment, we found that the 20 Ma Nazca age (and probably the 14 Ma age) are completely absent on the eastern part of the drainage divide. This striking difference argues for high rates of incision and denudation in that direction whereas the plateau-forming Nazca and Andamarca 4 (Huaylillas) ignimbrites are so well preserved on the western escarpment. We argue that this is due to uplift caused by the arrival of the Nazca ridge at that latitude after ~12 Ma, accompanied by a change in precipitation toward more humid conditions on the eastern side

of the orogen causing an asymmetrical response of erosion. However, the possibility of very directional deposition of the respective ignimbrites cannot be excluded.

## REFERENCES:

- Allmendinger, R.W., Jordan, T.E., Kay, S.M., Isacks, B.L., 1997. The Evolution of the Altiplano-Puna Plateau of the Central Andes. *Annu. Rev. Earth Planet. Sci.* 27, 139-174.
- Asociación Lagesa, C.F.G.S., 1996. *Geología de los cuadrangulos de Huancapi, Chincheros, Querobamba y Chavina*. Instituto Geologico Minero y Metalurgico.
- Baker, M.C.W., Francis, P.W., 1978. Upper Cenozoic volcanism in the Central Andes - Ages and volumes. *Earth. Planet. Sci. Lett.* 41, 175-187.
- Beck, S.L., Zandt, G., Myers, S.C., Wallace, T.C., Silver, P.G., Drake, L., 1996. Crustal-thickness variations in the Central Andes. *Geology.* 24, 407-410.
- Bellón, H.L., R., 1977. Spectre d'âges radiométriques du volcanisme cénozoïque du Pérou central (région de Castrovirreyna-Ayacucho-Nazca), *Réunion Annuelle des Sciences de la Terre*, p. 58.
- Bendel, V., Schmidt, B.C., 2008. Raman spectroscopic characterisation of disordered alkali feldspars along the join  $KAlSi_3O_8NaAlSi_3O_8$ : application to natural sanidine and anorthoclase. *European Journal of Mineralogy.* 20, 1055-1065.
- Brandmeier, M., Erasmi, S., Hansen, C., Höweling, A., Nitzsche, K., Ohlendorf, T., Mamani, M., Wörner, G., 2013. Mapping patterns of mineral alteration in volcanic terrains using ASTER data and field spectrometry in Southern Peru. *Journal of South American Earth Sciences.* 48, 296-314.
- De Silva, S.L., 1989a. Altiplano-Puna volcanic complex of the central Andes. *Geology.* 17, 1102-1106.
- De Silva, S.L., 1989b. Geochronology and Stratigraphy of the Ignimbrites from the 21° 30'S to 23° 30'S portion of the Central Andes of Northern Chile. *J. of Volc. and Geotherm. Res.* 37, 93-131.
- Decou, A., von Eynatten, H., Dunkl, I., Frei, D., Wörner, G., 2013. Late Eocene to Early Miocene Andean uplift inferred from detrital zircon fission track and U–Pb dating of Cenozoic forearc sediments (15–18°S). *Journal of South American Earth Sciences.* 45, 6-23.
- Decou, A., von Eynatten, H., Mamani, M., Sempere, T., Wörner, G., 2011. Cenozoic forearc basin sediments in Southern Peru (15–18°S): Stratigraphic and heavy mineral constraints for Eocene to Miocene evolution of the Central Andes. *Sedimentary Geology.* 237, 55-72.
- Delacour, A., Gerbe, M.-C., Thouret, J.-C., Wörner, G., Paquereau-Lebti, P., 2007. Magma evolution of Quaternary minor volcanic centres in Southern Peru, Central Andes. *Bulletin of volcanology* 69, 581-608.
- Ehlers, T.A., Poulsen, C.J., 2009. Influence of Andean uplift on climate and paleoaltimetry estimates. *Earth and Planetary Science Letters.* 281, 238-248.
- Forbiger, M., 2008. *Glazialmorphologische Detailkartierung mittels stereoskopischer Luftbildanalyse und GIS in der Westkordillere der südperuanischen Anden zwischen 14° und 15°S*, Geographisches Institut Rurecht-Karls-Universität, Heidelberg.
- Francis, P.W., Rundle, C.C., 1976. Rates of the production of the main magma types in the Central Andes. *Geol. Soc. Am. Bull.* 87, 474-480.
- Ghosh, P., Garzzone, C.N., Eiler, J.M., 2006. Rapid uplift of the Altiplano revealed through  $^{13}C$ - $^{18}O$  bonds in paleosol carbonates. *Science.* 311, 511-515.
- Gregory-Wodzicki, K.M., 2000. Uplift history of the Central and Northern Andes; a review. *GSA Bulletin.* 112, 1091-1105.

- Guevara, J.E.A., 2001. Geología y exploración del proyecto aurífero epitermal Incapacha (Puquio-Ayacucho-Peru), Facultad de Ingeniería Geológica, Minera y Metalúrgica. Universidad Nacional de Ingeniería, Lima, p. 169.
- Hampel, A., 2002. The migration history of the Nazca Ridge along the Peruvian active margin: a re-evaluation. *Earth and Planetary Science Letters*. 203, 665-679.
- Hartley, A., 2003. Andean uplift and climate change. *Journal of the Geological Society*. 160, 7-10.
- INGEMMET, 2001a. Mapa geológica del cuadrángulo de Querobamba. INGEMMET, Lima.
- INGEMMET, 2001b. Mapa Geológico del cuadrángulo de Chavina. Instituto Geológico Minero y Metalúrgico, Lima.
- James, D.E., 1971. Plate tectonic model for the evolution of the Central Andes. *Geological Society of America Bulletin*. 82, 3325-3346.
- Jordan, T.E., Isacks, B.L., Allmendinger, R.W., Brewer, J.A., Ramos, V.A., Ando, C.J., 1983. Andean tectonics related to geometry of subducted Nazca plate. *Geological Society of American Bulletin*. 94, 341-361.
- Jordan, T.E., Reynolds, J., Erikson, J.P., 1997. Variability in age of initial shortening and uplift in the central Andes, 16-33°S. *Tectonic uplift and climate change*, 41-61.
- Kay-Mahlburg, S., Mpodozis, C., Ramos, V.A., Munizaga, F., 1991. Magma source variations for mid-late Tertiary magmatic rocks associated with a shallowing subduction zone and a thickening crust in the central Andes (28 to 33°S). *Andean magmatism and its tectonic setting*. 265, 309.
- Kay, S.M., Coira, B.L., Caffee, P.J., Chen, C.-H., 2010. Regional chemical diversity, crustal and mantle sources and evolution of central Andean Puna plateau ignimbrites. *Journal of Volcanology and Geothermal Research*. 198, 81-111.
- Kuiper, K.F., Deino, A., Hilgen, F.J., Krijgsman, W., Renne, P.R., Wijbrans, J.R., 2008. Synchronizing Rock Clocks of Earth History. *Science* 320, 500-504.
- Lamb, S., Davis, P., 2003. Cenozoic climate change as a possible cause for the rise of the Andes. *Nature*. 425, 792-797.
- Lamb, S., Hoke, L., 1997. Origin of the high plateau in the Central Andes, Bolivia, South America. *Tectonics* 16, 523-649.
- Mégard, F., 1984. The Andean orogenic period and its major structures in central and northern Peru. *Journal of the Geological Society of London*, 141, 893-900.
- Min, K., Mundil, R., Renne, P.R., Ludwig, K.R., 2000. A test for systematic errors in  $^{40}\text{Ar}/^{39}\text{Ar}$  geochronology through comparison with U/Pb analysis of a 1.1-Ga rhyolite. *Geochimica et Cosmochimica Acta*, 64, 73-98.
- Mulch, A., Uba, C.E., Strecker, M.R., Schoenberg, R., Chamberlain, C.P., 2010. Late Miocene climate variability and surface elevation in the central Andes. *Earth and Planetary Science Letters*, 290, 173-182.
- Noble, D.C., Farrar, E., Cobbing, E.J., 1979. The Nazca Group of south-central Peru: Age, source, and regional volcanic and tectonic significance. *Earth and Planetary Science Letters*, 45, 80-86.
- Noble, D.C., McKee, E.H., Eyzaguirre, V.R., Marocco, R., 1984. Age and regional tectonic and metallogenetic implications of igneous activity and mineralization in the Andahuaylas-Yauri belt of Southern Peru. *Economic Geology* 79, 172-176.

- Paquereau-Lebti, J.-C.; Wörner, G.; Fornari, M., 2006. Neogene and Quaternary ignimbrites in the area of Arequipa, Southern Peru: Stratigraphical and petrological correlations. *Journal of Volcanology and Geothermal Research*, 251-275.
- Quang, C.X., Clark, A.H., Lee, J.K.W., Hawkes, N., 2005. Response of Supergene Processes to Episodic Cenozoic Uplift, Pediment Erosion, and Ignimbrite Eruption in the Porphyry Copper Province of Southern Peru. *Econ. Geol.* 100, 87-114.
- Roperch, P., Sempere, T., Macedo, O., Arriagada, C., Fornari, M., Tapia, C., García, M., Laj, C., 2006. Counterclockwise rotation of late Eocene–Oligocene fore-arc deposits in Southern Peru and its significance for oroclinal bending in the central Andes. *Tectonics* 25, TC3010.
- Ruiz, G., Carlotto, V., Van Heiningen, P., Andriessen, P., 2009. Steady-state exhumation pattern in the Central Andes–SE Peru. *Geological Society, London, Special Publications*, 324, 307-316.
- Salisbury, M.J., Jicha, B.R., De Silva, S.L., Singer, B.S., Jimenez, N.C., Ort, M.H., 2011.  $^{40}\text{Ar}/^{39}\text{Ar}$  chronostratigraphy of Altiplano-Puna volcanic complex ignimbrites reveals the development of a major magmatic province. *Geological Society of America Bulletin*, 123, 821-840.
- Schildgen, T.F., Hodges, K.V., Whipple, K.X., Reiners, P.W., Pringle, M.S., 2007. Uplift of the western margin of the Andean plateau revealed from canyon incision history, Southern Peru. *Geology*, 35, 523-526.
- Sébrier, M., Mercier, J.L., Macharé, J., Bonnot, D., Cabrera, J., Blanc, J.L., 1988. The state of stress in an overriding plate situated above a flat slab: The Andes of central Peru. *Tectonics* 7, 895-928.
- Semperé, T., Butler, R., Richards, D., Marshall, L., Sharp, W., Swisher, C., 1997. Stratigraphy and chronology of Upper Cretaceous–lower Paleogene strata in Bolivia and northwest Argentina. *Geological Society of America Bulletin*, 109, 709-727.
- Semperé, T., Hérail, G., Oller, J., Bonhomme, M.G., 1990. Late Oligocene-early Miocene major tectonic crisis and related basins in Bolivia. *Geology*, 18, 946-949.
- Steiger, R., Jäger, E., 1977. Subcommittee on geochronology: convention on the use of decay constants in geo- and cosmochronology. *Earth and Planetary Science Letters*, 36, 359-362.
- Thouret, J.C., Wörner, G., Gunnell, Y., Singer, B., Zhang, X., Souriot, T., 2007. Geochronologic and stratigraphic constraints on canyon incision and Miocene uplift of the Central Andes in Peru. *Earth and Planetary Science Letters*, 263, 151-166.
- Tosdal, R.M., Farrar, E., Clark, A.H., 1981. K-Ar Geochronology of the Late Cenozoic volcanic rocks of the Cordillera Occidental, southernmost Peru. *J. Volcanol. Geotherm. Res.* 10, 157-173.
- Wise, J., Noble, D., 2008. Late Pliocene inception of external drainage and erosion of intermontane basins in the highlands of Central Perú. *Revista de la Sociedad Geológica de España* 21, 73-91.
- Wörner, G.U., D.; Kohler, I.; Seyfried, H., 2002. Evolution of the West Andean Escarpment at 18°S (N. Chile) during the last 25 Ma: uplift, erosion and collapse through time. *Tectonophysics*, 183-198.

## MANUSCRIPT IV

---

# Temporal and compositional patterns and variations in ignimbrite volcanism in the Andes over the past 30 Ma

Brandmeier, M<sup>a</sup>, Erasmi, S<sup>b</sup>, Mamani, M<sup>c</sup>, Wörner, G<sup>a</sup>

<sup>a</sup> Georg-August- Universität Göttingen, GZG, Geochemisches Institut, Goldschmidstr.1, Göttingen D-37077, Germany

<sup>b</sup> Georg-August- Universität Göttingen, GZG, Geographisches Institut, Goldschmidstr.3, Göttingen D-37077, Germany

<sup>c</sup> Pontificia Universidad Católica del Perú, Av. Universitaria 1801, San Miguel, Lima 32, Peru

In preparation

---

## Abstract

*We analyzed temporal and compositional patterns of large volume ignimbrite magmatism in the Central Andes during the Neogene using geostatistical modeling. In order to examine the spatiotemporal pattern of so-called “ignimbrite flare-ups”, we mapped 201 ignimbrites (including some related domes), together with 1,602 ignimbrite samples (with geochronological and chemical data) using satellite imagery, available literature, maps and new data, creating a Web Mapping Application (WMA) that is now globally available.*

*Isotopic signatures containing information about the lower crust were used to delineate basement structures by creating kriging models, together with an error surfaces for  $^{208}\text{Pb}/^{204}\text{Pb}$ ,  $^{207}\text{Pb}/^{204}\text{Pb}$  and  $^{206}\text{Pb}/^{204}\text{Pb}$ ,  $^{143}\text{Nd}/^{144}\text{Nd}$  and Inverse Distance Weighing (IDW) interpolation for  $^{87}\text{Sr}/^{86}\text{Sr}$ .*

*Applying cluster analysis to clr-transformed major and trace element data, we grouped ignimbrites according to geochemical characteristics and compared our results to traditional geochemical parameters. Based on major elements, we found a rhyolitic and a dacitic “end-member”. Those “end-members” overlap in REE compositions with more or less pronounced negative Eu anomaly, depletion of MREEs (possibly due to amphibole fractionation) and enrichment/depletion in LREE. Based on these results, we argue, that a distinction between “rhyolitic, crystal-poor, small-volume” and “large-volume, crystal-rich monotonous*

*intermediate” is insufficient to capture differences in ignimbrite evolution and genesis. The large-volume, ca. 19 Ma Oxaya ignimbrite is compositionally very distinct from the young Altiplano Puna Volcanic Complex (APVC) Atana ignimbrite, implying a different genesis than suggested for the large-volume APVC ignimbrites. This finding agrees with differences in Sr isotopes, arguing for less crustal assimilation, possibly due to the thinner and colder crust at that time. Most rhyolitic ignimbrites are concentrated north and south of the Northern Puna, with only minor rhyolites as more differentiated equivalents of the prominent dacites occurring there as described by De Silva and Gosnold (2007). This observation is consistent with the model they propose, with accumulation of large bodies of dacitic magma in the upper crust with time, fed by mantle power input. It is important to note, that all these ignimbrites are younger than 10 Ma, while samples to the north and south record ages up to 26 Ma and therefore times with a crust that was not as thick and thermally evolved as assumed for the APVC.*

*To test our hypothesis that compositional signatures can be used to distinguish between ignimbrites, we applied discriminant analysis to selected ignimbrites. Classification results gave an 87.5% overall accuracy. The most important elements for discriminating our ignimbrites are La (LREE), Yb (HREE), Eu, Al<sub>2</sub>O<sub>3</sub>, K<sub>2</sub>O, P<sub>2</sub>O<sub>5</sub>, MgO, FeO<sub>t</sub> and TiO<sub>2</sub>. However, other REEs like Gd, Pr, Tm, Sm and Er also contribute to the discrimination functions. Thus, including these REEs helps to find more subtle differences that are particular to each ignimbrite.*

*In order to examine the spatiotemporal pattern of so-called “ignimbrite flare-ups, we calculated the cumulative areal extent and volume of ignimbrites through time. Calculating eruptive volumes is difficult due to the commonly buried source calderas of ignimbrites, the lack of knowledge of the real extent, average thickness and errors in ignimbrite correlation. Therefore we propose minimum estimates for the CVZ and for five N-S segments.*

*In total, we estimate eruptive volumes of 31,000 km<sup>3</sup>, with 2,400 km<sup>3</sup> for Southern Peru, 2,700 km<sup>3</sup> for Southernmost Peru, 8,400 km<sup>3</sup> for the Altiplano, 14,200 km<sup>3</sup> for the Northern Puna and 3,100 km<sup>3</sup> for the Southern Puna segments. Using the same assumptions as (De Silva and Gosnold, 2007), we calculate a minimum plutonic input of 7,200 km<sup>3</sup>, 8,100 km<sup>3</sup>, 25,200 km<sup>3</sup>, 42,600 km<sup>3</sup> and 9,300 km<sup>3</sup> for the respective segments during the past 30 Ma and observe a N-S “younging” of eruption ages and “ignimbrite pulses”. Major pulses occurred at 19-24 Ma (e.g. Oxaya, Nazca Group), 13-14 Ma (e.g. Huaylillas ignimbrites), 6-10 Ma (many of the Altiplano and Puna ignimbrites like the Vilama ignimbrite) and 3-6 Ma (e.g. Atana, Los Frailes, Toconao) and very young ignimbrites from 0-3 Ma (e.g. Lauca-Perez, Purico). We propose that large-volume ignimbrite eruptions occurred in the wake of*



*the subducting Juan-Fernandez ridge, with compression, uplift, shallow subduction and fluid release in a first stage, upon arrival of the ridge, and melting of the so “conditioned” crust due to renewed asthenospheric mantle flow above a steepening slab after the passing of the ridge.*

*The total estimates for the northern segments 1-3 and the Northern Puna are sub-equal, however, calderas and thus intra-caldera volumes for ignimbrites in these segments are not known and due to higher age, preservation level for the ignimbrites is much lower. Thus, it may be possible, that the latter ignimbrites represent volumes greater than in the Northern Puna. If further studies show that this is the case, the concept of an APVC flare-up should be revised and not viewed as a regionally and temporally restricted event of high-magma flux and batholith construction. Instead, we suggest a paradigm shift towards a dynamic model, with the “flare up” as a moving entity that has progressed across the Andes during the past 25 Ma, probably related to ridge subduction, with the Northern Puna flare up only being the most recent and best preserved remnant, and the Southern Puna Cerro Galán eruption possibly heralding another flare-up.*

KEYWORDS: *Ignimbrites, ignimbrite flare-up, log-ratios, kriging, multivariate statistics, discriminant analysis, geospatial statistics*

## 1 Introduction

---

The Central Volcanic Zone of the Andes (CVZ) is characterized by continental crust that has been thickened mostly by crustal shortening and lower crustal flow to 70 km during the last 25 Ma (Allmendinger et al., 1997; Beck et al., 1996; Yuan et al., 2002; Yuan et al., 2000). Subduction of the Nazca plate results in typical arc magmas, however, with significant crustal contributions (e.g. Davidson et al., 1990), that were erupted in numerous stratovolcanoes and - more rarely - isolated “monogenetic” centers (Davidson and De Silva, 1992; Delacour et al., 2007; Wörner et al., 2000).

Apart from these andesite-dacite volcanoes, the Central Andes are one of the largest Miocene ignimbrite provinces on earth. Many studies characterized the large-volume ignimbrite eruptions to the N and E of the Atacama Basin in the southern Central Andes and linked the age and erupted volumes to so-called “flare-ups” events, with individual ignimbrites reaching volumes of up to thousands of cubic kilometers (e.g. Atana ignimbrite: 2,200 km<sup>3</sup>, Puripicar: 1,500 km<sup>3</sup>) (De Silva, 1989b; Salisbury et al., 2011). These are assumed to be related to large scale melting in the mid to upper crust, with distinct pulses of unusually high eruption rates at 8 Ma, 6 Ma and 4 Ma (De Silva, 1989a; De Silva, 1989b; De Silva, 1989c; De Silva, 1991; De Silva and Francis, 1989; De Silva and Francis, 1991; De Silva and Gosnold, 2007; Francis et al. 1981; Francis et al., 1984; Francis et al., 1983; Gardeweg and Ramírez, 1987; Kay et al., 2010; Kay et al., 1988; Lindsay et al., 2001a; Lindsay et al., 2001b; Noble et al., 1979; Salisbury et al., 2011; Schnurr et al., 2007; Soler et al., 2007). In addition, an increasing amount of geophysical evidence indicates, that a large portion of the middle crust may be partially molten below the APVC (Schmitz et al., 1997; Zandt et al., 2003). This large partially molten zone is considered to have been the source of the >15.000 km<sup>3</sup> of ignimbrite magmas erupted in the Altiplano Puna Volcanic Complex (APVC) (De Silva, 1989), adding significantly to the volume of magmas related to the APVC. These ignimbrites are described as monotonous, crystal-rich dacites to rhyodacites, with some volumetrically minor rhyolites ( De Silva and Gosnold, 2007; Salisbury et al., 2011). Siebel et al. (2001) and Schnurr et al. (2007) studied relatively small (tens of cubic kilometers), rhyolitic ignimbrites from the southern Puna and propose a genetic relationship to the stratovolcano-forming andesites.

The APVC and its underlying zone of partial melts in the crust, however, represents only a small portion of ignimbrite magmatism in the Central Andes that has been particularly well studied and dated due to its accessibility, excellent exposure, and relatively young ages. In addition, large areas (and thus volumes) of ignimbrites are known throughout the Central

Andes from 14°S to 22°S to 28°S, some of which have been well mapped, dated and analyzed (e.g. Incapillo Caldera, Goss et al., 2009). Other, older plateau-forming and valley-filling ignimbrites, in particular in northernmost Chile and southernmost Peru are less well studied, but a stratigraphic framework exists (e.g. Lebtí et al. 2006; Noble et al., 1979; Quang, 2005; Thouret et al., 2007; Tosdal et al., 1984; Wörner et al. 2002).

However, we need to better understand the role of ignimbrite volcanism in the evolution of the Central Andean active margin with respect to crustal thickening, deformation and magmatic additions throughout the orogen and through time. Therefore we need to estimate erupted ignimbrite magma volumes and compositions for the entire past 25 Ma since crustal shortening and thickening began in all regions of the Central Andes. To that end, we have compiled published and new data on age, distribution and composition of ignimbrite deposits throughout the CVZ. This compilation is provided as globally available Web Mapping Application (WMA) and was used for a temporal and spatial analysis of volume, composition and ages of ignimbrite magmatism during the Neogene. New area and volume calculations, together with published data, are used to model temporal and spatial patterns of ignimbrite eruptions. Furthermore, our Andean Ignimbrite Database (AID) allows the application of advanced statistical methods for compositional data analysis (Aitchison and Greenacre, 2002; Buccianti et al., 2006), which is implemented into GIS and Statistica<sup>1</sup> for cluster and discriminant analysis on log-ratio transformed data, using major and trace elements. The increase in computational power and GIS technology allows us to apply and combine these methods to this large dataset and provide the first comprehensive analyses of Central Andean ignimbrite magmatism through space and time.

## 2 Methods

---

### 2.1 X-ray Fluorescence Spectrometry (XRF)

---

19 ignimbrite samples from Southern Peru were analyzed for major and trace elements using XRF (major elements) and ICP-MS analysis (trace elements). XRF allows the routine analysis of rocks, minerals, soils and solid synthetic materials. X-ray spectrometry has the capability to determine all elements of the Periodic Table from B to U.

The samples were prepared for measurement as glass disks. Because the surface and homogeneity of the specimen are essential for the accuracy and precision of the determination, we use a fully automated fusion technique, SGE 21 from Schoeps. This

---

<sup>1</sup> Software package by Statsoft: <http://www.statsoft.de/>

minimizes potential errors usually associated with manual preparation methods. The glass disks are used for both major and trace element determination and are prepared by using mixtures of lithium tetraborate and lithium metaborate. For the dilution 4200 mg of flux and 700 mg of sample are weighed in platinum-gold crucibles and fused for 15 min at 1100°C. The melt is poured into pre-heated, polished 32 mm-diameter moulds.

Major elements (SiO<sub>2</sub>, TiO<sub>2</sub>, Al<sub>2</sub>O<sub>3</sub>, MnO, MgO, CaO, Na<sub>2</sub>O, K<sub>2</sub>O, P<sub>2</sub>O<sub>5</sub>, Fe<sub>2</sub>O<sub>3</sub> given in wt-%) were analyzed using the SSTmAX-4-kW rhodium target X-ray tube for sample excitation. The XRF spectrometer (AXIOS-Advanced, PANalytical), is equipped with seven mostly laterally curved monochromators PX-10, LiF 220, InSb111, Ge111, PE002, PX-8 and PX-1. Flow-, scintillation-, and sealed Xe-counters are used and pulse-height selection is applied to reduce interferences from higher order spectral lines and background noise. The analytical precision is better than 1-2%. Detection limits vary from 3 to 0.5ppm for most of the measured trace elements.

## 2.2 Inductively Coupled Plasma Mass Spectrometry (ICP-MS) analysis

---

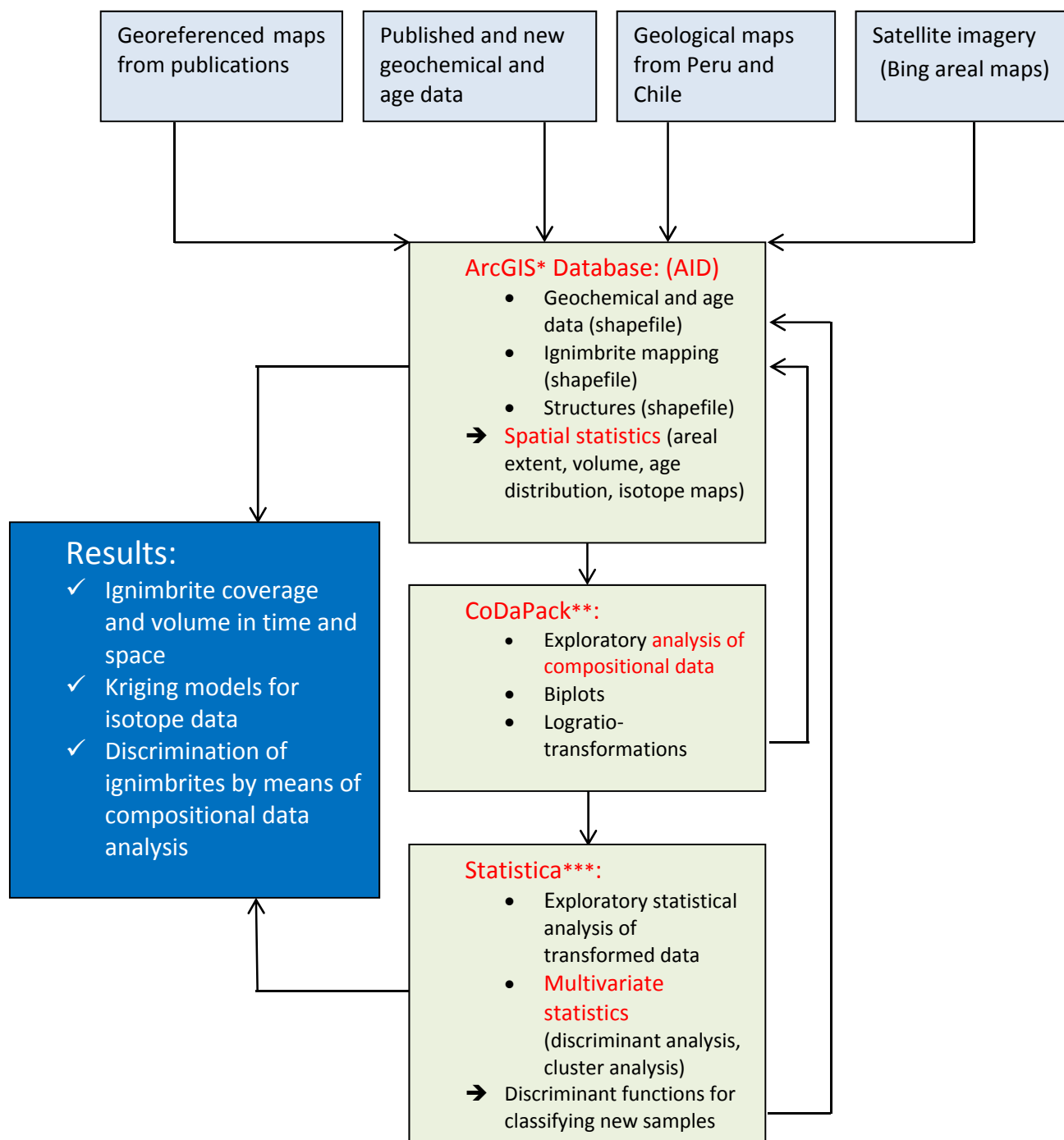
Trace elements were determined by ICP-MS analysis using a FISIONS VG PQ STE instrument with a VG UV-Microprobe laser system (266 nm). 100 mg of sample powder was dissolved under pressure in a mixture of 3 ml HF and 3 ml HClO<sub>4</sub> using the DAS 30 system of Pico Trace GmbH in Göttingen .

## 2.3 Database compilation and mapping

---

We constructed a GIS based database (Andean Ignimbrite Database, AID) for ignimbrites of the Andes with four main objectives: (a) to compile data from a growing amount of literature and to make it globally available and comparable for other researchers; (b) to put our newly dated and mapped ignimbrites of Southern Peru into context with the Miocene magmatic history of the Andes; (c) to apply multivariate statistics on compositional data of ignimbrites (d) use spatial statistics to model ignimbrite eruptions through time and space (Fig.1). A major innovation of the statistical approach was made by including log-ratios for the compositional data array (major and trace elements). This was done to avoid problems inherent in compositional data in the simplex like spurious correlation and sub-compositional incoherence (Pawłowsky-Glahn, 2006).

Manuscript IV - Temporal and compositional patterns and variations in ignimbrite volcanism in the Andes over the past 30 Ma



\* Software package © ESRI (<http://www.esri.de/>)

\*\*Software package © Dept. of Computer Science and Applied Mathematics  
<http://imae.udg.edu/codapack/>

\*\*\* Software package © StatSoft. Inc. 1984-2011 <http://www.statsoft.com/>

Fig. 1: Conceptual outline of analysis conducted in this chapter.

Geochemical and age data was compiled from literature and new analysis. The database includes metadata (e.g. references, names, location) major and trace elements, geochronologic information and isotope data. Mapping of ignimbrites was done by georeferencing and digitizing published, geological maps and by using satellite imagery and our own observations in the field. References are given for each ignimbrite and, where possible, further references about research on this particular ignimbrite are also included in the database. The AID has no claim on completeness and compiling was finalized in January 2013 but will hopefully be further extended with time.

## 2.4 Statistical analysis

---

A GIS database is a powerful tool to systematically analyze an amount of data that is no longer manageable without proper statistical methods. To address issues described Section 1, several approaches were used and are summarized in Fig. 1. As shown, analysis is basically divided into spatial statistics conducted in GIS and multivariate statistics of compositional data conducted in CoDaPack and Statistica and re-imported into GIS.

### 2.4.1 Geospatial statistics

---

#### 2.4.1.1 *Kriging models for variations in isotopes reflecting crustal domains*

---

As various studies have shown, lead isotopic compositions of igneous rocks in the central Andes reflect the composition of the underlying basement and thus delineate crustal domains (Aitchison et al., 1995; Mamani et al., 2008; Mamani et al., 2010; Wörner et al., 1992). Mamani et al. (2008) included metamorphic, intrusive and volcanic (lava and ignimbrite samples) for delineating crustal domains based on lead, strontium and neodymium isotopes. As argued by Mamani et al. (2008), lead isotopes represent the most reliable crustal signature and igneous rocks traversing the whole crustal column may well be a better “probe” to the composition than older intrusive and metamorphic rocks. Based on these findings, we developed statistical kriging models for lead isotopes. This allowed us to calculate a prediction surface and to estimate the confidence in any interpolated value based on the theory of regionalized variables (Oliver and Webster, 1990).

450 lava samples and 115 ignimbrite samples were included in the process. Exploratory data analysis was conducted to better understand the nature of the dataset and to see, whether the basic assumptions for kriging techniques were met. These assumptions are that data is continuous, not spatially clustered, spatially auto-correlated, stationary and normally

distributed. Unlike deterministic interpolation models, geostatistical interpolation methods such as kriging provide standard error values that indicate the accuracy of the prediction. To find the best predictive surface, parameters of the model have to be optimized during the kriging process and several models were compared and validated with a subset of random points that was used to test predictions based on the remaining data set kept apart before providing final results. Kriging models were calculated for  $^{208}\text{Pb}/^{206}\text{Pb}$ ,  $^{207}\text{Pb}/^{206}\text{Pb}$ ,  $^{204}\text{Pb}/^{206}\text{Pb}$  and for  $^{144}\text{Nd}/^{143}\text{Nd}$  isotopes. An inverse distance weighted (IDW) surface was calculated for  $^{87}\text{Sr}/^{86}\text{Sr}$  isotopes because data did not meet all criteria for kriging. In order to enhance differences, a Principal Component Analysis (PC) was computed for the five surfaces. The first PC should reflect most variance and therefore differences in the isotopic compositions. Results were used for delineating changes in basement composition as well as crustal assimilation as suggested by Mamani et al. (2008).

#### *2.4.1.2 Areal extent and volumes of ignimbrites through time as a measure of ignimbrite “flare-ups” during Andean orogeny*

---

Significant interest in caldera-forming explosive volcanism is due to its association with extreme hazard and environmental impact at all scales and because they are windows through which we can view formation of batholiths and their related magmatic systems vital to the evolution of the continental crust (De Silva and Gosnold (2007). The link between flare-ups and batholith formation has been demonstrated by Ducea (2001) for the Sierra Nevada Batholith in California and was also proposed by Hamilton and Myers (1967;) and Lipman (1984). Quantifying eruptive volume of ignimbrites over time is therefore vital to better understanding the evolution of the continental crust of the active continental margin of the Andes.

Our database, in UTM projection, provides the most complete ignimbrite mapping on an Andean scale. However, for area calculations, data had to be projected in the South America Albers Equal Area Conic Projection. Volume calculations are complicated by: (a) no information about paleo-topography; (b) variable unit thickness; (c) uncertainty in correlating packages of ignimbrites to single vs. multiple eruptions; (d) lack of information for many ignimbrites. Our new calculations were made using an average thickness of 50 m (as proposed by Salisbury et al. (2011) and are given as dense rock equivalent (conversion factor of 0.75, following Salisbury et al. (2011)) for all minor ignimbrites. For the 14 Ma Huaylillas ignimbrites, the Nazca ignimbrites and the “Oxaya-province” ignimbrites (Oxaya ignimbrite + part of the 19 Ma “Huayllias Formation”), we propose new minimum estimates for areal coverage and calculated the respective volumes based on averaged thickness

(Huaylillas: 200 m, Nazca outflow sheet: 100 m), and approximated thickness using interpolation techniques to calculate the 3D minimum surface volume (Oxaya-province ignimbrites). For the Nazca ignimbrites, we assume a minimum 3:1 intra-caldera:outflow ratio, as detailed mapping of the Pampas Galeras caldera was not published (Noble et al., 1979). For ignimbrites studied in detail, we compiled volume calculations and included them into the database. We then compare areal extent to eruptive volume of ignimbrites through time on an Andean scale and for five N-S segments separately in order to find spatial and temporal patterns in ignimbrite eruptions.

## 2.4.2 Multivariate statistics on compositional data

---

The composition of Andean ignimbrites has been discussed in many publications (e.g. De Silva and Francis, 1989; Kay et al., 2010; Lindsay et al., 2001b; Schnurr et al., 2007). However, these publications focus on selected areas and use common element ratios and geochemical plots to visualize differences in ignimbrites. Furthermore, the compositional range of ignimbrites is very restricted in comparison to lava samples as they are close to eutectic melts. Differences in composition may have several reasons, ranging from differences in source to process-related differences (e.g. assimilation, contamination, fractional crystallization). In this study we present the first approach of multivariate statistics on compositional data by using log-ratio transformation on an Andean-wide scale. This allows dealing with the following questions concerning ignimbrites: Are there differences in composition depending on location or age? Are there different groups of ignimbrites reflected in their composition? Does the basement have any influence on composition, similar to lead provinces discussed in the previous chapter? If there are significant differences in composition- what are the controls and processes responsible?

By exploring our transformed dataset and by applying methods of multivariate statistics, we will, step by step, get closer to answering the above stated questions. Two attribute fields were calculated as indices for analysis and for better data handling. Ignimbrite sheets are related to their source calderas with a "Caldera\_ID". "Ignimbrite\_ID" is used for grouping during multivariate analysis and also relates samples to mapped ignimbrites. Centered Log-ratio transform (clr) was conducted in CoDaPack for 1: Major elements only; 2: Rare Earth Elements (REEs); 3: Selected Large Ion Lithophile Elements (LILE) and High Field Strength Elements (HFSE). The centered log-ratio transform is calculated as:

$$clr(x) = z = \left[ \ln \frac{x_1}{g(x)}; \dots; \frac{x_D}{g(x)} \right] \text{ with } g(x) = \sqrt[D]{x_1 \dots x_D}$$



This three-fold approach was necessary for hierarchical cluster analysis. As compositional vectors can only be computed for complete datasets, the number of samples is reduced in each step due to missing values. Transformed data was imported into ArcGIS and Statistica for further analysis. Exploratory data analysis, cluster analysis and discriminant analysis were conducted in Statistica in order to gain information about compositional variations of ignimbrites. Cluster analysis is an exploratory data analysis tool which aims at sorting objects into groups (“clusters”) in a way that the degree of association between two objects is maximal if they belong to the same group and minimal otherwise. It helps to discover structures in data without explaining why they exist. We use k-means clustering algorithm provided in Statistica with squared Euclidean distance as measure of distance. We use compositional biplots and other exploratory data analysis tools to explain clustering results and the general structure of compositional data and show how clustering results relate to traditional geochemical parameters.

Discriminant Function Analysis can be used to determine which variables can be used to discriminate between groups (e.g. different ignimbrites). We use this method to test whether ignimbrites have a “compositional signature” that can be used for discrimination and thus “fingerprinting” ignimbrites.

### 3 Results and Discussion

---

#### 3.1 Database compilation and mapping

---

In total, the database includes 201 ignimbrites and calderas (and some related domes) of the Andes, with information about age, eruptive volume, area, description, caldera, related faults and references. Furthermore, age data, major and trace elements and isotopic data for 1,672 ignimbrite samples is provided. To make the database available worldwide for other scientists, it is published as WMA “Andes Ignimbrite Database” at: [www.arcgis.com/](http://www.arcgis.com/)

The whole database used in this study, including all results and metadata is provided separately on DVD. Authors interested in using the database and in adding or improving information are welcome to contact me and receive permission for editing. Thus, information can continually be improved, updated and used for further investigations.

New major and trace elements determinations for 19 ignimbrites of Southern Peru are reported in Table 1.

Table 1: Major and trace element analysis

Sample	ANDA-11-01	ANDA-11-02	ANDA-11-05	CHAV-11-21	PIG-11-01	PIG-11-04	SAN-11-04	SAN-11-06	PIG-12-45	PIG-12-09	PIG-12-08	PIG-12-10	PIG-12-22	PIG-12-28	PIG-12-11	PIG-12-03	PIG-12-07	COTA-08-01	COTA-08-09
sample																			
type*	p	v	p	p	v	p	p	v	p	a	a	a	p	a	p	v	p	v	v
Lat.	-73.942	-73.939	-73.907	-73.983	-73.656	-73.533	-73.586	-73.709	-73.549	-74.186	-74.242	-74.186	-72.264	-72.561	-74.186	-74.326	-74.312	-72.758	-72.703
Long.	-14.448	-14.445	-14.345	-14.637	-14.456	-14.224	-14.586	-14.636	-14.178	-14.127	-14.104	-14.126	-15.043	-14.709	-14.126	-13.941	-13.968	-15.137	-15.084
SiO <sub>2</sub>	71.33	67.43	71.37	71.31	59.05	72.34	72.04	69.77	71.16	65.22	68.06	64.07	58.93	71.83	66.36	64.52	59.49	62.27	73.93
TiO <sub>2</sub>	0.20	0.52	0.16	0.22	1.18	0.12	0.13	0.39	0.17	0.44	0.30	0.41	0.80	0.13	0.38	0.78	1.02	0.12	0.14
Al <sub>2</sub> O <sub>3</sub>	13.30	15.12	13.29	13.71	16.69	12.22	12.67	14.19	12.79	16.95	14.76	15.73	16.96	12.36	14.18	14.26	14.42	10.88	13.30
FeOt	1.14	2.30	0.99	1.10	5.51	0.84	1.03	1.53	1.09	1.75	1.24	1.84	4.37	0.85	2.31	3.22	4.64	0.71	0.79
MnO	0.06	0.07	0.10	0.08	0.13	0.05	0.07	0.05	0.08	0.09	0.10	0.08	0.09	0.07	0.06	0.07	0.10	0.06	0.06
MgO	0.19	0.62	0.36	0.23	1.94	0.22	0.29	0.26	0.15	0.83	0.32	0.97	2.04	0.09	0.58	0.81	1.34	0.09	0.10
CaO	0.84	1.64	0.63	0.91	4.28	0.83	0.58	0.88	0.75	1.91	1.24	2.22	4.07	0.42	1.53	2.04	3.10	0.54	0.74
Na <sub>2</sub> O	2.51	3.69	2.67	3.34	3.80	2.48	2.22	3.91	2.73	2.42	2.72	2.33	3.04	3.36	2.02	3.41	4.06	4.18	4.34
K <sub>2</sub> O	5.39	5.29	4.65	4.43	3.55	5.79	6.25	5.46	5.77	3.49	4.62	3.47	3.80	4.92	3.92	4.65	4.07	3.85	4.27
P <sub>2</sub> O <sub>5</sub>	0.04	0.07	0.06	0.04	0.49	0.05	0.02	0.03	0.03	0.08	0.07	0.10	0.25	0.01	0.08	0.18	0.38	0.02	0.02
total	98.97	99.70	99.76	98.27	98.69	99.14	99.61	99.45	94.83	93.37	93.57	91.43	94.84	94.14	91.69	94.30	93.13	82.80	97.78
LOI	4.81	2.97	5.58	4.40	3.06	4.84	4.58	3.30	2.62	6.02	4.95	5.95	2.88	4.73	5.99	2.75	1.65	0.58	0.62
La	40.85	58.62	15.74	44.81	66.07	43.80	41.61	63.54	38.05	40.06	38.36	37.47	50.32	35.87	34.42	42.66	46.15	29.42	35.60
Ce	63.89	98.67	28.52	71.61	111.56	71.55	67.10	105.09	69.02	73.47	68.10	66.83	91.49	59.32	60.19	82.84	90.65	54.86	64.11
Pr	7.20	11.22	3.32	7.80	14.25	7.80	7.76	11.88	7.85	7.97	8.04	7.53	10.93	5.92	6.93	10.43	11.72	6.08	7.03
Nd	25.45	40.84	12.50	27.78	58.19	27.56	27.33	42.89	26.10	27.48	28.27	26.04	37.86	16.76	23.55	39.84	45.93	19.53	22.22
Sm	4.36	6.71	3.13	4.53	10.97	4.83	4.74	7.05	4.48	4.50	4.71	4.24	6.24	2.68	4.03	7.85	9.18	3.32	3.59
Eu	0.74	1.36	0.61	0.77	2.33	0.53	0.57	1.16	0.63	1.10	1.04	1.08	1.48	0.20	0.91	1.43	1.85	0.60	0.70
Gd	3.71	5.37	3.64	3.98	9.77	4.09	3.97	5.67	3.57	3.56	3.71	3.34	4.96	2.38	3.23	6.30	7.36	2.64	2.83
Tb	0.50	0.71	0.63	0.53	1.27	0.54	0.53	0.74	0.41	0.41	0.45	0.39	0.54	0.29	0.39	0.84	0.95	0.31	0.31
Dy	2.92	4.03	4.38	3.14	7.13	3.02	3.04	4.21	2.09	2.14	2.38	2.00	2.63	1.64	2.03	4.61	5.14	1.58	1.59
Ho	0.54	0.75	0.89	0.59	1.30	0.54	0.55	0.79	0.38	0.42	0.46	0.39	0.49	0.34	0.39	0.88	0.96	0.29	0.29
Er	1.73	2.34	2.60	1.89	3.81	1.68	1.67	2.50	1.09	1.28	1.33	1.19	1.44	1.10	1.20	2.51	2.67	0.86	0.87
Tm	0.22	0.29	0.37	0.26	0.44	0.21	0.20	0.32	0.18	0.23	0.24	0.21	0.23	0.21	0.21	0.43	0.44	0.15	0.14
Yb	1.55	1.97	2.56	1.83	2.81	1.41	1.33	2.16	1.27	1.66	1.72	1.58	1.64	1.60	1.56	2.96	2.94	1.09	1.09
Lu	0.23	0.28	0.36	0.27	0.40	0.20	0.19	0.31	0.18	0.25	0.25	0.24	0.24	0.23	0.23	0.42	0.42	0.15	0.15
Y	15.96	21.36	28.77	18.62	37.09	15.84	17.17	23.58	13.00	14.02	15.21	13.30	16.24	13.14	13.89	27.45	29.42	10.40	10.36
Rb	200.22	273.96	138.67	158.68	133.07	150.28	163.50	244.67	150.87	114.30	140.27	115.99	183.51	176.55	161.64	173.66	160.71	132.64	126.83
Sr	109.73	235.59	86.17	123.11	474.08	48.55	36.84	135.84	96.70	242.32	144.53	258.10	461.80	21.78	172.29	164.55	219.85	76.76	116.91
Ba	649.32	1054.37	680.54	726.21	939.52	243.15	177.94	900.12	325.16	865.26	875.49	779.29	861.55	60.98	819.32	813.59	803.47	960.61	997.60

Table 1 (continued)

Sample	ANDA-11-01	ANDA-11-02	ANDA-11-05	CHAV-11-21	PIG-11-01	PIG-11-04	SAN-11-04	SAN-11-06	PIG-12-45	PIG-12-09	PIG-12-08	PIG-12-10	PIG-12-22	PIG-12-28	PIG-12-11	PIG-12-03	PIG-12-07	COTA-08-01	COTA-08-09
sample type*	p	v	p	p	v	p	p	v	p	a	a	a	p	a	p	v	p	v	v
Lat.	-73.942	-73.939	-73.907	-73.983	-73.656	-73.533	-73.586	-73.709	-73.549	-74.186	-74.242	-74.186	-72.264	-72.561	-74.186	-74.326	-74.312	-72.758	-72.703
Long.	-14.448	-14.445	-14.345	-14.637	-14.456	-14.224	-14.586	-14.636	-14.178	-14.127	-14.104	-14.126	-15.043	-14.709	-14.126	-13.941	-13.968	-15.137	-15.084
Cs	14.50	17.31	6.96	7.95	6.53	3.95	4.34	18.54	4.19	10.14	11.84	9.82	48.90	5.97	21.98	15.47	11.28	2.83	2.71
U	6.05	8.53	3.32	5.23	3.54	2.97	3.22	10.01	3.25	4.10	3.86	3.87	5.43	7.76	4.97	7.43	6.87	3.38	3.33
Th	16.80	29.66	9.50	18.14	14.73	13.26	14.36	34.09	14.80	14.87	12.68	13.39	24.22	32.13	15.60	22.85	21.83	14.47	14.82
Pb	24.31	23.93	20.31	18.88	30.40	18.17	21.48	26.40	19.44	24.03	22.69	21.78	13.81	26.41	23.93	24.67	18.79	17.57	17.42
Hf	3.33	7.27	2.58	3.88	10.03	3.98	4.05	7.75	3.83	7.43	4.90	6.53	6.26	5.29	5.73	10.71	10.58	3.60	3.65
Zr	93.61	238.55	63.19	107.14	390.68	95.67	102.83	246.48	84.53	207.74	152.17	238.93	208.14	114.29	193.58	275.31	275.10	86.49	89.42
Nb	14.23	15.71	19.67	15.35	19.65	16.25	16.76	17.16	14.71	14.33	15.18	12.89	13.90	21.97	12.86	17.36	18.08	12.05	11.83
Ta	1.29	1.09	1.35	1.23	1.09	1.06	1.08	1.22	1.01	1.09	1.08	0.99	1.03	1.59	1.03	1.34	1.29	0.97	0.96
Sc	3.50	4.94	3.02	3.80	8.90	2.98	2.97	4.35	3.56	3.39	3.50	3.32	8.26	2.42	3.96	9.66	11.35	2.53	3.16
Cr	35.99	28.37	29.51	33.17	30.03	44.88	29.31	28.25	25.46	30.07	32.44	27.93	28.75	25.87	26.35	41.73	36.40	34.38	25.94
Ni	8.78	24.75	6.64	7.52	44.87	6.05	7.26	14.69	1.26	1.05	0.49	1.01	10.11	0.37	2.09	2.16	0.98	9.20	0.22
Co	1.17	3.25	0.85	0.90	8.76	0.67	1.56	0.78	1.01	1.51	0.57	1.36	10.91	0.26	2.57	4.70	6.95	1.16	0.20
Cu	3.03	6.53	2.86	2.87	13.17	7.71	8.44	3.14	10.60	2.23	1.59	2.16	32.96	1.21	6.24	8.73	9.80	7.09	1.46
Zn	45.41	65.99	53.70	47.31	123.79	39.93	49.28	54.72	44.59	70.95	66.02	65.15	77.18	53.24	66.43	75.11	90.55	41.30	42.34
V	28.16	30.37	24.62	26.12	41.35	31.71	23.34	25.29	19.07	20.51	19.06	20.57	70.05	16.39	29.94	57.63	58.95	16.09	15.73

\* p= pumice, v = vitrophyre, a= Major elements (oxide weight-%) and Y (ppm) were obtained by XRF, trace elements are given in airfall ppm and were obtained by ICPMS

## 3.2 Statistical analysis

---

### 3.2.1 Geospatial statistics

---

Lavas and ignimbrites of a broad range of SiO<sub>2</sub> contents (54 wt% to 78 wt%) have previously been shown to have the isotopic composition of the local basement (Mamani et al., 2008; Mamani, 2009). This observation of a relatively constant “isotopic baseline value” means that extensive differentiation and assimilation takes place in the lower crust, in a MASH zone (Hildreth and Moorbath, 1988) before further differentiation at shallower levels. Furthermore, mass balance constraints on hyperbolic mixing relations, especially for lead isotopes, result in almost complete “crustal” values at even low proportions of assimilation. Thus, we can use isotope data of lava samples and ignimbrites (assuming that the distance from source to deposition is much smaller than the scale of crustal domains) and propose kriging models to better delineate crustal domains.

#### 3.2.1.1 *Kriging models and Principal Component analysis (PCA) for variations in lead, strontium and neodymium isotopes reflecting crustal domains*

---

##### 3.2.1.1.1 *Exploratory data analysis*

In order to fulfill the basic assumptions for a valid kriging model, data has to be checked for normal distribution, clustering, auto-correlation, stationarity and trends. First of all, the ignimbrite and lava dataset was compared to the previously used data including metamorphic and intrusive rocks (Fig.2A-C) (Mamani et al., 2008; Mamani, 2010). We found that metamorphic rocks and, to a lower degree, intrusive rocks show much more variability in lead isotopes than ignimbrites or lava samples as exemplified in Fig.2A-C for <sup>206</sup>Pb/<sup>204</sup>Pb. The mean value is different for metamorphic rocks while the median is very similar to the other groups. This is also reflected in the semivariograms of both datasets. Including only ignimbrite and lava samples fits model assumptions much better than the “noisier” dataset including metamorphic and intrusive rocks. The dataset of the AID including only Tertiary lava and ignimbrite samples was then checked for normal distribution, auto-correlation, trends, stationarity and clustering (histograms, normal Q-Q plots, Voronoi maps (Entropy) and semivariogram clouds). An example is given in Fig. 3A-D. After removing outliers, the above stated assumptions were accepted for each dataset. 505 samples (<sup>206</sup>Pb/<sup>204</sup>Pb), 515 samples (<sup>208</sup>Pb/<sup>204</sup>Pb), 539 (<sup>207</sup>Pb/<sup>204</sup>Pb) and 407 (<sup>144</sup>Nd/<sup>143</sup>Nd) samples were used in the models and 30 (56 <sup>206</sup>Pb/<sup>204</sup>Pb) for validation, respectively (see Appendix B for model summaries).

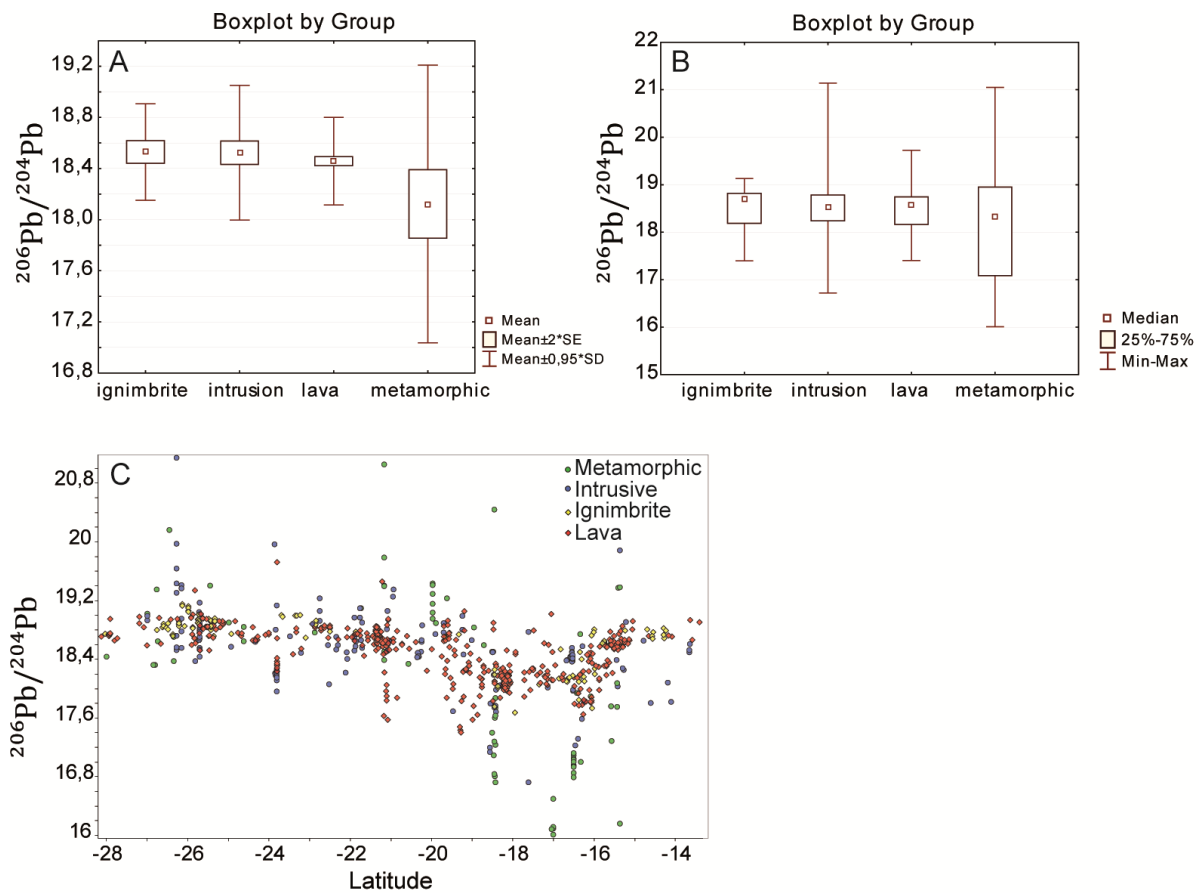


Fig. 2: Comparison of lead isotope data by sample type. A: Boxplots of  $^{206}\text{Pb}/^{204}\text{Pb}$  variations shown around the mean value for the respective groups (ignimbrites, intrusions, lava and metamorphic). B: same as A but variations are shown around the median. C:  $^{206}\text{Pb}/^{204}\text{Pb}$  values plotted along latitude.

### 3.2.1.1.2 Kriging

Predictive surfaces and prediction standard error maps for  $^{208}\text{Pb}/^{204}\text{Pb}$ ,  $^{207}\text{Pb}/^{204}\text{Pb}$ ,  $^{206}\text{Pb}/^{204}\text{Pb}$ ,  $^{144}\text{Nd}/^{143}\text{Nd}$  and an IDW interpolation for  $^{87}\text{Sr}/^{86}\text{Sr}$  are included in the supplementary database. Simple Kriging proved to return best models for our data and detailed model summaries are given in Appendix A. Fig.4A-B exemplifies results for  $^{206}\text{Pb}/^{204}\text{Pb}$ . Validation results with our data-subset are also included in the database and give mean errors of around zero. The predictions are quite robust but there are areas with very little data that cannot be predicted or validated very well as can be seen in the standard error map. Models were kept as simple as possible as we found that including anisotropy or using nested models could not improve prediction but made results more inaccurate. The

Manuscript IV - Temporal and compositional patterns and variations in ignimbrite volcanism in the Andes over the past 30 Ma

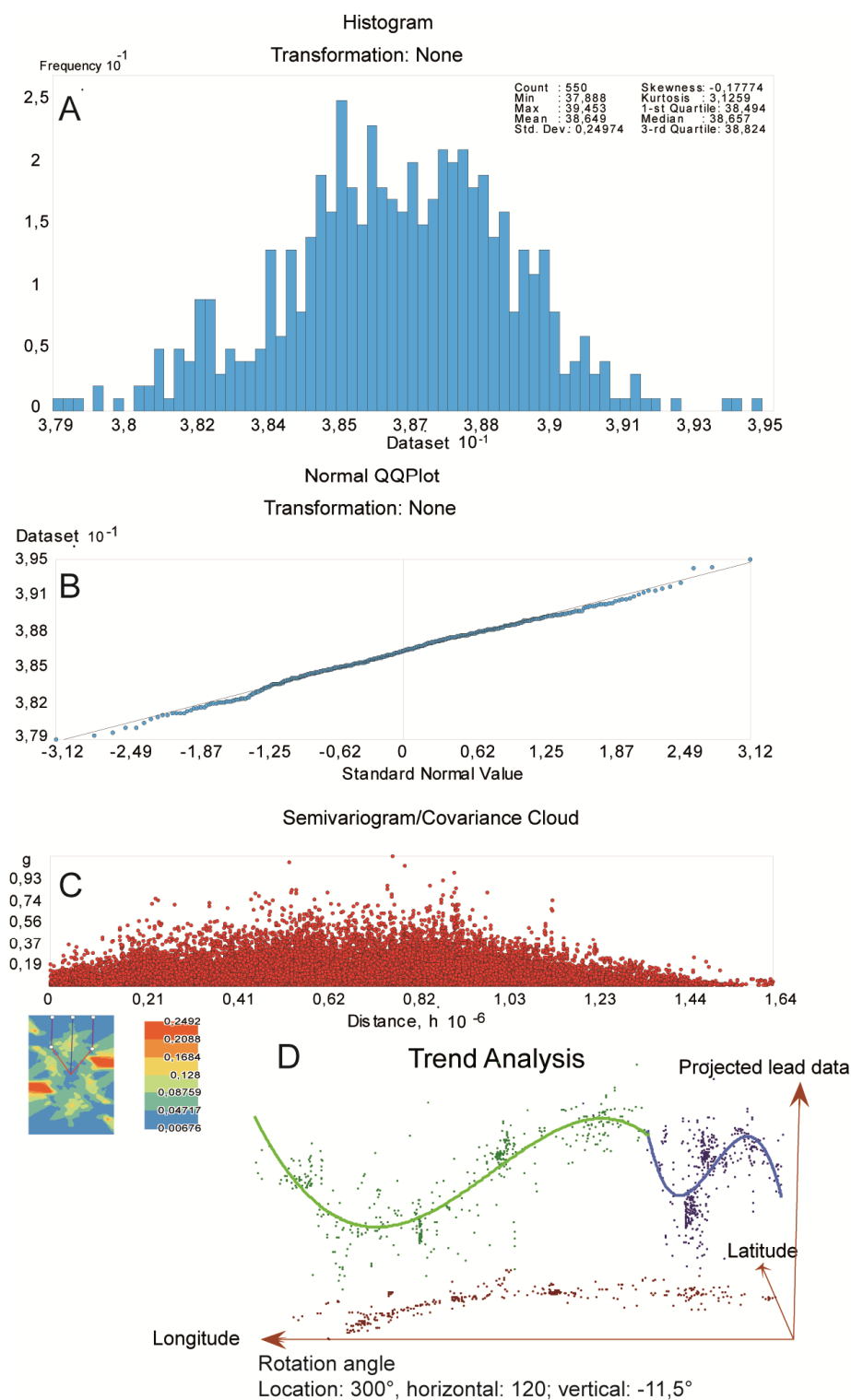


Fig. 3: Exploratory data analysis for  $^{208}\text{Pb}/^{204}\text{Pb}$ . A: Histogram: Normal distribution can be accepted for this dataset; B: Normal Q-Q plot; C: Semivariogram: Model type, major range, sill, partial sill and nugget parameters are estimated here (These parameters are given in Appendix B for each model). Changes in direction (anisotropy parameter) in the semivariogram can also be checked. D: Trend analysis: A global, polynomial trend is clearly visible. This trend corresponds to the change in basement domains.

most important factor to improve modeling would be to have spatially more evenly distributed data.

Comparing our model to the previously published map by (Mamani et al., 2008) with the same classification thresholds, differences are greatest in areas with a low sample density. However, as lead data is rather continuous and shows no real classes, a better way to visualize results is to give a continuous prediction surface with a prediction error. One striking difference are high  $^{206}\text{Pb}/^{204}\text{Pb}$  (and  $^{208}\text{Pb}/^{206}\text{Pb}$ ) values for part of the Mejillones Terrain and low  $^{206}\text{Pb}/^{204}\text{Pb}$  (and  $^{208}\text{Pb}/^{206}\text{Pb}$ ) values within the northern Paracas domain that cannot be due to a modeling error as there are enough samples in this location. This indicates either substructures within the Mejillone and Paracas Terrains or some other process capable of modifying lead isotopes. The samples related to the high values in the Mejillone domain are undated lava samples that are probably quite old (Mesozoic Chocolate arc? Lucassen et al. (2002)) and are therefore different in isotopic values.

$^{206}\text{Pb}/^{204}\text{Pb}$  indicates the same tendency as the other maps with the exception of some more radiogenic values within the Arequipa domain. Estimating lead isotope values for samples based on their location is now possible. Predictions for magmatic rocks are within a narrow error range as could be shown with our data-subset. Prediction errors for areas with a low sample density are still quite high and could be improved by adding more data to the database and re-running the model with or without changes in model parameters.

$^{87}\text{Sr}/^{86}\text{Sr}$  IDW map does not show a very homogeneous surface reflecting mantle and crustal mixtures with more radiogenic values for higher crustal components. As shown by Mamani et al. (2009), lead and strontium isotope ratios are defined by mixing of basement with mantle magma (Fig.5). For  $^{87}\text{Sr}/^{86}\text{Sr}$ , crustal assimilation does not modify values as easily as for lead isotopes due to the less pronounced bend of the  $^{87}\text{Sr}/^{86}\text{Sr}$  mixing hyperbola, and therefore  $^{87}\text{Sr}/^{86}\text{Sr}$  in the model reflects the amount of contamination within a crustal domain rather than the basement signature.

The combined information of all models with a reduction of noise was derived from Principal Component Analysis (PCA) (Fig.6). From five models, 3 PCs were calculated with the first two PCs explaining 99.9 % of the overall variability. The first PC clearly delineates the crustal domains as expected. The second PC still reflects the basement structure but is strongly influenced by the degree of assimilation. The high values within the Arequipa Domain correspond to the samples with a higher degree of assimilation (Direction of the Mollendo basement in Fig. 4). The more pronounced low values of the Mejillones Terrain correspond to the low degree of assimilation and more mafic nature of this area. The third PC reflects residual variations in  $^{87}\text{Sr}/^{86}\text{Sr}$  and  $^{143}\text{Nd}/^{144}\text{Nd}$  and therefore again the degree of

crustal assimilation within the domains (compare vertical axis of Fig. 4). High values correspond to higher  $^{144}\text{Nd}/^{143}\text{Nd}$  while the second PC reflects high  $^{87}\text{Sr}/^{86}\text{Sr}$ .

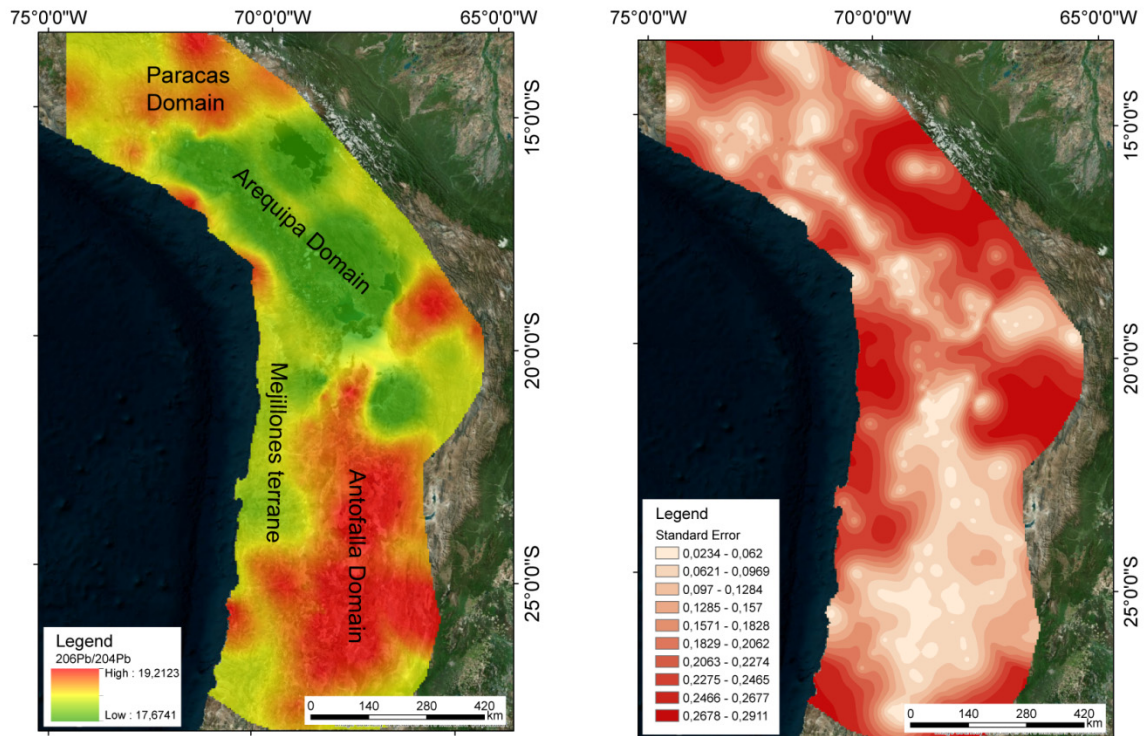


Fig. 4:  $^{206}\text{Pb}/^{204}\text{Pb}$  Kriging model (A) and error surface (B). Lead domains named after Mamani et al. (2010)

Thus, PC analysis can be used to decipher different processes acting simultaneously. The overriding effect of basement isotope signature is captured by PC 1 while the process of assimilation can be shown in PCs two and three. The advantage is noise reduction achieved by reducing dimensions from five original datasets to only three PCs. However, errors involved in the original interpolation models and due to sampling bias are propagated into the analysis and results have to be handled with care.



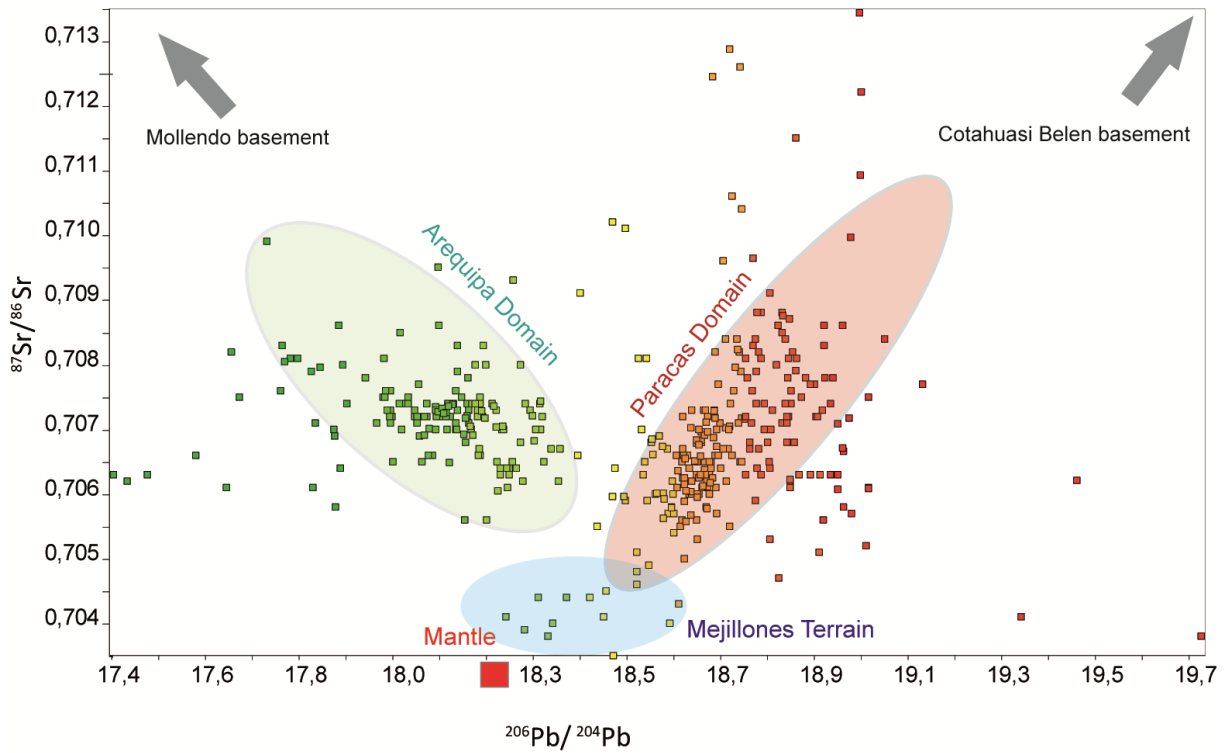


Fig. 5:  $^{87}\text{Sr}/^{86}\text{Sr}$  and  $^{206}\text{Pb}/^{204}\text{Pb}$  ratios for samples used for kriging. Data points are scaled from green to red according to Pb isotope values. As discussed in detail by Mamani et al. (2009), isotope signatures can be explained by mantle magma and crustal assimilation. Values for the basements and mantle used by Mamani et al. 2010 are: Mantle: Jurassic lava close to a mantle source: Sr and Pb contents [ppm] and isotopic ratios are 111/0.7033, 4/18.221, respectively; Paleozoic Cotahuasi basement: Sr and Pb content/ratios are 96/0.735, 11/20 respectively; Proterozoic Mollendo basement: Sr and Pb content/ratios are 150/0.73, 7/17, respectively.

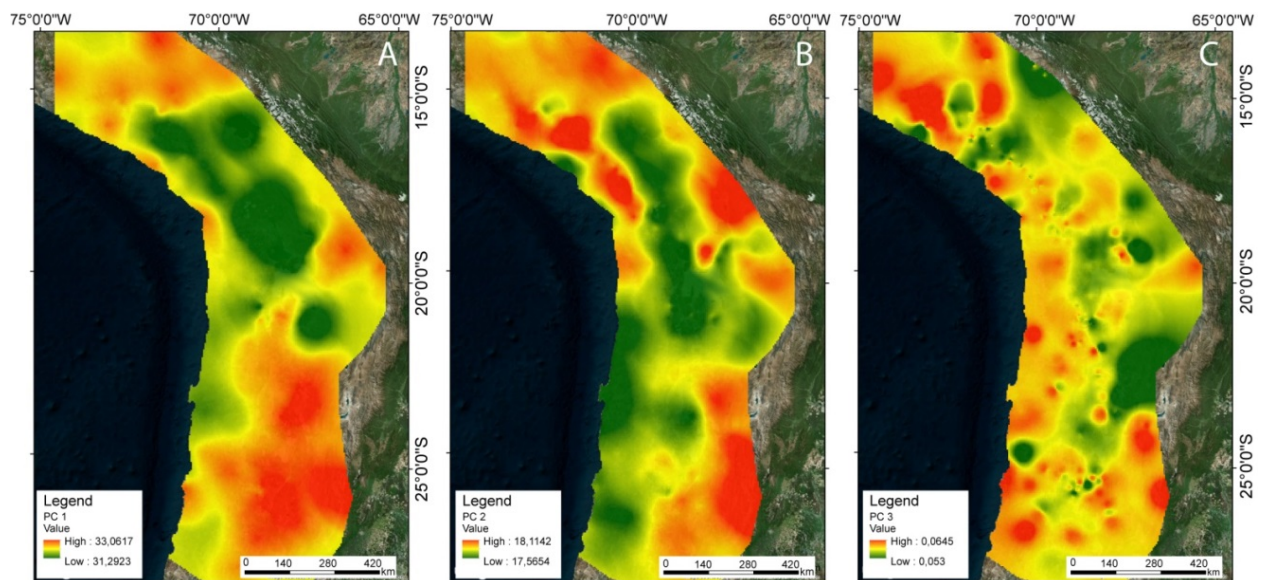


Fig. 6: Results of PC analysis. A: First PC; B: Second PC; C: Third PC.

### 3.2.1.2 Areal extent and volume estimates for ignimbrites through time as a measure of ignimbrite “flare-ups” during Andean orogeny

Apart from isotope data presented in the previous chapter, our database includes the most complete, Andean-scale mapping of ignimbrites. Using South America Albers Equal Area Conic Projection, we calculate the extent and volume (for details of calculated volumes and volumes from literature please refer to the database and Appendix B) of ignimbrites through time and additionally for five segments to find spatial variations in temporal eruption patterns (Figs 7-9).

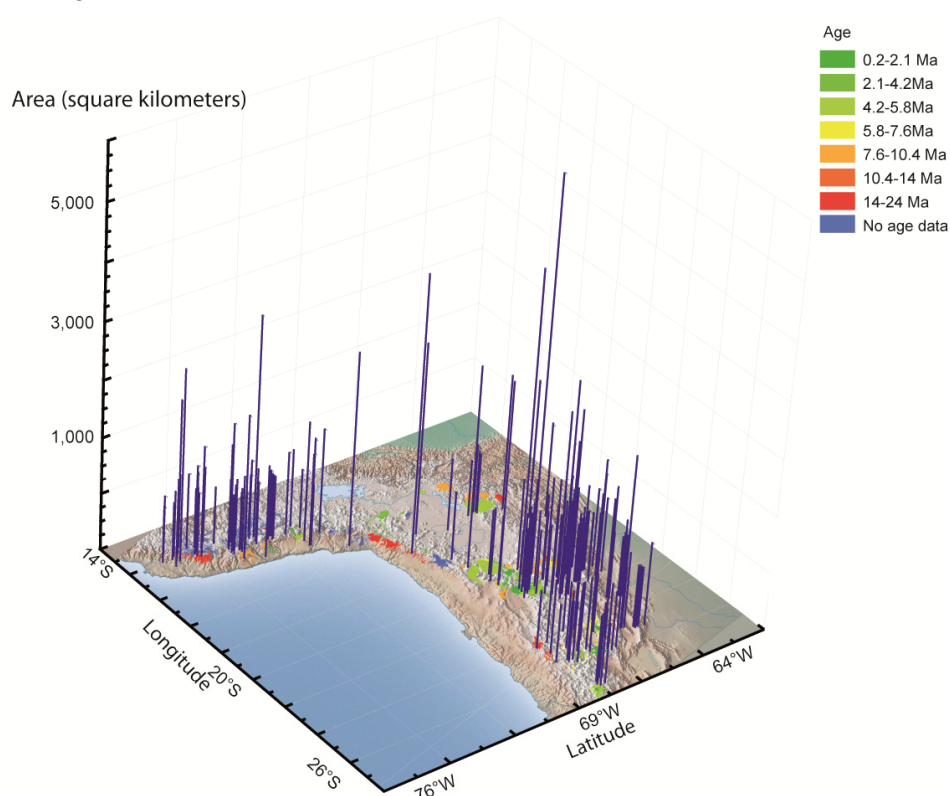


Fig. 7: Ignimbrite eruptions scaled by areal extent are projected on the basemap with mapped ignimbrites classified by age. The areal extent of each ignimbrite is available in the database.

Results for area calculations are shown as overview in Fig. 7 and are available in the database. Ignimbrite eruptions through time, together with a graph showing the respective, cumulative areal extent and volume are shown in Fig. 8 and can be viewed in a video clip (“Andes”) available in the electronic appendix.

The two estimates (area vs. volume) correlate well, with the exception of singular, big eruptions (at 19 Ma the 4,900 km<sup>3</sup> Oxaya ignimbrite, at 14 Ma the 1,800 km<sup>3</sup> Huaylillas

ignimbrites, at 6-4 Ma the big APVC calderas). This is due to extraordinary thickness and intracaldera volumes that are not reflected in the same magnitude using area calculations as aspect ratios of individual ignimbrites can be very different (Walker, 1983)). Relating areal extent to volumes is therefore an oversimplification as volumes generated by big eruptions can be to a great part intra-caldera volumes (e.g. La Pacana (Lindsay et al., 2001a), Vilama (Soler et al., 2007), Cerro Galán (Folkes et al., 2011) have intra-caldera:outflow ratios as large as 4:1 or 5:1), but shows the same trend. Compared to volume calculations, areal extent is better known for many ignimbrites and uncertainties concerning paleo-topography, thickness estimates and the intra-caldera volumes are avoided by using areal extent as a measure for eruptions. However, we cannot derive extrusion rates based on areal extent. Given all the uncertainties, advantages and disadvantages of the respective method, in the following, we combine the two measures in order to benefit of the advantages of both.

Ignimbrite eruptions on an Andean scale, given the resolution of age data, seem to be quite continuous through time, with major pulses at 19-24 Ma (Oxaya, Nazca Group), 14 Ma (Huaylillas ignimbrites), 6 and 8 Ma (many of the Altiplano and Puna ignimbrites like the Galán, Las Termas, Potrerros, Panizos, Vilama and Guacha ignimbrites, Andamarca 1 and 2 ignimbrites), 3-6 Ma (e.g. Atana, Los Frailes, Toconao, Caracote, Chuhuilla) and very young ignimbrites from 0-3 Ma (Lauca-Perez, Purico, Cerro Blanco, Pastos Grande). The minimum cumulative area covered by mapped ignimbrites through time is 90,000 km<sup>2</sup> and the corresponding minimum volume is 30,000 km<sup>3</sup>.

Around 14,000 km<sup>2</sup>/500 km<sup>3</sup> are from ignimbrites without known age. Following the eruptions between 24-16 Ma, a phase of relative quiescence followed. From 10 to 3 Ma, most of the ignimbrites erupted and coverage/volume of 65,000 km<sup>2</sup> /26,000 km<sup>3</sup> is reached. This period includes the three major eruptive pulses (8.4 Ma, 5.5 Ma, 4 Ma) described by (De Silva and Gosnold, 2007; Salisbury et al., 2011) for the Altiplano-Puna volcanic complex (Fig. 10). The strong pulse between 19 to 24 Ma is defined by the ignimbrites on the western flank of the Andes (e.g. Nazca, Oxaya, ignimbrites of the Huaylillas Formation). Many of the ignimbrites lacking radiometric ages are located in Southern Peru (blue color in Fig. 10) probably fall into the 14 Ma class (Huaylillas ignimbrites) and the 19-24 Ma pulse (Alpabamba 1) as described for the lower Cotahuasi region by Thouret et al. (2007). These ages were also found by Brandmeier et al. (Chapter IV) for part of the Andamarca and Puquio Formations in Southern Peru. The 14 Ma age is mainly represented in Southern

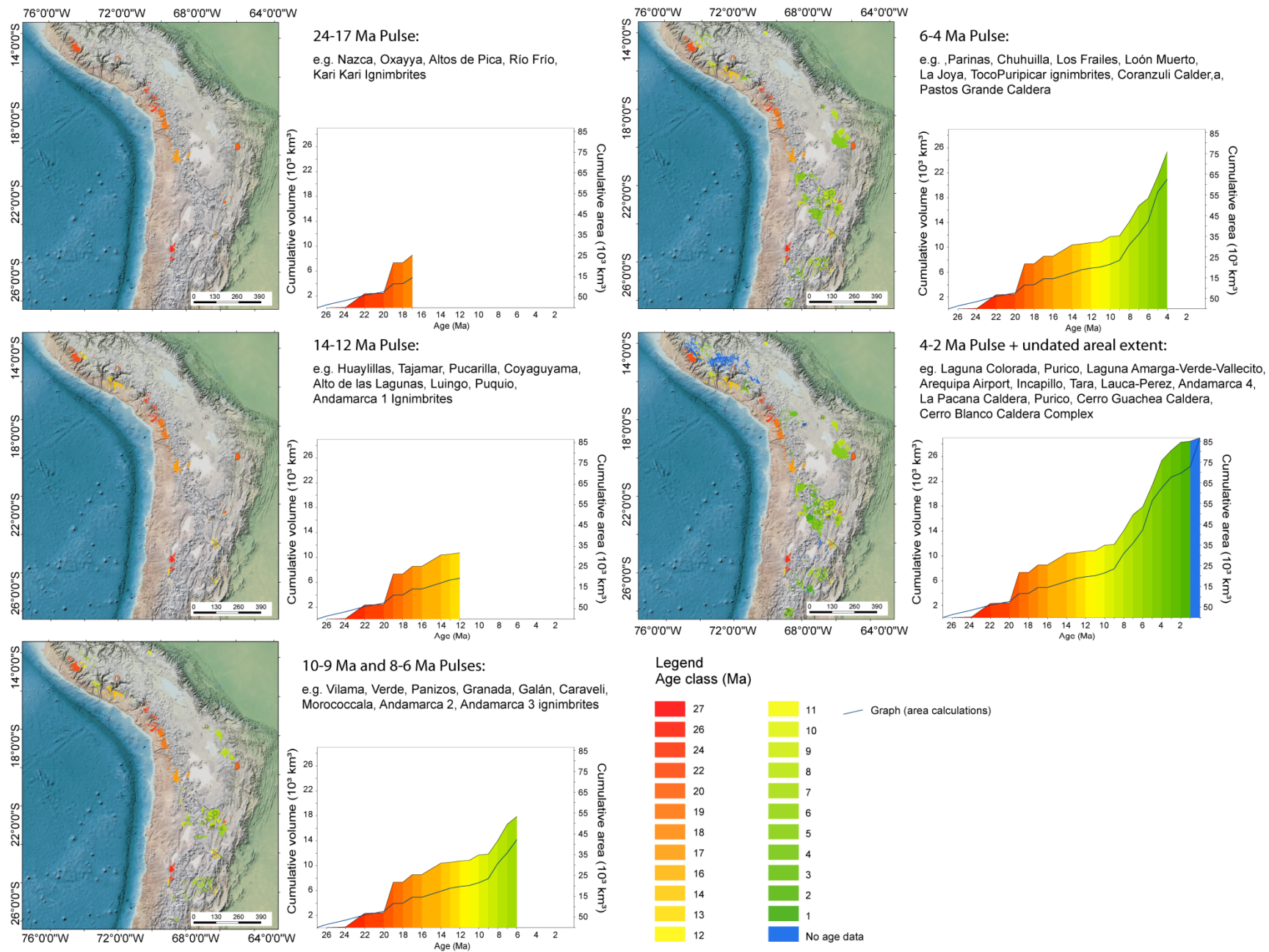


Fig. 8: Volume (calculated and compiled) and areal extent of ignimbrites over time. 5 time-intervals are shown together with cumulative areal extent and volume of ignimbrites. With decreasing age, the total coverage increases in pulses reflecting big eruptions. An Animation video is available as SOM. For details, please refer to the text and database.

Peru (Huaylillas and Andamarca 1 ignimbrites, Thouret et al. (2007), Brandmeier et al. (in prep.) and in some smaller ignimbrites in Chile/Argentina. To closer examine spatiotemporal patterns of eruptions, we divided the database into five segments (Fig. 9).

The first segment (Southern Peru, Western Cordillera) is characterized by present-day flat subduction of the Nazca plate (Gregory-Wodzicki, 2000), whereas in all other segments, the Nazca plate subducts at an angle of  $\sim 30^\circ$ . Segment two is Southernmost Peru with normal subduction, segment three corresponds to great part of the Altiplano ( $15^\circ$  to  $21^\circ$  and related part of the Eastern Cordillera, Western Cordillera (Cordillera Real) and Coastal Cordillera), and includes the Altos de Pica ignimbrite (Baker and Francis, 1978), the Oxaya and Lauca ignimbrites (Wörner et al., 2000; Wörner et al. 2002), the Soledad caldera (Redwood, 1987), the Morococala field (Morgan et al., 1998 and references herein), the Huaylillas Formation (Thouret et al., 2007 and references herein) and the Los Frailes Complex (Morgan et al., 1998 and references herein). Segment four corresponds (but also including the Coranzuli caldera) to the Altiplano Puna Volcanic Complex (APVC) studied by Salisbury et al. (2011) or the Northern Puna ignimbrites (Kay et al., 2010 and references herein) and segment five to the Southern Puna ignimbrite complex of Kay et al. (2010), including the southernmost Incapillo caldera (Goss et al., 2009), the Luingo caldera (Guzmán and Petrinovic, 2010) and smaller ignimbrites described by (Naranjo, 1992; Schnurr et al., 2007; Siebel et al., 2001). The Southern Puna differs from the Northern Puna in that the gradual shallowing of the subducting slab leading to the Chilean-Pampean flat slab starts south of  $\sim 24^\circ\text{S}$  (Kay and Coira, 2009). Furthermore, average topography is higher and lithosphere thinner (Kay and Coira, 2009) and references therein).

Spatiotemporal eruption patterns show that early Miocene eruptions mostly occurred along the western escarpment (e.g. Nazca, Oxaya, Huaylillas Formation, Río Frío ignimbrite (Noble et al., 1979; Schnurr et al., 2007; Thouret et al., 2007; Wörner, 2002)) and, to a minor degree, in the backarc (Kari Kari caldera (Francis, 1981), Verde ignimbrite (Petrinovic et al., 2010)). Eruptions continue until around 10 Ma (e.g. Tajamar ignimbrite, Luingo ignimbrite, Pairique Volcanic complex (Caffe et al., 2012), Los Frailes and Morococala ignimbrites (Kay and Coira, 2009)), accompanied by eruptions in Southern Peru (Andamarca 1 ignimbrites (Brandmeier et al. in prep.), Puquío ignimbrites, Río Chili ignimbrite (Lebti et al. 2006)) and ignimbrites in Chile (e.g. Vicuna ignimbrite, La Ola ignimbrite, Plato ignimbrite, Tamberia ignimbrite, Pedernales ignimbrite (Schnurr et al., 2007; Siebel et al., 2001)). On the Altiplano Puna Volcanic Complex (APVC), eruptions slowly initiated at 10 Ma and the first major pulse occurred at around 9-8 Ma (e.g. Vilama caldera backarc ignimbrites (Soler et al., 2007), Sifón

Manuscript IV - Temporal and compositional patterns and variations in ignimbrite volcanism in the Andes over the past 30 Ma

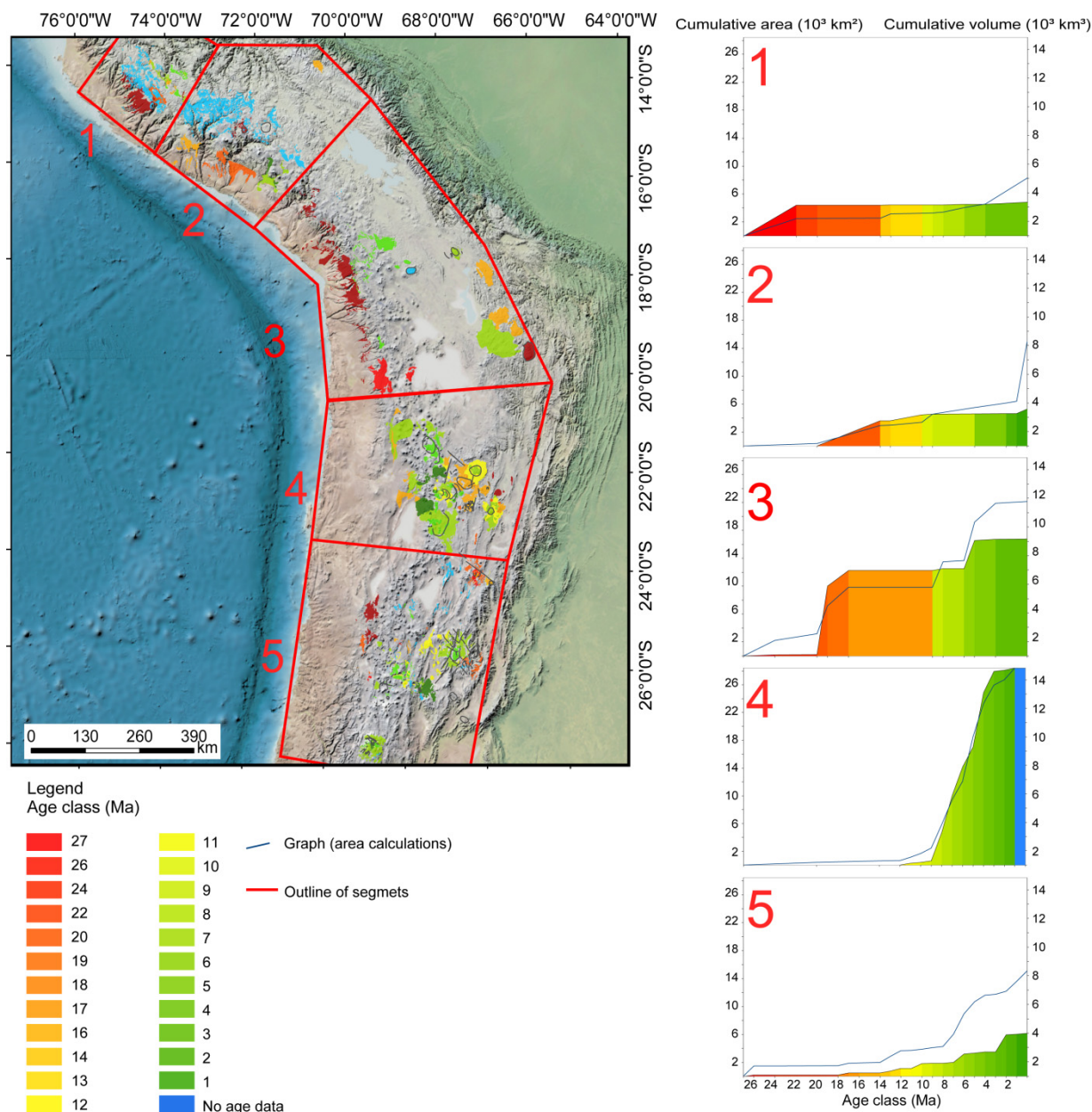


Fig. 9: The cumulative areal extent (blue line) and volume (colored graph) of different N-S segments of the Andes is shown over time. The first segment represents the area, where the Nazca plate subducts at an angle of 2-15° while in the other segments, the angle is 30° (Gregory-Wodzicki, 2000). Segment 3 contains the Altiplano, 4 the northern Puna and segment 5 the southern Puna with southernmost caldera (Incapillo) and the back-arc Cerro Galán Complex.

ignimbrite) as described by De Silva and Gosnold (2007), Kay et al. (2010) and Salisbury et al. (2011). In Southern Peru, the Andamarca 2 ignimbrites erupted (Brandmeier et al. in prep.). The major pulses observed for the APVC (De Silva and Gosnold, 2007; Kay et al., 2010; Salisbury et al., 2011) at ~6 Ma (e.g. Panizos caldera (Ort, 1993; Ort et al., 1996), Coranzuli caldera (Seggiaro and Aniel, 1989) backarc ignimbrites, Pastos Grandes caldera

ignimbrites, Lower Tara ignimbrite (De Silva and Gosnold, 2007) ) and ~4 Ma (e.g. Puripicar ignimbrite (De Silva and Gosnold, 2007), La Pacana, Tara ignimbrite (Lindsay et al., 2001b)) also occur in segment 5 (~7 Ma and ~3 Ma) but not so much in Southern Peru. This, however, is rather due to a lack of detailed mapping and dating. The Andamarca 2 (~6 Ma) and Andamarca 1 (~3.8 Ma) rather local but widespread ignimbrites found in Southern Peru by (Brandmeier et al. in prep.) are evidence for those events.

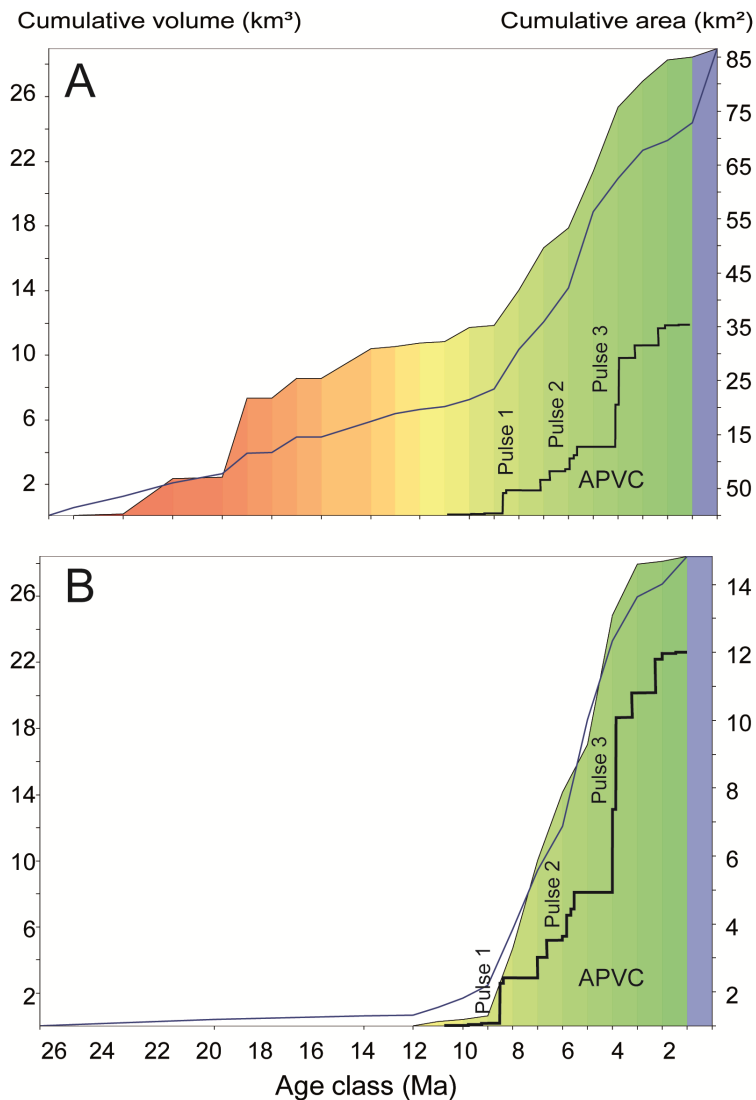


Fig. 10: A: Cumulative areal extent (left axis, blue graph) of the whole extent of the database compared to the cumulative volume (left axis, colored graph and black graph) of the Altiplano Volcanic Complex (APVC) adapted from (Salisbury et al., 2011). B: As in A, but with the cumulative area and volume of the APVC (segment 4 in Fig.9). The 3 major pulses found by De Silva (1991) and Salisbury et al. (2011) are clearly reflected in the areal extent and our new volume estimates (calculated and compiled) that also include the Coranzuli caldera. Pulses are less distinct due to ignimbrites erupting between 8 and 6 and 6 and 4 Ma (e.g. Cerro Panizos, 6.7 Ma, Atana with a maximum age of 4.2 Ma (Kay et al., 2010), Toconao at 4.65 (Kay et al., 2010), León Muerto ignimbrite at 5 Ma (Schnurr et al., 2007), Caracote ignimbrite at 5.4 Ma (Salisbury et al., 2011)).

A waning stage follows, with only minor eruptions (e.g. Incapillo Ignimbrite (Goss et al., 2009), Yura tuff, Arequipa Airport ignimbrite (Lebti et al. 2006), Cerro Blanco Ignimbrite (Kay et al., 2010 and references herein). A very good summary for eruptive patterns of the Central Andean Altiplano-Puna Plateau (segments 4 to 5) was published by Kay and Coira (2009) and the relationship to the development of plutons by De Silva (1991) and will not be discussed in detail. Several upper and lower plate parameters were shown to be interacting and causing changes in eruption style and magnitude. Dominant factors seem to be the rates of westward drift of the South American plate (Kay and Coira, 2009; Oncken et al., 2006) and the changing geometry of the subducting Nazca plate. The migration of the Juan Fernandez Ridge (Yáñez et al., 2001) is related to the Oligocene to middle Miocene deformation pattern and, for example, the amagmatic period in the northern Puna prior to 14 Ma (Kay and Coira, 2009) (Fig. 9, segment 3). According to Kay and Coira (2009), slab steepening, mantle melting and delamination after 16 Ma culminated in the widespread and big ignimbrite eruptions in the northern Puna (segment 4) from 10 Ma to 3 Ma. Fig. 10 shows a comparison of the ignimbrite pulses of the APVC found by De Silva (1991) and Salisbury et al. (2011) based on volume calculations and our findings using cumulative areal extent and volume as measures for ignimbrite eruptions over time.

Further to the north (segments 1 and 2), information is sparse. Figure 3 in (Allmendinger et al., 1997) shows the along-strike variation in elevation of the Altiplano and Puna. The average elevation of the Puna is higher than of the Altiplano. However, in Southern Peru, topography is higher than for the rest of the Altiplano, and high rates of orographic precipitation indicate high erosion rates that might be coupled with tectonics and the evolution of the orogen since ca. 19 or 8 Ma to 0 Ma (McQuarrie et al., 2008). Our results show that ignimbrite eruptions started around 24 Ma, earlier than in the Northern and Southern Puna segments. This north-south “younging” of ignimbrite pulses is shown in Fig. 9 and can be viewed in an attached movie. Eruptions started with the Nazca ignimbrites (Noble et al., 1979) at ~ 22 Ma (estimated volume: 2,200 km<sup>3</sup>) and continued with the “Oxaya-Province” ignimbrites at 19 Ma (estimated volume of 4,900 km<sup>3</sup>). At ~ 14-13 Ma big eruptions produced the Huaylillas (Thouret et al., 2007), the Puquio, the Andamarca 1 ignimbrites (Brandmeier et al. in prep.) and ignimbrites of the Chuntacala Formation (Tosdal et al., 1981). At 10-8 Ma the Caraveli ignimbrites (Thouret et al., 2007), the Andamarca 2 (Brandmeier et al. in prep.) and the Macusani (Cheilletz et al., 1992) ignimbrites erupted. From ca. 6 Ma to 3.8 Ma many smaller, rather local ignimbrites erupted (Andamarca 3 and 4) (Brandmeier et al. in prep.). The distribution of many of these ignimbrites is not very well known and areal and volume calculations are minimum estimates. The total areal ignimbrite



coverage (mapped coverage, including mapped but undated ignimbrites) and volume for all segments is given in Table 2. The total calculated (minimum) extent and volume for the Altiplano/Cordillera Occidental of Peru (segments 1 to 3, around 1,100 km length) amounts to 44,000 km<sup>2</sup> and 14,000 km<sup>3</sup>, respectively, and is comparable to the total extent and volume for the Puna (segments 4 and 5, around 1,000 km length) with 46,000 km<sup>2</sup> and 17,000 km<sup>3</sup> (Table 2). Overall average eruption rates are also given and were calculated by dividing the total volume by the age of the oldest eruption age. Those rates are highest for the Northern Puna (1020 km<sup>3</sup>/Ma) and the Altiplano (350 km<sup>3</sup>/Ma). As only for the APVC calderas are well studied and intracaldera volumes considered, the other figures would probably increase if the intracaldera volumes could be considered. The minimum average eruption rate per million years for the whole area considered is 1,200 km<sup>3</sup>/Ma.

Table 2: Areal extent, volume, average eruption rate and plutonic equivalent of ignimbrites mapped in the database for the segments outlined in Fig. 9. This database is a compilation and does not claim completeness.

Region	Areal extent	Estimated eruptive volume*	Plutonic input (3:1 or 5:1)	Average eruption rate (km <sup>3</sup> /Ma) and / km arc
Area Southern Peru Section 1	8,000 km <sup>2</sup>	2,400 km <sup>3</sup>	7,200 km <sup>3</sup> or 12,000 km <sup>3</sup>	112/0.5
Southernmost Peru Section 2	14,000 km <sup>2</sup>	2,700 km <sup>3</sup>	8,100 km <sup>3</sup> or 13,500 km <sup>3</sup>	135/0,5
Altiplano Section 3	22,000 km <sup>2</sup>	8,400 km <sup>3</sup>	25,200 km <sup>3</sup> or 42,000 km <sup>3</sup>	350/0.7
Northern Puna Section 4	33,000 km <sup>2</sup>	14,200 km <sup>3</sup>	42,600 km <sup>3</sup> or 71,000 km <sup>3</sup>	1020/3.4
Southern Puna Section 5	13,000 km <sup>2</sup>	3,100 km <sup>3</sup>	9300 km <sup>3</sup> or 15,500 km <sup>3</sup>	130/0.3
Total	90,000 km <sup>2</sup>	30,800 km <sup>3</sup>	92,400 km <sup>3</sup> or 154,000 km <sup>3</sup>	1200/14

De Silva and Gosnold (2007) propose that ignimbrite flare-ups in the Altiplano-Puna Region record a positive feedback between the mantle input, magma production, and upward migration of the magmatic system that promotes the accumulation of larger bodies of dacite magma in the upper crust with time. Long-lived, nested calderas reflect upper crustal processes and eruptions through time reflect the thermal maturation of the crustal column. Plutonic:volcanic ratios are thought to be in the range of 10:1 (Smith & Shawn in: Muffler

(1979)) to 3:1 to 5:1 ( De Silva and Gosnold, 2007; Lipman, 1984; Lipman, 2007; White et al., 2006). Those ratios are based on gravity data from the Southern Rocky Mountains Volcanic Field and the San Juan Mountains of Colorado (Lipman, 1984; Lipman, 2007) and on the best estimate of (White et al., 2006) considering all uncertainties, respectively. Using the same assumptions as ( De Silva and Gosnold, 2007), we calculate a minimum plutonic input for all segments and for the whole study area Table 2. Their reasoning is that each major eruption of the APVC evacuated magma bodies that were emplaced in a relatively short time and equate the erupted volume to a unique plutonic volume beneath the respective calderas ( De Silva and Gosnold, 2007). On an Andean scale, we lack all the detailed information about calderas and their longevity. The calculated plutonic input in Table 2 is therefore an educated guess at a minimum plutonic equivalent for the erupted volcanic volume.

Comparing average eruption rates of the past 26 Ma per kilometer arc for the different segments (for calculations, the age of the oldest eruption of the segment was used: 22 Ma for Southern Peru (Nazca Ignimbrite), 20 Ma for Southernmost Peru, 24 Ma for the Altiplano (Huaylillas Formation ignimbrites), 12 Ma for the Northern Puna (first ignimbrites Coranzuli area), 24 Ma for the southern Puna (Río Frío, Tal Ignimbrites)), we observe highest average eruption rates ( $r_m$ ) for the northern Puna segment ( $3.4 \text{ km}^3 \text{ Ma}^{-1} \text{ km (arc)}^{-1}$ ), followed by  $0.7 \text{ km}^3 \text{ Ma}^{-1} \text{ km (arc)}^{-1}$  for the Altiplano. For Southern Peru,  $r_m$  is smaller ( $0.5 \text{ km}^3 \text{ Ma}^{-1} \text{ km (arc)}^{-1}$ ), which is probably due to the lack of knowledge about intra-caldera volumes. However, these rates are comparable to the  $3 \text{ km}^3 \text{ Ma}^{-1} \text{ km (arc)}^{-1}$  rate of effusive volcanism found by (Francis, 1994) for the Central Andes during the last 10 Ma. The latter rate is higher due to the APVC eruptions only starting after  $\sim 10$  Ma. Average eruption rates during the time of big eruptions (“ignimbrite flare-ups” (e.g. steep slope in graphs of Fig. 9), the values change drastically: In Southern Peru,  $2,200 \text{ km}^3$  erupted within  $\sim 3$  Ma, equivalent to an  $r_m$  of  $4.1 \text{ km}^3 \text{ Ma}^{-1} \text{ km (arc)}^{-1}$ . In Southernmost Peru,  $2,250 \text{ km}^3$  erupted within  $\sim 4$  Ma, leading to a maximum  $r_m$  of  $2 \text{ km}^3 \text{ Ma}^{-1} \text{ km (arc)}^{-1}$ , on the Altiplano peak  $r_{ms}$  of  $4.1 \text{ km}^3 \text{ Ma}^{-1} \text{ km (arc)}^{-1}$  occurred during two steps within  $\sim 3$  Ma (mainly Oxaya and Altos de Pica ignimbrites) and a volume of  $\sim 6,100 \text{ km}^3$ . For the Northern Puna segment,  $r_m$  is highest ( $6.7 \text{ km}^3 \text{ Ma}^{-1} \text{ km (arc)}^{-1}$ ) between 8 Ma and 3 Ma with a volume of  $\sim 14,000 \text{ km}^3$ . For the Southern Puna, within  $\sim 5$  Ma,  $\sim 2,000 \text{ km}^3$  erupted, equivalent to a maximum  $r_m$  of  $1 \text{ km}^3 \text{ Ma}^{-1} \text{ km (arc)}^{-1}$ .

### A model for the spatio-temporal shift in ignimbrite-pulses

The most important observation from our data is, that timing of eruptions shows a N-S younging, with pulses of  $\sim 24$  -17 Ma old ignimbrites (e.g. Nazca, Oxaya, Altos de Pica),  $\sim 9$ -

10 Ma (e.g. Caraveli, Andamarca 2) and ~13-14 Ma (e.g. Andamarca 1, Huaylillas, Puquio, Chuntacala) ignimbrites ( Southern Peru, Altiplano) that are almost absent (amagmatic period prior to 16 Ma in the northern Puna (Coira et al., 1993)) or delayed in the northern and southern Puna (pulses at ~8 Ma, ~6 Ma and ~4 Ma). Furthermore, as described above, eruption rates are not continuous but show distinct “peaks” of big eruptions, so-called ignimbrite-flare ups (as described by De Silva and Gosnold (2007) for the APVC).

These differences in magmatic activity and magnitude reflect spatial variations in slab geometry, uplift and tectonic history of the Andes. Pulses in the Puna can be related to changes in slab geometry, the passing of the Fernández ridge and delamination events (Coira et al. 1993), while in Southern Peru causes for big ignimbrite eruptions are still not clear and early publications propose different orogenic events (Sébrier and Soler, 1991 and references herein) that to some degree agree with the timing of the eruptions observed. Big eruptions like the Nazca or Oxaya ignimbrites, require large amounts of crustal melting and therefore mantle flow. Passive ridge subduction can trigger the generation of magmas underneath an arc region due to its high volatile content and huge volumes of oceanic crust (Yáñez et al., 2002). Correlating the passing of the Juan-Fernández ridge with big ignimbrite eruptions, we observe that all big eruptions occurred after the passing of the ridge (see Fig. 11 and video clip). The arrival of the ridge as a high topographic element is likely to produce continental margin erosion, uplift and exhumation of the continental crust (Yáñez et al., 2002). Furthermore, as argued by (James and Sacks, 1999) for a shallow subduction setting, the fluids contained in the subducting ridge “condition” the crust for later melting. After the passing of the ridge, the slab steepens again and a hot asthenospheric wedge triggers melting in the pre-conditioned crust. We propose that those conditions favor the eruption of big ignimbrites like the Nazca, Oxaya and Huaylillas and, as also suggested by Coira et al. (1993), the APVC ignimbrites. This model agrees well with the back-migration of the arc in Southern Peru, described by Mamani (2010), starting at ~ 30 Ma, with first eruptions of Tacaza mafic lavas. However, the location of the Juan Fernández ridge prior to 22 Ma is not known. Ignimbrite melts for large-volume eruptions like the Nazca and Oxaya ignimbrites require the formation of large silicic magma chambers that can only accumulate over periods of  $10^6$  years (Jellinek and DePaolo, 2003), explaining the time-lag between slab-steepening and the eruption of the ignimbrites. The evolution and eruption mechanisms of such magma chambers is still a highly debated topic (Annen, 2009; Glazner et al., 2004; Gottsmann et al., 2009). It exceeds this study to discuss this topic in detail, however, “priming” of the crust for future melting by the passing of a ridge seems to be linked to “super-eruptions” in the order of thousand cubic kilometers of ignimbrite. The long-lived APVC system, in contrast to the

Manuscript IV - Temporal and compositional patterns and variations in ignimbrite volcanism in the Andes over the past 30 Ma

older Nazca/Oxaya and Huaylillas pulses, is located on an extraordinary thick, thermally evolved crust that favored melting. At ~20 Ma the crust was still thinner and thus colder, requiring a higher energy flux for melting. This might partly explain the less radiogenic Sr (<0.708 compared to >0.708 for the APVC/Northern Puna) values of those ignimbrites, arguing for less crustal assimilation and a higher percentage of mantle-derived melts (see database used for kriging models).

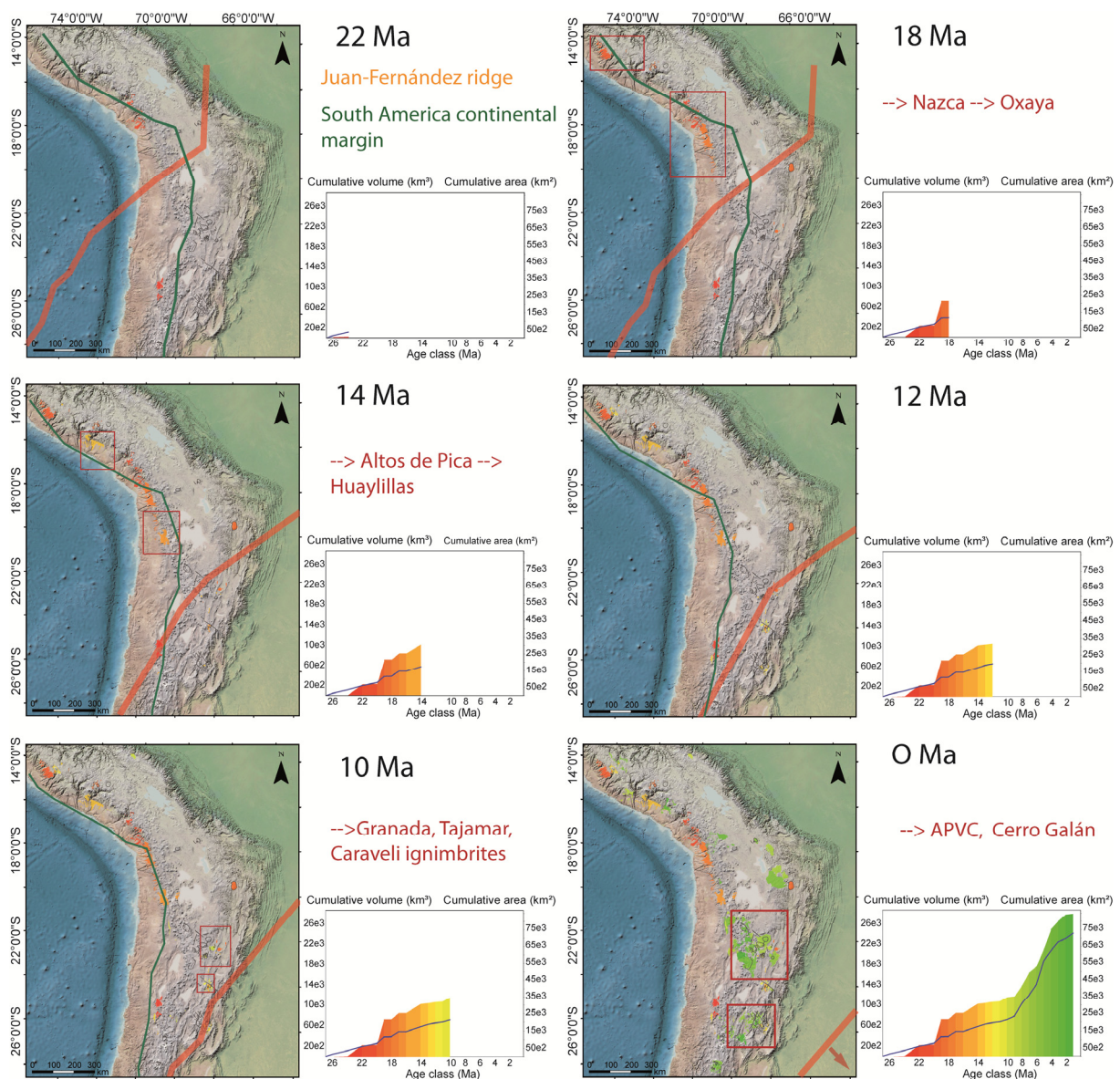


Fig. 11: Path of the Juan-Fernández ridge after (Yáñez et al., 2002; Yáñez et al., 2001) compared to the spatio-temporal pattern of ignimbrite eruptions (red squares highlight eruption areas). The ridge is shown in orange and the South America continental margin with respect to the ridge at that time in green (westward movement of the continent).

The arrival of the Nazca ridge (based on the assumption that the mirrored Tuamotu Plateau resembles the subducted part of the ridge) around 11.2 Ma at 11° S (Hampel, 2002) initiated shallow subduction in Southern Peru. From that position, the ridge moved in an S-E direction until the present position at 15°S and put an end to ignimbrite eruptions (last eruptions observed are the ~3.8 Ma Andamarca 4 ignimbrites described by Brandmeier et al. (in prep.).

### 3.2.2 Multivariate statistics on compositional data

---

Apart from temporal and spatial patterns of ignimbrite eruptions, compositional patterns of ignimbrites are linked to the thermal and structural evolution of the crust and partial crustal melting and magmatism in the mantle wedge related to the subduction of the Nazca plate and can therefore be used as tracers of these processes. Differences in composition may have several reasons due to processes interacting during the magmatic evolution. These are, for example, differences in the source, in physical parameters, assimilation, mixing of magmas, and crystal fractionation at different storage levels in the crust. Factors like the slab geometry or crustal thickness change over time and might cause changes in composition. However, ignimbrite melts are mostly highly evolved melts close to the ternary eutectic and therefore similar in composition. The large Puna ignimbrites are described as crystal-rich, calc-alkaline high-K dacites to rhyodacites of the “monotonous intermediate” type of Hildreth (1981). On the other hand, small-volume, crystal-poor, rhyolitic ignimbrites are widely distributed in the CVZ (Lebti et al. 2006; Siebel et al., 2001) and small-volume ignimbrites of the Southern Puna can be linked to further differentiated andesites (Schnurr et al., 2007; Siebel et al., 2001).

De Silva and Gosnold (2007 and references therein) found that major APVC ignimbrites can be distinguished by subtle differences in trace elements and mineral chemistry and propose that this is due to each eruption tapping a unique dacitic magma emplaced into the upper crust. In the following we will use the log-ratio approach to first explore differences in chemical composition without a-priori assumptions using cluster analysis. In a second step, we will use discriminant analysis to test hypothesis, whether ignimbrites have a unique “compositional signature”.

### 3.2.2.1 Cluster analysis applied to Ignimbrite whole-rock geochemistry

Results of cluster analysis are summarized in Table 3 and Figs. 12A and 13 and in the attached GIS database for all samples and with distances to the cluster centroids.

Table 3: Clustering steps and characteristics. Color-coded to match the plots in the following figures.

Step 1: Major elements	Description* *always with respect to all other elements, not in terms of concentrations	Step 2: REEs	Description* *always with respect to all other elements, not in terms of concentrations	Step 3: Ba, U, Th, Pb, Zr, Nb	Description* *always with respect to all other elements, not in terms of concentrations
1	More evolved: SiO <sub>2</sub> , K <sub>2</sub> O, Na <sub>2</sub> O, Al <sub>2</sub> O <sub>3</sub> high → rhyolitic	1	-Light REEs higher - steeper LREE pattern - moderate Eu anomaly	1	-Sr, Nb, Zr, Ba, Pb high -higher Rb, Nb, Pb than less evolved groups
1	More evolved: SiO <sub>2</sub> , K <sub>2</sub> O, Na <sub>2</sub> O, Al <sub>2</sub> O <sub>3</sub> high → rhyolitic	1	-Light REEs higher - steeper LREE pattern - moderate Eu anomaly	2	-Rb, Y, Th, U high -higher Rb, Nb, Pb than less evolved groups
1	More evolved: SiO <sub>2</sub> , K <sub>2</sub> O, Na <sub>2</sub> O, Al <sub>2</sub> O <sub>3</sub> high → rhyolitic	2	-Heavy REEs higher - flat REE pattern - stronger Eu neg. anomaly	3	-Sr, Zr, Ba, Pb high -higher Rb, Nb, Pb than less evolved groups
1	More evolved: SiO <sub>2</sub> , K <sub>2</sub> O, Na <sub>2</sub> O, Al <sub>2</sub> O <sub>3</sub> high → rhyolitic	2	-Heavy REEs higher - flat REE pattern -stronger neg. Eu anomaly	4	-Rb, Y, Nb, Th, U high -higher Rb, Nb, Pb than less evolved groups
2	Less evolved: MnO, FeOt, MgO, Ti <sub>2</sub> O <sub>3</sub> , P <sub>2</sub> O <sub>4</sub> , CaO high → dacitic	3	- HREEs higher - moderate Eu anomaly	5	-Rb, Nb, Th, U high -Sr and Y higher than more evolved groups
2	Less evolved: MnO, FeOt, MgO, Ti <sub>2</sub> O <sub>3</sub> , P <sub>2</sub> O <sub>4</sub> , CaO high → dacitic	3	- HREEs higher - moderate Eu anomaly	6	-Sr, Y, Zr, Ba, Pb high -Sr and Y higher than more evolved groups
2	Less evolved: MnO, FeOt, MgO, Ti <sub>2</sub> O <sub>3</sub> , P <sub>2</sub> O <sub>4</sub> , CaO high → dacitic	4	-Light REEs higher - steep HREE pattern	7	-Rb, Nb, Th, U high -Sr and Y higher than more evolved groups
2	Less evolved: MnO, FeOt, MgO, Ti <sub>2</sub> O <sub>3</sub> , P <sub>2</sub> O <sub>4</sub> , CaO high → dacitic	4	-Light REEs higher -steep HREE pattern	8	-Sr, Y, Zr, Ba, Pb high -Sr and Y higher than more evolved groups

Manuscript IV - Temporal and compositional patterns and variations in ignimbrite volcanism in the Andes over the past 30 Ma

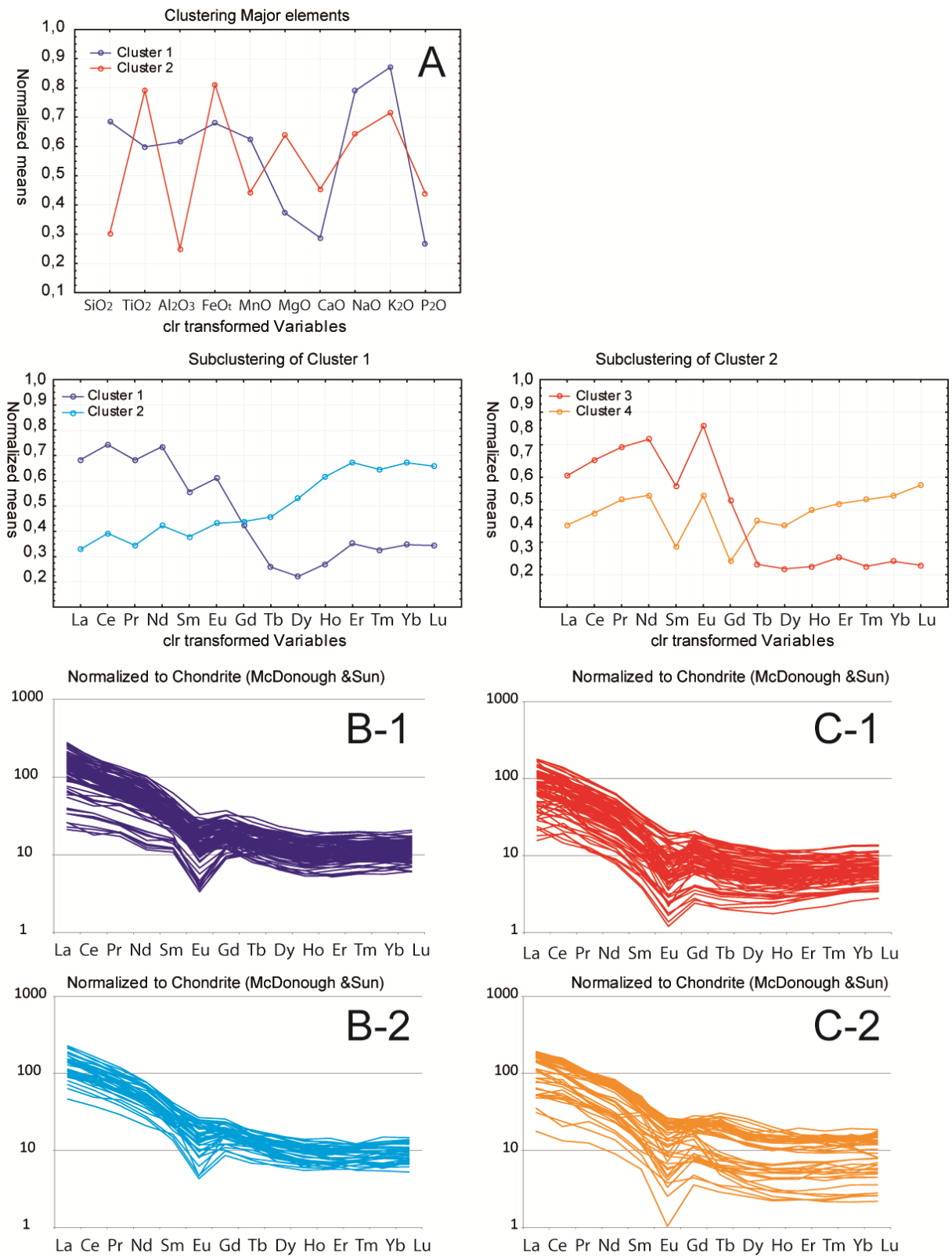


Fig. 12: Cluster analysis results for major elements (A) and REEs (B-C). A, B and C show normalized cluster means while B-1 and B-2 show chondrite-normalized REE plots for the respective clusters for comparison. C-1 and C-2 show the same for clusters 3 and 4.

The respective clustering steps will be presented in the following, starting with major elements in the first clustering step, REEs in a second and LILE in a third step. In order to understand the structure of the data, Principal Components (PCs) were calculated for major elements and are illustrated in compositional biplots. 74% of the variance can be explained by the first two PCs as shown in Fig. 14. Compositional biplots can provide essential information about the nature of compositions (Aitchison and Greenacre, 2002).

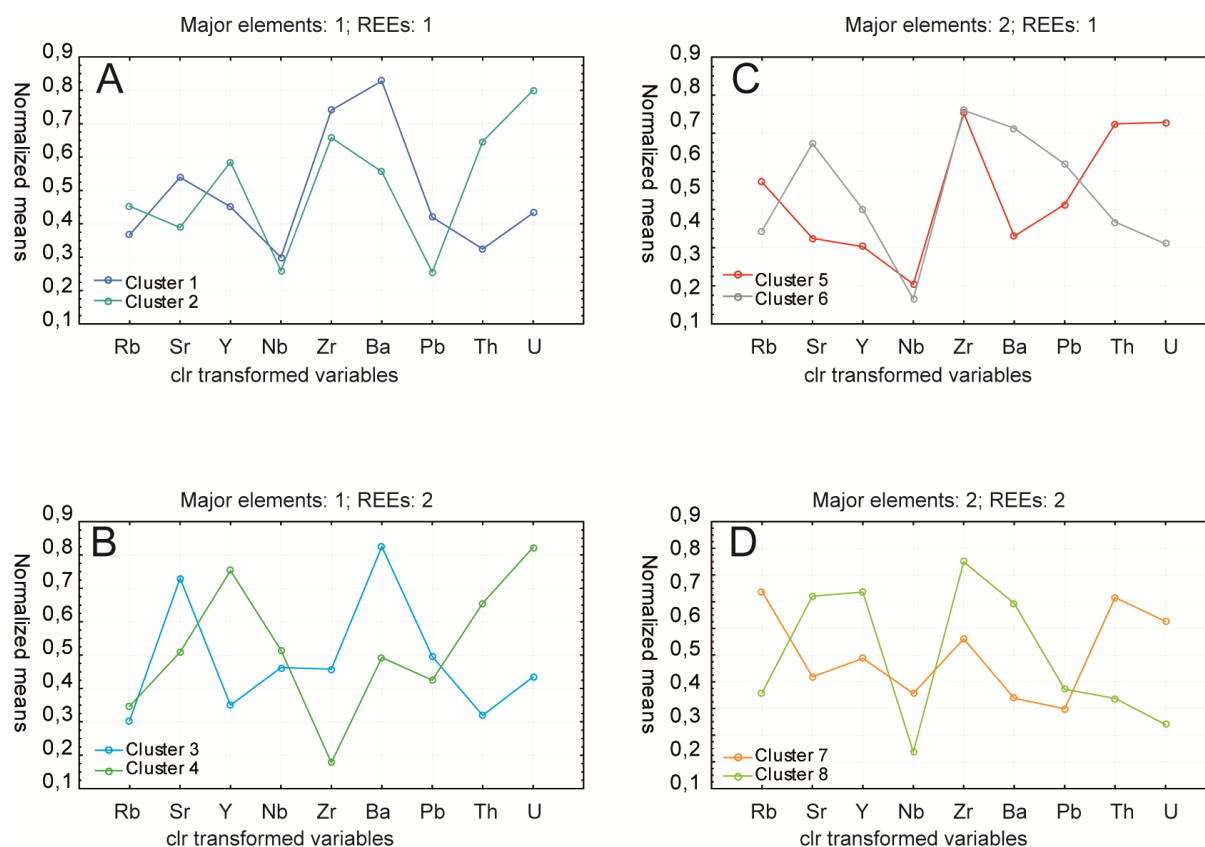


Fig. 13: Third clustering step including more trace elements. A and B from the major elements cluster 1 (for both sub-clusters of REEs); C and D from major elements cluster 2 (for both sub-clusters of REEs).

The distribution of the samples in the space spanned by the first two PCs in Fig. 14A suggests the existence of two end-members defined by major element composition.  $Al_2O_3$ ,  $Na_2O$  and  $K_2O$  vectors are arranged in a line close to the first PC and  $CaO$ ,  $MgO$  and  $FeO_t$ ,  $P_2O_4$  and  $TiO_2$  on the left side of the biplot with, for example,  $MnO$  and  $P_2O_4$  or  $K_2O$  and  $MgO$  being almost collinearly arranged, suggesting that the respective sub-compositions plot along a compositional line. Vertices being close to each other (e.g.  $TiO_2$  and  $FeO_t$  or  $Na_2O$  and  $Al_2O_3$ ) suggest that the respective ratios are almost constant. Fig. 14B shows a sub-composition with high variability that serves well to distinguish the two clusters. The rather systematic variations in composition close to eutectic melts (as most ignimbrites constitute



highly evolved melts) suggest that differentiation and mineral fractionation (e.g. feldspars, amphibole, titanite) and assimilation are the main process responsible for compositional differences observed in major elements. Those processes are both controlled by the minerals either crystalizing and removing elements or melting and setting elements free, according to distribution coefficients. The first clustering step clearly divides higher evolved samples from less evolved ones (e.g. samples more differentiated and therefore higher in  $\text{SiO}_2$ ,  $\text{K}_2\text{O}$  etc. from samples lower in  $\text{SiO}_2$  but higher in  $\text{FeOt}$ ,  $\text{MgO}$ ,  $\text{TiO}_2$  etc.). However, the boundary is drawn based on distances to the center of the cluster and cannot be interpreted in the sense of really having two “clouds” of data.

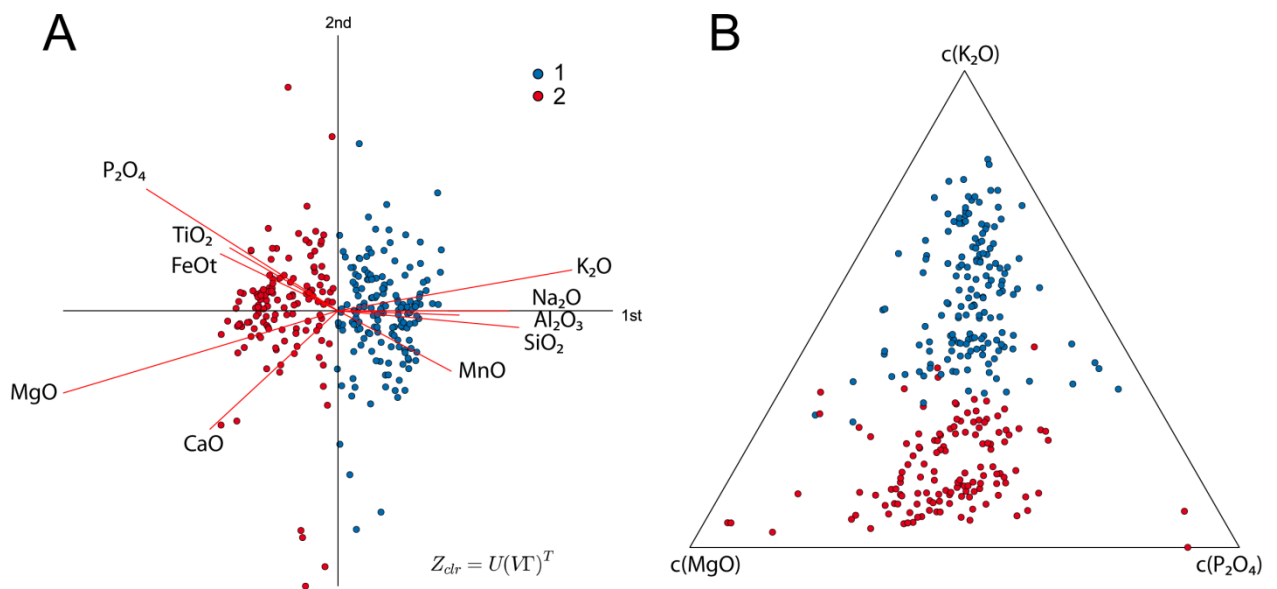


Fig. 14: A: Compositional biplot for major elements. 80 % of the variability is explained by the first and second PC. Results for the first step of cluster analysis are shown (compare to Fig.12). B: Centered ternary plot showing the sub-composition with highest variability.

To find more subtle differences in composition, rare earth elements (REEs) were used in a second clustering step. A major drawback is that compositional vectors can only be computed for a complete dataset. This means, that the number of samples is reduced significantly by including more and more trace elements due to a lack of information for some elements. For this reason, in the following, we will always proceed from the simple model (major elements-only) to more complex analysis.

The REEs sub-composition shows a more complex system with 88 % of the variability explained by the first two PCs (Fig. 15A). The sub-composition La-Eu-Yb (Fig. 15B) shows differences in ratios involving LREEs, MREEs and HREEs. Note that less evolved samples plot closer to Eu and the range in Yb and La is more restricted, while more evolved samples

span a wider range between Yb and La. This might indicate steeper HREE pattern for less evolved samples and a more pronounced negative Eu anomaly for the more evolved samples due to feldspar fractionation. Fig. 12B and C show chondrite-normalized REE diagrams for the respective groups. Differences between clusters are not easily seen. We will further discuss this matter in 3.2.2.1.1.

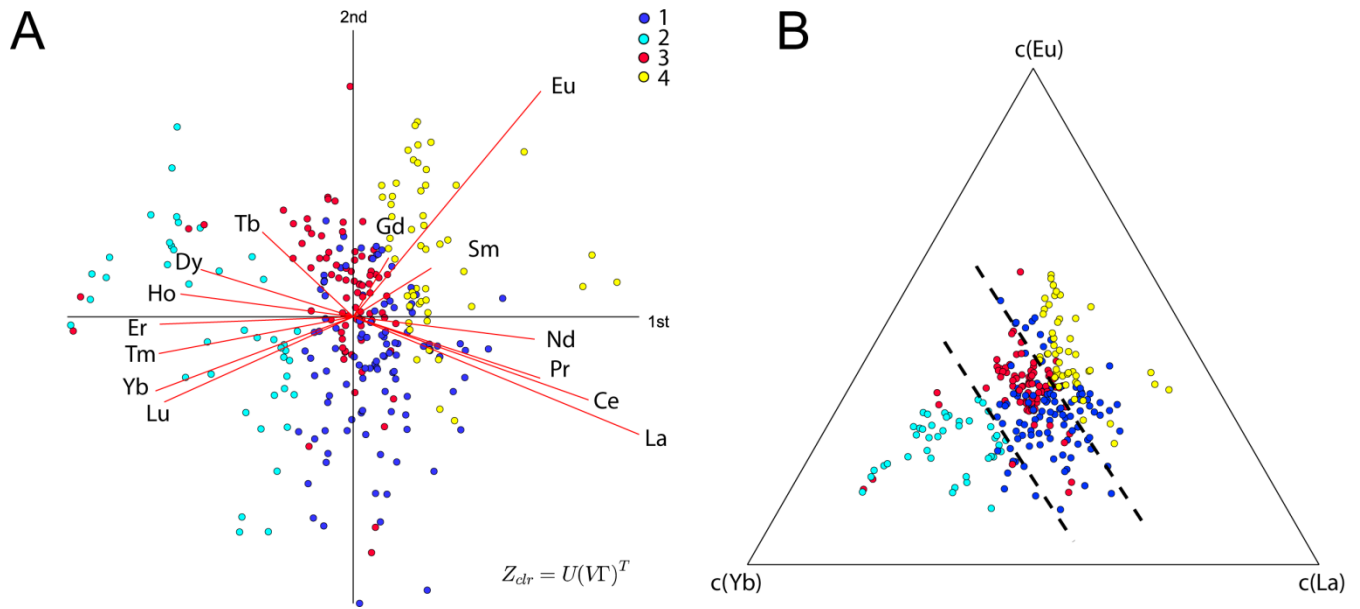


Fig. 15: A: Compositional biplot (1<sup>st</sup> and 2<sup>nd</sup> PC) REEs showing clustering results. B: Centered ternary diagram for the subcomposition Eu, Yb and La (clr transformed) that shows high variability in A. Note that the “boundary” for the more and less evolved groups shifts toward Eu and La, away from the HREE Yb and more towards Eu.

The last clustering step involved LILE. Fig. 16 shows the compositional biplot spanned by the first two PCs (A) and a sub-composition of Yb, U and Sr that shows high variability in the ratios. The clr variances are much higher for LILEs than for REEs (total clr variance of 2.9 compared to only 0.9). Fig. 16B shows that data scatters a lot and clusters cannot be defined easily. However, one systematic difference is clearly visible: All groups belonging to the less differentiated cluster are closer to the Sr corner, while all more evolved samples plot closer to U and Ba corners. This indicates that feldspar fractionation plays a role in modifying compositions as Sr and Ba have high partitioning coefficients of 28 and 22 for sanidine (8 for Eu), respectively (Leeman and Phelps, 1981). Clusters that plotted closest to the Eu-corner in step two are now closest to Sr (5, 6, 7 and 8), while clusters farther away from Eu (1 and 2) plot closer to Ba.

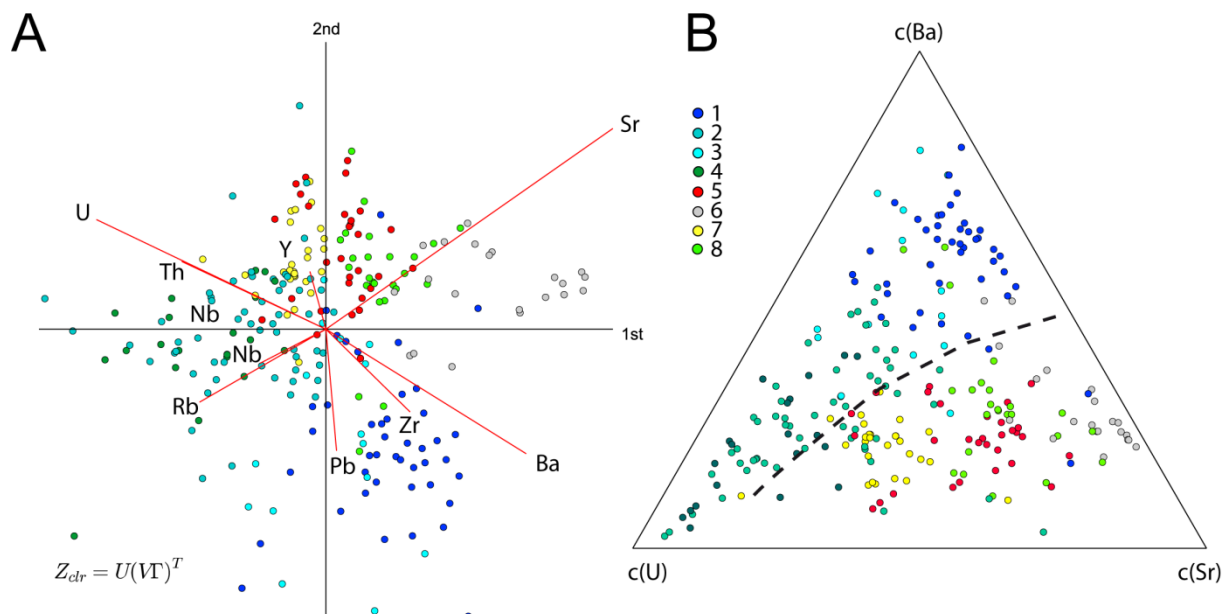


Fig. 16: A: Compositional biplot (1<sup>st</sup> and 2<sup>nd</sup> PC) for the last clustering step showing the resulting eight clusters. B: Centered subcomposition Ba, U, Sr (clr transformed). The line shows the boundary between more evolved and less evolved groups.

It is obvious, however, that ignimbrites do not form real “groups” with fixed compositional limits, but rather a continuous range of compositions. Using exploratory data analysis and hierarchical cluster analysis on clr transformed data, we defined eight groups representing “end-members” for this range of composition and found that variations in major and trace elements seem to be very coherent and therefore due to processes removing elements in a systematic way, e.g. differentiation and mineral fractionation. More “evolved” samples tend to show a more pronounced negative Eu anomaly, steeper LREE patterns and flatter HREE pattern in comparison to the less evolved groups.

### 3.2.2.1.1 How does clustering without a-priori assumptions relate to traditional geochemical parameters?

As clr transformation and clustering algorithms are rather abstract, we now compare our results to traditional geochemical and petrologic classifications and parameters. Using the same coloring as for the REE clusters (step 2), the data is now shown in Fig. 17 in a TAS diagram and AFM diagram for comparison. The more and less evolved groups are clearly distinguished in the TAS diagram with the more evolved group falling into the rhyolite field and the less evolved groups scattering between the dacite and rhyolite fields. In the AFM diagram, all samples plot on the calc-alkaline trend with the more evolved groups close to the alkaline elements. In comparison to both traditional diagrams, all major element

characteristics are visible at one glance in the clr biplot (Fig. 14), however no longer in terms of wt-% or %.

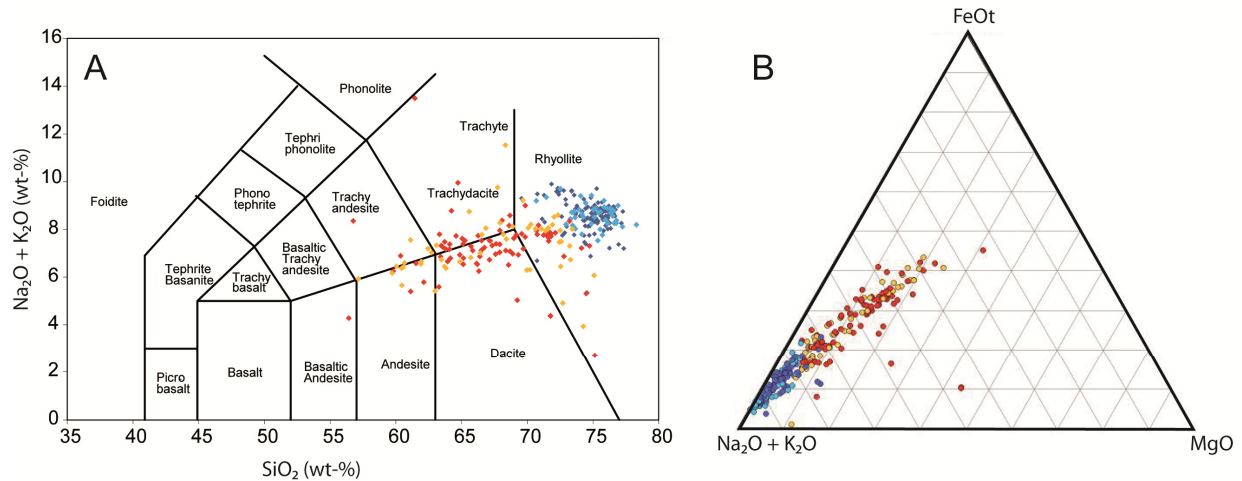


Fig. 17: Clustering results compared to A: TAS classification; B: AFM diagram. Colors for groups are the same as in all other figures and in Table 3.

The second clustering step based on REEs classified samples in a way that treats the REE log-ratios as a compositional signature. From a geochemical perspective, normalized REE diagrams include a wealth of information about different processes (e.g. “garnet signature” due to garnet as a residuum, Eu-anomaly due to plagioclase fractionation, steep LREE pattern due to LREE enrichment....). All these processes and changes can be visualized by individual parameters like the Eu anomaly or element ratios (Fig.17A-B). Clustering analysis looks for natural groups and no weights were applied to give more importance to one element over the others.

The Europium anomaly is one of the most striking features when considering REE plots. As Eu has two valences, it is easily incorporated into plagioclase substituting Ca in its 2+ valence. Plagioclase fractionation can therefore cause a pronounced negative Eu anomaly. However, partitioning of REEs into feldspars is dependent on many parameters and for Eu oxygen fugacity and temperature are controlling the valence state and partitioning (Capobianco and Drake, 1990). Fig.18A and B show histograms for calculated Eu/Eu\* for all samples of the respective classes obtained during the second step of clustering analysis (A: more evolved groups, B: less evolved groups).

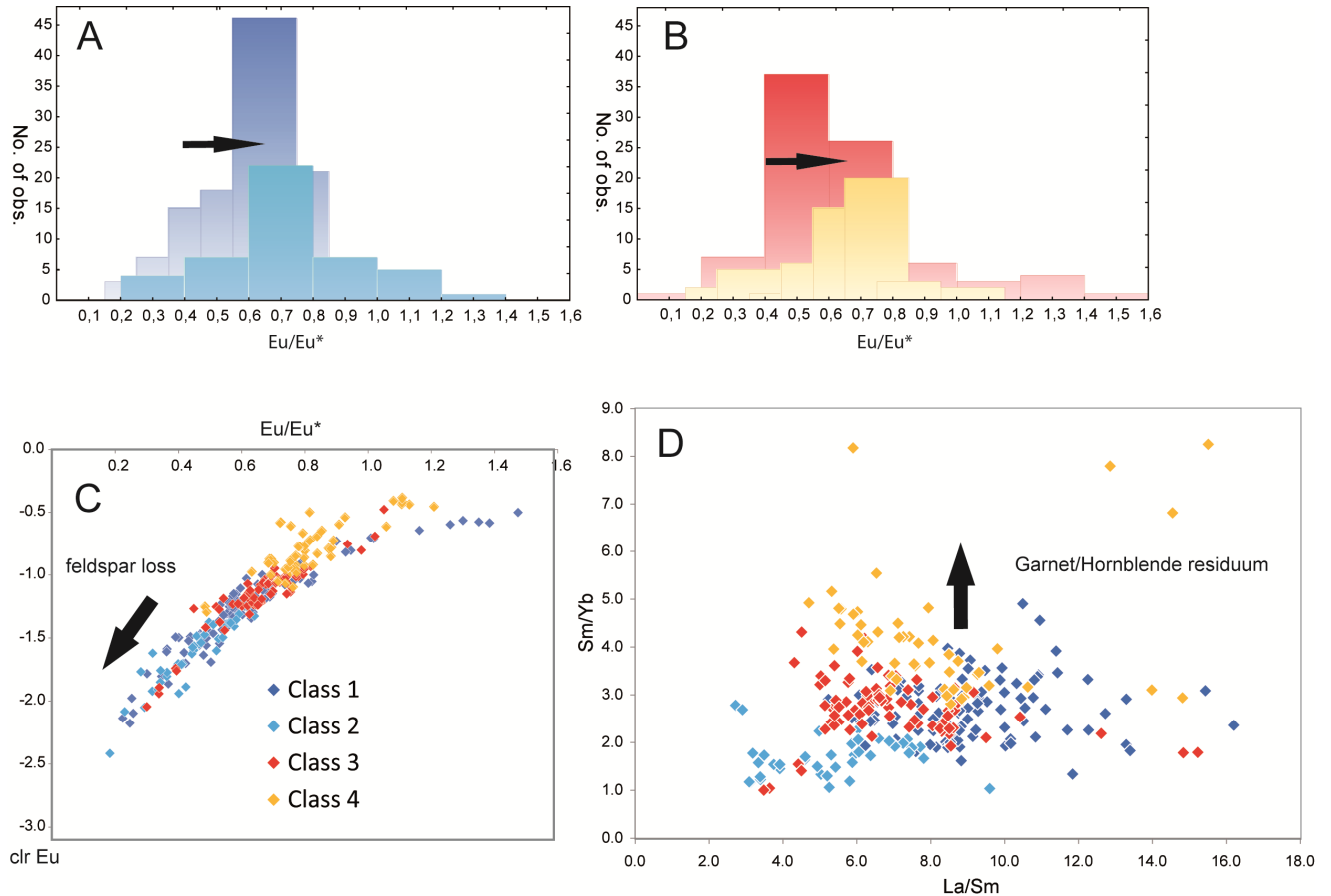


Fig. 18: Comparison of clustering results (step 2) to the Eu anomaly (A-C) and to traditional element ratios (D). High HREE ratios suggest high pressure residual phases like hornblende or garnet ( $Sm/Yb > 4$ ), while a more pronounced Eu anomaly suggests lower pressure fractionation of feldspar. However, other factors may influence these ratios and the Eu anomaly (e.g. oxygen fugacity, water pressure, accessory minerals).

A histogram shift caused by the europium anomaly is visible but not very pronounced. This can also be seen in Fig. 18D showing the relationship between calculated Eu anomaly and the clr transformed Eu value. A positive Eu anomaly corresponds to clr Eu values higher than  $\sim -0.75$ . However, samples with this clr value might still show a slightly negative Eu anomaly. This is due to Eu being considered with respect to all other elements and not normalized to chondritic composition. Fig. 18C shows the classical element ratios Sm/Yb and La/Sm plotted against each other for the respective classes. For less evolved groups, differences are mostly in the slope of the HREEs while for the more evolved samples, slopes for the LREEs are more variable (compare to Fig. 15). Less evolved samples have steeper HREE patterns and the least pronounced negative Eu anomaly with class 4 having the most pronounced slope (compare to Fig. 15). Higher Sm/Yb ratios suggest high-pressure residual phases (hornblende and/or garnet with  $Sm/Yb > 4$  (Kay et al., 2010)), while a negative Eu anomaly results from lower pressure feldspar fractionation.

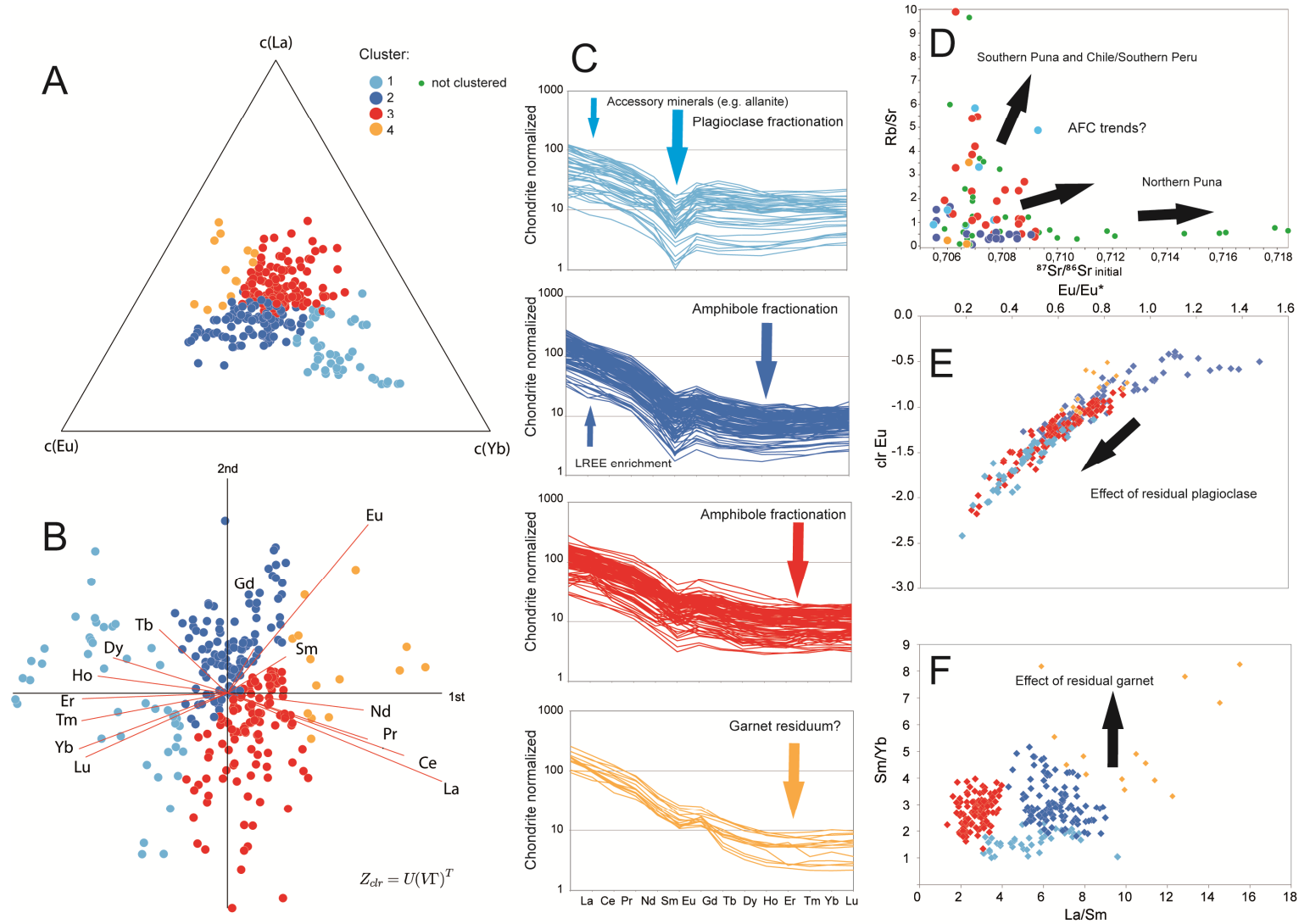


Fig. 19: Clustering results of an only-REE approach. A: Ternary diagram showing variations between La, Eu and Yb (clr transformed and centered data); B: Compositional biplot for the four resultant clusters. C: REE of respective clusters normalized to chondrite (McDonough and Sun, 1995) D: Rb/Sr as an indicator for fractional crystallization vs.  $^{87}\text{Sr}/^{86}\text{Sr}$  as an indicator for crustal assimilation. E:  $\text{Eu}/\text{Eu}^*$  vs. clr Eu showing the effect of plagioclase removal. F:  $\text{Sm}/\text{Yb}$  vs.  $\text{La}/\text{Sm}$  as indicator of a garnet residuum ( $\text{Sm}/\text{Yb} > 4$ ) and LREE enrichment.

However, for all diagrams shown, we observe an overlap of the rhyolitic vs. more dacitic clusters in REE composition that might dilute information contained in the REE signature. Thus, we ran another cluster analysis only using REEs to see, whether there are better defined groups independent of silica content. Results are shown in Fig.19. “End-members” are much better defined, with a gradient from cluster four indicating fractionation at higher pressure (possibly garnet) towards cluster one with a pronounced negative Eu anomaly suggesting plagioclase as a residual phase and depletion of LREE (La and Ce) due to accessory minerals (e.g. allanite, monazite). The moderate concave upward REE pattern is consistent with amphibole fractionation, removing middle REEs (Richards et al., 2006).

Our four classes combine several characteristics in REE patterns and we believe that treating the REE as a “compositional signature” can help to better distinguish ignimbrites. The REE system is considered as a whole, containing more information about the magmatic evolution than only variations in Eu anomaly or selected element ratios, and multivariate statistics can deal in n-dimensional space while the human observer is only capable of observing three dimensions at a time.

After this brief excursion, we come back to the hierarchical cluster analysis step 3. The complexity of the compositional system is reflected in the 3<sup>rd</sup> clustering step that includes HFSE and LILE elements. Variations are very high and not as systematic as for major and REE elements. Ba and Sr can be removed from the melt by sanidine and plagioclase fractionation, but their partitioning coefficients are strongly dependent on temperature (Capobianco and Drake, 1990). Feldspars are in terms of volume the most abundant mineral phase fractionating, and therefore have a controlling effect on trace element partitioning. Other mineral phases that are not that abundant (e.g. zircon, apatite) modify the resultant composition, especially if partitioning coefficients are very high (like for HREEs in zircon). Incompatible elements like U are enriched during differentiation, but the variability of the HFSE and LILE is much higher than for REEs and seems to be less systematic. As many different processes are interacting, the whole system is very complex. Garnet as a residual phase, for example, can cause a steep HREE pattern. Zircon as a late stage phase has the same effect. In a Zr/Hf against Zr (ppm) plot (Fig.20), the curved pattern indicates Zircon fractionation with Zr/Hf values ranging from around 20 to 40. These values are also typical for granitic zircons (Zaraisky et al., 2009). Therefore, the steeper HREE pattern of REE class 4 (yellow) (step 2, Fig.18D and Fig.19) might also be modified by zircon rather than by garnet as a residual phase.

Many factors like, for example, oxygen fugacity and temperature controlling partitioning coefficients for Eu, can cause subtle changes in composition. Thus, “compositional

signatures” of the highly evolved ignimbrites can be seen as a function of source and pre-eruptive processes like minerals fractionation (at different storage levels) and crustal assimilation. Processes themselves are dependent on parameters like, for example, p-T conditions, oxygen fugacity of a particular magma chamber and evolution. The “compositional signature” might therefore help to “fingerprint” ignimbrites on the basis of whole-rock analysis as will be shown in section 3.2.2.2.

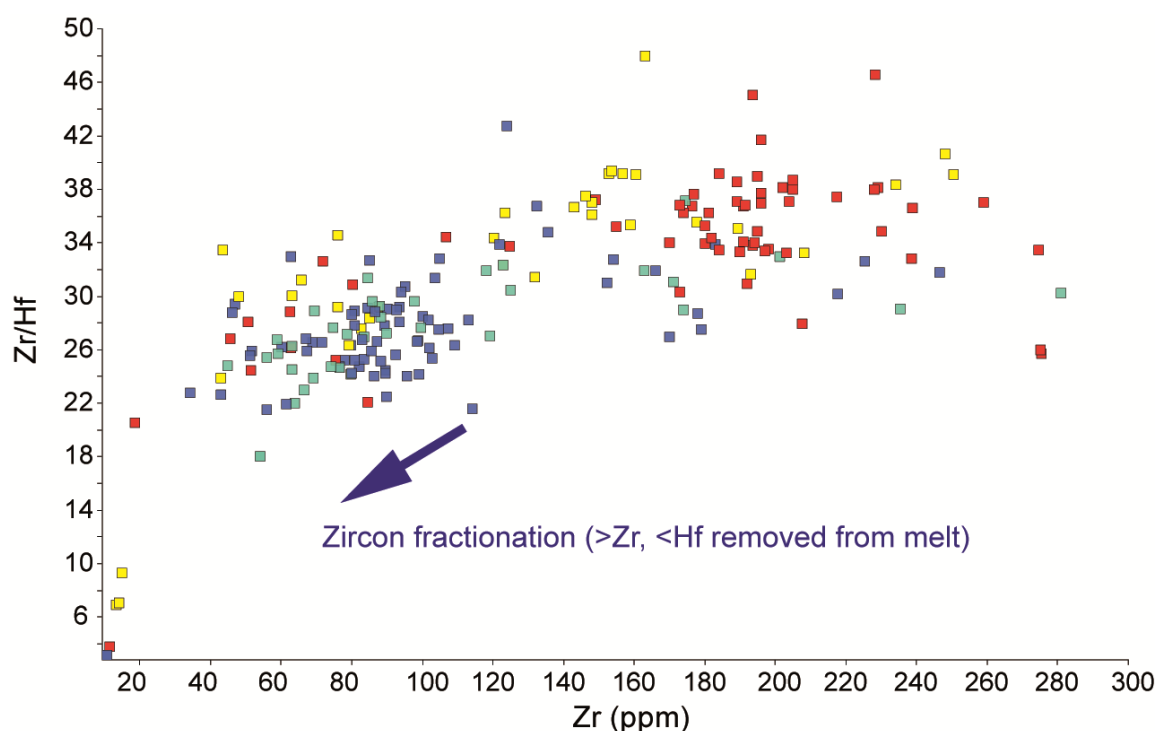


Fig. 20: Zircon fractionation. Colors correspond to the classes in Table 3, step 2.

### 3.2.2.1.2 Are there systematic correlations with age, location or volume?

On the basis of our data, we cannot see any statistically significant correlation of clustering results with location, age or basement. This is mainly due to missing data and too little samples or metadata for statistical tests. However, qualitatively looking at clustering results in more detail, rhyolitic samples (cluster 1 in step 1) are concentrated north and south of the APVC (e.g. Lauca-Perez, La Joya, Vallecito ignimbrites), with only minor rhyolites as more differentiated equivalents of the prominent dacites occurring there as described by De Silva and Gosnold (2007). Thus, most APVC ignimbrites and all backarc Cerro Galán samples fall into the dacitic cluster (e.g. Atana, Granada, Vilama ignimbrites). This observation agrees with the model proposed by De Silva and Gosnold (2007), with



accumulation of large bodies of dacitic magma in the upper crust with time, fed by mantle power input. It is important to note, that all these ignimbrites are younger than 10 Ma, while samples to the north and south record ages up to 26 Ma and therefore times with a crust that was not as thick and thermally evolved as assumed for the APVC. In contrast, many samples of the older, large-volume Oxaya, Huaylillas and Nazca ignimbrites fall into the rhyolitic cluster, together with many older ignimbrites from southern Chile (e.g. Río Frío, Trinchera). This difference is also clearly expressed in the results of the REE-only clustering (Fig. 19), with these ignimbrites being in cluster three with flat LREE pattern and less pronounced Eu anomaly. In contrast, the samples of the large-volume APVC Atana and Purico ignimbrites are in cluster 2, with more pronounced Eu/Eu\* and LREE enrichment.

In section 3.2.1.2 we already correlated timing of ridge subduction with “ignimbrite flare ups” and crustal thickening. However, another aspect to consider is how much crustal component and how much mantle derived material contribute to ignimbrite melts and whether this controls clustering. Crustal thickness changed over time and the young APVC ignimbrites erupted from a thermally matured, exceptionally thick crust with ideal conditions for the formation of melt. Relatively high  $^{87}\text{Sr}/^{86}\text{Sr}$  ( $> 0,708$ ) coincide with the dacitic Northern Puna ignimbrites (e.g. Atana, Vilama), while lower ratios concentrate in the Southern Puna and on the Altiplano (Fig.19D), as also obvious in the interpolation model in section 3.2.2.2.2. As shown in section 3.2.1.1.2 (Fig.5) and discussed by (Mamani, 2009), isotope ratios can be explained by mantle source and crustal assimilation and are constant over a broad range of  $\text{SiO}_2$  contents for the same volcanic center. This argues for a higher degree of crustal assimilation for the Northern Puna ignimbrites than for the ignimbrites observed in the Southern Puna, Northern Chile and Peru (e.g. Oxaya: 0.707, Nazca: 0.706 (Mamani et al., 2008), Laguna Amarga: 0.706 (Siebel et al., 2001)). Using Rb/Sr as an indicator for fractional crystallization, Fig.19D shows clearly the difference in assimilation vs. fractional crystallization for Northern Puna and Southern Puna and northern Altiplano ignimbrites.

Thus, the large-volume Oxaya and Nazca ignimbrites have a more rhyolitic composition, may not be as crystal-rich as the large-volume APVC ignimbrites and have erupted from a thinner, colder crust with less crustal assimilation.

Due to the overlapping nature of REE clusters of hierarchical cluster analysis, in the following, we will use the REE-only clusters for interpretation. All samples of the APVC (e.g. Atana, Purico ignimbrites) belong to the first two clusters, with more pronounced negative Eu anomalies and variable degree of LREE with the dacitic Atana and Purico ignimbrites belonging to cluster 2 and the rhyolitic Toconao, Coyaguayama samples to cluster 1 that is more depleted in LREE, indicating fractionation of accessory mineral phases (e.g. monazite,

allanite). The Toconao ignimbrite that is interpreted as evolved cap of the dacitic Atana ignimbrite (De Silva and Gosnold, 2007). Many small-volume, rhyolitic ignimbrite samples from the Southern Puna and Southern Peru fall into cluster 1 (e.g. Vallecito, Tamberia, Caraveli, Cyclop ignimbrites). This is also true for cluster two (e.g. Yura Tuff, Parinas, Tal ignimbrites). Cluster three, however, besides rhyolitic small-volume ignimbrites (e.g. La Joya, Laguna Amarga, Trinchera), also includes the large-volume Oxaya ignimbrite. Six rhyolitic samples are also contained in cluster three, suggesting rapid ascent with little plagioclase fractionation. For dacitic samples, only four small-volume, Southern Puna samples belong to cluster one (Plato, Caballo Muerto), while all samples from the large-volume APVC ignimbrites and many smaller ignimbrites (Río Frío, La Ola, Toba 1) belong to cluster 2. Cluster three includes two Oxaya samples and many samples from small-volume ignimbrites, while cluster 4 mainly contains samples from the Turco-ignimbrite and samples from Southern Peru.

Another observation based on location is a W-E trend with less “evolved” samples being preferentially located more to the east (backarc). Furthermore, samples from specific ignimbrite units mostly fall into distinct clusters. This observation argues for ignimbrites having a unique “compositional signature” that is a function of the source and basement (mainly seen in isotopic compositions, see 2.4.1.1) and all processes taking place during the magmatic evolution (e.g. assimilation, mixing, differentiation). As ignimbrites are close to eutectic melts, subtle variations are to a high degree controlled by last-stage processes in the magma chamber. A distinction between “rhyolitic, crystal-poor, small-volume” and “large-volume, crystal-rich monotonous intermediate” seems to be insufficient to capture differences in ignimbrite evolution and genesis. On the basis of these observations, in the following, we conduct discriminant analysis on a subset of data in order to test the hypothesis of ignimbrites having a distinct compositional signature.

### 3.2.2.2 Whole-rock compositional signatures as a “fingerprint” for discriminating ignimbrites?

---

Correlating ignimbrites on the basis of macroscopic features like, for example, lithics, phenocrysts or degree of welding is difficult (De Silva and Francis, 1989) as ignimbrites may look very similar and variability in color can be due to local oxidation and cooling and might be different for the same ignimbrite, depending on position. Isotopic dating is expensive and cannot exclude the possibility of two ignimbrites erupting within the same time interval. Thus, geochemical “fingerprinting” of ignimbrites constitutes an easy way to discriminate between ignimbrites. (deSilva and Francis, 1989). However, no single criterion can be used to

fingerprint ignimbrites and therefore statistical methods in an n-dimensional space are a feasible tool for this kind of question. Discriminant function analysis is a tool to determine whether groups (e.g. ignimbrites) differ with regard to the mean of a variable, and then to use this information to predict group memberships for new samples.

In order to test the discriminant power of compositional signatures, discriminant analysis was conducted for selected ignimbrites (Table 4) using major elements and REEs. Representative ignimbrites are those with more than five samples (e.g. Oxaya ignimbrite, Arequipa Airport Ignimbrite, La Joya, Atana, Río Frío, Parinas). The Pucarilla ignimbrite has several units that are highlighted in blue. The overall result of 90 % correctly discriminated ignimbrites strengthens our hypothesis that whole-rock compositional signatures can be used to distinguish ignimbrites. This analysis is based on known samples and could not be verified with additional samples due to a lack of sufficient data. Validation results therefore have to be considered with care as they are based on post-hoc probabilities. Applying discrimination functions to new samples is still not recommended as more training samples would be needed to calculate more robust functions. However, we believe that this approach can lead to an easily applicable method for identifying, distinguishing and correlating individual ignimbrites if reliable compositional vectors could be calculated and measurements for more trace elements were available for all samples. To prove this hypothesis, another discriminant analysis was conducted with a smaller set of ignimbrites with enough samples to keep a dataset apart for validation (Table 5). Variables in the model were all major and REEs except  $\text{Na}_2\text{O}$ , Tb and Ho. Validation results with an overall accuracy of 87.5% are quite good. Misclassified samples are from the Arequipa Airport Ignimbrite, Yura Tuff and La Joya Ignimbrite that are from the same area but have different ages.

So far, discriminant analysis was handled as “black box” model. However, canonical analysis and discriminant functions provide information about how discrimination was achieved and what elements contribute to the model. For the discrimination of the 12 selected ignimbrites, four discriminant functions suffice for discrimination (first three roots have an Eigenvalue > 75%) and respective canonical scores for each ignimbrite are shown in Fig.21. The first two functions already discriminate between Atana, Río Frío and Parinas ignimbrites. Adding the third function, Toba 1, Oxaya, Yura tuff, Purico ignimbrite and Caraveli ignimbrites appear in distinct groups. Further addition of the fourth function, perfectly discriminates the Turco ignimbrite and further discriminates Oxaya ignimbrite. The Arequipa (airport) ignimbrite, Yura tuff and La Joya ignimbrite plot very close in all diagrams

Table 4: Results of Discriminant analysis. Note that classifications results are post-hoc predictions with no separate data set for validation.

Class	Ignimbrite unit	Percent	1	2	3	4	5	6	7	8	9	10	11	12	13	14	15	16	17	18	19	20	21	22	23	24	25	26	27	28	29	30	31
1	Arequipa Airport ignimbrite	76.9	10	0	0	1	0	0	0	0	0	0	0	0	0	2	0	0	0	0	0	0	0	0	0	0	0	0	0	0	0	0	0
2	Atana	100	0	4	0	0	0	0	0	0	0	0	0	0	0	0	0	0	0	0	0	0	0	0	0	0	0	0	0	0	0	0	
3	Cerro Blanco	100	0	0	2	0	0	0	0	0	0	0	0	0	0	0	0	0	0	0	0	0	0	0	0	0	0	0	0	0	0	0	
4	La Joya ignimbrite	84.6	1	0	0	11	0	0	0	0	0	0	0	0	0	1	0	0	0	0	0	0	0	0	0	0	0	0	0	0	0	0	
5	Oxaya Ignimbrite	100	0	0	0	0	10	0	0	0	0	0	0	0	0	0	0	0	0	0	0	0	0	0	0	0	0	0	0	0	0	0	
6	Purico LPI I	100	0	0	0	0	0	2	0	0	0	0	0	0	0	0	0	0	0	0	0	0	0	0	0	0	0	0	0	0	0	0	
7	Turco-Ignimbrite	100	0	0	0	0	0	0	6	0	0	0	0	0	0	0	0	0	0	0	0	0	0	0	0	0	0	0	0	0	0	0	
8	Toba 1	100	0	0	0	0	0	0	0	4	0	0	0	0	0	0	0	0	0	0	0	0	0	0	0	0	0	0	0	0	0	0	
9	Hualfín Unit- Pucarilla Ignimbrite	60	0	0	0	0	0	0	0	0	3	0	0	0	0	0	0	0	0	0	0	0	0	0	0	0	0	2	0	0	0	0	
10	Luingo I Ignimbrite	100	0	0	0	0	0	0	0	0	0	2	0	0	0	0	0	0	0	0	0	0	0	0	0	0	0	0	0	0	0	0	
11	Alto de Las Lagus Ignimbrite	100	0	0	0	0	0	0	0	0	0	0	2	0	0	0	0	0	0	0	0	0	0	0	0	0	0	0	0	0	0	0	
12	Coyaguayma ignimbrite	100	0	0	0	0	0	0	0	0	0	0	0	2	0	0	0	0	0	0	0	0	0	0	0	0	0	0	0	0	0	0	
13	Toconao	100	0	0	0	0	0	0	0	0	0	0	0	0	3	0	0	0	0	0	0	0	0	0	0	0	0	0	0	0	0	0	
14	Yura Tuff	83.3	1	0	0	0	0	0	0	0	0	0	0	0	0	5	0	0	0	0	0	0	0	0	0	0	0	0	0	0	0	0	
15	Parinas	100	0	0	0	0	0	0	0	0	0	0	0	0	0	0	9	0	0	0	0	0	0	0	0	0	0	0	0	0	0	0	
16	Cyclop	50	0	0	0	0	0	0	0	0	0	0	0	0	0	0	0	2	0	0	0	0	0	0	1	1	0	0	0	0	0	0	
17	Rio Frío	100	0	0	0	0	0	0	0	0	0	0	0	0	0	0	0	0	9	0	0	0	0	0	0	0	0	0	0	0	0	0	
18	Pedernales	100	0	0	0	0	0	0	0	0	0	0	0	0	0	0	0	0	0	2	0	0	0	0	0	0	0	0	0	0	0	0	
19	Rio Negro	100	0	0	0	0	0	0	0	0	0	0	0	0	0	0	0	0	0	0	2	0	0	0	0	0	0	0	0	0	0	0	
20	Lauca-Perez	100	0	0	0	0	0	0	0	0	0	0	0	0	0	0	0	0	0	0	0	2	0	0	0	0	0	0	0	0	0	0	
21	Trinchera	100	0	0	0	0	0	0	0	0	0	0	0	0	0	0	0	0	0	0	0	0	2	0	0	0	0	0	0	0	0	0	
22	Caraveli	100	0	0	0	0	0	0	0	0	0	0	0	0	0	0	0	0	0	0	0	0	0	6	0	0	0	0	0	0	0	0	
23	Laguna Amarga	100	0	0	0	0	0	0	0	0	0	0	0	0	0	0	0	0	0	0	0	0	0	0	3	0	0	0	0	0	0	0	
24	Vallecito	100	0	0	0	0	0	0	0	0	0	0	0	0	0	0	0	0	0	0	0	0	0	0	0	3	0	0	0	0	0	0	
25	Purico LPI II	100	0	0	0	0	0	0	0	0	0	0	0	0	0	0	0	0	0	0	0	0	0	0	0	6	0	0	0	0	0	0	
26	Arremo Unit- Pucarilla Ignimbrite	50	0	0	0	0	0	0	0	0	1	0	0	0	0	0	0	0	0	0	0	0	0	0	0	0	3	1	1	0	0	0	
27	Jasimaná Unit- Pucarilla Ignimbrite	85.79	0	0	0	0	0	0	0	0	0	1	0	0	0	0	0	0	0	0	0	0	0	0	0	0	0	6	0	0	0	0	
28	Luingo II Ignimbrite	100	0	0	0	0	0	0	0	0	0	0	0	0	0	0	0	0	0	0	0	0	0	0	0	0	0	3	0	0	0	0	
29	Archibarca	100	0	0	0	0	0	0	0	0	0	0	0	0	0	0	0	0	0	0	0	0	0	0	0	0	0	0	3	0	0	0	
30	El Misti	87	0	0	0	0	0	0	0	0	0	0	0	0	0	0	0	0	0	0	0	0	0	0	0	0	0	0	0	7	1	0	
31	Ubinas	100	0	0	0	0	0	0	0	0	0	0	0	0	0	0	0	0	0	0	0	0	0	0	0	0	0	0	0	0	3	0	
Total		90.1	12	4	2	12	10	2	6	4	4	2	3	2	3	8	9	2	9	2	2	2	2	6	4	4	6	5	7	4	3	7	4

Table 5: Discriminant analysis with independent validation for selected ignimbrites. REE clusters are given for comparison.

Discriminant analysis				REE cluster											
Class	Ignimbrite unit	REE cluster	Percent	1	2	3	4	5	6	7	8	9	10	11	12
1	Arequipa Airport Ignimbrite	1	90.9	10	0	0	0	0	0	1	0	0	0	0	0
2	Atana Ignimbrite	3	100	0	3	0	0	0	0	0	0	0	0	0	0
3	La Joya Ignimbrite	1	100	0	0	11	0	0	0	0	0	0	0	0	0
4	Oxaya Ignimbrite	1	100	0	0	0	9	0	0	0	0	0	0	0	0
5	Turco Ignimbrite	4	100	0	0	0	0	5	0	0	0	0	0	0	0
6	Toba I	4	100	0	0	0	0	0	3	0	0	0	0	0	0
7	Yura Tuff	1	100	0	0	0	0	0	0	5	0	0	0	0	0
8	Parinas	1	100	0	0	0	0	0	0	0	8	0	0	0	0
9	Río Frío Ignimbrite	3	100	0	0	0	0	0	0	0	0	7	0	0	0
10	Caraveli Ignimbrite	2	100	0	0	0	0	0	0	0	0	0	5	0	0
11	Purico LPII	3	100	0	0	0	0	0	0	0	0	0	0	5	0
12	El Misti pyroclastics	4	100	0	0	0	0	0	0	0	0	0	0	0	6
Total			98.7	10	3	11	9	5	3	6	8	7	5	5	6

Validation				REE cluster											
Class	Ignimbrite unit	REE cluster	Percent	1	2	3	4	5	6	7	8	9	10	11	12
1	Arequipa Airport Ignimbrite	1	50	1	0	1	0	0	0	0	0	0	0	0	0
2	Atana Ignimbrite	3	100	0	1	0	0	0	0	0	0	0	0	0	0
3	La Joya Ignimbrite	1	50	0	0	1	0	0	0	1	0	0	0	0	0
4	Oxaya Ignimbrite	1	100	0	0	0	1	0	0	0	0	0	0	0	0
5	Turco Ignimbrite	4	100	0	0	0	0	1	0	0	0	0	0	0	0
6	Toba I	4	100	0	0	0	0	0	1	0	0	0	0	0	0
7	Yura Tuff	1	100	0	0	0	0	0	0	1	0	0	0	0	0
8	Parinas	1	100	0	0	0	0	0	0	0	1	0	0	0	0
9	Río Frío Ignimbrite	3	100	0	0	0	0	0	0	0	0	2	0	0	0
10	Caraveli Ignimbrite	2	100	0	0	0	0	0	0	0	0	0	1	0	0
11	Purico LPII	3	100	0	0	0	0	0	0	0	0	0	0	1	0
12	El Misti pyroclastics	4	100	0	0	0	0	0	0	0	0	0	0	0	2
Total			87.5	1	1	2	1	1	1	2	1	2	1	1	2

due to compositional similarity. However, all functions combined, discrimination still works quite well. Coefficients of each function and variable help to better understand the nature of the functions. High values indicate a strong influence of the respective variable. Coefficients are given in Table 6. Comparing the position of each ignimbrite in the plots of Fig.21 to the

equations for the respective roots, we find that the Parinas ignimbrite (strong negative value for root 2, negative value for root 1, 3 and 4) is characterized by all elements contributing negatively to the respective functions (e.g. La, Sm, Yb, Eu, K<sub>2</sub>O, Al<sub>2</sub>O<sub>3</sub>). In contrast, the Atana ignimbrite has positive values for root 1, 2 and 3, showing the opposite trend (with MgO, P<sub>2</sub>O<sub>4</sub>, TiO<sub>2</sub>, Pr, Lu making the roots positive). This is consistent with the “less evolved” cluster 3, while the Parinas ignimbrite is more evolved (cluster 1). The Oxaya ignimbrite is very similar in roots 1 and 2 to the Toba 1 and Turco ignimbrite. However, roots 3 and 4 that are strongly influenced by Al<sub>2</sub>O<sub>3</sub>, Nd, FeO<sub>t</sub>, P<sub>2</sub>O<sub>5</sub> (negative root 3, Toba 1, positive for Oxaya and Turco) and Eu, Pr, Sm, Tm and Er (positive root 4, Turco and Toba 1, negative for Oxaya) clearly distinguish the three ignimbrites. The only means root 4 can become negative is by SiO<sub>2</sub> or MnO. This is why the rhyolitic Oxaya samples are negative, while the Toba 1 and Turco ignimbrites have positive values. This means, the respective elements have most discriminant power for the respective ignimbrites.

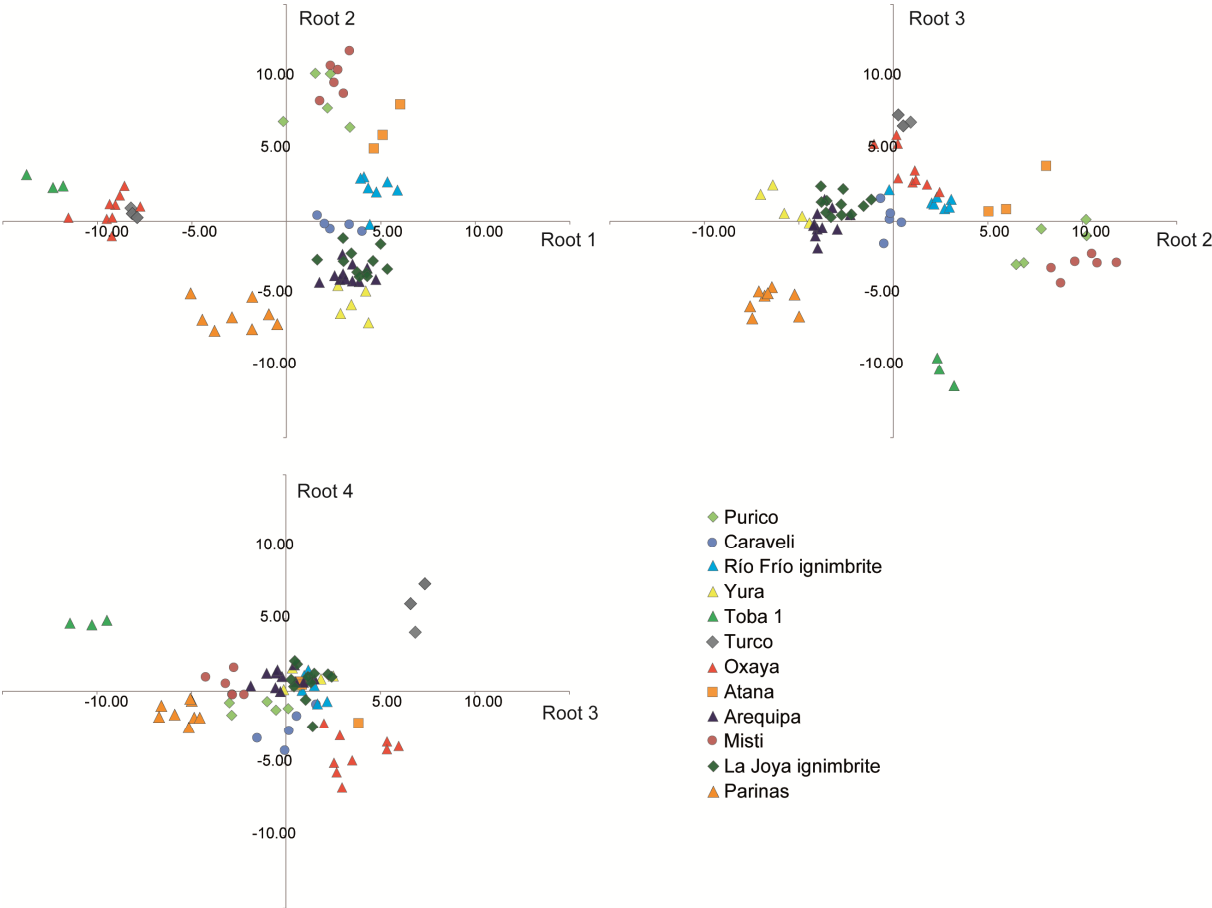


Fig. 21: Canonical scores for each ignimbrite for the four most important discriminant functions (roots).

Table 6: Coefficients for each variable in each discriminant (canonical) function. 10% highest and lowest values are highlighted in green and red, respectively. In the model, roots 1 to 4 discriminate between the ignimbrites.

	Root 1	Root 2	Root 3	Root 4	Root 5	Root 6	Root 7	Root 8	Root 9	Root 10	Root 11
TiO <sub>2</sub>	0.758	0.110	1.820	0.190	-0.007	0.943	-0.265	-0.046	-0.145	0.455	-0.007
Gd	-0.728	0.051	0.723	0.683	1.353	0.051	0.056	0.403	-0.114	0.764	0.525
Dy	-0.380	-0.140	-0.038	0.715	1.370	1.789	-0.116	0.426	0.820	2.036	2.309
Eu	0.866	-1.872	0.095	3.521	3.047	1.618	-0.965	0.649	-0.350	3.061	2.308
MnO	0.123	-0.421	1.176	-0.108	1.022	0.857	0.115	-0.071	0.038	1.264	0.352
K <sub>2</sub> O	1.498	-1.536	0.873	1.238	-0.576	0.842	0.828	0.609	-0.378	0.296	0.611
Pr	4.477	-0.577	0.441	2.492	1.049	1.690	0.979	-0.297	-0.127	1.583	-1.469
La	-3.601	-0.445	1.308	1.646	0.671	1.750	-0.531	0.106	-0.005	2.321	2.514
Nd	1.363	-0.300	-1.090	0.400	2.204	-2.483	-0.432	1.977	1.049	-0.194	2.919
Al <sub>2</sub> O <sub>3</sub>	-0.153	1.903	-2.548	0.746	0.433	-1.343	1.831	-0.712	-0.405	0.139	0.436
Sm	-1.619	0.311	-0.320	1.902	0.833	1.226	-1.226	0.260	-0.977	1.393	0.350
Tm	2.209	-0.717	-0.585	2.943	2.075	0.327	-0.393	1.092	0.220	0.621	1.857
FeO <sub>t</sub>	-0.268	0.976	-1.060	0.272	0.195	-0.853	1.025	-0.259	-0.132	0.799	0.811
Lu	0.578	1.847	-0.162	0.851	1.631	0.587	-0.440	-0.471	0.661	1.890	2.683
Yb	-2.574	-2.354	1.175	0.864	1.139	1.441	-1.043	1.632	-1.757	1.097	0.089
P <sub>2</sub> O <sub>5</sub>	0.885	0.714	-0.812	0.819	0.312	-0.044	0.354	0.284	0.239	0.294	0.739
MgO	1.277	0.741	0.358	0.987	-0.095	-0.072	1.289	-0.117	-0.595	0.912	0.353
Er	1.051	-0.176	-0.451	2.866	0.529	-0.916	-0.920	-0.154	0.454	1.901	-0.026
Ce	-0.406	-0.404	-0.409	1.557	0.971	0.416	-1.438	-0.021	0.736	1.192	1.221
SiO <sub>2</sub>	-0.220	-0.287	1.127	-0.223	0.731	0.397	-0.395	-0.062	-0.011	1.377	0.797
CaO	0.157	-0.216	0.001	0.056	0.330	1.000	0.469	-0.278	0.257	0.463	0.964
Eigenval	34.804	28.281	15.704	7.588	5.501	4.215	1.801	1.421	0.722	0.345	0.139
Cum.Prop	0.346	0.628	0.784	0.859	0.914	0.956	0.974	0.988	0.995	0.999	1.000

The most important elements for discriminating ignimbrites are La (LREE), Yb (HREE), Eu, Al<sub>2</sub>O<sub>3</sub>, K<sub>2</sub>O, P<sub>2</sub>O<sub>5</sub>, MgO, FeO<sub>t</sub> and TiO<sub>2</sub>. This is not surprising, as variations in these elements, for ignimbrite melt close to the ternary eutectic, are mainly controlled by differences in the degree of assimilation, differentiation and mineral fractionation. However, other REEs like Gd, Pr, Tm, Sm and Er also contribute a lot to the discrimination functions, especially in root 4 (Table 6). Thus, including these REEs helps to find more subtle differences that are particular to each ignimbrite.

In summary, most of the variability in major and trace elements in ignimbrite whole-rock composition seems to be mainly controlled by assimilation, mineral fractionation at deeper crustal levels (HREE depletion by amphibole and/or garnet as a residuum) and late-stage magmatic processes like mineral fractionation and differentiation in a shallow magma

chamber. Other factors, like differences in source, physical parameters or assimilation are probable to cause subtle changes in composition. The link between elements is very systematic in compositional biplots and was exemplified using traditional geochemical plots and parameters for comparison. Based on the assumption that ignimbrite eruptions tap a unique magma chamber and have a unique evolution, we tested the hypothesis that we can use major and REE composition to “fingerprint” ignimbrites. Discriminant function analysis gave an overall accuracy of 88 % and canonical functions provided information about the role of elements for discrimination.

Finally, to make a case for the statement of Section 3.2.2.1.2 that a “distinction between “rhyolitic, crystal-poor, small-volume” and “large-volume, crystal-rich monotonous intermediate” seems to be insufficient to capture differences in ignimbrite evolution and genesis”, we now use the above discriminated ignimbrites to show how small and large volume ignimbrites of different ages have variable compositions. The large-volume, ca. 19 Ma Oxaya ignimbrite is compositionally very distinct from the young APVC Atana ignimbrite, suggesting a different genesis than suggested for the large-volume APVC ignimbrites.

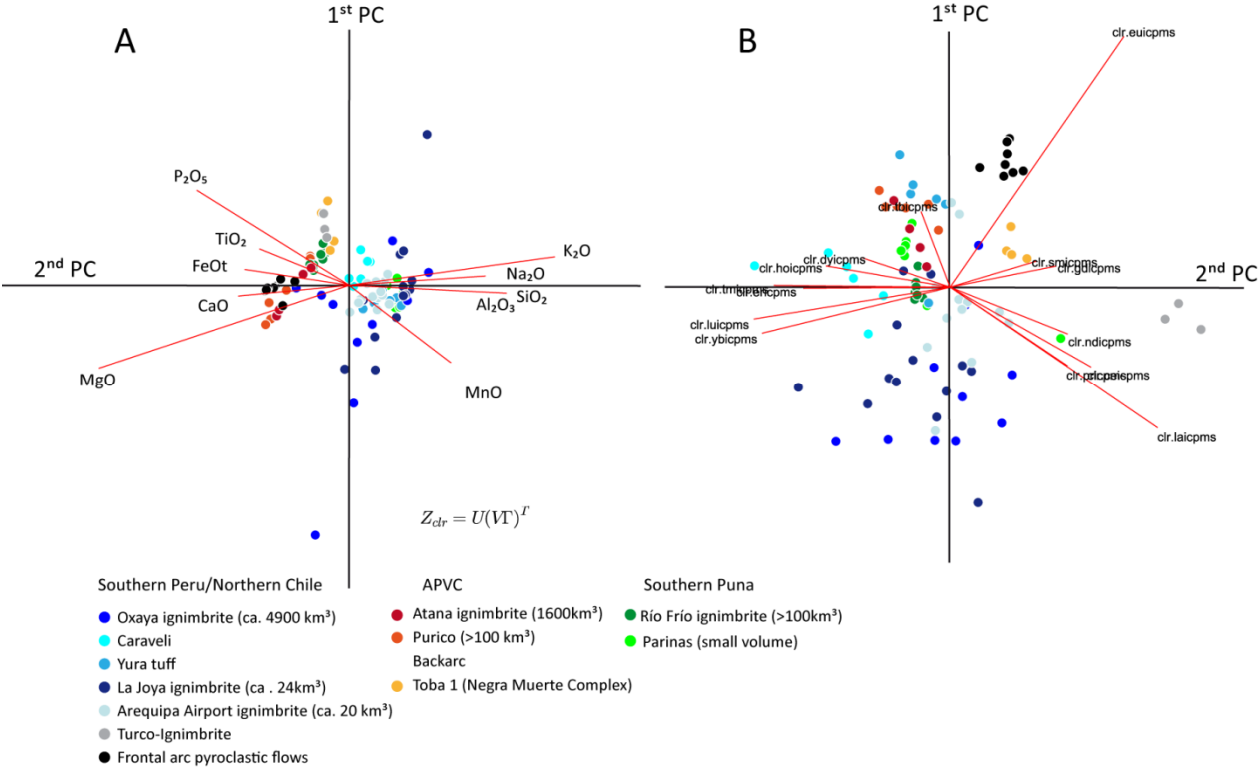


Fig. 22: Compositional biplots (A: Major elements; B: REEs) for the ignimbrites used for discriminant analysis. Representative large-volume ignimbrites and small-volume ignimbrites of different areas are shown. We observe more rhyolitic compositions for the old, large volume Oxaya ignimbrite, while the young Atana and Purico APVC ignimbrites are more dacitic. This suggests a different genetic model for the Oxaya ignimbrite than the large-volume APVC ignimbrites.



## 4 Summary and Conclusions

---

Timing of ignimbrites, their composition and volume are closely linked to the thermal and structural evolution of the crust and partial crustal melting and magmatism in the mantle wedge related to the subduction of the Nazca plate and can therefore be used as tracers of these processes. We calculated eruptive volumes of ignimbrites over time and applied different methods of geospatial and multivariate statistics on our new Ignimbrite Database in order to explore patterns and compositional variations in explosive volcanism in the Andes. We believe that this approach has several advantages: 1) A database can be made available as WMA to other scientists and can constantly be enlarged; 2) Spatial and temporal statistical analysis provides a better understanding of the magmatic history and basement structure of the Andes; 3) Compositional variations in magmatic rocks can be traced and analyzed statistically by using log-ratio transformation that circumvents problems inherent in compositional data due to the simplex data space.

Differences in the basement of the Andes and assimilation in the lower crust are the main reason for the isotopic composition of magmatic rocks in the Central Andes (Mamani et al., 2008; Mamani et al., 2010). We used simple kriging on our compiled data and propose new probability models for the three lead isotope systems, together with an error value for each interpolated pixel. Adding interpolation models for Nd and Sr isotope systems, we derived information about the degree of crustal assimilation versus mantle input in the respective magmatic rocks. For ignimbrites, we observe more radiogenic Sr ( $>0.708$ ) values for the Northern Puna ignimbrites than for ignimbrites of the Southern Puna, the Altiplano and Southern Peru, arguing for a higher crustal component in those ignimbrites. Least radiogenic values in Sr and Nd isotope systems correspond to ignimbrites from the Arequipa domain of Mamani et al. (2008). One major problem involved with our kriging models is, that samples are not evenly distributed and errors are still high for some areas. However, models fit quite well and delineate the different lead domains proposed by (Mamani et al., 2008) and references herein).

We used cluster analysis on clr-transformed major and trace element data to group ignimbrites according to geochemical characteristics and compared our results to traditional geochemical parameters. Based on major elements, we found a rhyolitic and a dacitic “end-member”. Those “end-members” overlap in REE compositions with more or less pronounced negative Eu anomaly, depletion of MREEs (possibly due to amphibole fractionation) and enrichment/depletion in LREE. Based these results, we argue, that a distinction between “rhyolitic, crystal-poor, small-volume” and “large-volume, crystal-rich monotonous inter-

mediate” seems to be insufficient to capture differences in ignimbrite evolution and genesis. The large-volume, ca. 19 Ma Oxaya ignimbrite is compositionally very distinct from the young APVC Atana ignimbrite, suggesting a different genesis than suggested for the large-volume APVC ignimbrites. This finding agrees with differences in Sr isotopes, arguing for less crustal assimilation, possibly due to the thinner and colder crust at that time. Most rhyolitic ignimbrites are concentrated north and south of the Northern Puna, with only minor rhyolites as more differentiated equivalents of the prominent dacites occurring there as described by De Silva and Gosnold (2007). This observation agrees with the model proposed by De Silva and Gosnold (2007), with accumulation of large bodies of dacitic magma in the upper crust with time, fed by mantle power input. It is important to note, that all these ignimbrites are younger than 10 Ma, while samples to the north and south record ages up to 26 Ma and therefore times with a crust that was not as thick and thermally evolved as assumed for the APVC.

To test our hypothesis that compositional signatures can be used to distinguish between ignimbrites, we applied discriminant analysis to selected ignimbrites. Classification results show that the method works very well if there is enough data to calculate robust statistics. Validation on a small subset gave an 87.5% overall accuracy. The most important elements for discriminating our ignimbrites are La (LREE), Yb (HREE), Eu, Al<sub>2</sub>O<sub>3</sub>, K<sub>2</sub>O, P<sub>2</sub>O<sub>5</sub>, MgO, FeO<sub>t</sub> and TiO<sub>2</sub>. However, other REEs like Gd, Pr, Tm, Sm and Er also contribute to the discrimination functions. Thus, including these REEs helps to find more subtle differences that are particular to each ignimbrite.

In order to examine the spatiotemporal pattern of so-called “ignimbrite flare-ups”, we mapped 201 Andean ignimbrites (including some related domes) using satellite imagery and available maps. Using South America Albers Equal Area Conic Projection, we calculated the cumulative areal extent of ignimbrites through time and propose new estimates for ignimbrite cover, eruptive volumes and timing of ignimbrite eruptions. Calculating eruptive volumes is difficult due to the commonly buried source calderas of ignimbrites, the lack of knowledge of the real extent, average thickness and errors in ignimbrite correlation. Therefore we propose estimates for minimum coverage and volume for the CVZ and for five N-S segments ( Southern Peru, southernmost Peru, Altiplano, Northern and Southern Puna).

As ignimbrite eruptions represent the surface manifestation of plutonic activity, eruptive volumes can help us to understand processes taking place in the upper crust. In total, we estimate eruptive volumes of 31,000 km<sup>3</sup>, with 2,400 km<sup>3</sup> for Southern Peru, 2,700 km<sup>3</sup> for Southernmost Peru, 8,400 km<sup>3</sup> for the Altiplano, 14,200 km<sup>3</sup> for the Northern Puna and 3,100 km<sup>3</sup> for the Southern Puna segments. Using the same assumptions as ( De Silva and Gosnold, 2007), we calculate a minimum plutonic input of 7,200 km<sup>3</sup>, 8,100 km<sup>3</sup>, 25,200 km<sup>3</sup>,

42,600 km<sup>3</sup> and 9,300 km<sup>3</sup> for the respective segments during the past 30 Ma and observe a N-S “younging” of eruption ages and “ignimbrite pulses”. Major pulses occurred at 19-24 Ma (Oxaya, Nazca Group), 13-14 Ma (Huaylillas and Puquio ignimbrites), 6-10 Ma (many of the Altiplano and Puna ignimbrites like the Galán, Las Termas, Potrerros, Panizos, Vilama and Guacha ignimbrites) and 3-6 Ma (e.g. Atana, Los Frailes, Toconao, Caracote, Chuhuilla) and very young ignimbrites from 0-3 Ma (Lauca-Perez, Purico, Cerro Blanco, Pastos Grande). We propose that big ignimbrite eruptions (e.g. Nazca, Huaylillas, Oxaya, APVC eruptions) occurred in the wake of the subducting Juan-Fernandez ridge, with compression, uplift, shallow subduction and fluid release in a first stage, upon arrival of the ridge, and melting of the so “conditioned” crust due to renewed asthenospheric mantle flow above a steepening slab after the passing of the ridge.

The total estimates for the northern segments 1-3 and the Northern Puna are sub-equal, however, calderas and thus intra-caldera volumes for ignimbrites in these segments are not known and due to higher age, preservation level for the ignimbrites is much lower. Thus, it may be possible, that the latter ignimbrites represent volumes greater than in the Northern Puna. If further studies show that this is the case, the concept of an APVC flare-up should be revised and not viewed as a regionally and temporally restricted event of high-magma flux and batholith construction. Instead, we suggest a paradigm shift towards a dynamic model, with the “flare up” as a moving entity that has progressed across the Andes during the past 25 Ma, probably related to ridge subduction, with the Northern Puna flare up only being the most recent and best preserved remnant, and the Southern Puna Cerro Galán eruption possibly heralding another flare-up.

## REFERENCES:

- Aitchison, S.J., Harmon, R.S., Moorbath, S., Schneider, A., Soler, P., Soria-Escalante, E., Steele, G., Swainbank, I., Wörner, G., 1995. Pb isotopes define basement domains of the Altiplano, Central Andes. *Geology*, 17.
- Aitchison, J., Greenacre, M., 2002. Biplots of compositional data. *Journal of the Royal Statistical Society: Series C (Applied Statistics)* 51, 375-392.
- Allmendinger, R.W., Jordan, T.E., Kay, S.M., Isacks, B.L., 1997. The Evolution of the Altiplano-Puna Plateau of the Central Andes. *Annu. Rev. Earth Planet. Sci.* 27, 139-174.
- Annen, C., 2009. From plutons to magma chambers: Thermal constraints on the accumulation of eruptible silicic magma in the upper crust. *Earth and Planetary Science Letters* 284, 409-416.
- Baker, M.C.W., Francis, P.W., 1978. Upper Cenozoic volcanism in the Central Andes - Ages and volumes. *Earth. Planet. Sci. Lett.* 41, 175-187.
- Beck, S.L., Zandt, G., Myers, S.C., Wallace, T.C., Silver, P.G., Drake, L., 1996. Crustal-thickness variations in the Central Andes. *Geology* 24, 407-410.
- Brandmeier, M., Mamani, M., Jicha, B.; Wörner, G., Age and distribution of Neogene ignimbrites in Southern Peru as tracers for uplift, erosion and changes in the Andean drainage divide between the Pacific and Atlantic Oceans. (in preparation)
- Buccianti, A., Mateu-Figueras, G., Glahn, V.P., 2006. Compositional data analysis in the geosciences: from theory to practice. Geological Society.
- Caffe, P.J., Trumbull, R.B., Siebel, W., 2012. Petrology of the Coyaguayma ignimbrite, northern Puna of Argentina: Origin and evolution of a peraluminous high SiO<sub>2</sub> rhyolite magma. *Lithos* 134, 179-200D
- Capobianco, C.J., Drake, M.J., 1990. Partitioning of ruthenium, rhodium, and palladium between spinel and silicate melt and implications for platinum group element fractionation trends. *Geochimica et Cosmochimica Acta* 54, 869-874.
- Cheilletz, A., Clark, A.H., Farrar, E., Pauca, G.A., Pichavant, M., Sandeman, H.A., 1992. Volcano-stratigraphy and <sup>40</sup>Ar/<sup>39</sup>Ar geochronology of the Macusani ignimbrite field: monitor of the Miocene geodynamic evolution of the Andes of southeast Peru. *Tectonophysics* 205, 307-327.
- Coira, B., Mahlburg, K., Viramonte, J., 1993. Upper Cenozoic magmatic evolution of the Argentine Puna-A model for changing subduction geometry. *International Geology Review* 35, 677-720.
- Davidson, J.P., De Silva, S.L., 1992. Volcanic rocks from the Bolivian Altiplano: Insights into crustal structure, contamination, and magma genesis in the central Andes. *Geology* 20, 1127-1130.
- Davidson, J.P., De Silva, S.L., Escobar, A., Feeley, T., Bohron, W., 1990. Evaluation of magma sources for Central Andean volcanics. In: *Chilean Geological Congress Abstracts*.
- De Silva, S., 1989a. The origin and significance of crystal-rich inclusions in pumice from two Chilean ignimbrites. *Geol Mag* 126, 159-175.
- De Silva, S.L., 1989b. Altiplano-Puna volcanic complex of the central Andes. *Geology* 17, 1102-1106.
- De Silva, S.L., 1989c. Geochronology and Stratigraphy of the Ignimbrites from the 21° 30'S to 23° 30'S portion of the Central Andes of Northern Chile. *J. of Volc. and Geotherm. Res.* 37, 93-131.

- De Silva, S.L., 1991. Styles of zoning in central Andean ignimbrites ; insights into magma chamber processes. *The Geological Society of America Andean Magmatism and Its Tectonic Setting* 265, 217-231.
- De Silva, S.L., Francis, P.W., 1989. Correlation of large ignimbrites - two case studies from the central Andes of Northern Chile. *J. of Volc. and Geotherm. Res.* 37, 133-149.
- De Silva, S.L., Francis, P.W., 1991. Volcanic evolution of the Central Volcanic Zone of the Andes - Where should we go from here? *Congreso Geologico Chileno 1991. Resumenes Expandidos Servicio Nacional de Geologia y Minería Chile*, 490-493.
- De Silva, S.L., Gosnold, W.D., 2007. Episodic construction of batholiths: Insights from the spatiotemporal development of an ignimbrite flare-up. *Journal of Volcanology and Geothermal Research* 167, 320-335.
- Delacour, A., Gerbe, M.-C., Thouret, J.-C., Wörner, G., Paquereau-Lebti, P., 2007. Magma evolution of Quaternary minor volcanic centres in Southern Peru, Central Andes. *Bulletin of volcanology* 69, 581-608.
- Ducea, M., 2001. The California arc: Thick granitic batholiths, eclogitic residues, lithospheric-scale thrusting, and magmatic flare-ups. *GSA today* 11, 4-10.
- Folkes, C.B., Wright, H.M., Cas, R.A., De Silva, S.L., Lesti, C., Viramonte, J.G., 2011. A re-appraisal of the stratigraphy and volcanology of the Cerro Galán volcanic system, NW Argentina. *Bulletin of volcanology* 73, 1427-1454.
- Francis, P.W., Baker, M. C. W. & Halls C., 1981. The Kari Kari Caldera, Bolivia, and the Cerro Rico Stock. *Journal of Volcanology and Geothermal Research* 10, 113-124.
- Francis, P.W., McDonough, W.F., Hammill, M., O'Callaghan, L.J., Thorpe, R.S., 1984. The Cerro Purico shield complex, north Chile. *Andean Magmatism - chemical and isotopic constraints*, 106-123.
- Francis, P.W., O'Callaghan, L., Kretzschmar, G.A., Thorpe, R.S., Sparks, R.S.J., Page, R.N., de Barrio, R.E., Gillou, G., Gonzalez, O.E., 1983. The Cerro Galan Ignimbrite. *Nature* 301, 51-53.
- Francis, P.W.H., C. J., 1994. Late Cenozoic rates of magmatic activity in the Central Andes and their relationships to continental crust formation and thickening. *Journal of the Geological Society, London* 151, 845-854.
- Gardeweg, M., Ramírez, C.F., 1987. La Pacana caldera and the Atana Ignimbrite — a major ash-flow and resurgent caldera complex in the Andes of northern Chile. *Bulletin of Volcanology* 49, 547-566.
- Glazner, A.F., Bartley, J.M., Coleman, D.S., Gray, W., Taylor, R.Z., 2004. Are plutons assembled over millions of years by amalgamation from small magma chambers? *GSA today* 14, 4-12.
- Goss, A.R., Kay, S.M., Mpodozis, C., Singer, B.S., 2009. The Incapillo Caldera and Dome Complex (similar to 28 degrees S, Central Andes): A stranded magma chamber over a dying arc. *Journal of Volcanology and Geothermal Research* 184, 389-404.
- Gottsmann, J., Lavallée, Y., Martí, J., Aguirre-Díaz, G., 2009. Magma–tectonic interaction and the eruption of silicic batholiths. *Earth and Planetary Science Letters* 284, 426-434.
- Gregory-Wodzicki, K.M., 2000. Uplift history of the Central and Northern Andes; a review. *GSA Bulletin* 112, 1091-1105.
- Guzmán, S., Petrinovic, I., 2010. The Luingo caldera: The south-easternmost collapse caldera in the Altiplano–Puna plateau, NW Argentina. *Journal of Volcanology and Geothermal Research* 194, 174-188.

- Hamilton, W., Myers, W.B., 1967. The nature of batholiths. US Government Printing Office.
- Hampel, A., 2002. The migration history of the Nazca Ridge along the Peruvian active margin: a re-evaluation. *Earth and Planetary Science Letters* 203, 665-679.
- Hildreth, W., 1981. Gradients in Silicic Magma Chambers: Implications for Lithospheric Magmatism. *J. Geophys. research* 86, 10153-10192.
- Hildreth, W., Moorbath, S., 1988. Crustal contributions to arc magmatism in the Andes of Central Chile. *Contrib. Mineral. Petrol.* 98, 455-489.
- James, D.E., Sacks, I.S., 1999. Cenozoic formation of the Central Andes: a geophysical perspective. *Geology and Ore Deposits of the Central Andes* 7, 1-25.
- Jellinek, A.M., DePaolo, D., 2003. A model for the origin of large silicic magma chambers: precursors of caldera-forming eruptions. *Bulletin of volcanology* 65, 363-381.
- Kay, S.M., Coira, B.L., 2009. Shallowing and steepening subduction zones, continental lithospheric loss, magmatism, and crustal flow under the Central Andean Altiplano-Puna Plateau. *Backbone of the Americas: shallow subduction, plateau uplift, and ridge and terrane collision* 204, 229.
- Kay, S.M., Coira, B.L., Caffee, P.J., Chen, C.-H., 2010. Regional chemical diversity, crustal and mantle sources and evolution of central Andean Puna plateau ignimbrites. *Journal of Volcanology and Geothermal Research* 198, 81-111.
- Kay, S.M., MaksaeV, V., Moscoso, R., Mpodozis, C., Nasi, C., Gordillo, C.E., 1988. Tertiary Andean magmatism in Chile and Argentina between 28°S and 33°S: Correlation of magmatic chemistry with a changing Benioff zone. *Journal of South American Earth Sciences* 1, 21-38.
- Lebtí, P.P.T., J.-C.; Wörner, G.; Fornari, M., 2006. Neogene and Quaternary ignimbrites in the area of Arequipa, Southern Peru: Stratigraphical and petrological correlations. *Journal of Volcanology and Geothermal Research*, 251-275.
- Leeman, W.P., Phelps, D.W., 1981. Partitioning of rare earths and other trace elements between sanidine and coexisting volcanic glass. *Journal of Geophysical Research: Solid Earth (1978–2012)* 86, 10193-10199.
- Lindsay, J.M., De Silva, S., Trumbull, R., Emmermann, R., Wemmer, K., 2001a. La Pacana caldera, N. Chile: a re-evaluation of the stratigraphy and volcanology of one of the world's largest resurgent calderas. *Journal of Volcanology and Geothermal Research* 106, 145-173.
- Lindsay, J.M., Schmitt, A.K., Trumbull, R.B., De Silva, S.L., Siebel, W., Emmermann, R., 2001b. Magmatic evolution of the La Pacana caldera system, Central Andes, Chile: Compositional variation of two cogenetic, large-volume felsic ignimbrites. *Journal of Petrology* 42, 459-486.
- Lipman, P.W., 1984. The roots of ash flow calderas in western North America: Windows into the tops of granitic batholiths. *Journal of Geophysical Research: Solid Earth* 89, 8801-8841.
- Lipman, P.W., 2007. Incremental assembly and prolonged consolidation of Cordilleran magma chambers: Evidence from the Southern Rocky Mountain volcanic field. *Geosphere* 3, 42-70.
- Lucassen, F., Escayola, M., Romer, R.L., Viramonte, J., Koch, K., Franz, G., 2002. Isotopic composition of Late Mesozoic basic and ultrabasic rocks from the Andes (23–32 S)—implications for the Andean mantle. *Contributions to Mineralogy and Petrology* 143, 336-349.
- Mamani, M., Tassara, A., Wörner, G., 2008. Composition and structural control of crustal domains in the central Andes. *Geochemistry, Geophysics, Geosystems* 9, Q03006.

- Mamani, M., Wörner, G., Sempere, T., 2010. Geochemical variations in igneous rocks of the Central Andean orocline (13 S to 18 S): Tracing crustal thickening and magma generation through time and space. *Geological Society of America Bulletin* 122, 162-182.
- McDonough, W.F., Sun, S.s., 1995. The composition of the Earth. *Chemical Geology* 120, 223-253.
- McQuarrie, N., Ehlers, T.A., Barnes, J.B., Meade, B., 2008. Temporal variation in climate and tectonic coupling in the central Andes. *Geology* 36, 999-1002.
- Morgan, G.B., London, D., Luedke, R.G., 1998. Petrochemistry of Late Miocene Peraluminous Silicic Volcanic Rocks from the Morococala Field, Bolivia. *Journal of Petrology* 39, 601-632.
- Muffler, L.J.P., 1979. Assessment of geothermal resources of the United States--1978. US Department of the Interior, Geological Survey.
- Naranjo, P.C., 1992. Hoja Salar de la Isla-Carta Geologica de Chile, No. 72, In: *Mineria, S.N.d.G.y. (Ed.)*. Servicio Nacional de Geologia y Minería, Santiago
- Noble, D.C., Farrar, E., Cobbing, E.J., 1979. The Nazca Group of south-central Peru: Age, source, and regional volcanic and tectonic significance. *Earth and Planetary Science Letters* 45, 80-86.
- Oliver, M.A., Webster, R., 1990. Kriging: a method of interpolation for geographical information systems. *International Journal of Geographical Information Systems* 4, 313-332.
- Oncken, O., Hindle, D., Kley, J., Elger, K., Victor, P., Schemmann, K., 2006. Deformation of the Central Andean Upper Plate System — Facts, Fiction, and Constraints for Plateau Models, In: Oncken, O., Chong, G., Franz, G., Giese, P., Götze, H.-J., Ramos, V., Strecker, M., Wigger, P. (Eds.), *The Andes*. Springer Berlin Heidelberg, pp. 3-27.
- Ort, M.H., 1993. Eruptive processes and caldera formation in a nested downsag-collapse caldera: Cerro Panizos, central Andes Mountains. *Journal of Volcanology and Geothermal Research* 56, 221-252.
- Ort, M.H., Coira, B.L., Mazzoni, M.M., 1996. Generation of a crust-mantle magma mixture: magma sources and contamination at Cerro Panizos, central Andes. *Contrib. Mineral. Petrol.* 123, 308-322.
- Pawlowsky-Glahn, V.E., J.J., 2006. Compositional data and their analysis: an introduction, In: Buccianti, A.M.-F., G.; Pawlowsky-Glahn, V. (Ed.), *Compositional Data Analysis in the Geosciences: From Theory to Practice*. The Geological Society of London, pp. 1-10.
- Petrinovic, I.A., Martí, J., Aguirre-Díaz, G.J., Guzmán, S., Geyer, A., Paz, N.S., 2010. The Cerro Aguas Calientes caldera, NW Argentina: An example of a tectonically controlled, polygenetic collapse caldera, and its regional significance. *Journal of Volcanology and Geothermal Research* 194, 15-26.
- Quang, C.X., Clark, A.H., Lee, J.K.W., Hawkes, N., 2005. Response of Supergene Processes to Episodic Cenozoic Uplift, Pediment Erosion, and Ignimbrite Eruption in the Porphyry Copper Province of Southern Peru. *Econ. Geol.* 100, 87-114.
- Redwood, S.D., 1987. The Soledad Caldera, Bolivia: A Miocene caldera with associated epithermal Au-Ag-Cu-Pb-Zn meralization. *Geol Soc America Bulletin* 99, 395-404.
- Richards, J.P., Ullrich, T., Kerrich, R., 2006. The late Miocene–Quaternary Antofalla volcanic complex, southern Puna, NW Argentina: protracted history, diverse petrology, and economic potential. *Journal of Volcanology and Geothermal Research* 152, 197-239.
- Salisbury, M.J., Jicha, B.R., De Silva, S.L., Singer, B.S., Jimenez, N.C., Ort, M.H., 2011.  $^{40}\text{Ar}/^{39}\text{Ar}$  chronostratigraphy of Altiplano-Puna volcanic complex ignimbrites reveals the development of a major magmatic province. *Geological Society of America Bulletin* 123, 821-840.

- Schmitz, M., Heinsohn, W.-D., Schilling, F., 1997. Seismic, gravity and petrological evidence for partial melt beneath the thickened central Andean crust (21–23 S). *Tectonophysics* 270, 313-326.
- Schnurr, W.B.W., Trumbull, R.B., Clavero, J., Hahne, K., Siebel, W., Gardeweg, M., 2007. Twenty-five million years of silicic volcanism in the southern central volcanic zone of the Andes: Geochemistry and magma genesis of ignimbrites from 25 to 27 °S, 67 to 72 °W. *Journal of Volcanology and Geothermal Research* 166, 17-46.
- Sébrier, M., Soler, P., 1991. Tectonics and magmatism in the Peruvian Andes from late Oligocene time to the Present. *Andean magmatism and its tectonic setting* 265, 259-278.
- Seggiaro, R., Aniel, B., 1989. Los ciclos piroclásticos del área Tiomayo-Coranzulí, Provincia de Jujuy. *Revista de la Asociación Geológica Argentina* 44, 394-401.
- Siebel, W., Schnurr, W.B.W., Hahne, K., Kraemer, B., Trumbull, R.B., Bogaard, P.v.d., Emmermann, R., 2001. Geochemistry and isotope systematics of small- to medium-volume Neogene-Quaternary ignimbrites in the southern central Andes: evidence for derivation from andesitic magma sources. *Chemical Geology* 171, 213-237.
- Soler, M.M., Caffè, P.J., Coira, B.L., Onofre, A.T., Kay, S.M., 2007. Geology of the Vilama caldera: A new interpretation of a large-scale explosive event in the Central Andean plateau during the Upper Miocene. *Journal of Volcanology and Geothermal Research* 164, 27-53.
- Thouret, J.C., Wörner, G., Gunnell, Y., Singer, B., Zhang, X., Souriot, T., 2007. Geochronologic and stratigraphic constraints on canyon incision and Miocene uplift of the Central Andes in Peru. *Earth and Planetary Science Letters* 263, 151-166.
- Tosdal, R.M., Clark, A.H., Farrar, E., 1984. Cenozoic polyphase landscape and tectonic evolution of the Cordillera Occidental, southernmost Peru. *Geol.Soc.Am.Bull.* 95, 1318-1332.
- Tosdal, R.M., Farrar, E., Clark, A.H., 1981. K-Ar Geochronology of the Late Cenozoic volcanic rocks of the Cordillera Occidental, southernmost Peru. *J. Volcanol. Geotherm. Res.* 10, 157-173.
- Walker, G., 1983. Ignimbrite types and ignimbrite problems. *Journal of Volcanology and Geothermal Research* 17, 65-88.
- White, S.M., Crisp, J.A., Spera, F.J., 2006. Long - term volumetric eruption rates and magma budgets. *Geochemistry, Geophysics, Geosystems* 7.
- Wörner, G., Hammerschmidt, K., Henjes-Kunst, F., Lezaun, J., Wilke, H., 2000. Geochronology ( $^{40}\text{Ar}/^{39}\text{Ar}$ , K-Ar and He-exposure ages) of Cenozoic magmatic rocks from Northern Chile (18-22 degrees S): implications for magmatism and tectonic evolution of the central Andes. *Revista Geologica De Chile* 27, 205-240.
- Wörner, G., Moorbath, S., Harmon, R.S., 1992. Andean Cenozoic volcanic centers reflect basement isotopic domains. *Geology* 20, 1103-1106.
- Wörner, G.U., D.; Kohler, I.; Seyfried, H., 2002. Evolution of the West Andean Escarpment at 18°S (N. Chile) during the last 25 Ma: uplift, erosion and collapse through time. *Tectonophysics*, 183-198.
- Yáñez, G., Cembrano, J., Pardo, M., Ranero, C., Selles, D., 2002. The Challenger–Juan Fernández–Maipo major tectonic transition of the Nazca–Andean subduction system at 33–34 S: geodynamic evidence and implications. *Journal of South American Earth Sciences* 15, 23-38.
- Yáñez, G.A., Ranero, C.R., Huene, R., Díaz, J., 2001. Magnetic anomaly interpretation across the southern central Andes (32–34 S): The role of the Juan Fernández Ridge in the late Tertiary evolution of the margin. *Journal of Geophysical Research: Solid Earth* (1978–2012) 106, 6325-6345.



- Yuan, X., Sobolev, S., Kind, R., 2002. Moho topography in the central Andes and its geodynamic implications. *Earth and Planetary Science Letters* 199, 389-402.
- Yuan, X., Sobolev, S., Kind, R., Oncken, O., Bock, G., Asch, G., Schurr, B., Graeber, F., Rudloff, A., Hanka, W., 2000. Subduction and collision processes in the Central Andes constrained by converted seismic phases. *Nature* 408, 958-961.
- Zandt, G., Beck, S., Ruppert, S., Ammon, C., Rock, D., Minaya, E., Wallace, T., Silver, P., 1996. Anomalous crust of the Bolivian Altiplano, central Andes: Constraints from broadband regional seismic waveforms. *Geophysical research letters* 23, 1159-1162.
- Zaraisky, G.P., Aksyuk, A.M., Devyatova, V.N., Udoratina, O.V., Chevychelov, V.Y., 2009. The Zr/Hf ratio as a fractionation indicator of rare-metal granites. *Petrology* 17, 25-45.

## SUMMARY, CONCLUSIONS AND OUTLOOK

Mechanisms and processes in a subduction orogeny like the Andes are very complex and linked to each other, e.g. active deformation, uplift and magmatism associated crustal growth and ore formation are closely related and make the convergent margin of the Andes a perfect site for investigating these feedbacks. Metaphorically speaking, many parts of the puzzle are still missing due to the complexity of the system and the dimensions and different scales that need to be considered.

This PhD thesis investigated timing, cause and location of “ignimbrite flare ups” during the evolution of the Central Andean uplift and related volcano-tectonic structures and calderas with shallow intrusive stocks to mineralization by applying methods of remote sensing, GIS and geospatial statistics together with traditional geological fieldwork,  $^{40}\text{Ar}/^{39}\text{Ar}$  geochronology and geochemical analysis. Timing of ignimbrites, their composition and volume are closely linked to the thermal and structural evolution of the crust, partial crustal melting and magmatism in the mantle wedge related to the subduction of the Nazca plate and were therefore used as tracers of these processes. With our results, we add some more parts to the n-dimensional puzzle of the Andean orogeny. Our main results and conclusions are as follows:

### REGIONAL SCALE (SOUTHERN PERU):

- 1) We characterized and classified different types of alteration related to volcano-tectonic structures and proposed an index of alteration based on typical IR absorption features of alteration minerals. Together with our geochronological results, we propose that buried and overprinted caldera structures located in the area are related to pulses of ignimbrite eruptions occurring at 22 Ma, 14 Ma, 9 Ma and, rather locally, between 6 Ma and 3 Ma. Associated stratovolcanoes of Barroso age (6-3 Ma) are strongly affected by alteration, ranging from silicification to argillic alteration. The large-volume ignimbrite eruptions are temporally associated with a backward migration of the arc and slab-steepening (after ~24 Ma) (Fig. 1). The model of ore formation over a shallowing subduction zone or during the initial steepening of a formerly flat subduction zone related to fluid release proposed by Kay and Mpodozis (2001) and makes these alteration settings target areas for mineral exploration.
- 2) Comparing the stratigraphic record east of the drainage divide in southern Peru to stratigraphy found by other authors for the western escarpment, we found that the ~20 Ma Nazca age (and probably the ~14 Ma Huaylillas age) are completely absent on the

eastern part of the drainage divide. This striking difference either argues for those ignimbrite eruptions being very asymmetrical, or for high rates of incision and denudation in the east, whereas the plateau-forming Nazca and Huaylillas ignimbrites are well preserved on the western escarpment. We argue that this might be due to uplift caused by the arrival of the Nazca ridge at that latitude after ~12 Ma, accompanied by a change in precipitation towards more humid conditions on the eastern side of the orogen.

- 3) Based on incision rates observed for river valleys draining towards the Atlantic, we suggest a minimum incision of ~300 m prior to 14 Ma, of ~500-800 m after ~6 Ma (in the Río Caracha valley and the Río Visca valley) and renewed incision of 200 to 300 m after ~3.8 Ma. For the Visca valley, we know of at least one more event (~9.4 Ma) that filled the valley and cannot be quantified in terms of re-incision. Suggested causes for incision and changes in incision rates are uplift (mainly from 14 Ma to 3.8 Ma) and a change in climate and drainage system with related base-level changes. Our findings agree with an increase of erosion rates in the Eastern Cordillera at 15-10 Ma (Gregory-Wodzicki, 2000) that would have changed the drainage pattern. Uplift in the order of 2,000-3,500m in the Altiplano and Eastern Cordillera since ~10 Ma (Gregory-Wodzicki, 2000; Thouret et al., 2007) are confirmed by river incision of at least 1 km during that time, with at least one more phase of incision (9-6 Ma) that cannot be quantified.

#### ANDEAN SCALE:

- 1) Isotopic signatures containing information about the lower crust were used to delineate basement structures by creating kriging models, together with an error surfaces for  $^{208}\text{Pb}/^{204}\text{Pb}$ ,  $^{207}\text{Pb}/^{204}\text{Pb}$  and  $^{206}\text{Pb}/^{204}\text{Pb}$ ,  $^{143}\text{Nd}/^{144}\text{Nd}$  and Inverse Distance Weighing (IDW) interpolation for  $^{87}\text{Sr}/^{86}\text{Sr}$ .
- 2) Applying cluster analysis to clr-transformed major and trace element data, we grouped ignimbrites according to geochemical characteristics and compared our results to traditional geochemical parameters. Based on major elements, we found a rhyolitic and a dacitic “end-member”. Those “end-members” overlap in REE compositions with more or less pronounced negative Eu anomaly, depletion of MREEs (possibly due to amphibole fractionation) and enrichment/depletion in LREE. Based on these results, we argue, that a distinction between “rhyolitic, crystal-poor, small-volume” and “large-volume, crystal-rich monotonous intermediate” is insufficient to capture differences in ignimbrite evolution and genesis. The large-volume, ca. 19 Ma Oxaya ignimbrite, for

example, is compositionally very distinct from the ~4 Ma Atana ignimbrite, implying a different genesis model than suggested for the large-volume APVC ignimbrites.

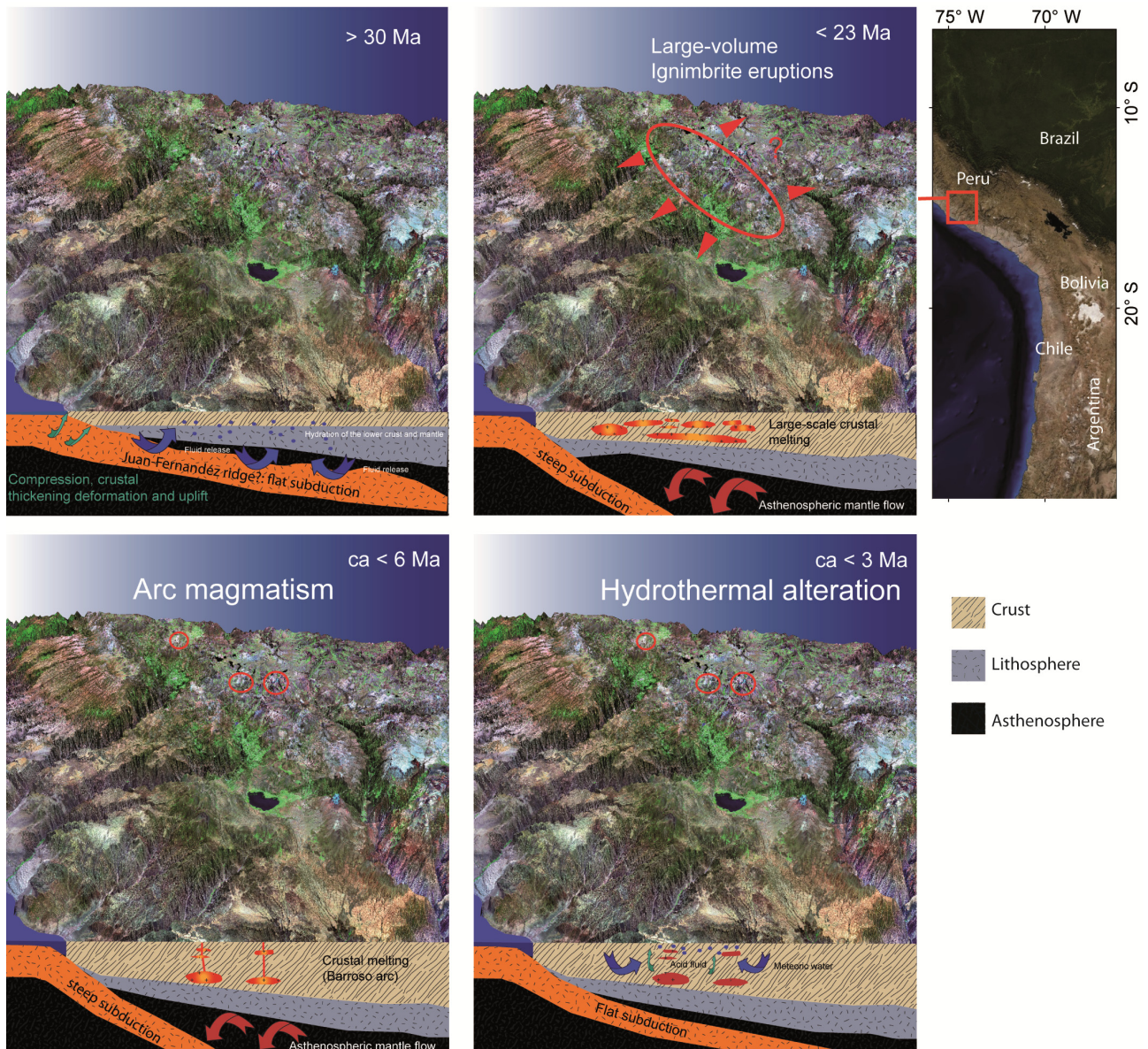


Fig. 1: Schematic lithospheric cross sections across the Southern Peruvian present-day flat-slab transect showing temporal changes in subducting slab geometry (ridge subduction?) together with related crustal processes as an example for the proposed relationships between slab geometry, ridge subduction and ignimbrite pulses. The Landsat image of the study area in Southern Peru is draped over ASTER DEM data. Prior to 24 Ma the active arc had migrated towards the east due to flat subduction (ridge subduction?). Crustal thickness was probably half of its present-day thickness. A first stage of deformation and uplift are well documented after 26 Ma. Big ignimbrite eruptions occurred over a steepening slab (~22 Ma and ~14 Ma), with large-scale melting of the “conditioned” crust in the wake of the ridge (or at least flat-slab setting in Southern Peru (Sandeman, 1995). Backward migration of the arc is reflected in local pyroclastic eruptions and stratovolcanoes of Huayllillas (24-10 Ma) and Barroso age (6-3 Ma). The latter stratovolcanoes are characterized by strong hydrothermal alteration, ranging from silicification to argillic that was mapped and characterized in the present work. After 14 to 10 Ma another stage of uplift occurred, documented by high incision rates (Thouret et al., 2007) and this study).

This finding agrees with differences in Sr isotopes, arguing for less crustal assimilation, possibly due to the thinner and colder crust at that time. Most rhyolitic ignimbrites are concentrated north and south of the Northern Puna, with only minor rhyolites as more differentiated equivalents of the prominent dacites occurring there as described by De Silva and Gosnold (2007). This observation is consistent with the model proposed for the APVC ignimbrites (De Silva and Gosnold, 2007), with accumulation of large bodies of dacitic magma in the upper crust with time, fed by mantle input. It is important to note, that all these ignimbrites are younger than 10 Ma, while samples to the north and south record ages up to 26 Ma and therefore times with a crust that was not as thick and thermally evolved as assumed for the APVC.

- 3) Discriminant analysis on clr-transformed major and REE data was shown to be a feasible tool for fingerprinting ignimbrites based on subtle differences in composition.
- 4) We extend the concept of ignimbrite “flare-ups” proposed by De Silva et al. (1989) to an Andean scale from Southern Peru to the southernmost caldera (Incapillo caldera) and found a N-S younging of pulses, starting the 22 Ma eruption of the Nazca ignimbrites and ending with the last pulse of the APVC at 2 Ma. We propose that “super-eruptions” on the scale of more than 1000 km<sup>3</sup> occurred in the wake of the subducting Juan-Fernandez ridge due to large-scale melting of the “conditioned” crust due to strong, renewed asthenospheric mantle flow over a steepening slab (Fig.1). Differences in crustal thickness at the time of eruption might be in a causal relationship with differences in composition observed for the APVC large-volume ignimbrites in comparison to the Oxaya and Nazca ignimbrites. The latter are more rhyolitic and more radiogenic Sr isotopic composition, arguing for a higher crustal component. Our total estimate of eruptive volumes is 31,000 km<sup>3</sup>, with 2,400 km<sup>3</sup> for Southern Peru, 2,700 km<sup>3</sup> for Southernmost Peru, 8,400 km<sup>3</sup> for the Altiplano, 14,200 km<sup>3</sup> for the Northern Puna and 3,100 km<sup>3</sup> for the Southern Puna segments. The total estimates for the northern segments 1-3 and the Northern Puna are sub-equal, however calderas and thus intra-caldera volumes for ignimbrites in these segments are not known and due to higher age, preservation level for the ignimbrites is much lower. Thus, it may be possible, that the latter ignimbrites represent volumes greater than in the Northern Puna. If further studies show that this is the case, the concept of an APVC flare-up should be revised and not viewed as a regionally and temporally restricted event of high-magma flux and batholith construction. Instead, we suggest a paradigm shift towards a dynamic model, with the “flare up” as a moving entity that has progressed across the Andes during the past 25 Ma, probably related to ridge subduction, with the

Northern Puna flare up only being the most recent and best preserved remnant, and the Southern Puna Cerro Galán eruption possibly heralding another flare-up. This hypothesis is strengthened by the fact that seismic tomographic studies (Heit et al., 2007; Koulakov et al., 2006) indicate higher upper mantle temperatures today beneath the Puna plateau than beneath the Altiplano and the APVC.

Our model is in agreement with the proposed younging of shortening and plateau development (Allmendinger et al., 1997; Riller and Oncken, 2003) and shows the intricate relationship between changes in slab geometry, ridge-subduction, deformation and uplift, magmatism and ore formation.

- 5) We provide a geo-service tool (WMA) for Andean ignimbrites that includes a wealth of data and metadata for future research that can be viewed, queried and edited upon request.

However, many questions are left open, are only answered partially or even lead to more questions to be answered. Some of these questions involve the mechanism behind the big Nazca and Oxaya eruptions, and whether this is different from the mechanism of the large-volume APVC ignimbrites. Differences in composition and the striking observation that we find almost no trace of these ignimbrites east of the western escarpment either argues for very asymmetric eruptions or high erosion rates towards the east. For the Nazca ignimbrites, erosion and denudation might have removed a lot of material due to higher humidity. The arid conditions on the Altiplano argue against such a mechanism for the Oxaya ignimbrites. However, we do not know the exact timing of the climatic change. Furthermore, for many ignimbrites in Southern Peru and Northern Chile, calderas are not known and distribution, thickness and age of the deposit not well constrained. More detailed studies addressing these issues, as well as changes in slab geometry over time are necessary to further develop the reasoning behind a dynamic flare-up concept proposed here. But perhaps...

“The more you know, the more you realize how much you don't know - the less you know, the more you think you know.”

(David T. Freeman)

## REFERENCES:

- Allmendinger, R.W., Jordan, T.E., Kay, S.M., Isacks, B.L., 1997. The Evolution of the Altiplano-Puna Plateau of the Central Andes. *Annu. Rev. Earth Planet. Sci.* 27, 139-174.
- De Silva, S.L., 1989. Altiplano-Puna volcanic complex of the central Andes. *Geology* 17, 1102-1106.
- De Silva, S.L., Gosnold, W.D., 2007. Episodic construction of batholiths: Insights from the spatio-temporal development of an ignimbrite flare-up. *Journal of Volcanology and Geothermal Research* 167, 320-335.
- Riller, U., Oncken, O., 2003. Growth of the central Andean Plateau by tectonic segmentation is controlled by the gradient in crustal shortening. *The Journal of Geology* 111, 367-384.
- Sandeman, H.A.C., A.H.; Farrer, E., 1995. An Integrated Tectono-Magmatic Model for the Evolution of the Southern Peruvian Andes (13°-20°S) since 55 Ma. *International Geology Review*, 1039-1073.
- Thouret, J.C., Wörner, G., Gunnell, Y., Singer, B., Zhang, X., Souriot, T., 2007. Geochronologic and stratigraphic constraints on canyon incision and Miocene uplift of the Central Andes in Peru. *Earth and Planetary Science Letters* 263, 151-166.

## PERSONAL INFORMATION

## Melanie Brandmeier



📍 Valentinsbreite 9, 37077 Göttingen, Germany

☎ +495513922216 📠 +4917632496107

✉ [mbrandm@gwdg.de](mailto:mbrandm@gwdg.de)

Sex: female | Date of birth: 08/10/1980 | Nationality: German

## WORK EXPERIENCE

Since 15.11.2010

**Research Assistant (pHD)**

Georg-August-University Göttingen, GZG, Institute for Geochemistry

- Geochemistry, Remote sensing (ASTER satellite data, DEMs) and GIS applications
- Fieldwork Peru (September 2011 and September/October 2012)

01.07.-01.10.2009

**Scholarship**

University of Wollongong, Australia

October 2009

**Visiting scientist CSIRO, Perth**

- Analysis of multispectral ASTER data, alteration mapping

01.03.- 30.06..2009

**Research Assistant**

Georg-August-University Göttingen, GZG, Institute for Geochemistry

- GIS, Remote sensing,
- writing of a DFG proposal with Prof. Dr. G. Wörner

## EDUCATION AND TRAINING

2006-2008

**Master (Diplom) in Geography, Geology and Geochemistry**  
**Master-Thesis: "Raten und Prozesse der Tafoniverwitterung auf Korsika"**

Grade A  
with honors

Eberhard-Karls-Universität Tübingen

Subjects included: GIS, Remote Sensing (ENVI), Geochemistry, stable and radiogenic Isotopes, Geomorphology, Climatology, Paleoclimatology, Thermodynamics for Geoscientists, Marine Geochemistry, Geochemistry of the earth crust and mantle, Magmatic, metamorphic and sediment petrology, environmental Geochemistry



- 2005-2006 **Stay abroad**  
 Universidad Nacional de Tucumán, Argentina  
 Subjects included: Clay mineral systematics and XRD, Optical Mineralogy, ArcGIS for Geoscientists, Geology
- 2003-2005 **Bachelor (intermediate Diplom) in Geography, Latin America Studies and Environmental Psychology** Grade A  
 KU Eichstätt-Ingolstadt  
 Subjects included: Soil systematic and formation processes, Geomorphology, Physical Geography, Climatology, Vegetation Geography
- 2000-2002 **Management Assisstant** Grade A  
 Academy for management and languages (Foley) Freiburg
- 1991-2000 **Abitur** 1.7  
 Wernher von Braun Gymnasium Friedberg

## PERSONAL SKILLS

Mother tongue(s) German

Other language(s)

	UNDERSTANDING		SPEAKING		WRITING
	Listening	Reading	Spoken interaction	Spoken production	
English	C1	C1	C1	C1	C1
	Toefl				
Spanish	B2	B2	B2	B2	B2
French	A1	A1	A1	A1	A1
	Abitur				

Levels: A1/2: Basic user - B1/2: Independent user - C1/2 Proficient user  
 Common European Framework of Reference for Languages

**Job-related skills**

- good command of ArcGIS, ENVI, RiverTools
- Experience in Fieldspectrometry and alteration mapping
- Experience in interdisciplinary work as Geographer

**Computer skills**

- good command of Microsoft Office™ tools
- good command of Adobe Illustrator
- good command of ArcGIS, ENVI and RiverTools

**Driving licence** Full current driving license

## ADDITIONAL INFORMATION

## Publications

- Brandmeier, M., 2010, Remote sensing of Carhuarazo volcanic complex using ASTER imagery in Southern Peru to detect alteration zones and volcanic structures – a combined approach of image processing in ENVI and ArcGIS/ArcScene: Geocarto International, v. 25, p. 629-648.
- Brandmeier, M., Kuhlemann, J., Krumrei, I., Kappler, A., and Kubik, P.W., 2011, New challenges for tafoni research. A new approach to understand processes and weathering rates: Earth Surface Processes and Landforms, v. 36, p. 839-852.
- Brandmeier, M., Erasmi, S., Hansen, C., Höweling, A., Nitzsche, K., Ohlendorf, T., Mamani, M., Wörner, G., 2013. Mapping patterns of mineral alteration in volcanic terrains using ASTER data and field spectrometry in Southern Peru. Journal of South American Earth Sciences 48, 296-314

## Conferences

- Székely, B., Karátson, D., Brandmeier, M., Wörner, G., Dominger, P., Nothegger, C.: 2011, Erosional patterns of ancient ignimbrite paleosurface in the Central Andes: Geophysical Research Abstracts, Vol. 13, EGU General Assembly 2011.
- Brandmeier, M., Erasmi, Wörner, G., 2012, Mapping patterns of mineral alteration in volcanic terrains using ASTER data and field spectrometry in Southern Peru: 32. Wissenschaftlich-Technische Jahrestagung der DGPF.
- Brandmeier, M., 2010, Remote sensing of Carhuarazo volcanic complex using ASTER imagery in Southern Peru to detect alteration zones and volcanic structures – a combined approach of image processing in ENVI and ArcGIS/ArcScene: Vol. 13, EGU General Assembly 2011.

## References

Prof. Dr. Wolfgang Siebel  
Supervisor of Radiogenic Isotope Lab  
Wilhelmstr. 56  
72074 Tübingen  
phone: +49(0)7071/2974991  
e-mail: [wolfgang.siebel@unituebingen.de](mailto:wolfgang.siebel@unituebingen.de)

Dr. Stefan Erasmi  
Geographisches Institut  
Abt. Kartographie, GIS & Fernerkundung  
Goldschmidtstr. 5, 37077 Göttingen  
Phone: +49(0)551/39-8003  
e-mail: [serasmi@uni-goettingen.de](mailto:serasmi@uni-goettingen.de)

Prof. Dr. Gerhard Wörner  
Georg-August-Universität Göttingen  
Fakultät für Geowissenschaften und Geographie  
Geowissenschaftliches Zentrum Göttingen (GZG)  
Abteilung Geochemie  
Goldschmidtstraße 1, 37077 Göttingen  
Phone: +49(0)551/39-3971  
e-mail: [gwoerne@gwdg.de](mailto:gwoerne@gwdg.de)  
Internet: [www.uni-geochem.gwdg.de](http://www.uni-geochem.gwdg.de)



Melanie Brandmeier  
Göttingen, 24.01.2014